Numerical and Experimental Investigation of the Centrifugal Solar Particle Receiver

Numerische und Experimentelle Untersuchung eines Zentrifugalen Solarpartikelreceivers

Der Fakultät für Maschinenwesen der Rheinisch-Westfälischen Technischen Hochschule Aachen vorgelegte Dissertation zur Erlangung des akademischen Grades eines Doktors der Ingenieurwissenschaften

von

Serdar Hiçdurmaz

ABSTRACT

Particle solar receivers promise economical and operational advantages compared to molten salt based solar receivers. The Centrifugal Solar Particle Receiver (CentRec) is a promising design because it allows active control on particle residence time and particle outlet temperature. Particles moving as a thin film in an inclined rotating drum under centrifugal and gravity forces are heated by concentrated sunlight. In the present work, the main objective is to develop a numerical thermal model and evaluate the thermal performance of the CentRec. To do so, particles are modeled as discrete phase instead of continuum to better reflect the particle interactions, and resulting effects of these interactions, e.g. mixing, on the thermal performance. The Discrete Element Method (DEM) tool LIGGGHTS is used to simulate the particle motion. The developed simulation model is validated with a set of experiments conducted. A scaling approach is developed to scale-down the particle film characteristics in CentRec because of huge computational power requirement of large-scale receivers. An optical system consisting of diffuse lamps, GoPro cameras etc. is developed to record the particle motion in CentRec. A tracer recognition and tracking algorithm is developed to detect the particles' velocity and the film thickness for various combinations of particle mass flow rate and receiver rotation speed. A separate thermal model is developed in MATLAB, which uses the particle positions calculated with the DEM simulation. All heat transfer mechanisms being effective in CentRec are developed, validated and embedded to the main thermal code. A novel radiation penetration model and a novel reflection model are developed to distribute the solar irradiation to the individual particles. Moreover, long-range and short-range thermal radiation models are considered separately to calculate the emissive heat exchange between large surfaces and between individual particle pairs, respectively. All radiation models are based on some approximations to reduce the computational burden significantly. Besides, a particle scale conduction model from literature is modified for the current application. Supplementary sub-models, namely convection and conduction loss models, are also developed and integrated to the thermal model. The complete thermal model is applied to several CentRec sizes to measure the thermal performance. A considerable effect of the particle mass flow rate on the receiver thermal efficiency is found. Convection loss is the main thermal loss mechanism for the considered receiver sizes. The thermal losses are quantified for various combinations of operational parameters and receiver sizes. The findings are to be used for further scaling-up the CentRec technology.

Keywords: Particle receivers, discrete element method, concentrating solar power, centrifugal solar particle receiver

ZUSAMMENFASSUNG

Partikel-Solarreceiver versprechen wirtschaftliche und betriebliche Vorteile im Vergleich zu Solarreceivern auf der Basis von Flüssigsalz. Der Zentrifugal- Partikelreceiver (CentRec) ist ein vielversprechendes Konzept, da er eine aktive Steuerung der Partikelverweilzeit und der Partikelaustrittstemperatur ermöglicht. Die Partikel bewegen sich als dünner Film in einer geneigten, rotierenden Trommel unter Zentrifugal- und Gravitationskräften und werden durch konzentriertes Sonnenlicht erhitzt. Das Hauptziel der vorliegenden Arbeit besteht darin, ein numerisches thermisches Receivermodell zu entwickeln und die thermische Leistung des CentRec zu bewerten. Zu diesem Zweck werden die Partikel als diskrete Phase statt als Kontinuum modelliert, um die Partikelinteraktionen und die daraus resultierenden Auswirkungen dieser Interaktionen, z. B. die Vermischung, auf die thermische Leistung besser zu berücksichtigen. Für die Simulation der Partikelbewegung wird die Diskrete-Elemente-Methode (DEM) mit dem Software-Paket LIGGGHTS verwendet. Das entwickelte Simulationsmodell wird mit einer Reihe von durchgeführten Experimenten validiert. Es wird ein Skalierungsansatz entwickelt, um die Eigenschaften des Partikelfilms in CentRec zu verallgemeinern, da große Receiver eine enorme Rechenleistung benötigen würden. Ein optisches System bestehend aus Lampen, Kameras usw. wird entwickelt, um die Partikelbewegung im CentRec aufzuzeichnen. Es wird ein Algorithmus zur Erkennung und Verfolgung von Tracer-Partikeln entwickelt, um die Geschwindigkeit der Partikel und die Filmdicke für verschiedene Kombinationen von Partikelmassenstrom und Receiverdrehzahl zu ermitteln. Ein separates thermisches Modell wird in MATLAB entwickelt, das die mit der DEM-Simulation berechneten Partikelpositionen verwendet. Alle Wärmeübertragungs-mechanismen, die in CentRec wirksam sind, werden modelliert, validiert und in den thermischen Hauptcode eingebettet. Ein neuartiges Strahlungsdurchdringungsmodell und ein neuartiges Reflexionsmodell werden entwickelt, um die Sonneneinstrahlung auf die einzelnen Partikel zu verteilen. Darüber hinaus werden thermische Fern- und Nahbereichsstrahlungsmodelle getrennt betrachtet, um den Strahlungsaustausch zwischen großen Oberflächen bzw. zwischen einzelnen Partikelpaaren zu berechnen. Alle Strahlungsmodelle beruhen auf Näherungen, um den Rechenaufwand erheblich zu verringern. Außerdem wird ein aus der Literatur stammendes Partikel-Wärmeleitungsmodell für die aktuelle Anwendung modifiziert. Ergänzende Untermodelle, nämlich Konvektions- und Leitungsverlustmodelle, werden ebenfalls entwickelt und in das thermische Modell integriert. Das vollständige thermische Modell wird auf verschiedene CentRec-Größen angewandt, um die thermische Leistung zu bestimmen. Es wurde ein erheblicher Einfluss des Partikelmassenstroms auf den thermischen Wirkungsgrad des Receivers festgestellt. Konvektionsverluste sind der Hauptmechanismus für thermische Verluste bei den betrachteten Receivergrößen. Die thermischen Verluste werden für verschiedene Kombinationen von Betriebsparametern und Receivergrößen quantifiziert. Die Ergebnisse sollen für die weitere Skalierung der CentRec-Technologie genutzt werden.

Stichworte: Partikelreceiver, Diskrete-Elemente-Methode, konzentrierende Solarenergie, zentrifugaler solarer Partikelreceiver

ACKNOWLEDGEMENTS

This PhD study could not have been accomplished without help and guidance of several people. Firstly, I would like to express my gratitude to my technical advisor, Dr.-Ing Reiner Buck to give me the chance of pursuing PhD in DLR Institute of Solar Research and to guide me throughout the work with his ideas and insightful feedbacks. Secondly, I would like to thank my academic supervisor Univ.-Prof. Dr.-Ing. Bernhard Hoffschmidt, my co-supervisor Prof. Dr.-Ing. Harald Kruggel-Emden and our institute co-director Univ.-Prof. Dr.-Ing. Robert Pitz-Paal for their continuous support and feedbacks. Dr.-Ing Lars Amsbeck deserves thank for his guidance and encouragements for the first 18-month-period of this study as the advisor.

I also would like to thank to several people, Andreas Krause and Jens Rheinländer for their support in the experiments, Johannes Grobbel for running Monte Carlo simulations for several validation cases and for his collaboration in two conference papers, Markus Alois Reichart for discussions about particle technology, and all colleagues in the Particle Systems Group for their support, ideas and introducing the German language and culture to me.

I would like to give my special thanks to Evan Fair Johnson for insightful discussions sparking off new ideas about particle technologies in the last seven years. His help and collaboration on particle scale heat transfer models and support for the adjustment of his Monte Carlo Ray Tracing code for the “reflection model” calculations are well appreciated.

Finally, I would like to express my deepest gratitude to my mother and deceased father, Gülşen and Münür, and my brother Gökay for their emotional support throughout my life and being such a lovely family. My final thanks are to my beautiful wife, Kübra, for her companionship, support and love.

The author acknowledges the DLR-DAAD Research Fellowship Programme for their financial support during the thesis period.

LIST OF CONTENTS

ABSTRACT iii
ZUSAMMENFASSUNG iv
ACKNOWLEDGEMENTS vi
LIST OF CONTENTS vii
LIST OF FIGURES x
LIST OF TABLES xvi
LIST OF ACRONYMS xviii
LIST OF SYMBOLS xix
1. Introduction 1
1.1 Background and Motivation 1
1.2 Solar Particle Receiver Concepts 2
1.2.1 Centrifugal Solar Particle Receiver Concept 4
1.3 Research Questions and Thesis Overview 6
2. Discrete Element Method (DEM) Model 8
3. Experiment Design and Results 13
3.1 Experimental Set-up 14
3.1.1 CentRec Set-up 14
3.1.2 Optical Elements 15
3.1.3 Experiment Design 15
3.2 Image Processing Routine 16
3.2.1 Tracer Recognition 18
3.2.2 Tracer Tracking 19
3.3 Experiment Results 21
4. DEM Model Validation 27
4.1 Scale – down Approach 27
4.2 DEM Parameter Calibration 36
4.3 Comparison of Experiment and Numerical Results 41
5. Numerical Thermal Model 44

5.1 Radiation Model 47
5.1.1 Radiation Penetration Model 48
5.1.1.1 Model Development 49
5.1.1.2 Model Validation and Application 56
5.1.2 Reflection Model 62
5.1.3 Long-range Thermal Radiation Model 74
5.1.4 Short – range Thermal Radiation Model 77
5.2 Particle Scale Conduction Model 85
5.2.1 Conduction Through Contact Area 86
5.2.2 Conduction Through Interstitial Fluid 88
5.2.3 Inner Particle Conduction 91
5.2.4 Model Validation 92
5.3 Conduction Loss Model 96
5.4 Convection from Cylindrical Cavities 99
6. Thermal Model Application to Centrifugal Solar Particle Receiver 103
6.1 Thermal Coupling Time Step for the CentRec Application 103
6.2 Model Application 108
6.2.1 Effect of Rotational Speed and Particle Mass Flow Rate 109
6.2.2 Effect of the Receiver Size 117
6.3 Sensitivity Analysis 119
6.3.1 Particle Absorptivity 120
6.3.2 Material Thermal Conductivity 122
6.3.3 Aperture Ratio 123
7. Conclusion and Future Work 125
REFERENCES 128
APPENDICES 141
Appendix 1 141
Appendix 2 142

LIST OF FIGURES

Figure 1-1 Illustration of several particle receiver concepts **(a)** free falling particle receiver **(b)** obstructed flow particle receiver **(c)** particle-suspension-in-a-tube receiver. 3

Figure 1-2 (a) Centrifugal solar particle receiver **(b)** particle film descending through rotating receiver wall. 5

Figure 1-3 (a) Schematic view of the centrifugal receiver **(b)** representation of the components of gravity. 6

Figure 3-1 The optical elements ① the ring light ② the camera for the particle tracking ③ the camera for the film thickness ④ the bar light ⑤ the circular pin. 14

Figure 3-2 The picture of dots used for the characterization of the motion between the receiver wall and the camera. 17

Figure 3-3 Pixel deviation from the mean value in one rotation for each tracer point at the corners of the picture of dots based on parameters listed in Table 3-1. 18

Figure 3-4 (a) The undistorted image **(b)** the segmentated and filtered image. 19

Figure 3-5 The pin pressed against the receiver wall **(a)** in empty receiver **(b)** during experiment. 22

Figure 3-6 The film thickness for various mass flow rates and rotational speeds based on parameters listed in Table 3-1.The vertical error bar corresponds the uncertainty of the measurement technique and is the same for all measurement points (± 0.5 mm). It is only shown for the mass flow rate of 0.092 kg/s to provide legibility. The horizontal error bar shows the measurement uncertainty of the device measuring the rotational speed. 23

Figure 3-7 The axial advance of the tracer in one rotation for various mass flow rates and rotational speeds based on parameters listed in Table 3-1. The vertical error bar corresponds the mean standard deviation of measurements. The horizontal error bar shows the measurement uncertainty of the device measuring the rotation speed. 23

Figure 3-8 The ratio of the length of the stationary zone to the cavity circumference for various mass flow rates and rotational speeds based on parameters listed in Table 3-1. The figure is split to two plots to increase legibility of the figure. The vertical error bar corresponds the mean standard deviation of the measurement points. The horizontal error bar shows the measurement of uncertainty of the device measuring the rotation speed. 24

Figure 3-9 Rough representation of the stationary and moving zones, which are depicted with dark brown and light brown colors, respectively. 26

Figure 4-1 (a) Feeding of the particles to the cavity **(b)** location of particle feeder **(c)** the side view of the tilted receiver. 29

Figure 4-2 Time variation of particle outlet mass flow rate for three receiver sizes. 30

Figure 4-3 Tangentially averaged film thickness averaged for 150 turns. The error bar is the mean standard deviation. 0 and 1 in x axis correspond inlet and exit of the receiver, respectively. 32

Figure 4-4 Qualitative comparison of axial velocities for the three receiver sizes. A view of **(a)** stationary zone **(b)** moving zone. The color bar is the axial velocity in m/s. 33

Figure 4-5 The arc-like section volumes to be used in the determination of the velocity profiles. The tangential positions of volumes are 45°, 90° and 135° in counter clockwise direction. The nondimensional axial positions are 0.3, 0.5 and 0.7. 33

Figure 4-6 Axial velocity profile in radial direction at non-dimensional axial position of z = 0.3 for tangential position of **(a)** 45° **(b)** 90° and **(c)** 135°. 34

Figure 4-7 Axial velocity profile in radial direction at non-dimensional axial position of z = 0.5 for tangential position of **(a)** 45° **(b)** 90° and **(c)** 135°. 35

Figure 4-8 Axial velocity profile in radial direction at non-dimensional axial position of z = 0.7 for tangential position of **(a)** 45° **(b)** 90° and **(c)** 135°. 36

Figure 4-9 View of the damming edge at the exit of the receiver. 37

Figure 4-10 View of stationary particles and welded wire mesh from the receiver in operation. 38

Figure 4-11 Comparison of experiment and simulation results for the cases listed in Table 4-3.....39

Figure 4-12 The coefficient pairs (best points) matching the experiment (moving film thickness) results of the combination of various rotational speeds and mass flow rates. 41

Figure 4-13 Comparison of experiment and simulation results in terms of moving film thickness at the non-dimensional axial position of 0.83. The mass flow rate is **(a)** 0.092 kg/s **(b)** 0.218 kg/s **(c)** 0.312 kg/s **(d)** 0.489 kg/s.....43

Figure 4-14 Comparison of experiment and simulation results in terms of particle axial velocity on the surface **(a)** 0.092 kg/s **(b)** 0.218 kg/s **(c)** 0.312 kg/s **(d)** 0.489 kg/s. 43

Figure 5-1 Schematic view of particle scale heat transfer modes. 45

Figure 5-2 Schematic cross-sectional view of the CentRec along with the representative rays: (1) solar irradiation, (2) reflection to other parts of the particle film, (3) reflection to particle distributor, (4) reflection to collector ring, (5) reflection to aperture, i.e. reflection loss. 48

Figure 5-3 Photons striking particle bed in MCRT, showing **(a)** general geometry, and **(b)** a ray reflecting specularly many times before being absorbed. 49

Figure 5-4 (a) Bed absorptivity for various particle absorptivities and solid fractions for β = 45º, where each point is a MCRT simulation result and lines representing best curve fits **(b)** bed absorptivity at various incidence angles and solid fractions, for a particle absorptivity of 0.6 [80]. 51

Figure 5-5 Transmitted fraction of incident radiation at various depths, for f_s =0.60, α_p = 0.60, β=90°. Red and blue lines show results by post-processing the MCRT results with two different methods [80]. 51

Figure 5-6 Transmitted fraction for f_s =0.20, with **(a)** α_p = 1.00, and **(b)** α_p = 0.20 [80]..52

Figure 5-7 Local solid fraction distribution of a particle film taken from CentRec simulation and peak – valley approximation (black and red dots) to find effective bulk solid fraction (red dashed line). Zero depth corresponds the topmost particle plus 1 radius. 53

Figure 5-8 Transmission curves for particle films with a thickness of 20 radii, 8 radii, 6 radii and 4 radii, with particle emissivity of 0.86. 53

Figure 5-9 Two distinct transmission regions: (0-2 radii) a nonlinear decay; (2-8 radii) a linear decay for 90° of incidence angle, 0.64 of bulk solid fraction and 0.86 of particle emissivity. 54

Figure 5-10 2D view of particle film with non-flat free surface due to sparse particles slightly sitting up higher than the rest of the bed. 55

Figure 5-11 Local solid fraction distribution for five different sets of particle positions generated by removing a number of particles from top surface. The film thickness is the z- location of the topmost particle center plus one radius, whereas 0 depth corresponds to wall. 58

Figure 5-12 Transmitted curve and local solid fraction at depths in particle bed, for six incidence angles. Cases I-V represent the original particle bed and beds where a layer of thickness 0.6, 0.8, 1.0, and 1.2 radii has been removed from top, respectively. 59

Figure 5-13 Transmission curve and local solid fraction, for six incidence angles. Cases CR1 and CR2 are from the bottom part of the receiver circumference, and CR3 and CR4 are from the top part of the receiver circumference (Legend same as 60

Figure 5-14 Incidence angle distribution on the receiver wall in CentRec. 61

Figure 5-15 Comparison of MC results and algorithm-based results for four different CentRec simulations. 62

Figure 5-16 The local coordinate system to be used in the reflection model. Azimuth angle (θ) varies between 0 and 2π. Zenith angle (γ) varies between 0 and $\pi/2$. 63

Figure 5-17 Representation of generated parallel rays (red) and reflections from the particle film (black) for **(a)** γ=10° **(b)** γ=45° and **(c)** γ=80°. The blue dots represent particles' center. 64

Figure 5-18 The hemispherical density distribution of the reflected rays. The generated parallel rays have an azimuth angle of 180°. 65

Figure 5-19 (a) Particle film flow in CentRec simulation for a cavity diameter of $100d_p$. **(b)** Meshed particle film surface. The back – yellow surface is the particle distributor and the front – red surface is the collector ring. 66

Figure 5-20 Representation of regions enclosed by zenith angle and azimuth angle intervals for rays emitted from **(a)** discrete surface next to particle distributor **(b)** mid surface to all other surfaces. Black region, white region and gray region represents angle intervals from these two surfaces to the particle distributor, the collector ring and the aperture plane, respectively. The colored regions show the intervals to other discrete surfaces. 68

Figure 5-21 The flow diagram of the reflection model. The blue boxes are calculated in each time step while the green boxes are calculated once for a given input parameter set. 70

Figure 5-22 Representation of generated rays that have an incidence angle of 45° at the aperture. 71

Figure 5-23 Flux distribution on the particle film before any reflection for a discrete surface size of **(a)** $L_{cav}/36$ **(b)** $L_{cav}/18$ and **(c)** $L_{cav}/9$. The unit of the contour is W/m^2. 72

Figure 5-24 Reflection to other parts of the receiver for a discrete surface size of **(a)** $L_{cav}/36$ **(b)** $L_{cav}/18$ and **(c)** $L_{cav}/9$. The unit of the contour is W/m^2. 73

Figure 5-25 Comparison of model and MCRT results for various particle emissivity values in terms of emission loss through the aperture. Wall emissivity equals the particle emissivity for each case. 77
Figure 5-26 (a) Original particle film section **(b)** unrolled particle film section. 79
Figure 5-27 The radiative conductivity for various ray numbers at 1000 K. 80
Figure 5-28 Scatter plot of particle temperatures for ray number of **(a)** 10^1 and **(b)** 10^4 per particle. 80
Figure 5-29 Scatter plot of RDF for all particle pairs (black dots) with the best curve (solid red line) and upper and lower limits representing mean + SD and mean – SD, respectively (dashed red lines). Particle emissivity is 0.86 and bulk solid fraction is 0.5. 81
Figure 5-30 Local solid fraction variation in z direction where wall corresponds to z = 0. 82
Figure 5-31 RDF curves for various distances to the wall for particle emissivity of 0.86 and wall emissivity of 1. 83
Figure 5-32 The RDF curves for particle pairs for various wall emissivities. Particles center lies on **(a)** $0 < z < 1d_p$ **(b)** $1d_p < z < 2d_p$. Particle emissivity is 0.86. 83
Figure 5-33 The RDF curves for particle – wall pairs for different wall emissivities. Each dot represents a single particle. Particle emissivity is 0.86. 84
Figure 5-34 (a) Initial temperature distribution **(b)** steady-state temperature distribution. In both cases, the maximum temperature difference is 10 K. 84
Figure 5-35 The comparison of model results based on derived RDFs with MCRT results. The wall emissivity is assumed the same as the particle emissivity for both cases. 85
Figure 5-36 Schematic view of **(a)** non-contacting particles **(b)** contacting particles with an overlap. 87
Figure 5-37 Schematic view of **(a)** non-contacting particle - wall **(b)** contacting particle - wall with overlap. 88
Figure 5-38 Material thermal conductivity of bauxite particles for various temperatures measured by [134]. 93
Figure 5-39 Comparison of the developed model with the experiment results. 94
Figure 5-40 Contribution of each heat transfer mode to bed thermal conductivity for d_p = 0.4 mm at f_s = 0.613. 95
Figure 5-41 Contribution of each heat transfer mode to film thermal conductivity for particle film sections from the CentRec simulation **(a)** stationary zone (f_s = 0.51) **(b)** moving zone (f_s = 0.49). Particle diameter is 1.2 mm. 96
Figure 5-42 Schematic view of CentRec. The yellow outer shell is the insulation layer, and the black inner shell is the receiver wall. 97
Figure 5-43 Trapezoid prism-shaped cells representing wall and insulation 97
Figure 5-44 Interaction of particles with wall cells. 99
Figure 5-45 Representation of convective and stagnant zones for no-wind condition. 101
Figure 5-46 Experiment results obtained by Flesch et al. [150] along with interpolated results for tilt angle of 45°. Cross marks (x) correspond to experimental measurement points. 102

Figure 6-1 Steady-state temperature distribution on particle film surface for Case I given in Table 6-1 and long-range reduced coupling time step of **(a)** 9.6° **(b)** 19.2° **(c)** 38.4° **(d)** 76.8° **(e)** 153.7° **(f)** 307.4°. The color bar is the temperature with unit of Kelvin. 105

Figure 6-2 Comparison of various bulk - scale reduced coupling time steps in terms of **(a)** radiation loss through aperture and **(b)** particle outlet temperature for the Case I given in Table 6-1. 106

Figure 6-3 (a) Radial temperature distribution at the exit **(b)** outlet temperature at the exit for two different reduced coupling time steps for particle - scale sub-models. Dashed lines are the mean value +/- standard deviation. 107

Figure 6-4 A realistic flux distribution on the particle film provided by [152]. The color bar unit is kW/m^2. The mean heat flux on the aperture is 3 MW/m^2. 109

Figure 6-5 Thermal efficiency and loss percentages for cases considered in Table 6-2. 111

Figure 6-6 Tangentially and temporally averaged steady state temperature profiles **(a)** 167.8 rpm – 73.4 g/s **(b)** 167.8 rpm – 35.7 g/s **(c)** 160.1 rpm - 73.4 g/s **(d)** 160.1 rpm - 35.7 g/s. Non-dimensional axial positions of 0 and 1 corresponds to exit and inlet, respectively. The unit of color bar is Kelvin, and upper and lower limits are 673.15 K and 1350 K, respectively. 113

Figure 6-7 Temperature distribution on the particle film section exposed to the uniform flux for cases that particle scale conduction and radiation heat transfer are enabled and disabled in the simulation. **(a)** 160.1 rpm and 35.7 g/s **(b)** 167.8 rpm and 73.4 g/s. 116

Figure 6-8 Particle outlet temperature variation for the cases in Figure 6-7. Solid lines denote the mean outlet temperature while dashed lines denote +/- mean standard deviation of temperatures of particles at the exit. **(a)** 160.1 rpm and 35.7 g/s **(b)** 167.8 rpm and 73.4 g/s. 117

Figure 6-9 Temperature distribution of layers forming the particle film for Case I in Table 6-5 and for three particle emissivity/absorptivity values. The results for the first three layers are plotted only for absorptivity of one for the sake of legibility because lines overlap completely for the current resolution. 121

Figure 6-10 Effect of particle absorptivity on particle-particle RDF for average particle – wall distance of 3d_p. 122

Figure 6-11 Flux distribution on the particle film for cavity diameter of 17 cm. **(a)** Case II and **(b)** Case III in Table 6-5. The unit of the colorbar is MW/m2. 124

Figure A-1 A particle split by many parallel layers, resulting in spherical segments with different shape and particle volume fraction. 144

Figure A-2 A 2D schematic view of the particle film section. k_1 to k_6 are the layer numbers corresponding to tips of the total 6 unshaded particles with colored circumference. 144

LIST OF TABLES

Table 3-1 Experiment parameters.....16
Table 3-2 Number of the detected tracers. 24
Table 4-1 Receiver dimensions considered in the scale-down approach. 30
Table 4-2 DEM particle properties.....37
Table 4-3 Preliminary DEM Particle Contact Properties. 38
Table 5-1 Cavity dimension considered in the validation study of the reflection model. .71
Table 5-2 Distribution of solar irradiation to particles and other parts of the receiver for the current model and MCRT. 73
Table 6-1 Set of parameters used in the determination of thermal coupling time steps for bulk - scale models (Case I) and particle – scale models (Case II).....104
Table 6-2 The set of parameters considered in the simulation of scaled-down CentRec. 110
Table 6-3 Simulation parameters considered for three different receiver sizes where the mass flow is proportional to the incident power. 118
Table 6-4 Modified simulation parameters for the cases listed in Table 6-3. The mass flow rate and flux at aperture is inversely proportional.....119
Table 6-5 List of cases for various receiver dimensions and operational parameters considered in the sensitivity analysis. 120
Table 6-6 Simulation results for three particle absorptivities in terms of efficiency, losses and particle outlet temperature. Case I in Table 6-5 is considered. 121
Table 6-7 Effect of material thermal conductivity to the temperature of layers at the receiver outlet for Case I in Table 6-5. 123
Table 6-8 The effect of aperture diameter to receiver efficiency, losses and particle outlet temperature for receiver diameters of 17 cm and 25 cm.....124
Table A.1 The coefficients in Eq. (5-1) and (5-2) for particle emissivity of 0.86.....141

LIST OF ACRONYMS

CAD	Computer Aided Drawing
CFD	Computational Fluid Dynamics
CSP	Concentrating Solar Power
DC	Direct Current
DEM	Discrete Element Method
FDC	Finite Difference Code
FEM	Finite Element Method
HSV	Hue Saturation Value
HTF	Heat Transfer Fluid
MCRT	Monte Carlo Ray Tracing
PIV	Particle Image Velocimetry
PTV	Particle Tracking Velocimetry
PV	Solar Photovoltaics
RDF	Radiation Distribution Factor
RGB	Red Green Blue
SD	Standard Deviation
SHIP	Industrial Solar Process Heat
SS	Steady State
STE	Solar Thermal Electricity
TRL	Technology Readiness Level
TSE	Thermal Energy Storage
UDF	User Defined Function
ZBS	Zehner Bauer Schluender Model

LIST OF SYMBOLS

Latin

A_i	Surface area of ith element
A_{surf}	Surface area of the particle film section
A_{tot}	Total area of inner cavity
b	Coefficient of linear fit for transmission decay in the particle film
Bi	Biot number
c	Correction factor in the radiation penetration algorithm
c	Correction factor accounting for artificial softening in conduction model
C	Wall specific heat capacity
c_n	Damping constant in normal direction
c_p	Temperature dependent particle specific heat capacity
c_t	Damping constant in tangential direction
d	Depth in the particle film defined for rays' transmission in the particle film
d_{cav}	Cavity diameter
d_p	Particle diameter
dt	Real time difference between two consecutive frames in image processing routine
e	Restitution coefficient
E	Young's modulus
E	Emissive power of an element
E_b	Blackbody emissive power
E_{DEM}	Reduced Young's modulus used in DEM simulation
E_i	Energy carried by a ray
E_{real}	Real Young's modulus
f_s	Solid fraction of particle bulk
F_{ji}	View factor from element *j* to element *i*
F_n	Normal force
F_t	Tangential force
F_{fluid}	Net force applied by fluid phase
g	Gravity
G^d	Diffuse irradiation to an element

G^s	Specular irradiation to an element
Gr	Grashof number
h	Convective heat transfer coefficient
H	Half overlap distance in the conduction model or distance between tips of the sphere
I	Moment of inertia
J	Net radiosity from an element
k	The number of a layer in radiation absorption algorithm, k = 1, 2, …
k_f	Fluid thermal conductivity
k_n	Spring stiffness in normal direction
k_{rad}	Radiative conductivity
k_s	Solid thermal conductivity
k_t	Spring stiffness in tangential direction
k_w	Wall thermal conductivity
l_{sec}	Axial length of the particle film section
l_x, l_y	Dimensions of the particle film section in transverse directions
L_{exp}	Axial length of the cavity in the experiment
L_{sim}, L_{cav}	Axial length of the cavity in the simulation
$\dot{m}_{exp}$	Particle mass flow rate in the experiment
m_p	Particle mass
$\dot{m}_{sim}$	Particle mass flow rate in the simulation
M	Map matrix
M_R	Fictitious torque
$\vec{n}$	Normal direction vector
n_p	Number of particles forming the particle film surface
$n_{un,p}$	Number of unshaded particles in the radiation penetration algorithm
Nu	Nusselt number
$q^{\|\|}$	Net heat flux to a discrete surface forming an enclosed cavity
q_{abs}	Absorption function as a function of depth
$q_{abs,l}$	Absorption in a layer at any depth
q_{pfp}	Particle-to-particle heat conduction via interstitial fluid
q_{pfw}	Particle-to-wall heat conduction via interstitial fluid

q_{pp}	Particle-to-particle heat conduction via contact area
q_{pw}	Particle-to-wall heat conduction via contact area
q_{ss}	Heat flow at steady state
q_{tr}	Transmitted fraction of the rays at any depth in the particle film
Q_{conv}	Convective loss from entire cavity
r_c	Contact radius
$r_{c,true}$	Corrected contact radius in conduction algorithm
r_{exp}	Radius of the cavity in the experiment
r_{ij}	Base radius of cone in conduction model
r_{sim}	Radius of the cavity in the simulation
r_p	Particle radius
r_{sf}	Effective radius for heat transfer in conduction model
R	Resultant reflection matrix
R_{el}	Reflection matrix found for a discrete surface
R_{inc}	Reflection matrix
Re	Reynolds number
Ri	Richardson number
s_{true}	Corrected distance between particle centers in conduction algorithm
t	Time
t	Thickness of the thin layer being utilized in radiation penetration algorithm
t_{exp}	Particle film thickness measured in the experiment
t_{mesh}	Thickness of the wire mesh structure welded to the cavity wall
$t_{mov,exp}$	Moving particle film thickness measured in the experiment
t_{film}	Particle film thickness
t_{sim}	Particle film thickness found in the simulation
T_{air}	Ambient air temperature
u_{wind}	Wind velocity
$\ddot{x}$	Second derivative of position, i.e. acceleration
x_n	Position of tracer particle at n^{th} frame
x_p	Particle's position in x- coordinate
$v_{n,rel}$	Relative normal velocity
$v_{t,rel}$	Relative tangential velocity

v_n	Velocity of tracer particle at nth frame
V_{ij}	Volume of Voronoi polyhedron
V_{max}	Maximum relative velocity between contacting particles
V_p	Particle volume
w_{exp}	Rotational speed of the cavity in the experiment
w_{sim}	Rotational speed of the cavity in the simulation
y_p	Particle's position in y- coordinate

Greek

α	Receiver tilt angle
α_{bed}	Bed absorptivity
α_p	Particle absorptivity
$\alpha_{discrete\ volume}$	The fraction of energy of a ray absorbed by the discrete surface
a_n	Acceleration of a tracer particle at nth frame
a_n	Coefficient of polynomial fit for non-linear transmission decay in the particle film, n = 0, 1, …, 4
β_{ref}	Expansion coefficient at reference temperature
γ	Zenith angle varying between 0 and π/2
γ_{inc}	Zenith angle of incoming ray
γ_{gen}	Zenith angle of generated rays
$\gamma_{inc,avg}$	Cos-averaged zenith angle of incoming ray
γ_{ref}	Zenith angle of reflected rays
ε^d	Diffuse emissivity
ε^s	Specular emissivity
ε_{ap}	Emissivity and absorptivity of the aperture plane
ϵ	Bed porosity
ϵ_p	Particle emissivity
Ω	Circumference angle
Δt_{DEM}	DEM time step
ΔT	Temperature difference between two layers/surfaces
θ	Azimuth angle varying between 0 and 2π

θ_{gen}	Azimuth angle of generated ray
θ_{inc}	Azimuth angle of incoming ray
θ_{ref}	Azimuth angle of reflected ray
θ_{rel}	Relative rotation of contacting particles
$\ddot{\theta}$	Second derivative of angular position, i.e. angular acceleration
μ	Sliding friction coefficient
μ_r	Rolling resistance
η_{th}	Receiver thermal efficiency
ν	Poisson's ratio
ν_{ref}	Gas kinematic viscosity at reference temperature
ρ	Wall density
ρ^d	Diffuse reflectivity
ρ^s	Specular reflectivity
σ	Stefan-Boltzmann constant
δ_n	Normal overlap
δ_t	Tangential overlap

1. INTRODUCTION

1.1 Background and Motivation

Solar energy technologies are considered to play an important role in the energy transition from carbon-based economy to net zero target by 2050 [1]. Although the utilization of the sun's power had already been researched back in the 1970s during the petrol crisis around the globe, the real potential behind the solar energy has started to be discovered since 2000s after the alarming climate change obliges societies to abandon carbon-based fuels. The major solar technologies can be categorized into two main groups: solar photovoltaics (PV) and solar thermal systems. While solar PV directly converts both diffuse and direct solar irradiation into direct-current (DC) electricity, solar thermal collectors require the direct solar irradiation to heat a heat transfer fluid (HTF). In solar thermal systems, concentrating the solar irradiation by the help of a mirror configuration to a focal line or a focal point can further increase the temperature of the HTF such that the obtained solar heat is utilizable in the generation of solar thermal electricity (STE) or industrial solar process heat (SHIP). Despite the extensive usage of non-concentrated solar thermal collectors such as flat plate collectors mostly for domestic hot water in last decades, many utility-scale concentrating solar power plants (CSP) have also been commissioned, especially in Spain and the USA after 2005 [2]. However, due to the significant reduction in the price of solar PV modules in the last decade, the investments shifted to PV after 2010s, and the worldwide installed PV capacity exceeds 840 GW as of 2021 while only 6.3 GW CSP for power generation has been installed [3, 4]. Nevertheless, CSP systems do not only generate electricity but also can provide hot steam or air in a wide range of temperatures from 80°C to more than 600°C, to be used in many industrial applications like food, agriculture, mining, textile, paper etc. [5, 6]. Moreover, the value of CSP increases with the fact that energy can be stored as sensible and latent heat in a much cheaper way than in electrochemical batteries like lithium-ion batteries. Coupling the thermal energy storage (TES) to concentrating solar thermal collectors, CSP systems can provide dispatchable electricity or process heat around the clock. Moreover, CSP systems can also provide daily, weekly or even seasonal energy storage in some extreme cases [7-10]. CSP plants can be divided into two main groups in terms of the technology: Line-focus and point-focus systems. Line focus systems track the sun in a single-axis and concentrate the sunlight onto a tube where a working fluid passes through. Common examples are Fresnel and Parabolic Through type collectors. However, the concentration ratios are not so high, and high temperature rises cannot be achieved with this technology. Nevertheless, line focus systems are very useful for applications requiring temperatures up to 400°C, potentially up to 550°C in the future. Theoretically, for an efficient power generation, the peak temperature in a thermodynamic cycle like Brayton or Rankine cycle should be as high as possible. This can be achieved by increasing the concentration ratio in CSP plants. For this reason, two-axis tracking systems are utilized, and sunlight is concentrated to a focal point. The common example of point-focus systems are tower type systems. In tower type CSP, many mirror units distributed over a large land area track the sun during daytime and reflect the sunlight onto the top of a tower where a heat transfer fluid flows. Thanks to very high

concentration ratios (~1000), the fluid temperature can reach to elevated temperatures of 550°C to 1000°C. Many CSP tower plants have been commissioned since 2010 [2], and they mostly employ nitrate-based molten salt as heat transfer fluid. Although molten salt-based solar towers have been state-of-the-art design in commercial scale, they have several drawbacks like low maximum HTF temperature (~560 °C) and high component cost. Thus, a new heat transfer fluid is proposed for high temperature CSP applications [11, 12]. In this type of systems referred as particle receivers, sand-like granular particles with diameters from several hundred micron to several millimeters are utilized as heat absorbing medium. Particle solar receivers promise higher thermal efficiency and lower operational and component cost compared to molten salt-based solar receivers in solar tower applications [13, 14]. The candidate granular materials such as sintered bauxite is non-toxic, inert, abundant and resistant to high temperatures. The heated particles are stored in large storage bins, thus should have high storage density. Several particle receiver designs have been engineered in recent years to maximize the thermal efficiency while minimizing the cost and operational risks.

1.2 Solar Particle Receiver Concepts

Solid particles have been considered as heat absorbing medium in tower type receivers since the 1980s [11]. Various designs to maximize the receiver thermal efficiency and minimize the cost have been proposed for several decades [15-18]. Each design has pros and cons in terms of flow control, maintenance, design complexity etc. The classification of the designs can be made based on if the particles are directly or indirectly irradiated. In indirectly irradiated solar particle receivers, the solar irradiation first heats up the tubes or walls in which the particles pass through, then the heat is transferred to the particles. However, indirectly irradiated receivers suffer from low wall to particle heat transfer coefficients. Directly irradiated solar particle receivers can overcome this problem because particles generally move in enclosed cavities with an aperture facing the heliostat field so that the solar irradiation can directly heat up the moving particles. However, a potential problem with the directly irradiation particle receivers is the high free/forced convection loss and flow stability in case of wind. There are also concepts where particles are directly irradiated and not susceptible to wind thanks to transparent tubes [19] but the high thermal stresses on the transparent tubes is a potential problem. The proposed solar particle receiver concepts in the literature are summarized in several review studies [13, 20, 21]. Thus, for the sake of brevity, only receiver designs reaching a certain level of Technology Readiness Level (TRL) are mentioned in this part.

A freely falling particle curtain in an open cavity was first proposed by Hruby et al. [12]. Particles released from top of the receiver form a curtain shape while being irradiated by the concentrated sunlight, as depicted in Figure 1-1(a). Prior on-sun tests show relatively low thermal efficiency (~50%) for a temperature rise of 200 – 250 °C [22]. Some modifications in the design like active air flow control, reduced cavity size, aperture covers, mass flow rate and outlet temperature controls are applied to the basic design to reduce thermal and particle losses [15, 23]. Moreover, a multistage concept is also investigated to increase the particle residence time and curtain opacity [24, 25]. The latest on-sun testing results show that the receiver thermal efficiency

can reach 60 – 90% for a flow rate of 2 - 7 kg/s and mean flux up to 700 kW/m^2 [26]. The addressed main challenges are mainly the dust formation, back-wall heating in spite of increased curtain opacity, wear and erosion in materials and thermal expansion of mechanical components [15].

Another proposed design is an "obstructed flow particle receiver". In this design, particle retention time and particles' downward velocity can be adjusted with the chevron type porous obstacles, as shown in Figure 1-1(b). Moreover, an opaquer particle curtain, which reduces backwall heating, can be obtained. The preliminary on-sun tests conducted in 2015 resulted in a thermal efficiency of around 63% for an average solar flux of 200 kW/m^2, with a temperature increase of around 50 °C/m [27]. Further tests were conducted in 2017 with an average flux of 230 – 280 kW/m^2 by using cheaper natural red sand. The on-sun tests yielded a thermal efficiency of 60 – 70% and a temperature increase of 130°C in 1.2 m [28]. The main problem in this concept is that the tip of the porous chevrons are exposed to the solar flux directly and have enduring contact to irradiated hot particles, thus deformations occur due to material softening and particle sintering [29]. In order to optimize the particle retention time and downward velocity, the shape and spacing of chevrons are optimized [30].

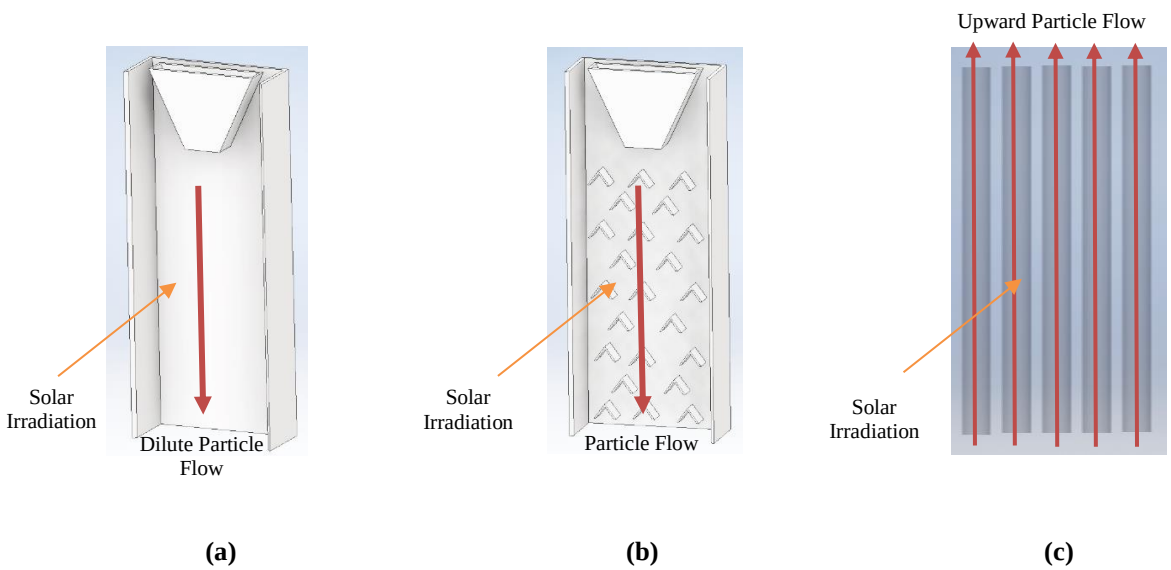

Figure 1-1 Illustration of several particle receiver concepts **(a)** free falling particle receiver **(b)** obstructed flow particle receiver **(c)** particle-suspension-in-a-tube receiver.

An alternative design is a fluidized flow in narrow tubes such that irradiated walls transfer the heat to a dense suspension of fine particles (< 100 microns), and the external air flow like wind has no effect on particle motion, as depicted in Figure 1-1(c). This indirect particle receiver concept is first proposed by Flamant et al. [31]. Contrary to circulating fluidized beds, a dense particle suspension in narrow tubes moves in upward direction with relatively high solid volume fraction (0.26 – 0.34) and low fluidizing air superficial velocity. An average wall to suspension heat transfer coefficient of 400 kW/m^{2}K is achieved by applying flux densities of 200 – 250 kW/m^2 [31]. The

on-sun tests have shown that thermal efficiency of the system can be increased to around 70% with a temperature increase of 167 – 205 °C [32]. However, due to uneven flux distribution on the tube-arrangement, thermal deformation occurs on tube surfaces. The maximum solar flux (~500 kW/m^2) is limited by the temperature that the tube withstands during the real operation [33]. The other downsides of the design are mainly corrosion, parasitic loss due to air compressors, design complexity and fluidization problems due to non-uniform solar flux distribution [33, 34].

A rotating particle receiver concept is also another approach where particle bulk is used as HTF in a rotating drum. In this design, particles are fed into an inclined rotating drum like rotary kiln while being exposed to the concentrated sunlight through the aperture. The solar rotary kilns were proposed for waste treatment [35] and calcination processes [36, 37]. Thanks to continuous particle mixing in rotary kilns, high thermal efficiency can be obtained but the dust formation is the main problem in such designs [38]. Wu [17] proposed a new design, referred to as centrifugal solar particle receiver (CentRec), where particles are moving in centrifuging regime with much higher rotational speeds compared to ones of the slipping and the cascading regimes at which rotary kilns and dryers operate, respectively [39, 40]. The new design is explained in detail in the following sub-chapter.

1.2.1 Centrifugal Solar Particle Receiver Concept

The Centrifugal Solar Particle Receiver, is a direct absorption receiver using ceramic particles as HTF. The CentRec is a promising design compared to other particle receiver concepts because it allows for an active adjustment of particle residence time and thus particle film conditions by adjusting the rotational speed of the drum. In this receiver type, the ceramic particles which are accelerated centrifugally and gravitationally, descend through the inclined rotating receiver while being directly exposed to the solar irradiation through the aperture. The direct heating and adjustable residence time allows larger temperature increase between inlet and outlet. Wu [17] demonstrated that an opaque particle film flowing on the receiver wall can be obtained for various combinations of the receiver (drum) rotational speed and the particle mass flow rate by employing a proof-of-concept scale receiver with 17 cm cavity diameter. For 8 g/s being very low mass flow rate for CentRec and 670 kW/m^2 of mean heat flux at the aperture, thermal efficiencies up to 75% are achieved in a solar simulator. Ebert et al. [41] scaled up the design to ~1.5 m of cavity diameter and tested the stability of the particle film. Amsbeck et al. [42] carried out first tests with infrared heaters and proved scalability of the concept. Due to some technical problems in the infrared heater, particle temperatures up to 700°C could be achieved. Finally, the CentRec has been demonstrated to reach 965 °C of particle outlet temperature at the Juelich Solar Tower [43, 44]. Figure 1-2(a) shows an experiment scale CentRec with a tilt angle of 45°. In Figure 1-2(b), the particle film obtained during the operation is shown.

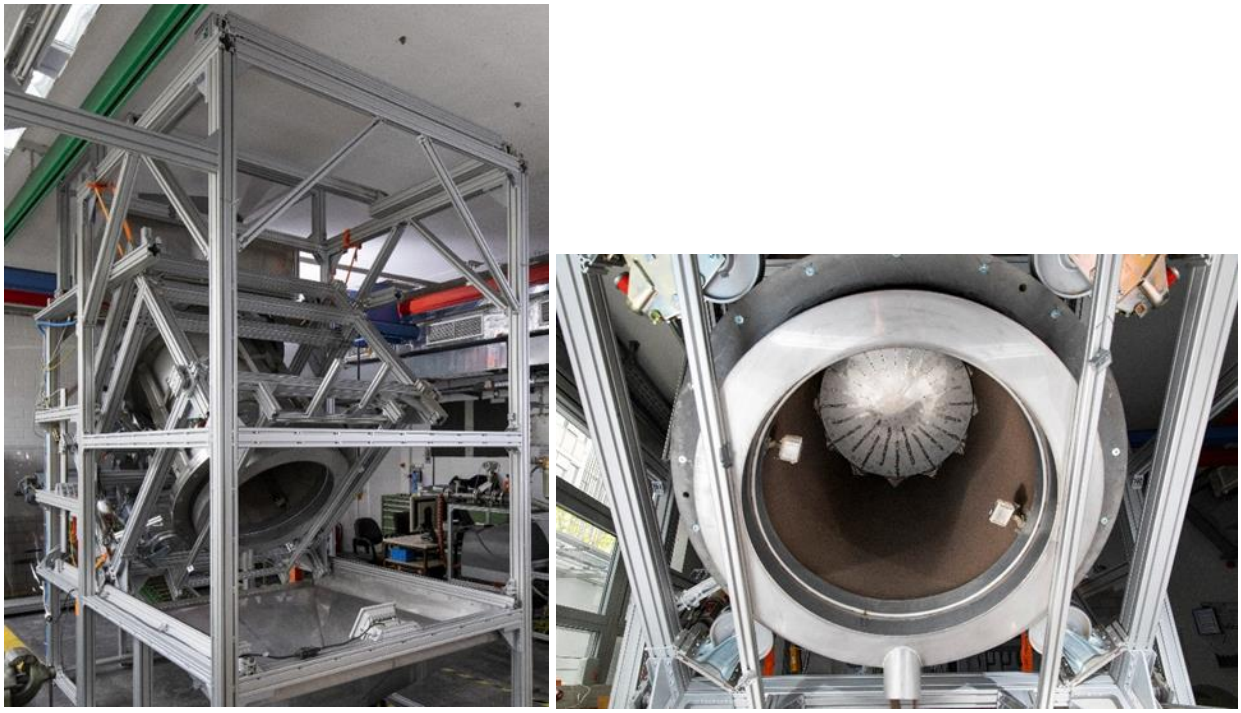

(a) **(b)**

Figure 1-2 (a) Centrifugal solar particle receiver **(b)** particle film descending through rotating receiver wall.

Particles are introduced at the top end of the spinning CentRec cavity, forming a thin particle film on the inside wall due to centrifugal effects. Centrifugal, gravity and particle-wall friction force are the three main external forces acting on the particle film flowing on the receiver wall. In an inclined receiver, gravity force has three components according to the cylindrical coordinate system shown in Figure 1-3. The first component ($g\sin(\alpha)$) is always in the axial (-z) direction. The second one ($g\cos(\alpha)\sin(\Omega)$) is normal to the receiver wall and pointing either inward or outward the cylinder depending on the circumference angle (Ω). The third one ($g\cos(\alpha)\cos(\Omega)$) is tangent to the receiver wall, where α and g are receiver inclination and gravitational acceleration, respectively. The magnitude of the second and third components of the gravity force changes with the particles' tangential position during the rotation, and causes a zig-zag particle movement relative to the receiver, i.e. particles also slightly move in the tangential direction relative to the receiver in the moving zone. The centrifugal force points always outward the cylinder. The superposition of the centrifugal force and the second component of gravity ($g\cos(\alpha)\sin(\Omega)$) gives the net force on the particle film, in the direction normal to the receiver wall. The particle wall friction coefficient times this superposition force gives the net friction force between particle film and wall, which is oriented in axial (z) direction. Dependent on circumference angle, this friction force either counterbalance the first component of gravity ($g\sin(\alpha)$), which causes particles being stationary relative to the receiver (stationary zone at lower part of the circumference in Figure 1-3(b)), or is less than the first component of gravity ($g\sin(\alpha)$) so that particles move in axial (-z) direction (moving zone at upper part of circumference in Figure 1-3(b)). Simulations and experiments have shown this leads to an upper "moving zone" where particles descend in the axial

direction, and a lower "stationary zone" where particles do not move relative to the wall. The existence and size of stationary and moving zones are strong functions of rotational speed, particle-wall friction coefficient and receiver tilt angle. This formulation is valid for a single particle moving on the receiver but in reality, there are also interparticle friction forces acting on particles, which increases the complexity.

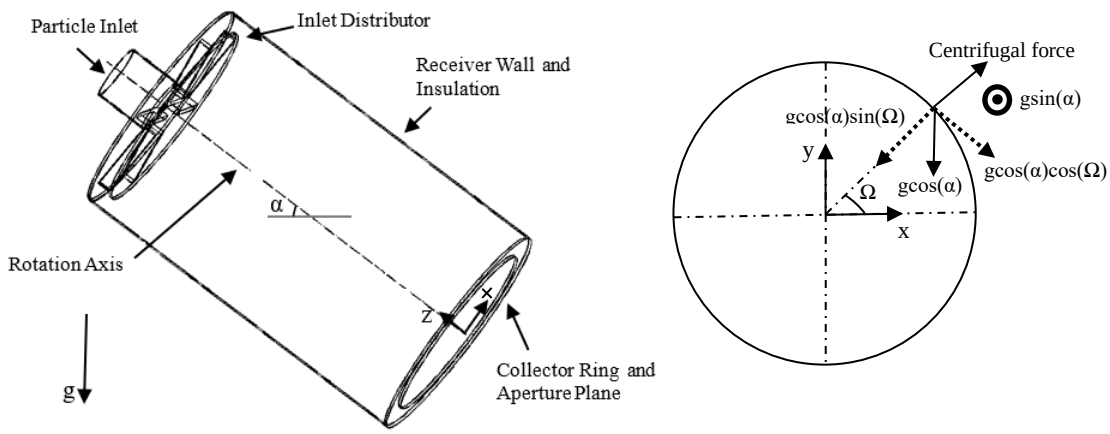

(a) **(b)**

Figure 1-3 (a) Schematic view of the centrifugal receiver **(b)** representation of the components of gravity.

The relative motion of particles within the particle film is mainly dominated by interparticle friction forces and the particle-particle rolling resistance, which accounts for the resistance of a single particle to roll over a surface due to several mechanisms like its non-spherical nature and friction on the particle-to-particle contact area. In the moving zone, the particles move, not only in the axial direction, but also relative to neighboring particles and they eventually mix in all directions (radial, tangential and axial) due to sliding and rolling over neighboring particles. This mixing effect, especially in radial direction, enhances the effective thermal conductivity of the moving particle film due to heat transfer resulting from mass transport, and eventually reduces the risk of high temperature gradients in radial direction. The axial velocity profile of the particle film in the radial direction is also an important optimization parameter because it directly affects the particles' average residence time in the receiver.

1.3 Research Questions and Thesis Overview

To date, only simplistic thermal models assuming that particles have only prescribed uniform axial velocity are utilized for CentRec. However, these models neglect the particle mixing effect being crucial for the viability of the technology. For the case that no mixing occurs in the radial direction, there would be very large temperature gradients in radial direction for thick particle films due to low thermal conductivity of the film. This would significantly increase the radiation and convection loss, and eventually reduce the thermal efficiency. Moreover, available models also

do not take the particle scale heat transfer into account, instead use a constant thermal conductivity. However, the particle packing is continuously changing during the particle movement, correlations derived for static beds cannot be applied directly. For these reasons, several research points/directions are addressed in this study:

1. A discrete particle model accounting all particle interactions is to be developed to model the motion of each particle in the simulation. By means of this model, the particle behavior under various forces resulting from changing operational parameters can be simulated.
2. An experimental apparatus is to be designed to measure the flow characteristics of the particle bulk. A novel image processing algorithm is to be developed to post-process the generated raw data. The results are to be used in the validation of further simulation models.
3. There is no available tool, commercial or open source, to model thermal behavior of the CentRec in a feasible computational time. The models being available in DEM codes lack of model details, and some sub-models like conduction are very primitive to cover all physical details. The thermal code should not only represent the reality but also be computationally efficient to simulate a million-particle thermal simulation.
4. A new ray penetration model along with emission and reflection models for CentRec application is to be developed to avoid costly ray tracing tools. The new model should be independent of particle number and compatible with DEM simulations.

To address the abovementioned research questions, the thesis is structured as follows.

In Chapter 1, background information about CSP system and motivation is discussed. The particle receiver concepts along with CentRec designs are explained.

In Chapter 2, the Discrete Element Method (DEM) model details are discussed and how it can be applied to current CentRec technology is explained.

In Chapter 3, the developed experimental apparatus and experiment results are discussed. The effect of the operational parameters on the particle motion is also revealed.

In Chapter 4, the developed DEM model results are compared with the experiment results. The theory used for scaling down the particle motion in CentRec is discussed and validated.

In Chapter 5, a novel thermal model being compatible with DEM is developed. Each sub heat transfer model is explained and validated. The thermal loss models are also developed and applied to CentRec simulations.

In Chapter 6, the developed thermal model is applied to CentRec DEM simulations. A parametric study investigating the effect of operational parameters on CentRec thermal behavior is discussed. The effect of the receiver size along with the strategies to thermally scale up the receiver is discussed. A sensitivity analysis for some important model parameters is conducted.

In Chapter 7, most important conclusions from the thesis are listed. An outlook for future studies is also discussed in detail.

2. DISCRETE ELEMENT METHOD (DEM) MODEL

Thanks to the advances in computer technology, numerical modeling of particle flows has become more feasible from the computational point of view in recent years. Considering the excessive number of particles to be simulated in large systems, approaches have been developed for certain types of particle flows. The modeling efforts to simulate the particle motion in a fluid can be roughly categorized into two groups. In the first approach, referred to as "continuum approach" or "two fluid model", the particle phase is modelled as continuous like the fluid phase; thus, both phases interpenetrate through each other continuously. The Navier-Stokes equations are solved for each phase while constitutive models are applied to the particle phase to determine fluid-like properties such as granular temperature and granular viscosity [45]. The continuum approach can be applied to many applications including fluidized beds [46, 47] and moving bed particle heat exchangers [48]. For the applications where particle – particle or particle – wall interactions like contact mechanism, collision time etc. are of great interest, the particle phase needs to be modelled as "discrete phase". This second approach is called "discrete approach" or "Lagrangian approach". Although continuum approaches are computationally much less expensive and applicable to large systems, discrete approaches give more realistic results and more insights into the detailed physics. In some cases, discrete approaches are also utilized where particle interactions are neglected if the number of particles per volume is not high. "Dispersed phase model" is a popular approach for low solid volume fraction applications, i.e. dilute flows. This model can be applied to circulating fluidized beds [47], trickle flow heat exchangers [49], free falling particle receivers [50], pneumatic particle conveyors [51]. However, in all these applications, solid volume fraction of the dispersed phase is less than 0.2 because in dispersed phase models, particle - particle interactions are neglected, particle – wall interactions represented in a simplified way and only the drag force is modelled and besides gravity contributes to particle motion [52].

In the numerical modeling of the particle motion in the CentRec application, the discrete approach is preferred for two reasons. Firstly, the particle mixing in the moving zone of the particle film should be modelled accurately. This is important as the radial displacement of the particles exposed to the solar irradiation needs to be modeled accurately to estimate the temperature gradients in the radial direction. Secondly, due to wall effects, particle packing structure is not homogeneous in radial direction. As reported in the literature, the particle packing may have non-negligible effect on the effective bulk thermal conductivity of the particle film in the near wall region [53, 54]. Thus, the discrete approach should be preferred to estimate particle packing structure more accurately. Due to these reasons, continuum approaches are disregarded in this study.

For the purpose of modeling particle interactions more accurately, Discrete Element Method (DEM) is commonly utilized in particle simulations [55]. The method is first proposed by Cundall and Strack [56]. In this approach, the net force and torque acting on each particle by other particles and surrounding fluid is calculated in every time step, and the trajectory of each particle is calculated by means of Newton's second law. A supplementary CFD model can be coupled to

the DEM model such that the momentum exchange between particle and fluid phase is calculated in every coupling time step. In this study, DEM is considered for the sake of the accuracy in spite of the high computational burden for many particle systems (>1 million). However, particle – air interactions are assumed to be negligible because the drag forces acting on particles are quite small compared to gravity and centrifugal effects. This assumption may not be valid if strong fluid forces, like from wind, are present in the receiver but such effects are not considered throughout this study for the particle motion modeling. Thus, CFD-DEM coupling is out of scope of this work, but wind-induced convection loss is discussed in Chapter 5.4.

In the DEM formulation, the net force acting on a particle can be written as follows.

$$m_p\ddot{\vec{x}} = \sum_{i=1}^{N} \vec{F}_{n,i} + \sum_{i=1}^{N} \vec{F}_{t,i} + \vec{F}_{fluid} + m_p\vec{g} \tag{2-1}$$

In Eq. (2-1), N is the number of particles in contact with a particle. $F_{n,i}$ and $F_{t,i}$ are the normal and tangential forces applied by particles in contact. If a particle does not contact to any particle or wall, these terms are simply zero. F_{fluid} is the net force applied by the fluid phase. Finally, m_p, g and $\ddot{\vec{x}}$are the mass of a particle, gravitational acceleration and particle instantaneous acceleration. Other forces like electrostatic and magnetic forces or cohesion are neglected in this study. The torque balance can be written as follows.

$$I_p\ddot{\vec{\theta}} = \sum_{i=1}^{N} \vec{r}_{p,i} \times \vec{F}_{t,i} + \overrightarrow{M_R} \tag{2-2}$$

Tangential forces applied by contacting particles create an external torque, which is the first term on the right-hand side of Eq. (2-2). The moment of inertia and angular acceleration are denoted as I_p and $\ddot{\vec{\theta}}$. In the current DEM formulation, particles are modelled as spherical and monodispersed with particle radius "r_p". However, in reality, particles are not perfect spheres. In order to take the non-spherical shape of a particle into account, a fictitious torque "$\overrightarrow{M_R}$", which is always applied in the reverse direction of the rotation is considered. This fictitious torque not only accounts for the resistance of non-spherical particles to roll over a surface due to their shape but also other effects like micro slip and friction on the contact surface, plastic deformation around the contact and viscous hysteresis [57].

In order to model dense particle flows, the "soft sphere" approach has been developed and utilized in many DEM simulations [56, 58, 59]. In this approach, particles are allowed to overlap during contact. To use a larger time step to capture particle – particle contacts in the "soft sphere"

approach, the particles' Young's Modulus, and eventually particles' stiffness, can be artificially reduced to speed up simulations. However, it should be checked during the simulation if particle overlap creates non-negligible change in particle packing structure and motion. In this study, the open source code LIGGGHTS is utilized for the particle simulations [59]. In this code, there are several built-in tangential and normal force models as well as several rolling resistance models. Grobbel [60] selected and tested a combination of the models being suitable for CentRec application and sintered bauxite particles used in this study. Thus, the current model is built upon the model he created to not duplicate the same work.

The normal force between two particles contacting each other can be calculated as follows.

$$\vec{F}_n = \left(k_n \delta_n - c_n v_{n,rel}\right)\vec{n} \tag{2-3}$$

The normal overlap and relative normal velocity are denoted as δ_n and $v_{n,rel}$, respectively. The spring stiffness "k_n" and damping constant "c_n" in normal direction needs to be calculated by using Eq. (2-4) and (2-5). Finally, $\vec{n}$ is the normal direction vector to the contact surface area. The k_n and c_n is calculated according to a nonlinear Hertz model [61]. In this model, these parameters are also considered as a function of normal overlap as formulated below for monodispersed particles.

$$k_n = \frac{2E}{3(1-\nu^2)}\sqrt{\frac{r_p \delta_n}{2}} \tag{2-4}$$

$$c_n = -\frac{\ln e}{\sqrt{(\ln e)^2 + \pi^2}}\sqrt{\frac{5 m_p E}{3(1-\nu^2)}\sqrt{\frac{r_p \delta_n}{2}}} \tag{2-5}$$

In Eq. (2-4), Young's modulus, Poisson's ratio and radius of a particle are denoted as E, ν and r_p, respectively. Similarly, the restitution coefficient and mass of a particle are represented by e and m_p, respectively in Eq. (2-5). The restitution coefficient is a collision-related property unlike other parameters being material or size-related. It indicates how elastic the particle collision is. It varies between 0 (perfectly inelastic collision) and 1 (perfectly elastic collision). Thus, the damping constant is always equal to or greater than zero.

The tangential force has a similar representation as the normal force but this time, the condition if sliding occurs or not needs to be accounted for. In the LIGGGHTS documentation, the

model is named as "tangential history model" [62] but it is poorly described. Grobbel [60] reported the tangential force model details as follows.

$$\overrightarrow{F_t} = \begin{cases} -k_t\overrightarrow{\delta_t} - c_t\vec{v}_{t,rel} & \text{if } k_t\left|\overrightarrow{\delta_t}\right| \leq \mu\left|\overrightarrow{F_n}\right| \text{ (no slip)} \\ -\dfrac{\overrightarrow{\delta_t}}{\left|\overrightarrow{\delta_t}\right|}\mu\left|\overrightarrow{F_n}\right| & \text{if } k_t\left|\overrightarrow{\delta_t}\right| > \mu\left|\overrightarrow{F_n}\right| \text{ (sliding)} \end{cases} \tag{2-6}$$

In Eq. (2-6), the tangential overlap is denoted as $\overrightarrow{\delta_t}$ while the sliding friction coefficient is denoted as μ. If the sliding condition is not met (no slip), the tangential force is similar to the normal force formula but the spring stiffness, damping constant and relative velocity in tangential direction are considered and denoted as k_t, c_t and $\vec{v}_{t,rel}$, respectively. However, if the sliding occurs, there is no damping term in the tangential force formula. The tangential overlap $\overrightarrow{\delta_t}$ at any time during contact is found by integrating the tangential relative velocity from the time the contact starts to the current time step, as shown in Eq. (2-7). Because the velocity in previous steps affects the tangential overlap in the current time step, the model is referred to as "history model".

$$\overrightarrow{\delta_t} = \int_{t_i}^{t} \vec{v}_{t,rel}\, dt \tag{2-7}$$

Similar to Eq. (2-4) and (2-5), k_t and c_t can be calculated as follows.

$$k_t = \frac{2E}{(2-\nu)(1+\nu)}\sqrt{\frac{r_p\delta_n}{2}} \tag{2-8}$$

$$c_t = -\frac{\ln e}{\sqrt{(\ln e)^2 + \pi^2}}\sqrt{\frac{10m_pE}{3(2-\nu)(1+\nu)}\sqrt{\frac{r_p\delta_n}{2}}} \tag{2-9}$$

For the calculation of the tangential and normal forces in the DEM, the particle radius, restitution coefficient and material properties namely, Young's modulus, Poisson's ratio and particle density must be provided. Finally, the non-spherical nature of the particle needs to be accounted for because in current DEM simulation, all particles are assumed to be perfect spheres.

Although there are attempts to model the shape of non-spherical particles directly in the DEM [63], they are not applicable to high-number-particle simulations due to excessive computational requirement. In reality, the rolling of non-spherical particle over a flat surface or another non-spherical particle requires more torque compared to the spherical particles. Note that even a spherical particle encounters a rolling resistance due to several effects such as friction on the contact area; thus, the rolling resistance, which is mostly found experimentally, accounts for the combination of all resistances on a particle to roll over a surface. This rolling resistance is represented by a fictitious torque in the current DEM simulation and defined as follow [57, 64].

$$M_R = -\frac{k_t {r_p}^2 \theta_{rel}}{4} \tag{2-10}$$

The relative rotation of contacting particles is denoted as θ_{rel} in radians. The built-in model "EPSD2" in LIGGGHTS is suggested by Grobbel [60], based on experiments with sintered bauxite particles. In this model, the rolling resistance is proportional with tangential stiffness "k_t" up to a limit determined by rolling resistance μ_r, as seen in Eq. (2-11).

$$|M_R| \leq \frac{\mu_r r_p |F_n|}{2} \tag{2-11}$$

The complete mathematical model describing the single particle motion in a particle bulk is explained in the equation set (2-1) - (2-11). Besides the model parameters like material properties, the DEM time step needs to be specified for the numerical model. In the DEM solver algorithm, a particle's position in the next time step is calculated based on the position, velocity and acceleration in the current time step size. Thus, large time step size may cause large displacement of a particle in a single time step. This may lead to the physically unrealistic overlap of two particles approaching each other, and eventually unrealistic normal force applied to each other. In order to avoid such cases, the time step size should be determined carefully. Grobbel [60] suggested to select the DEM step size by considering the collision time being a function of particle radius ,density, Young's modulus (E), Poisson's ratio (υ) and relative velocity between particles (V_{max}).

$$\Delta t_{DEM} = 0.287 \left(\frac{2{m_p}^2 (1-\upsilon^2)^2}{r_p E^2 V_{max}} \right)^{0.2} \tag{2-12}$$

3. EXPERIMENT DESIGN AND RESULTS

Some of the content in this chapter is published by the author:

Hicdurmaz S., Buck R., Hoffschmidt B., 2022, Image Analysis of Particle Flow in Centrifugal Solar Particle Receiver. ASME. J. Sol. Energy Eng. 144(3): 030903.

In the experimental part of this study, a set of experiments is designed to measure the flow characteristics of the particle film under various operational conditions. An optical system consisting of diffusively radiating lamps and GoPro® cameras, shown in Figure 3-1, is integrated to the lab scale CentRec, shown in Figure 1-2, to determine the particle flow characteristics. Although 2D feature tracking-like approaches are used in measurement of particle velocity in other solar particle receiver concepts [65], the common approaches to track the motion of moving granular particles are Particle Image Velocimetry (PIV) and Particle Tracking Velocimetry (PTV) [66, 67]. In PIV, the velocity field of a group of particles in a region of interest is measured by assuming that the particle phase is a continuum. However, in PTV, the discrete motion of individual particles is tracked. Unlike this study, where tracer particles move in a particulate medium, in most PIV studies tracer particles are injected to the gaseous or liquid medium and tracked with high-speed cameras to investigate the flow behavior of a moving fluid [68, 69]. Although PIV systems give accurate results in dense flow regimes, PTV technique is advantageous in dilute systems because it tracks each individual particle and provides more detailed information about individual particle motion. In this study, PTV is preferred because DEM based simulation can also calculate particle trajectories, thus a particle scale comparison can be done. Gollin et al [70] states that PTV technique suffers from two difficulties. The first is the accurate determination of the particle position and the second is the linear approximation of the particle trajectory between measured particle positions. To accurately determine the particles' position requires the calibration of the camera to eliminate the optical distortion such as fisheye effect [71, 72]. Later, a 2D image of tracers moving in a particle bulk is obtained for each camera frame. However, it is very likely that the whole periphery of the tracer is not distinguishable due to eclipsing of neighboring particles. Liebl [73] developed a deterministic approach to decide whether the detected pixel group constitute a traced particle (tracer) or not. In this study, this deterministic approach is tailored for CentRec application. After finding the tracers' position in 2D images, a tracking algorithm connecting these positions in sequential frames is needed. Ouellette et al. [74] developed a particle tracking algorithm, called 4 Best Estimate, based on the theory that the tracer's position in the current frame can be best estimated by using the previous two frames and one following frame. Although the trajectory of a particle is assumed as linear between two consecutive frames, this assumption does not cause a large error for CentRec application because the axial displacement of a tracer in one full rotation of the receiver is considered as the validation parameter instead of using the full trajectory of tracers. In addition to this, the film thickness and the ratio of the length of the stationary part, i.e. the length of the arc where particles' velocity is zero relative to the receiver

circumference, are also measured for various rotational speeds and mass flow rates. Later, these parameters will be used in the validation of the numerical model.

Figure 3-1 The optical elements ① the ring light ② the camera for the particle tracking ③ the camera for the film thickness ④ the bar light ⑤ the circular pin.

3.1 Experimental Set-up

3.1.1 CentRec Set-up

In the experiment, a closed loop particle circulation system is employed. The particles leaving the receiver are transported to the storage tank via a conveyor belt and a bucket elevator, respectively. Then, the hopper located above the receiver is filled with the particles from the storage tank. The receiver cavity diameter is 80 cm, whereas the axial length is 120 cm. The receiver inclination angle is set to 45°. In this study, a passive particle feeding system is utilized by means of an orifice plate. Orifice plates with hole diameters of 16, 22.5, 25 and 30 mm are calibrated, and the corresponding mass flow rates are found as 0.092, 0.238, 0.312 and 0.489 kg/s, respectively [75]. In order to be able to track the particle motion, ZrO_2 based white tracer particles are mixed with the reddish-brown ceramic particles. The weight ratio of the tracers to the particles is 0.01. While the mean sieve diameters of the tracers and the particles are 0.983 mm and 0.967 mm, respectively, the static angle of reposes are found as 22.14° and 27.02° because the tracers are more spherical [73]. The ceramic particles are SG 16/30 type provided by Saint Gobain® and their size distribution can be found in [73]. Before starting the experiment, the receiver aperture is enclosed

by a rectangular black-painted plate to create a dark room in the cavity so that the contrast between tracers and particles under the light of the lamp is increased.

Previous experiments have shown that the friction between moving particles and the metallic receiver wall is not high enough to ensure an opaque particle film [17, 41]. Thus, a wire mesh is welded to the receiver wall to obtain a rough surface on the wall. Particles getting stuck between wires form a stationary particle layer on the wall [44]. It is assumed that stationary particles remain in contact to the wall until the operation ends [42]. In solar operation these particles never get exposed to solar rays if the particle film is thick enough but they provide a rough surface for the moving film.

3.1.2 Optical Elements

In the experiment, two GoPro HERO3+ Silver cameras and two diffusive radiating lamps are employed, shown in Figure 3-1. While one camera (② in Figure 3-1) is responsible for tracking the white tracers, the other one (③ in Figure 3-1) focuses on the circular pin (⑤ in Figure 3-1) pressed against the wall. The center of the region of interest of the camera ② is exactly at the mid-level of the receiver's axial length while the axial position of the pin is 40 cm distant to mid-level. The pin is marked with 1 mm-thick black lines as seen in Figure 3-5(a). In the post-processing, the film thickness is measured by counting the black lines starting from the top. The angle of view of the cameras is 90° and 100° in horizontal and vertical direction, respectively. The recorded video has a screen resolution of 1920 x 1080 pixels. Finally, the frame rate of the camera is 60 fps.

The lamps are selected based on the homogeneity of the light on the moving particle film, the brightness, the contrast between the tracer and the particle, and the set-up complexity [73]. The distance between the camera and the receiver wall is an important optimization parameter. If it is too small, the picture becomes blurry; if it is too big, then the tracer recognition is badly affected. This distance is optimized as 135 mm by Liebl [73]. Finally, the radial and tangential image distortion resulting from the nature of the camera lens is calibrated by the help of the chessboard image for the optimized distance [73]. Due to the undistortion, the original image is cropped to 1800 x 960 pixels, and 60 pixels from top, bottom, left and rights are removed. For the given optimized distance and the screen resolution, 1 pixel corresponds to 0.07586 mm, which gives a cropped image size of 136.56 mm x 72.83 mm. The width of the image corresponds to ~ 5% of the receiver circumference. A laser emitting green light is mounted on the stationary black-painted plate enclosing the cavity such that it appears in the camera's ③ field of view in every rotation of the receiver. Thus, by counting image frames after the frame in which the laser spot appears in the camera's field of view the angular position of both cameras can be found in each frame.

3.1.3 Experiment Design

In this experimental study, two independent and three dependent parameters are utilized. The independent parameters adjusted by the user are receiver rotational speed and particle mass flow rate. Depending on the independent parameters, three dependent parameters which are also

the validation parameters for the numerical model are measured. The dependent parameters are the particle film thickness, the axial advance of tracers in one rotation and the ratio of the length of the stationary zone to the cavity circumference. The other parameters like receiver dimension, the type and size of particle and tracers are the same for all experiment runs in this study. The dependent parameters are measured for all possible combinations of independent parameters. All the parameters used in the experiment are listed in Table 3-1. The independent parameters are later used in derivation of the non-dimensional numbers being utilized for scaling of particle flow in different CentRec sizes.

Table 3-1 Experiment parameters.

	Parameter	Unit	Value
Fixed Parameters	Cavity diameter	m	0.8
	Cavity length	m	1.2
	Receiver inclination	degree	45
	Diameter of wire welded to cavity wall	mm	1
	Size of rectangular mesh formed by wires	mm	4 x 4
	Ceramic particle mean sieve diameter	mm	0.983
	Tracer particle mean sieve diameter	mm	0.967
	Tracer to particle ratio	-	0.01
	Cropped image dimension	mm	136.56 (hor.) x 72.83 (ver.)
	Pixel edge length	mm	0.07586
Independent (Operational) Parameters	Receiver rotational speed	rpm	62, 63, 64, 65, 66, 67
	Particle mass flow rate	kg/s	0.092, 0.238, 0.312, 0.489
Dependent Parameters	Tracers' axial advance in 1 rotation	mm	Measured
	Particle film thickness	mm	Measured
	Ratio of the length of the stationary zone to the cavity circumference	-	Measured

3.2 Image Processing Routine

The image processing routine of the recorded videos is mainly composed of two steps, namely the tracer recognition and the tracer tracking. As an image processing tool, a script is developed by Liebl [73] in Python by using functions listed in the OpenCV library. The developed approach is similar to 2D Particle Tracking Velocimetry (PTV). One can calculate the tracer's local velocity based on the camera's frame rate and tracer locations in sequential frames but this is not preferred here because the axial velocity averaged for one rotation is enough for this study. First, the frames are extracted from the recorded video and corrected to eliminate distortion. Then, the center of gravity of each tracer in each frame is determined by the tracer recognition algorithm and

stored in a text file. Due to the receiver's rotating imbalance and the misalignment of the assembly structure, carrying cameras and lamps, relative to the receiver centerline, there is a relative motion between the rotating receiver wall and the rotating cameras during the experiment although all the components are fixed to each other well and rotate at the same speed. This relative motion is characterized by the help of the picture of dots glued to the receiver wall, which is seen in Figure 3-2. The distance between each dot is 5 mm in both horizontal and vertical direction. The x- and y- coordinates of the pixels containing the center of gravity of each white point in the image are stored in each frame during 100 rotations. It is found that each white point deviates from its mean value such that the shape of the deviation vs. frame number curve is sinusoidal. Thus, a sinusoidal curve, showing how much a single white point deviates from its mean value in a specified frame, is fitted with R^2 >0.97 by averaging the results of 100 turns, as seen in Figure 3-3. Then, to correct the tracers' position, the below procedure is followed for each tracer.

- The four-corner calibration points closest to the tracer's position are determined.
- By using the frame number, the angular position of the camera is determined. Then, the corresponding amount of the deviations in four corner calibration points are determined by using the angular position and sinusoidal fit of each point.
- The deviation at the tracer's position is interpolated by employing the 2-D spline interpolation function scipy.interpolate.griddata in Python.
- This procedure is repeated for each tracer and the resulting position matrix is stored in a text file for each frame.

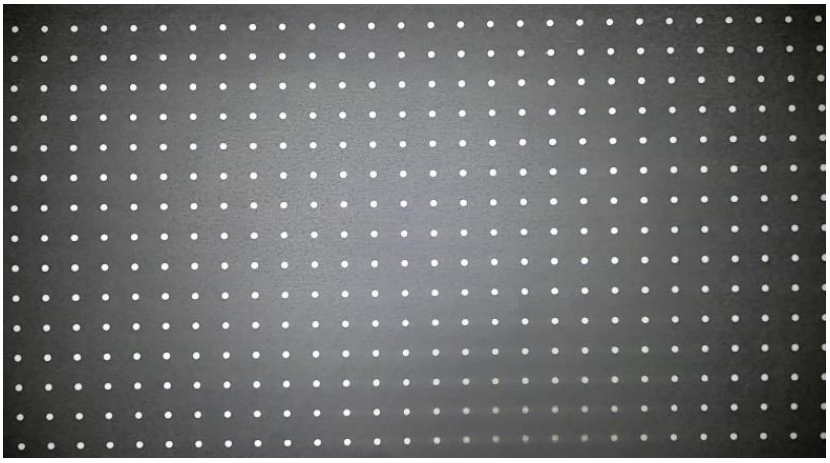

Figure 3-2 The picture of dots used for the characterization of the motion between the receiver wall and the camera.

The approach discussed above is evaluated and the error resulting from using sinusoidal curves in characterization is found as ~1 pixel, corresponding 0.076 mm. Considering the fact that the tracer mean sieve diameter is around 0.983 mm, this error can be assumed as very small.

Finally, the corrected tracer's positions are used by the tracking algorithm and particle trajectories are found by connecting the tracer's position in each frame. The details of the recognition and tracking algorithms are discussed in the following sections.

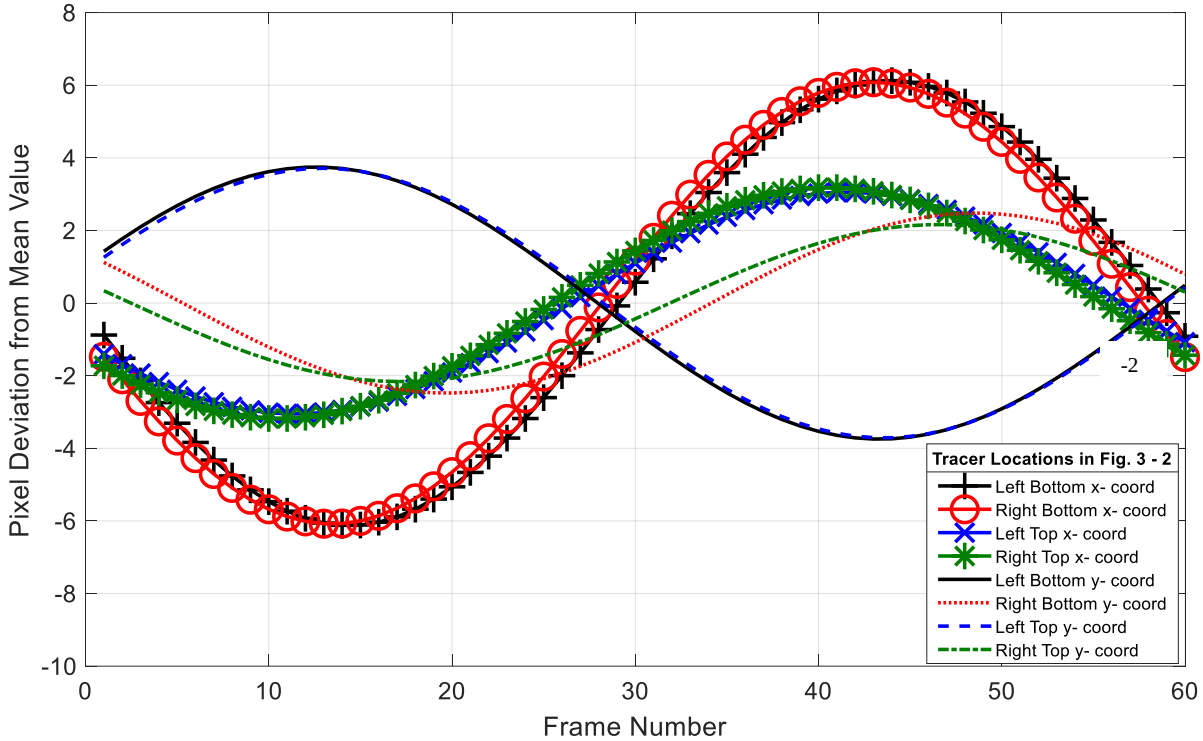

Figure 3-3 Pixel deviation from the mean value in one rotation for each tracer point at the corners of the picture of dots based on parameters listed in Table 3-1.

3.2.1 Tracer Recognition

To distinguish tracers from ceramic particles, a deterministic approach is followed. The procedure consists of two parts namely, segmentation and filtering. In the segmentation part, the RGB pixel value of each pixel in the frame is determined and converted to HSV (Hue, Saturation, Value) value. A sensitivity parameter used in the determination of the upper and the lower bound of the HSV pixel value is defined such that it varies between 0 (only pure white is considered as tracer) and 100 (no segmentation). In the pre-tests, it is observed that if the sensitivity parameter is set as <30 then the tracers located near the edge of the image are not captured because of the bad illumination relative to the center. However, if it is set as >70, some reddish-brown ceramic particles located around the center of the image are also detected as tracer due to relatively high illumination at the center. Thus, there is a compromise between tracers located at the center and edges. Tracers located at the center are preferred to the ones at the edges because the ones at the center likely appear again in the next frame while the ones at the edge may disappear. Thus, the sensitivity parameter is set to 30, so the regions higher than HSV value of 225 are considered as tracer candidate. Note that pure white corresponds to a HSV value of 255.

In the filtering step, the detected potential tracers are quantified according to their area, circularity and aspect ratio. A threshold value for each criterion is defined and only candidates fulfilling the predefined criterion are accepted as tracer. Firstly, the pixels whose HSV value is in the predefined range (>225) are determined and the area of the region composed of those neighboring pixels is calculated. Note that the sieve diameter of a tracer is measured as 0.987 mm, meaning that particle diameter to pixel length ratio is ~13. In the pre-tests, the range of pixel area, in which a single tracer likely exists, is optimized as 50 pixel to 200 pixel by trial and error. This is because sometimes a part of a tracer is eclipsed by a particle and then only the non-eclipsed part is visible. Thus, in order to not lose the track, the lower bound for the area criterion is optimized as 50 pixel^2, which is far below 169 pixel^2. Similarly, in order to prevent to recognize two or more adjoining tracers as a single one, an upper bound is defined. Secondly, a threshold value of 0.3 for the circularity of the detected region is defined as minimum. Finally, the minimum aspect ratio which is the ratio of the thinnest to widest length within the detected region is defined as 0.01. Figure 3-4 shows the undistorted and the filtered images. The circles in Figure 3-4 represent the tracer candidates fulfilling all conditions. Note that criteria thresholds for all parameters are empirical and found by trial and error. During the image processing, the user may adjust these threshold values manually to improve tracking resolution. It is strongly recommended to select original and filtered images randomly often and compare them. The detected regions fulfilling all abovementioned criteria are regarded as "tracer" and the center of gravity of the region is saved in a text file to be used in the tracking algorithm later.

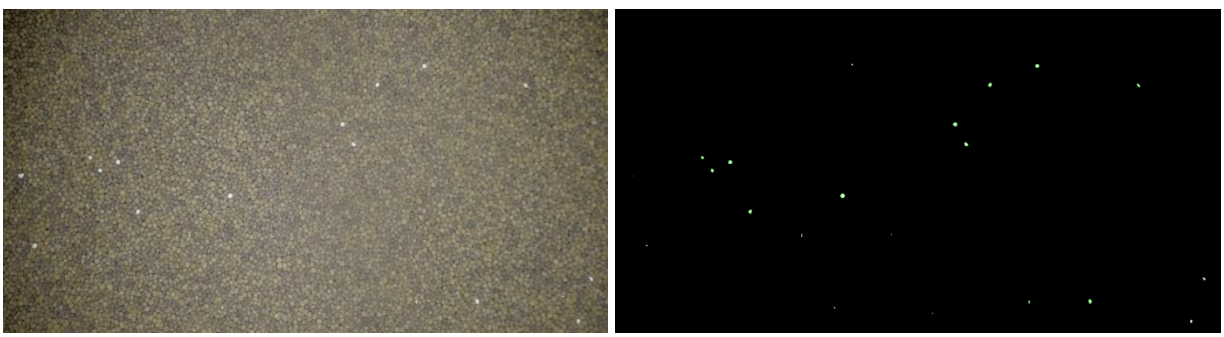

(a) **(b)**

Figure 3-4 (a) The undistorted image **(b)** the segmentated and filtered image.

3.2.2 Tracer Tracking

In order to determine the trajectory of tracers, a particle tracking algorithm called 4BestEstimate is integrated to the image processing code [74]. In this approach, the decision of which tracers will be appended to the tracking matrix, is made by evaluating 4 frames, namely the previous two frames, the current frame and the next frame. A search radius where the potential position of the tracer detected in the current frame may be found in the next frame within, is defined by the user. This user-defined parameter should be adjusted carefully such that it is not smaller

than the advance of the tracer between two consecutive frames. Setting this parameter very high increases the computational burden because then more candidate tracers are to be checked. Basically, the tracking procedure for tracers is as follows:

1. In the first frame of the video, all the tracers found in Frame 1 are saved into the tracking matrix. Each row of the matrix represents a track of a new tracer.
2. The candidate tracers in Frame 2 within the search radius are listed, and the one being closest to the positions in Frame 1 is appended to the tracking matrix. If there is no candidate tracer, the track is finished. It is because tracers may sink into deeper layers due to mixing. Similarly, if a new tracer appears in Frame 2, a new track starts.
3. For the found couples, a 2D velocity vector with x and y components is calculated as stated in Eq. (3-1), where v, x and t are velocity, position and time. "dt" corresponds to the real time between two consecutive frames. If a new track starts here, it is appended to a new row of the tracking matrix. For those particles, the algorithm starts from step 2.

$$v_n = \frac{x_n - x_{n-1}}{dt} \tag{3-1}$$

4. Based on the velocity calculated in step 3, the position of the tracer is estimated in the Frame 3. Then, the search radius is applied around the estimated position. Possible position triplets are determined based on the first three frames.
5. The velocity and acceleration are calculated by using Eq. (3-1) and Eq. (3-2) respectively. $v_n$is calculated by using Frame 2 and Frame 3 while v_{n-1} is found by using Frame 1 and Frame 2.

$$a_n = \frac{v_n - v_{n-1}}{dt} \tag{3-2}$$

6. The position of the potential candidates in Frame 4 for detected potential location triplets in step 4 is estimated by using the Eq. **(**3-3) [74].

$$x_{n+2} = x_n + 2v_n dt + a_n(2dt)^2 \tag{3-3}$$

7. The quartets of which the first two elements are certain and the last two elements are candidates, are determined by using the search radius around the potential position found in step 6. If a new tracer appears in this step, a new track starts from step 2.
8. The found couples from Frame 2 and Frame 3 are appended to the tracking matrix if and only if a track continues in Frame 4. If 2 or more potential quartets fulfill this condition,

then the one which has minimum distance between the positions in Frame 3 and Frame 4 is preferred.

9. The procedure repeats starting from step 2 for the next frame. In each iteration, only the position from Frame 3 is appended to the tracking matrix. The potential tracer in Frame 4 is only used for selection of the triplets Frames 1 - 3.

It should be noted that if track is lost in any step then it is terminated instead of searching the potential candidates in the future steps. Especially in the moving zone, particles may sink into the non-visible part of the film and reappear in the next frame. Considering that there might be closely moving tracers in the image, further tracking for sinking-reappearing tracers is not preferred in this study to be on the safe side because it is very hard to estimate if the same tracer is the reappearing one or not. A more detailed explanation about the tracking algorithm and the code can be found in [73, 74].

3.3 Experiment Results

As shown in Table 3-1, the experiments are run for all combinations of 6 different rotational speeds and 4 different particle mass flow rates. It is observed that reducing the rotational speed to below 62 rpm causes particles to move in the cavity freely due to insufficient centrifugal forces especially for high flow rates (>0.48 kg/s). Moreover, rotating the receiver at a speed of more than 67 rpm causes that increasing friction force prevents particle motion. The opening between the particle distributor and the receiver wall, as may be seen in Figure 1-2(b), is ~ 1 cm, so as the rotational speed and the flow rate increases, the opening may be clogged. That is why the particle mass flow rate is limited to ~0.5 kg/s in this experiment. Finally, as rotational speed and flow rate decreases, the welded wire mesh becomes visible, indicating that the thickness of the particle film is small. Thus, 6 rotational speeds (62, 63, 64, 65, 66 and 67 rpm) and 4 mass flow rates (0.092, 0.218, 0.312, 0.489 kg/s) are investigated to cover the operational range of the CentRec. The videos are recorded for 5 minutes for each measurement point.

In Figure 3-5, the marked pin in the empty and filled receiver is shown. Note that the thickness of black lines and the distance between them is equal to each other and 1 mm. Thus, one can count the black lines to find the film thickness. Figure 3-6 presents the film thickness for the investigated operational parameters. It can be stated that the film thickness increases with the rotational speed and the particle mass flow rate. As rotational speed increases, the friction between particles forming the particle film increases; thus, the axial velocity profile in the radial direction gets less steep. Note that the values presented in Figure 3-6 have an uncertainty of ± 0.5 mm. It is because one can say only with naked eye whether a cap of a sphere (particle) is located between two lines on the pin. A more sophisticated code can also detect the exact position of the tip of the spherical cap as suggested by Liebl [73].

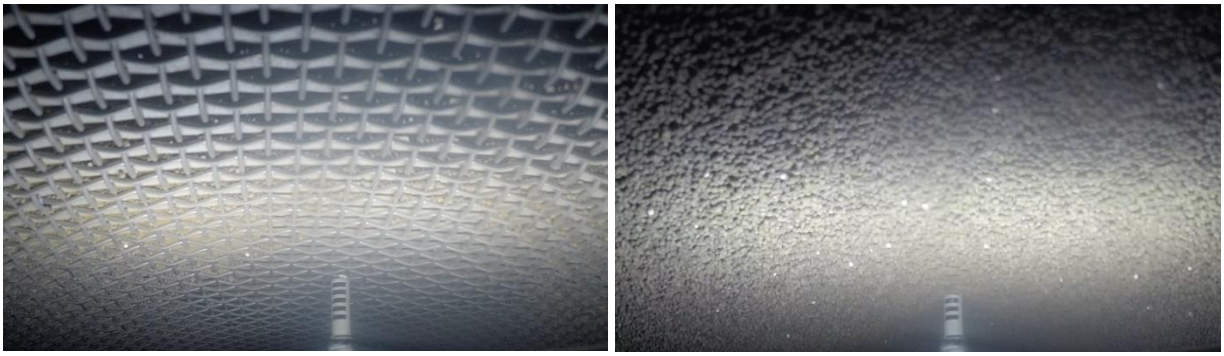

(a) **(b)**

Figure 3-5 The pin pressed against the receiver wall **(a)** in empty receiver **(b)** during experiment.

In this study, the film thickness is defined as the distance between the tip of the topmost particle and the receiver wall. However, due to the dynamic nature of the particle film, some particles may sit slightly higher than the others, thus the film thickness is not constant throughout the receiver circumference but has an uncertainty of 1 particle radius. Here it is assumed that there is no pile formation in any part of the particle film due to centrifugal and gravity forces. That's why a more detailed code is not considered here but the film thickness measurement is made with naked eye by watching the recorded images and a large uncertainty is assumed, which is half of the distance between two lines on the pin. For example, the film thickness for a rotational speed of 67 rpm and a mass flow rate of 0.489 kg/s varies between 9 and 10 mm because the spherical cap of the topmost particles is always observed in between 9th and 10th lines from the pin tip. Due to the fact that the gap between particle distributor and receiver wall is 10 mm, there may be clogging effect for these operational parameters, which may eventually make that result erroneous. Another point to be emphasized here is that the wire mesh welded to the receiver wall has a diameter of 1 mm which result in a total wire thickness varying between 1 and 2 mm due to assembling technique shown in Figure 3-5(a). Thus, there is a stationary particle layer that gets entrapped in the wire mesh. The pre-tests have shown that this layer consist of not more than 1 particle in radial direction.

Due to the opaque nature of particles, only the ones located in the innermost layer of the particle film can be observed. In Figure 3-7, the axial advance of those particles in one rotation is presented for various rotational speeds and mass flow rates. From Figure 3-7, it can be deduced that the free surface velocity of the film increases with increasing flow rate; in other words, a thicker film yields higher free surface velocity for the same rotational speed. Moreover, the axial advance of particles decreases with increasing rotational speed for the same mass flow rate. The axial advance values for rotational speeds of 62 and 64 rpm and mass flow rate of 0.489 kg/s are not presented here because the trajectory of the particles in one rotation could not be captured with the available image height. The number of tracers detected for each measurement point is also shown in Table 3-2. A mean standard deviation of measurements is also found for each measurement point and represented as vertical error bar as shown Figure 3-7. No relation between the mean standard deviation and operational parameters is observed. For some measurement points,

this deviation is relatively small. This is because only a low number of tracers could be tracked, as can be noticed in Table 3-2, thus the deviation for those measurements should be approached cautiously.

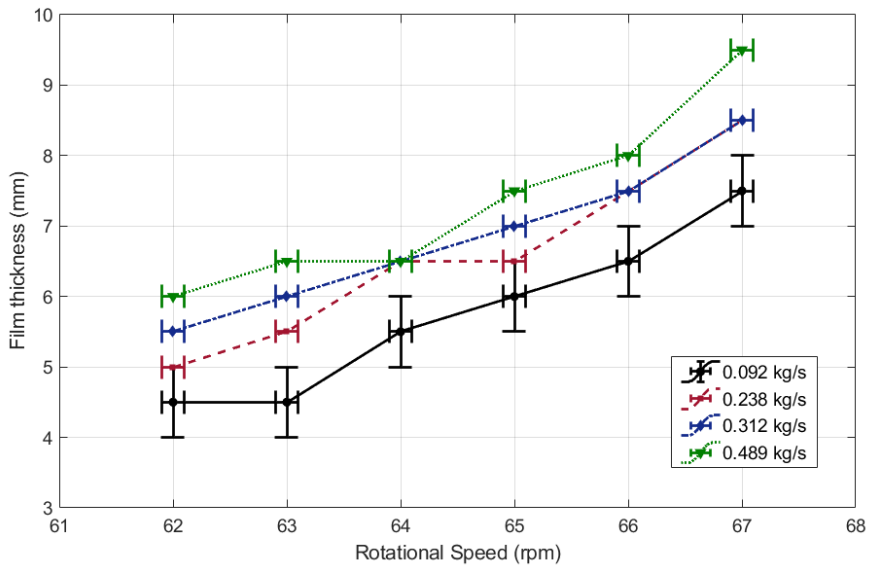

Figure 3-6 The film thickness for various mass flow rates and rotational speeds based on parameters listed in Table 3-1.The vertical error bar corresponds the uncertainty of the measurement technique and is the same for all measurement points (± 0.5 mm). It is only shown for the mass flow rate of 0.092 kg/s to provide legibility. The horizontal error bar shows the measurement uncertainty of the device measuring the rotational speed.

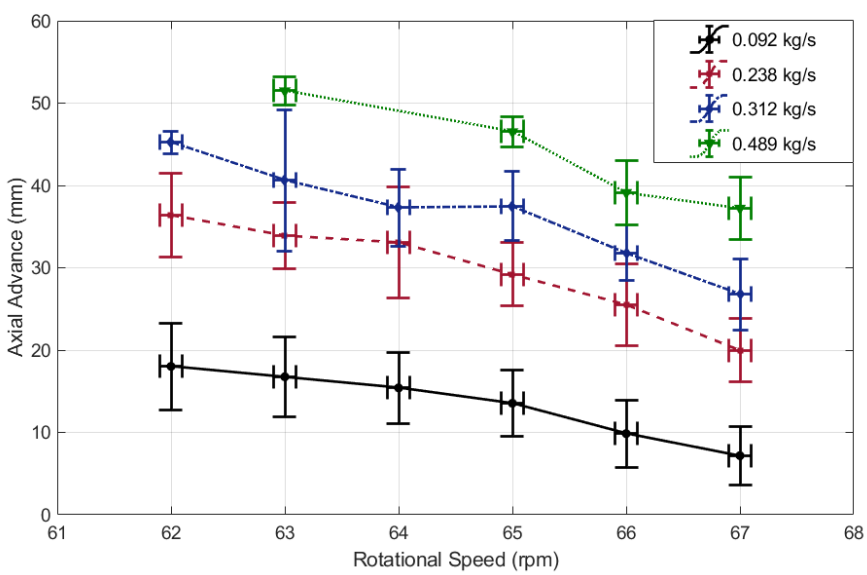

Figure 3-7 The axial advance of the tracer in one rotation for various mass flow rates and rotational speeds based on parameters listed in Table 3-1. The vertical error bar corresponds the mean standard deviation of measurements. The horizontal error bar shows the measurement uncertainty of the device measuring the rotation speed.

Table 3-2 Number of the detected tracers.

	Orifice Diameter (mm)	16	22.5	25	30
	Corr. Flow. Rate (kg/s)	**0.092**	**0.238**	**0.312**	**0.489**
Rotational Speed (rpm)	**62**	135	3	2	-
	63	148	14	7	4
	64	187	15	10	-
	65	171	23	11	2
	66	217	52	23	4
	67	134	31	21	4

In Figure 3-8, the ratio of the length of the stationary zone to receiver circumference is shown for various rotational speeds and mass flow rates. From Figure 3-8, it can be observed that this ratio has almost no dependency to rotational speed except for 0.092 kg/s of mass flow rate. In the calculation of this ratio, firstly, the frames in which the tracer position does not change relative to the previous frame are counted. Then, it is divided to the number of frames corresponding to one receiver rotation. However, it should be noted that the results presented in Figure 3-8 are sensitive to the distance criterion chosen to determine if a tracer starts to move in between two consecutive frames. In other words, the ratio changes with the user-defined distance indicating that a tracer starts to move if it is exceeded. Thus, this distance is set to 1 mm because the accuracy of pixel deviation correction approach is 1 mm, so the potential noise that may result from this is eliminated.

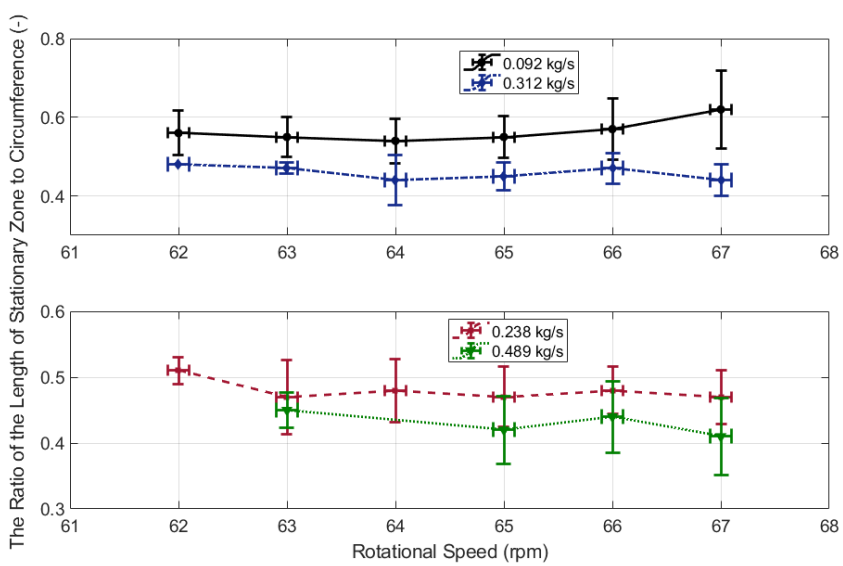

Figure 3-8 The ratio of the length of the stationary zone to the cavity circumference for various mass flow rates and rotational speeds based on parameters listed in Table 3-1. The figure is split to two plots to increase legibility of the figure. The vertical error bar corresponds the mean standard deviation of the measurement points. The horizontal error bar shows the measurement of uncertainty of the device measuring the rotation speed.

For the same rotational speed, the ratio of the length of the stationary zone to the receiver circumference decreases with increasing flow rate. In other words, as the film gets thicker, the length of the stationary zone on the innermost (visible) region gets smaller for the same rotational

speed. It proves that the length of the stationary zone is also changing in radial direction. In other words, a particle's stationarity is not only changing with the angular position but also radial position in the receiver. This behavior is roughly depicted in Figure 3-9.

One of the challenges in the image processing part is the low number of particles appearing in all frames. Especially in the moving zone, the mixing of the film is very strong; thus, tracers sink into the film, which makes tracking very difficult. In Table 3-2, the number of tracers tracked for each experiment is tabulated. As can be noticed, the number of tracers is very low for high mass flow rates because the image height is not large enough to capture the tracer's complete axial advance taken in one receiver rotation. In order to increase the accuracy, a track is always started from the stationary zone because starting a track in the moving zone would lead to less accuracy in measurement of axial advance and stationary zone ratio due to low camera frame rate.

In the post processing of the recorded videos, there are several potential sources of error. Firstly, there is a reprojection error, defined as the distance between the measured position and the projected position of a point in the image plane. This error is found as 0.0523 pixel for the type of cameras used in this study and given distance between particle film and camera by Liebl [73]. Secondly, there is an error resulting from the curve fit to characterize pixel deviation. This error is also found to be approximately one pixel in each calibration point. Lastly, there is also an error due to linear interpolation of the particle trajectory between sequential frames. However, in this study, only the axial displacement of particles, which is a path-independent parameter, in one rotation is measured. Thus, the overall optical error is calculated as ~1 pixel, which is negligibly small compared to particle's axial advance in one rotation. There is also a potential error, which is hard to quantify, in the tracer detection algorithm but this is minimized by optimizing the empirical parameters as discussed in Section 3.1. If a tracer could not be detected via detection algorithm, then the track is automatically terminated. Moreover, the movement pattern of all trajectories is checked. If any trajectory does not have the common pattern, i.e. movement in the stationary zone or unphysical upward motion in the moving zone, it is omitted. This situation is very likely due to that a pixel region is detected as tracer although it is not the case. There may be also the case that one tracer sinks and another one reappears in the location where the first one is supposed to be in the next frame. In order to eliminate this risk, the tracer to particles ratio is kept low (0.01). Thus, the average distance between tracers in a frame is increased. Finally, there may be also an error in the tracking algorithm such that the same tracer is not tracked during its trajectory although all tracers are detected correctly in each frame. However, this situation also causes a different trajectory pattern and can be noticed by the user. For a more robust model, a pattern recognition algorithm can also be employed in the future study. Moreover, using a camera with higher frame rate and 3D tracking technique may reduce the errors in the tracking algorithm.

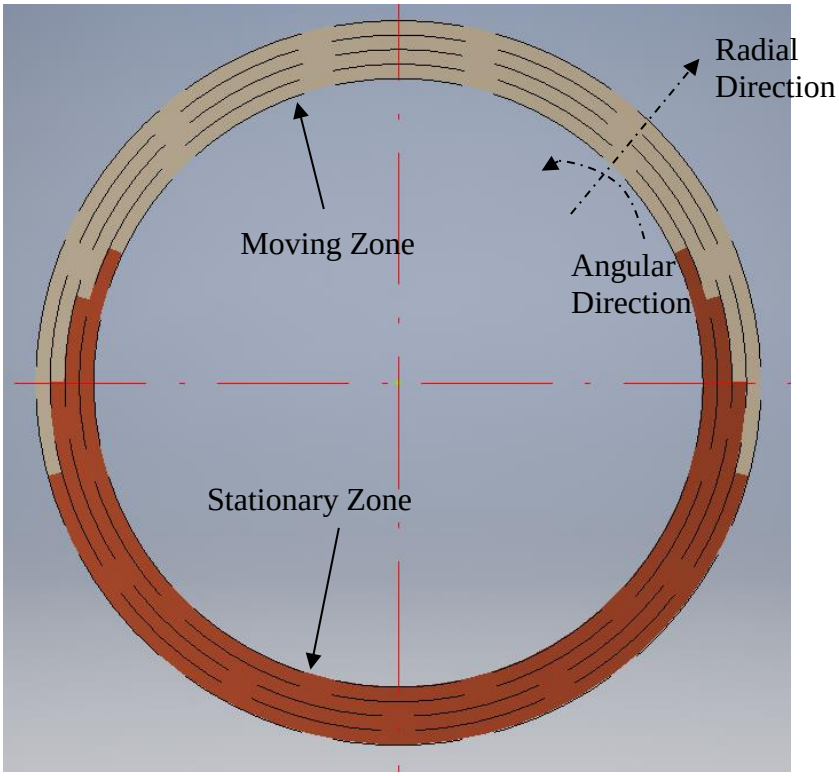

Figure 3-9 Rough representation of the stationary and moving zones, which are depicted with dark brown and light brown colors, respectively.

4. DEM MODEL VALIDATION

In order to validate the numerical model described in Chapter 2, the experiment results found in Chapter 3.3 are utilized. However, the receiver size considered in the experimental study is too large to be simulated by DEM with the available computational resources. For example, if the particle diameter, the particle film thickness and the particle film porosity are assumed as 1 mm, 4 mm and 0.5, respectively, the number of particles in the simulation is around 7.5 million for the receiver size in the experiment case. However, as receiver size increases, the optimum film thickness is also expected to increase. This is due to that for the same flux density at the aperture, the intercepted energy increases with the square of the receiver diameter. The mass flow rate should also be proportional to the intercepted energy in order to maintain the same temperature increase between inlet and outlet. Thus, the mass flow rate is proportional to the square of the receiver diameter in case of the same flux at aperture and aspect ratio (length to diameter ratio) for different receiver sizes. This leads to an increase in the film thickness as receiver size increases. For a large receiver with a cavity diameter of 2.5 m and film thickness of 10 d_p, the number of particles in the simulation is around 200 million. However, the highest particle number considered in this study is around 1.25 million because the computation time being more than one week for reaching cold steady-state is avoided. One second simulation of that many particles takes 2 hours with Intel Xeon E5-2697v3 processors (14 cores). In the light of these calculations, it is inevitable to develop a strategy to scale-down the receiver such that a similar velocity field and a film thickness distribution can still be obtained by considering a small-scale receiver.

4.1 Scale – down Approach

The approach to scale-down the particle film assumes that if the net force acting on a particle film during the particles' residence time is the same, the velocity field is also the same regardless of the receiver size. There are two major forces acting on the particle film. The first one is the gravity, being independent of all operational parameters. The second is the fictitious centrifugal force, which is not a real force but an effect that a matter experiences during the circular motion, that pushes the matter outward of the circular path. The friction force is a result of various combination of these two forces during the motion. Gravity is assumed to be the same for all particles regardless of the receiver size. In order to also apply the same centrifugal force to the moving film, the rotational speed must be adjusted as follows.

$$w_{exp}^2 r_{exp} = w_{sim}^2 r_{sim} \tag{4-1}$$

The experimental and simulation rotational speed are denoted as w_{exp} and w_{sim}, respectively. Similarly, the cavity radius is denoted as r_{exp} and r_{sim}. The scale-down approach is valid if the cavity diameter is much higher than the particle diameter so that the cavity wall can be

assumed as flat relative to the single particle. To obtain the same film thickness, the mass flow rate also needs to be adjusted.

$$\frac{\dot{m}_{exp}}{r_{exp}} = \frac{\dot{m}_{sim}}{r_{sim}} \tag{4-2}$$

Finally, the cavity length is also adjusted to have the same aspect ratio (cavity length/diameter).

$$\frac{L_{exp}}{r_{exp}} = \frac{L_{sim}}{r_{sim}} \tag{4-3}$$

The scale-down approach claims that by applying the three scaling laws, one can obtain the same velocity and film thickness distribution along the receiver. In the simulations, particles are introduced into the domain with a linear velocity being the same as the cavity's linear velocity and zero axial velocity, as seen in

Figure **4-1**(a). The radial location of particle generation domain is 10 d_p away from the cavity wall, as depicted in Figure 4-1(b). The receiver tilt angle is set to 45°, as seen in Figure 4-1(c), throughout the study.

In order to check the applicability of the new approach to CentRec, three receiver sizes are considered, as shown in Table 4-1. The particle diameter for all sizes is 1.2 mm so the cavity diameter is 100 times d_p for the smallest receiver size. For these simulations, DEM parameters found in the calibration study discussed in Chapter 4.2 are utilized so that the presented results are realistic for CentRec case. However, the scale-down approach itself is independent of the DEM parameters and should work for any particle type.

The particle – surface friction coefficient is set to a very high value (10,000) so that the particles touching the cavity wall do not move relative to the wall. This numerical trick is done to obtain a stationary particle layer like in the real operation. The details of this trick are discussed in Chapter 4.2. In Figure 4-2, the particle mass flow rate at the outlet of the receiver is plotted for all sizes. As can be noticed, after a certain period of time, the mean outlet mass flow rate is equal to the inlet mass flow rate; however, there is a certain level of fluctuations around a mean value. The fluctuations at the outlet may indicate that the film thickness changes periodically because the instantaneous number of particles in the receiver also changes with time slightly. During the initial filling period, there is quite large particle loss through the aperture. This is mainly because the wire mesh is not modelled in the CAD model of the receiver. This transient effect is not the representation of reality and only occurs due to implicit modelling of the wire mesh through the high friction value. More details can be found in Chapter 4.2.

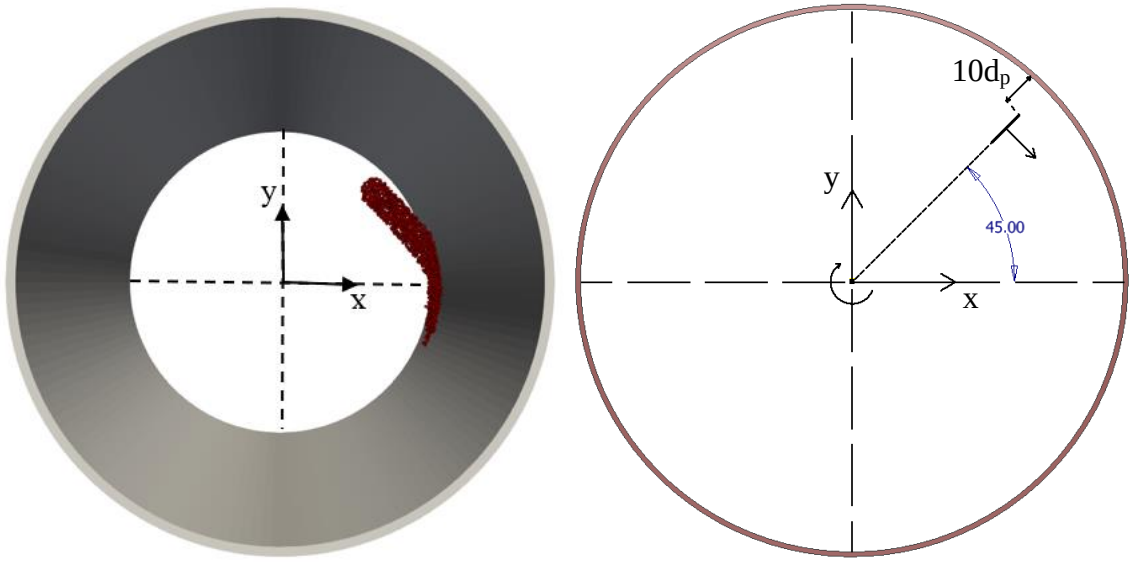

(a) **(b)**

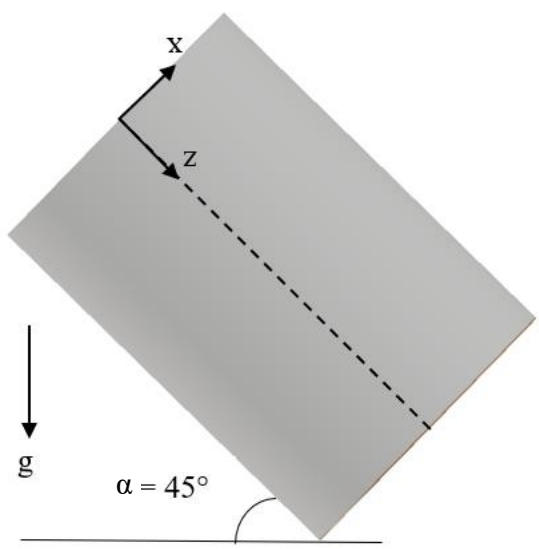

(c)

Figure 4-1 (a) Feeding of the particles to the cavity **(b)** location of particle feeder **(c)** the side view of the tilted receiver.

Table 4-1 Receiver dimensions considered in the scale-down approach.

	Unit	D12	D17	D25
Cavity Diameter	m	0.12	0.17	0.25
Cavity Length	m	0.171	0.242	0.356
Mass Flow Rate	g/s	35.7	50.58	74.38
Rotational Speed	rpm	160.08	134.50	110.91
Particle Inlet Speed	m/s	1.01	1.20	1.45
Particle number in the simulation (x10^5)	-	1.6	3.3	7

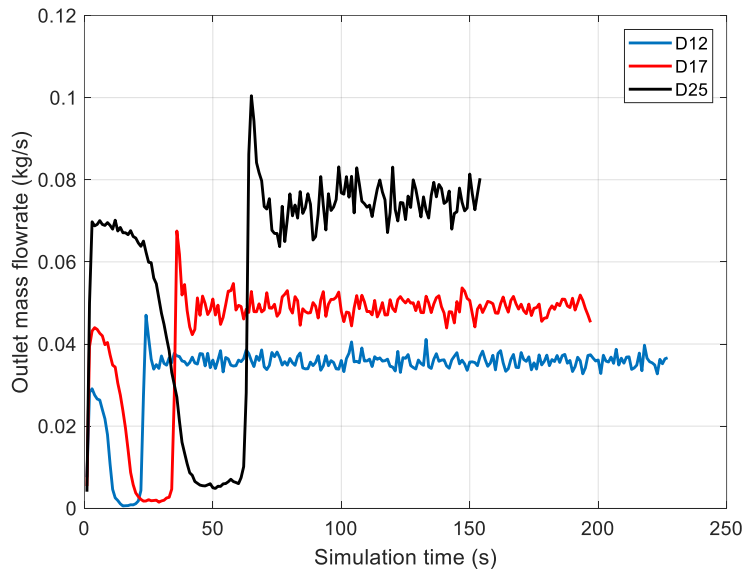

Figure 4-2 Time variation of particle outlet mass flow rate for three receiver sizes.

After obtaining the cold steady state, meaning that the inlet and outlet mass flow rate are equal to each other, the velocity and film thickness distribution for three sizes are compared. The film thickness for any axial segment of the particle film is calculated by averaging the radial position of the particles located at the particle film surface. Firstly, the surface area of the axially-cut film section is calculated.

$$A_{surf} = l_{sec}\pi(d_{cav} - 2t_{film}) \tag{4-4}$$

The axial length of the film section is denoted as l_{sec} while the film thickness is denoted as t_{film}. Because the surface area is also function of the film thickness, the calculation of the film thickness requires an iterative solution. Then, the number of particles forming the particle film surface is calculated as follows.

$$n_p = \frac{A_{surf} d_p f_s}{V_p} \tag{4-5}$$

Particle diameter, volume and bulk solid fraction are denoted as d_p, V_p and f_s. The solid fraction can be estimated according to the procedure described in Chapter 5.1.1.1. However, for the particle type considered in this study and the relevant operational range, the solid fraction is found as 0.5 ± 0.02 in the CentRec simulations. Thus, an average value of 0.5 is assumed in this calculation. Note that in Eq. (4-5), it is assumed that the particles forming the film section is evenly distributed in tangential and axial directions; thus, there is no pile formation. Later, the radial position of all particles in the enclosed hollow cylinder-like volume is found by using the particles' x and y positions. Then, particles are sorted by their radial positions in ascending order, and a sorted radial position vector "r_p" is formed.

$$r_p = sort(\sqrt{x_p^2 + y_p^2}, 'ascend') \tag{4-6}$$

The first n_p elements of the vector r_p correspond to the particles forming the particle film. Then, the film thickness for a given axially-cut section of the film is found as follows.

$$t_{film} = \frac{d_{cav}}{2} - \frac{\sum_{i=1}^{n_p} r_p[i]}{n_p} + \frac{d_p}{2} \tag{4-7}$$

In Eq.(4-7), the average radial position of n_p particles being farthest from the wall is subtracted from the cavity radius. Moreover, the particle radius should be added because the radial position of a particle is defined as the distance between the particle center and the cavity centerline. However, the film thickness is defined as the distance between the cavity wall and the tip of the spherical cap of the particle. Eqs. (4-4) - (4-7) are needed to be solved iteratively with an initial guess for t_{film}. The assumption that the film thickness is zero in Eq. (4-4) in the first iteration is enough for the convergence in this study.

In Figure 4-3, tangentially averaged film thickness in the axial direction for the three receiver sizes are plotted. The trend of the film thickness for the three receiver sizes are quite similar with the largest deviation of $0.1d_p$. For all sizes, the film thickness is getting smaller near the exit. For the considered rotational speed and mass flow rate couples, the change in the film thickness in the axial direction is not large. There is also a slight difference in the film thickness in tangential direction. The porosity of the film is ~ 0.48 in the stationary zone while it is ~0.52 in the

moving zone. Due to continuity, there is ~8% difference between film thickness of the two zones for the considered operational parameter set.

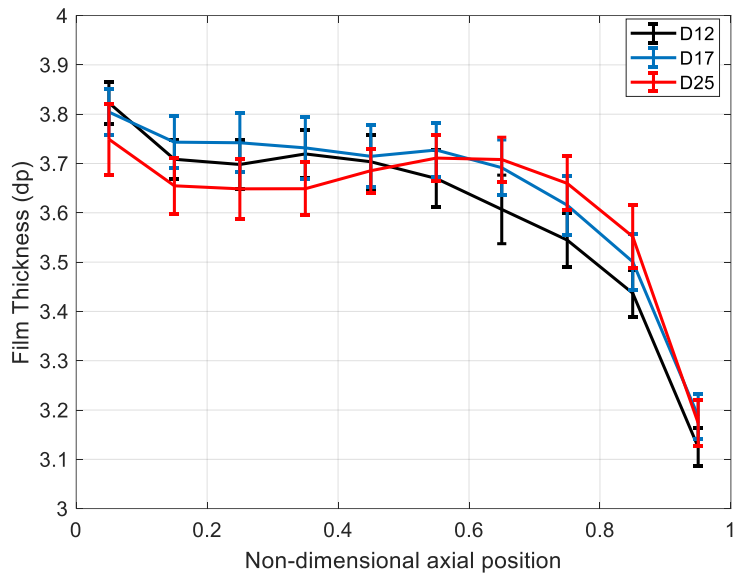

Figure 4-3 Tangentially averaged film thickness averaged for 150 turns. The error bar is the mean standard deviation. 0 and 1 in x axis correspond inlet and exit of the receiver, respectively.

In Figure 4-4, the axial velocities of the particles in the three receiver sizes are qualitatively compared by representing receivers in concentric manner. The moving and stationary zones are noticeable. The angular positions where the stationary zone starts and ends for all sizes are quite similar. Moreover, the axial velocity profiles on the surface in the moving zone are also similar. In order to compare the velocity profiles quantitatively and in deeper parts of the particle film, nine combinations of three different tangential and axial positions are determined as shown in Figure 4-5. In each arc-like particle film section, the axial velocity profiles in radial direction are determined by averaging the results for 150 turns. In Figure 4-6, the axial velocity profiles in the radial direction at nondimensional axial position of z = 0.3 are presented for three different tangential positions located in the moving zone. The profiles for the sizes D12 and D25 match very well in all tangential positions; however, there is a slightly lower velocity profile obtained for D17 at 90° and 135°. This is probably due to that the film thickness at z = 0.3 for D17 is slightly higher, as can also be noticed in Figure 4-3.

In the velocity profile figures, it can also be noticed that the axial velocity profile in the radial direction follows a linear trend from 1 d_p to film thickness value for all cases. Because the stationary particles do not move relative to the wall, the axial velocity is always zero for $r_p < 1d_p$ region. In Figure 4-6(a), the data points are fitted by a linear curve between $1d_p$ and $4d_p$. Although there is hump-like shape in the velocity profile due to particle layering effect resulting from the

existence of the wall (see Chapter 5.1.1.1 for details), the linear velocity profile assumption may be useful for further scaling-up of the CentRec but this is out of the scope of this study.

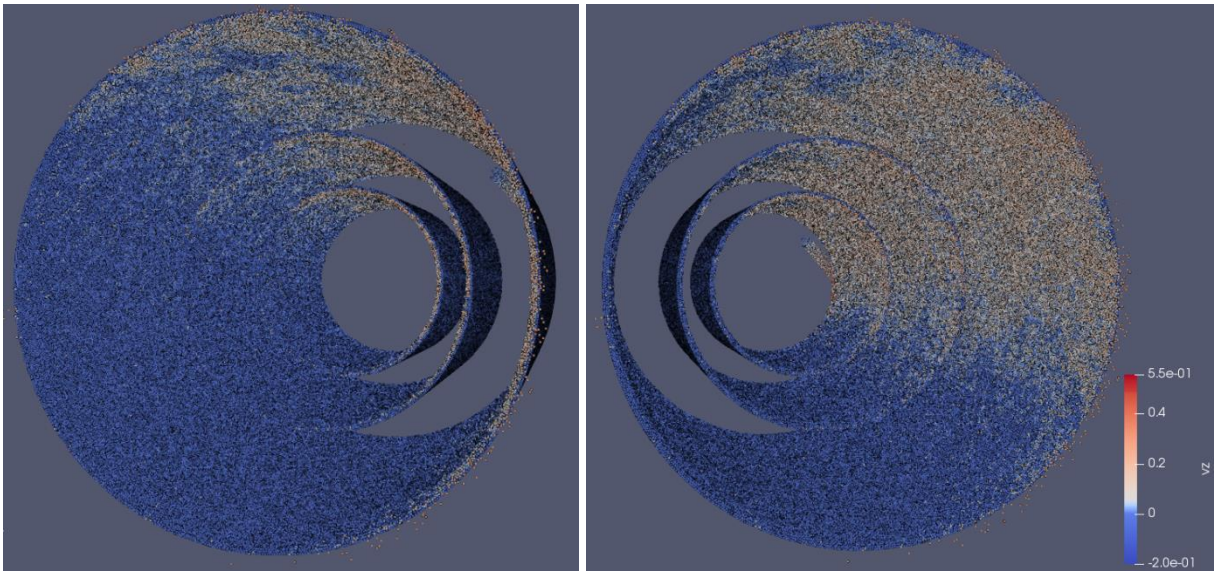

(a) **(b)**

Figure 4-4 Qualitative comparison of axial velocities for the three receiver sizes. A view of **(a)** stationary zone **(b)** moving zone. The color bar is the axial velocity in m/s.

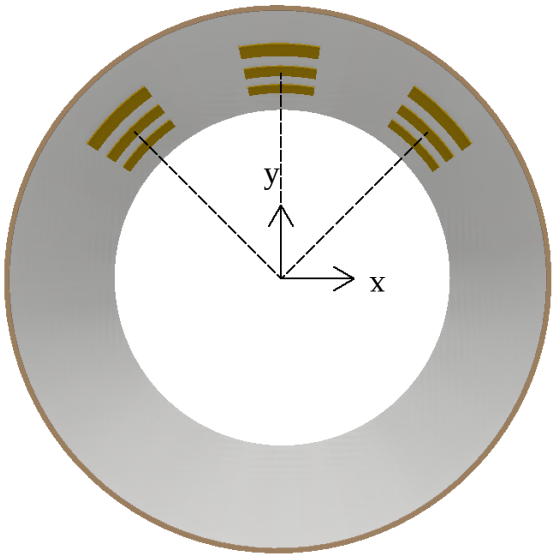

Figure 4-5 The arc-like section volumes to be used in the determination of the velocity profiles. The tangential positions of volumes are 45°, 90° and 135° in counter clockwise direction. The nondimensional axial positions are 0.3, 0.5 and 0.7.

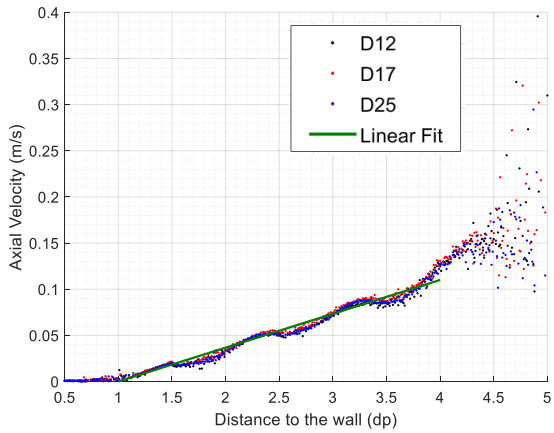

(a)

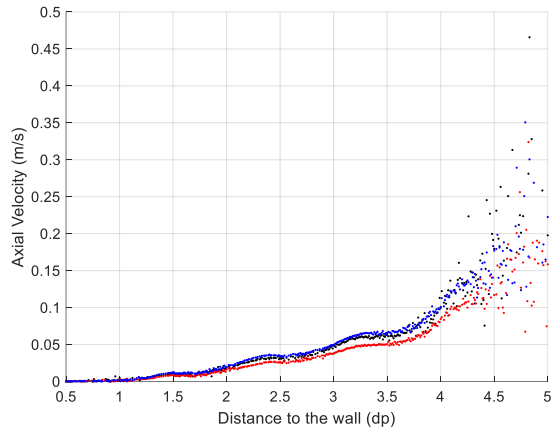

(b)

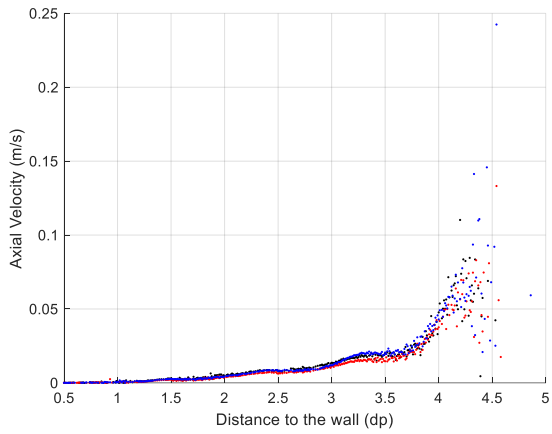

(c)

Figure 4-6 Axial velocity profile in radial direction at non-dimensional axial position of z = 0.3 for tangential position of **(a)** 45° **(b)** 90° and **(c)** 135°.

Similar deviations are also observed for D25 at 45° and z = 0.5 in Figure 4-7 and for D12 at 45° and D17 at 135° for z=0.7 in Figure 4-8. However, in general, there is a very good agreement between particle velocity profiles up to the calculated film thickness. There is no detectable trend for the particles of which centers are beyond ~4.5 d_p for 45° and 90°, and beyond ~4 d_p for 135°. These particles being located on the surface of the film probably move freely or collide with several particles in the moving zone while being exposed to less amount of the friction force. Thus, their motion is not representative for the flow behavior. Note that each circle in these figures corresponds to the average velocity of the particles in the representative location so the figures do not give any information about the particle packing density in the radial direction.

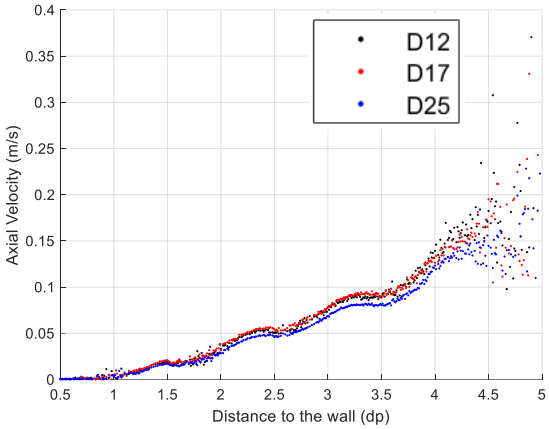

(a)

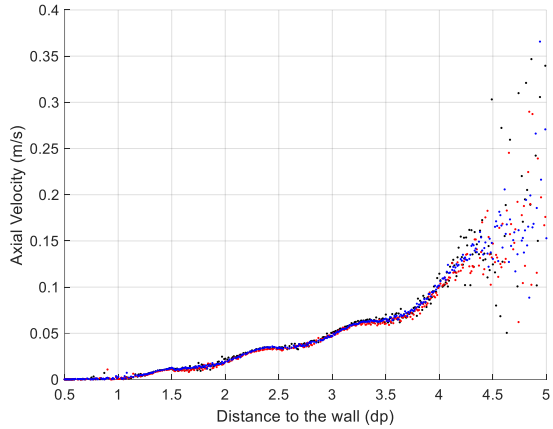

(b)

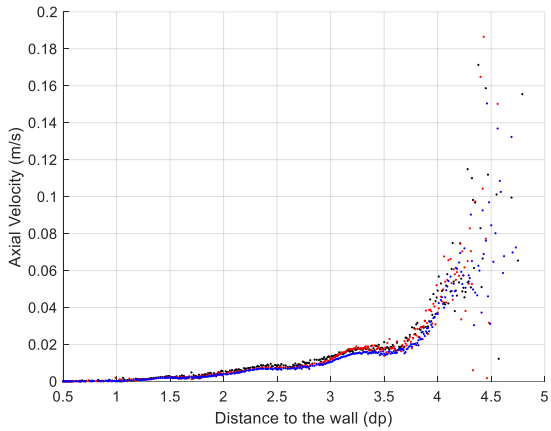

(c)

Figure 4-7 Axial velocity profile in radial direction at non-dimensional axial position of z = 0.5 for tangential position of **(a)** 45° **(b)** 90° and **(c)** 135°.

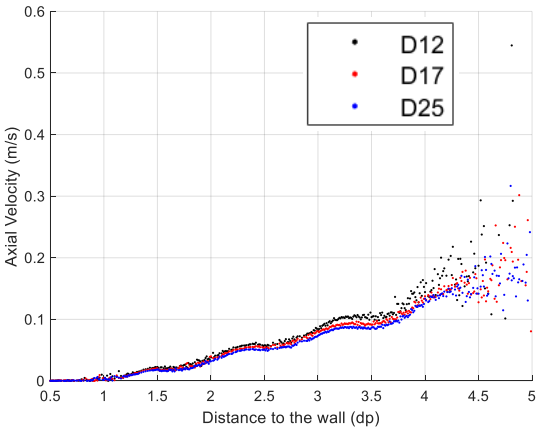

(a)

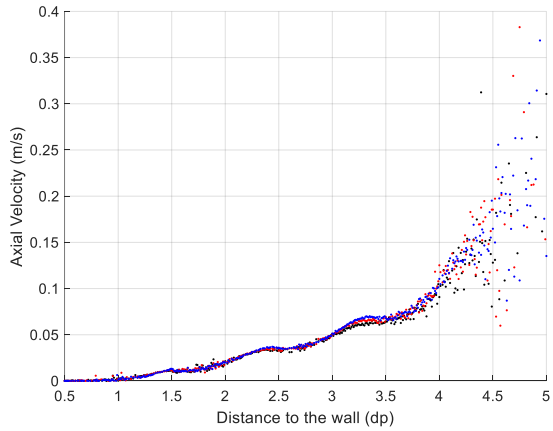

(b)

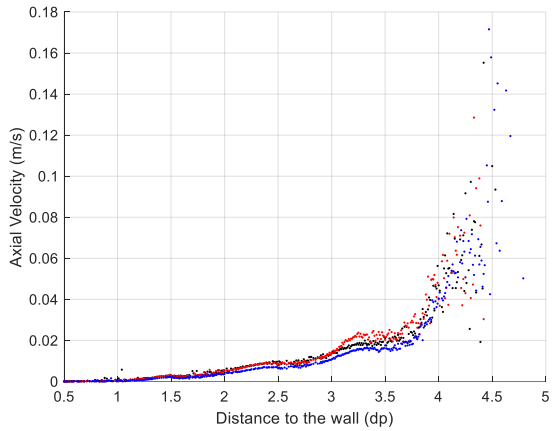

(c)

Figure 4-8 Axial velocity profile in radial direction at non-dimensional axial position of z = 0.7 for tangential position of **(a)** 45° **(b)** 90° and **(c)** 135°.

4.2 DEM Parameter Calibration

The DEM model requires several input parameters to be measured or calibrated for the particle simulations, as discussed in Chapter 2. The input parameters are namely particle diameter, Young's modulus, Poisson's ratio, particle density, sliding friction coefficient, rolling resistance and restitution coefficient. Although the first four parameters are inherently related to a single particle, the last three coefficients are defined for particle-particle and particle-wall interactions. In this study, only SG 16/30 particles used in the experiments are considered in the CentRec simulations. The density of the particles is provided by the manufacturer. The Young's Modulus of the sintered bauxite particles are measured by Bagepalli et al. [76]. Liebl [73] measured the mean sieve diameter of SG 16/30 particles but Grobbel [60] suggested to use an area-weighted mean diameter, also referred to as Sauter diameter, in DEM simulations because it is often used in empirical correlations. Note that Grobbel [77] reported SG 16/30 particles as SG10H because it was named in previous studies in that way but they are the same particle type. The particle properties are listed in Table 4-2. Although it is reported that the circularity of the particle is 0.94, there is 22% difference between sieve and Sauter diameter for particles. For perfectly spherical particles, they are expected to be same. The reason why there is such deviation is that the sieve diameter is based on the smallest cross-sectional area of the non-spherical particle. However, in the measurement of the Sauter diameter, particles are stagnant on a plate such that the larger cross-sectional area of the particle tends to be parallel to the plate; thus, the larger cross-sectional area is measured. To eliminate this problem, Sauter diameter may be measured on a vibrating plate while particles are rolling so that all cross-sectional areas within the particle can be considered. However, it is out of the scope of this study.

Table 4-2 DEM particle properties

Sieve Diameter	mm	0.983
Sauter Diameter	mm	1.2
Density	kg/m^3	3560
Young's Modulus	MPa	209
Poisson's Ratio	-	0.3

In the experiments, a wire mesh is welded onto the cavity wall to obtain a stationary particle layer. However, modeling the mesh with a wire diameter of 1 mm along the cavity wall results in very large CAD file size and also reduces DEM computational speed significantly. Thus, the effect of the wire mesh on the particle motion is considered implicitly. Firstly, the sliding friction coefficient between particle and wall is set to a very high value to prevent particle's sliding on the cavity wall but particles can still rotate on the wall without sliding. If the rolling resistance is also set to very high value to prevent rolling, it is observed that DEM gives very unrealistic results. Thus, to eliminate the particle rolling in axial direction, a damming edge with a thickness of 1 d_p is modelled at the exit of receiver, as seen in Figure 4-9. The particle IDs are monitored during the simulation, and the validity of the numerical trick is confirmed. Although the stationary layer can be obtained with this approach, there is still a contact between wire mesh and particles in reality. The stationary layer, which is obtained a few minutes after stopping the particle flow to the receiver from the particle inlet, can be seen in Figure 4-10. The size of the mesh is 4 mm x 4 mm, thus roughly 65% of the surface area is covered with particles while the rest is covered by metallic wires. However, the particle - wire contact is neglected in this study for the sake of the model simplicity, and particle-wire interactions are assumed to be the same as particle – particle interactions. For this reason, wall properties are not of interest in this study and they are assumed to be the same as the particles.

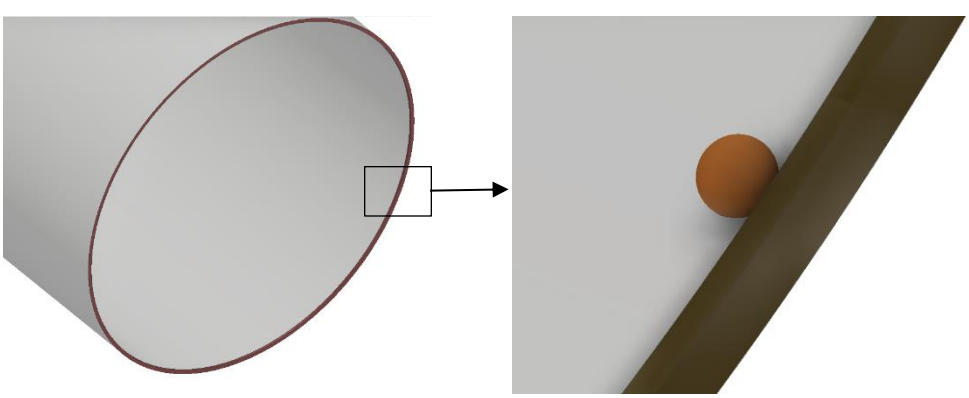

Figure 4-9 View of the damming edge at the exit of the receiver.

Figure 4-10 View of stationary particles and welded wire mesh from the receiver in operation.

Grobbel [77] calibrated the sliding friction coefficient, rolling resistance and restitution coefficient for particle contacts and for SG 16/30 particles. In that study, a plate impact experiment is modeled for the calibration of the restitution coefficient while the static angle of repose and vibrating conveyor experiments are used for the calibration of sliding friction coefficient and rolling resistance. To check the applicability of the parameters found by Grobbel [77] to CentRec application, the results of the simulation for a specific case is compared with experiment results. DEM parameters for three different cases including the parameter set calibrated by Grobbel [77] are listed in Table 4-3.

Table 4-3 Preliminary DEM Particle Contact Properties.

	Case I [77]	**Case II**	**Case III**
Rolling Resistance	0.16	0.16	0.3
Sliding Friction Coefficient	0.56	0.7	0.6
Restitution Coefficient	0.46	0.46	0.46

In the comparison, the simulations are run for a 12-cm-diameter receiver to reduce the number of particles being simulated. Thus, the rotational speed and the mass flow rate are adjusted as 170.4 rpm and 0.0327 kg/s, corresponding 66 rpm and 0.218 kg/s for a receiver with 80 cm diameter. In Figure 4-11, the tip of each curve corresponds the film thickness and the film surface velocity. Because in the experiment, only film surface velocity could be measured, the comparison can only be made for the film surface, not for the deeper section of the particle film. As can be seen

in Figure 4-11, the case using parameters found by Grobbel [77] underestimates the film thickness by 50% while it results in 200% higher axial velocity. This quite large deviation shows that the values found by Grobbel [77] are not applicaple to the CentRec case with the assumptions made in this study. The potential reasons of such deviation may be one of the aspects below or combination of them as of the knowledge of the author.

- The measurement of Sauter diameter of particles may not be accurate.
- Particles used in the previous study and current study might not be the same even if the particle type is reported as the same by the manufacturer because they are provided by the manufacturer in a 5-year-interval.
- Assuming the wire mesh - particle contact as particle-particle contact may lead to some error.
- In the simulation, the stationary particle film thickness is 1 particle diameter (1.2 mm), whereas in the experiment it is assumed as wire mesh thickness (2 mm).
- There may be slight error due to comparing the simulation results for the scaled down receiver with the experiment results for the experiment scale receiver
- Deviation in the results may occur because the parameters were calibrated in experiments being different than CentRec experiment.

The reason why there is such deviation may be one of the reasons above or any combination of them and some other unanticipated reasons. Nevertheless, a new calibration study based on CentRec experiments discussed in Chapter 3 is done to calibrate a new parameter set.

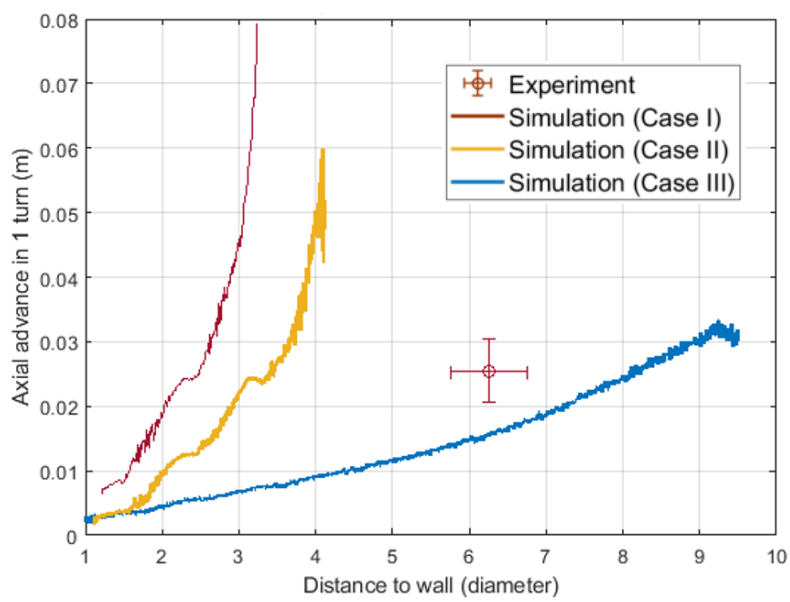

Figure 4-11 Comparison of experiment and simulation results for the cases listed in Table 4-3.

In the DEM parameter calibration study, the operational parameters are scaled for 12-cm-diameter receiver as described in Chapter 4.1. For the calibration, the ranges for 3 DEM particle contact properties need to be determined. Grobbel [77] found that the particle bulk flow on a vibrating plate is not sensitive to restitution coefficient. In CentRec, the particle collisions are also much less dominant than the particle sliding and rolling due to the dense particle packing. Thus, the restitution coefficient is assumed to be the same as the one of that case to reduce the number of calibration simulations. In Figure 4-11, the results for two other property sets listed in Table 4-3 are also presented. Figure 4-11 shows that the experimental axial advance and film thickness pair can be matched by adjusting the sliding friction coefficient and rolling resistance. The simulation with a calibrated coefficient pair should match the experimental results for all mass flow rate and rotational speed pairs. Firstly, a representative experiment point being 64 rpm and 0.218 kg/s is selected to determine the ranges of the coefficients. The ranges for sliding friction coefficient and rolling resistance are found as 0.7 – 1.1 and 0.23 – 0.28, respectively, by trial and error for this operational point. In other words, the simulation results for parameter couples of 0.7 – 0.28 and 1.1 – 0.23 match the experimental results. For rolling friction being lower than 0.23, the simulation results (film thickness) do not match with the experiment unless friction coefficient is much higher than 1. In previous calibration studies, the sliding friction coefficient and rolling resistance was calibrated as 0.83 - 0.17 [78], 0.53 - 0.37 [76], respectively, for different type of sintered bauxite particles having 0.4 mm of diameter. Finally, the intervals for rolling and sliding friction coefficients are specified as 0.01 and 0.05, respectively. It means that for each operational point (mass flow rate and rotation speed), 54 simulations need to be run. In Chapter 3.3, the film thickness and the axial advance in 1 turn of the particles located at the surface of the particle film is found for the combination of 6 different rotational speeds and 4 different mass flow rates. Thus, if the calibration simulation is run for all experiment points, the resulting simulation number is 54 x 6 x 4 = 1296. In order to reduce this number, only 3 rotational speeds (62, 64 and 66 rpm) and 2 mass flow rates (0.092, 0.238 kg/s) are considered.

In the calibration simulation, large standard deviations in particle axial velocities are observed. Thus, the film thicknesses for 6 different experiment points are considered for the calibration. Figure 4-12 shows the "best" points for the simulation so that its results match with the experiment in terms of the moving film thickness. In the experiment, the moving film thickness is defined as follows.

$$t_{mov,exp} = t_{exp} - t_{mesh} \tag{4-8}$$

The experimentally found film thickness "t_{exp}" plotted in Figure 3-6 is the distance between the tip of the particles on the free surface and the wall. The mesh thickness "t_{mesh}" is assumed as 2 mm, being 2 times the wire diameter because of wire-knitting, seen in Figure 4-10. However, in the simulation, the moving film thickness is found as follows.

$$t_{mov,sim} = t_{sim} - d_p \tag{4-9}$$

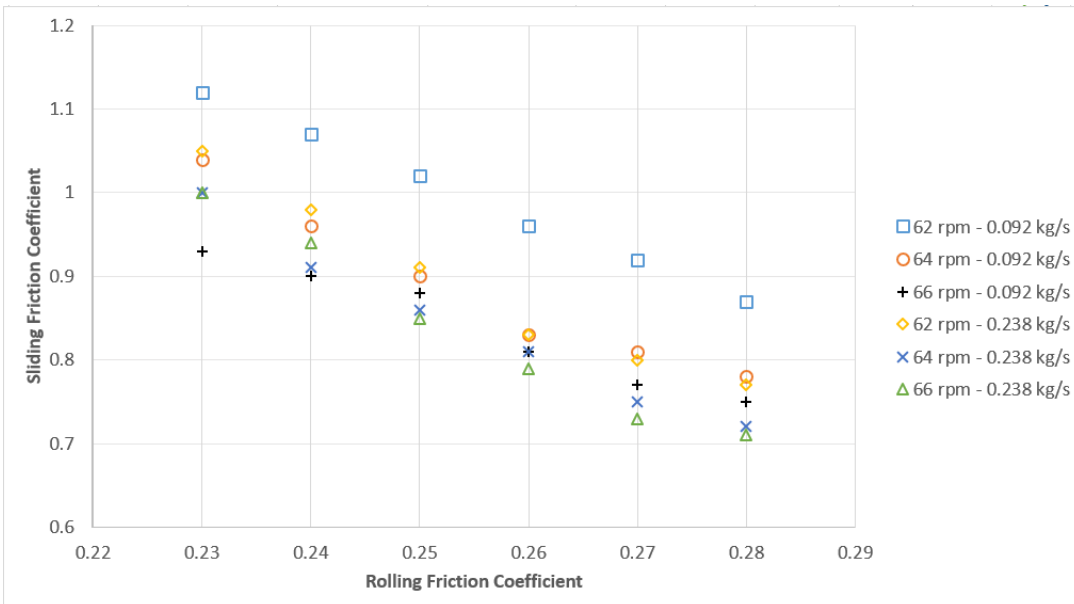

Figure 4-12 The coefficient pairs (best points) matching the experiment (moving film thickness) results of the combination of various rotational speeds and mass flow rates.

The simulation-based film thickness "t_{sim}" is the same as t_{film} in Eq. (4-7). In Figure 4-12, except for 62 rpm – 0.092 kg/s, which results in the smallest film thickness, the best points follow a very similar trend. For 62 rpm – 0.092 kg/s, the moving film thickness is only $2d_p$, so the mesh effects may not be negligible for such a thin film. However, as film thickness increases, the trend becomes similar for all the best points. If one excludes the result of 62 rpm – 0.092 kg/s, the sliding friction coefficient of 0.81 and the rolling resistance of 0.26 gives the least erroneous result. Increasing or decreasing the rolling resistance results in a larger difference between best points.

4.3 Comparison of Experiment and Numerical Results

DEM simulations using the calibrated particle contact properties are run for all combinations of rotation speed and particle mass flow rate considered in the experiments. In the experiment, particles are introduced into the receiver with the help of a circular shape particle distributor, as seen in Figure 1-2(b). Thanks to the rotating particle distributor, particles have almost the same tangential velocity with the receiver when they contact the particle film. However, in the simulation, particles are created in a cylindrical domain near the particle film, as seen in Figure 4-1(a) because the scaling-down of the particle distributor causes particle clogging in the scale-down approach. Although the inlet tangential velocities are similar for both cases, the location of the first contact of the particles is slightly different. Although this small difference may have an effect on particle velocity profile and film thickness near the inlet, it is assumed that this

effect is non-observable in the mid-receiver where particle's axial velocity is measured and near the exit where film thickness is measured.

In Figure 4-13, the moving film thickness found by experiment and simulation is compared for four different flow rates. Note that the experiment scale receiver has a diameter of 0.8 m and a length of 1.2 m while simulation scale has a diameter of 0.12 m and a length of 0.18 m. The rotational speeds and mass flow rates presented in Figure 4-13 and Figure 4-14 are adjusted accordingly based on the scale down methodology for simulation cases. The numerical model estimates the experimental film thickness very well at the axial measurement level for not only the flow rates considered in the calibration study being 0.092 kg/s and 0.238 kg/s but also at higher flow rates resulting in thicker films. Figure 4-14 shows the comparison of axial velocity at the mid-level found by simulation and experiment. The results are in good agreement for the lowest mass flow rate. However, for higher mass flow rates, the simulation predicts the velocity around 20% smaller than the experiment for the complete range of rotational speeds except for 67 rpm/s. As of the knowledge of the author, there may be 2 main reasons of such discrepancy. The first reason is that in the simulations it is observed that as rotational speed increases, the film thickness at the mid-level fluctuates with time. The fluctuations of the film thickness in the middle of the receiver also cause the fluctuations in the axial velocity profile. Although the simulation results are found by time averaging over 200 turns, the fluctuations are not periodic for all cases. Thus, this effect may create some error in axial velocity found by the simulations. However, this effect hardly explains such a big deviation. The second and more probable reason is that the manufacturing tolerances in the receiver wall may cause that the axial velocity profile is not similar for all regions of the receiver in the tangential direction. Recent experiments conducted in the Synlight solar simulator facility located in Juelich/Germany shows that there are low-velocity and high-velocity regions over the circumference of the receiver [79]. The reason of such flow behavior has not been revealed yet, but the effect of manufacturing tolerances in the cavity wall and the wire mesh arrangement on the particle velocity and film thickness is currently investigated by researchers. The simulation model that takes such details into account is addressed as a future study.

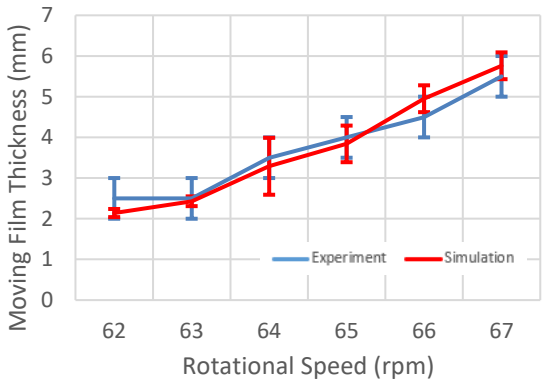

(a)

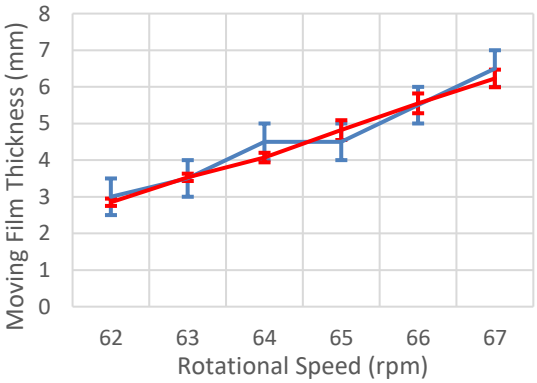

(b)

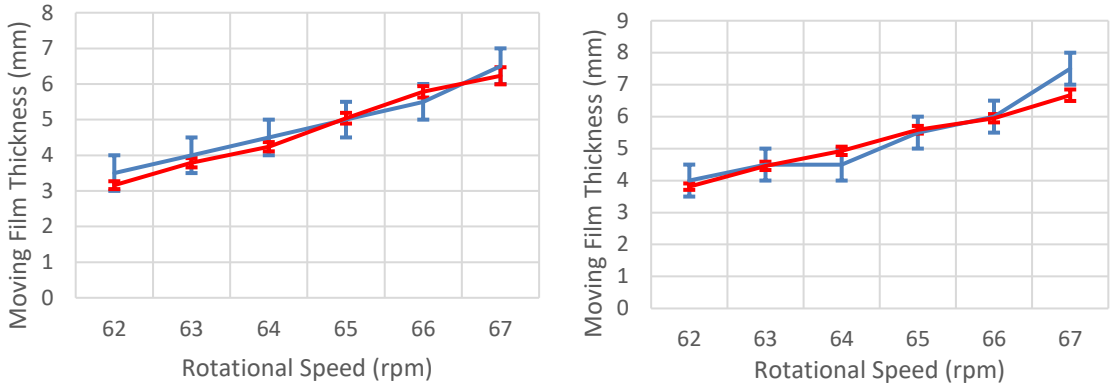

(c) **(d)**

Figure 4-13 Comparison of experiment and simulation results in terms of moving film thickness at the non-dimensional axial position of 0.83. The mass flow rate is **(a)** 0.092 kg/s **(b)** 0.218 kg/s **(c)** 0.312 kg/s **(d)** 0.489 kg/s.

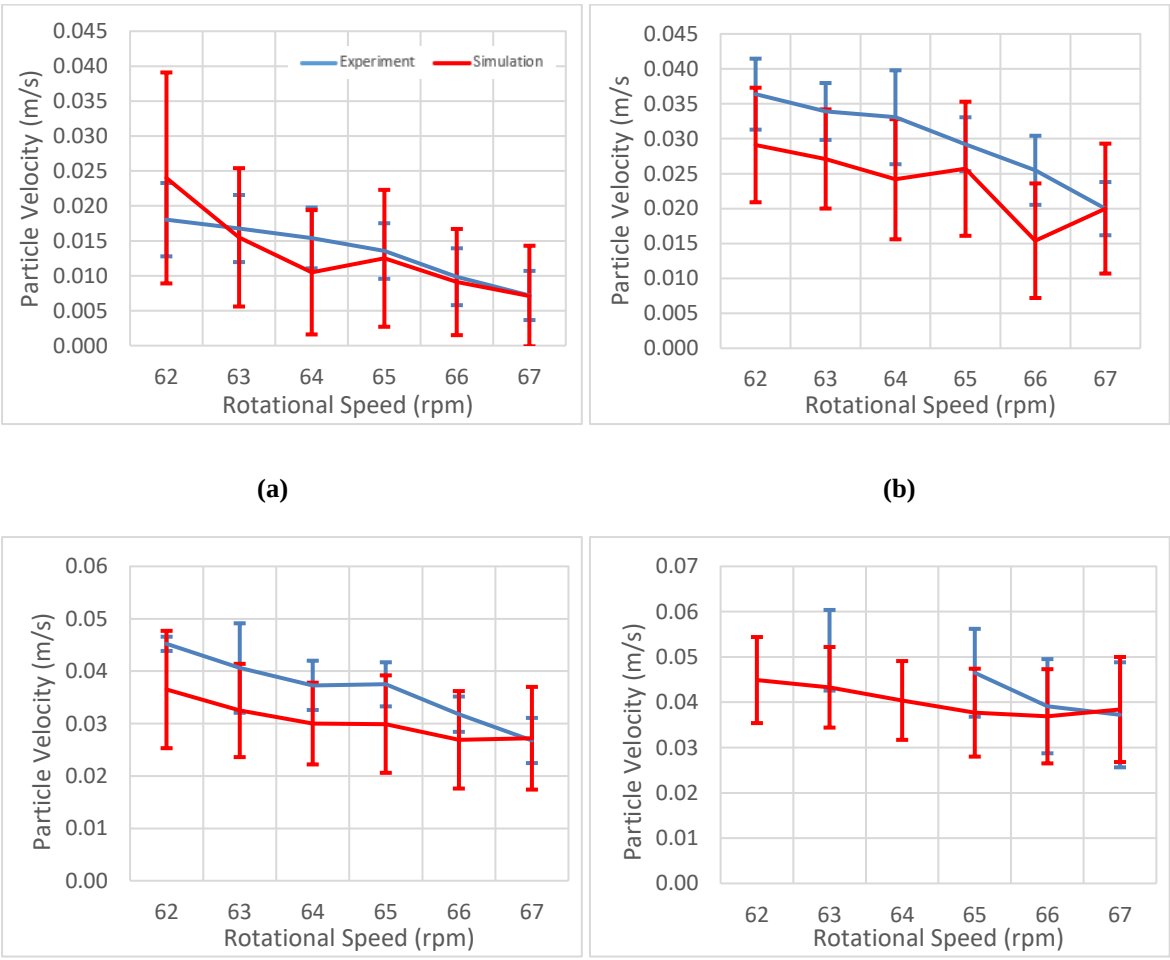

(a) **(b)**

(c) **(d)**

Figure 4-14 Comparison of experiment and simulation results in terms of particle axial velocity on the surface **(a)** 0.092 kg/s **(b)** 0.218 kg/s **(c)** 0.312 kg/s **(d)** 0.489 kg/s.

5. NUMERICAL THERMAL MODEL

Some of the content in this chapter is published by authors including the thesis author:

E. F. Johnson, S. Hicdurmaz, R. Buck, and B. Hoffschmidt, 2022. Beam radiation penetration in particle beds for heat transfer modeling of a centrifugal solar particle receiver. Journal of Quantitative Spectroscopy and Radiative Transfer, vol. 295, no. 108403.

The content of the journal paper, not created by thesis author directly, is cited as [80] while the content created directly by the thesis author is not cited in the thesis.

To model heat transfer in the context of particle flows is of great interest to several industries including nuclear pebble bed reactors [81, 82], fluidized beds [83] and laser sintering technology [84]. In recent years, thermal modeling of particle-based CSP systems has been also investigated by researchers to optimize the thermal efficiency of solar particle receivers [60, 85, 86] and particle heat exchangers [87-89]. In the development of thermal models for particle flows, although models are utilized to calculate the heat transfer at the particle scale, bulk scale approaches are also very useful, especially in stagnant packed beds. An effective bulk thermal conductivity for a stagnant bed is broadly investigated for the bulk region [90], where wall effects on the particle packing are negligible, and the near-wall region [54]. This thermal conductivity is mainly a function of particle and fluid thermal properties, particle size and temperature, bed porosity and pressure. Zehner et al. [91] developed a bulk thermal conductivity model, also known as ZBS model and being applicable to stagnant packed beds, by considering two touching half non-perfect spheres in a unit cylinder. Later, the model was improved in a way that it includes pressure and radiation effects [92, 93], and it was validated by several studies for the bulk region [81, 90]. However, in CSP applications using solid particles as heat absorption medium, particles are moving in dense [94] or dilute [49] regimes. Thus, models developed for stagnant beds are not directly applicable to moving beds due to continuously changing packing structure and particle mixing effect. For this reason, particle scale heat transfer models are utilized in moving particle beds. In a particle bed, the heat is mainly transferred via the mechanisms listed below and labeled with numbers shown in Figure 5-1.

- Particle – particle conduction
  - Through contact area (1)
  - Through interstitial fluid (2)
- Particle – particle radiation (3)
- Particle – fluid convection (4)
- Particle – wall conduction
  - Through contact area (5)
  - Through interstitial fluid (6)
- Particle – wall radiation (7)
- Wall – fluid convection (8)

- Inner particle conduction (9)

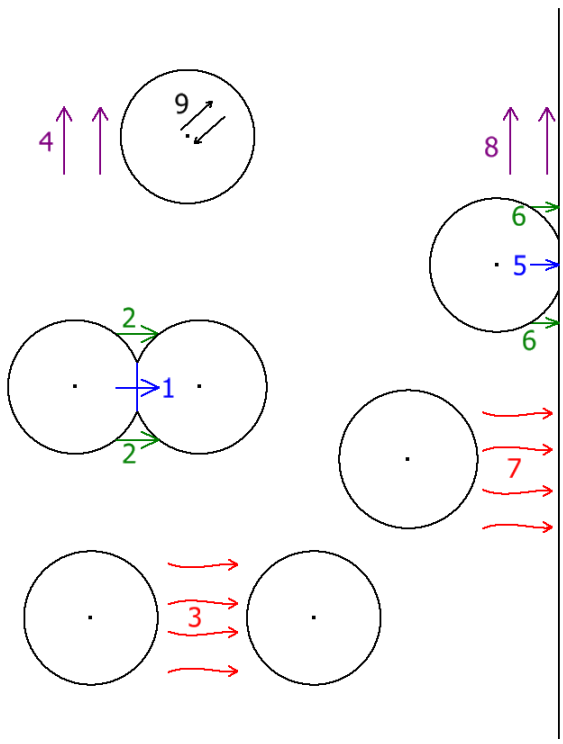

Figure 5-1 Schematic view of particle scale heat transfer modes.

To model particle – fluid heat transfer in DEM-based particle simulations, CFD coupling is often employed [95, 96]. In this approach, the heat transfer between particle and its surrounding fluid is calculated by an interphase heat transfer coefficient. In CentRec, particle – fluid convection is considered as two separate mechanisms: 1. The convection heat transfer between particle and interstitial fluid filling the void between particles, 2. The convection heat transfer between particle film as a bulk and circulating air inside the rotating cavity. The second mechanism, being convection loss from cavity receivers, is discussed in detail in Chapter 5.4. However, the first mechanism is not modelled in this study for several reasons. In a rotating particle receiver (CentRec), it is assumed that the velocity field for particles and interstitial air is similar, especially in the tangential direction. However, there may be some relative motion of air in radial and axial direction because of temperature gradients in the particle film. In other words, the heat may also be convected inside the film by mass transport of air. Here, it should be stated that for small particles (~1 mm of diameter), the interphase heat transfer coefficient is relatively high [46] so that temperature distribution of air and particle phase can be assumed as being the same. Although high interphase heat transfer coefficients increase the role of the heat transfer by air mass transport, due to the fact that thermal inertia (ρc_p) of air is much lower than the one of a particle, the heat loss/gain from/to particles due to this mechanism is negligibly small during the particle's residence time in the receiver. It should also be noted that the effect of this mechanism is proportional to the air

relative motion in radial and axial direction. However, in a relatively packed film, the presence of particles also makes air motion difficult. Thus, it is assumed that the movement of air has negligible effect on particle temperature distribution, and heat is transferred via stationary fluid by conduction. A more detailed investigation can be done by modeling the air side flow with DEM-CFD modeling approach. However, doing this is avoided here. Similarly, wall-fluid convection is not modelled in this study by assuming wall to bed heat transfer to happen only due to radiation and conduction. The other heat transfer mechanisms listed above are discussed in detail in the following sub-chapters.

In the literature, several thermal models have already been implemented to DEM codes. However, they have some limitations and inadequacies in terms of heat transfer-related sub-models being employed. LIGGGHTS® - Public, which is also used to model cold particle flow in this study, only considered the particle - particle conduction via contact area, which is much less dominant than particle - fluid - particle conduction, due to the very small contact radius [62]. There is also no radiation model implemented. Rocky DEM®, a commercial software, also suffers from same limitations. Only conduction via particle-particle contact area is modelled but in this time, load applied on particles is also taken into consideration [97]. MFIX [98], being another open source code, lacks a proper documentation of sub-heat transfer models. To eliminate these problems, researchers generally developed their in-house thermal codes and couple them to DEM solvers [95, 99]. Grobbel [60] developed a thermal code applied to particle flows under vacuum condition. In the absence of interstitial fluid or at very low pressures, conduction through the contact area become more dominant. Because it is hard to estimate the contact radius between non-spherical touching particles, Grobbel [60] used ZBS model, which was also tailored for non-spherical particles, to derive a correlation for particle scale heat conductance. However, this approach requires cumbersome numerical calibration in prior. Recently, Johnson et al. [100] published an open source thermal code for granular flows to be used in particle heat exchangers by considering particle scale radiation and conduction for particle-particle and particle-wall interactions. Although, the complete model is validated by experiment, the particle conduction model may contain some errors, and it was pointed out as future work [101]. Moreover, the implemented radiation model is derived for the bulk region but in the CentRec application, the wall effects, affecting particle packing structure, is not negligible.

In the development of the heat transfer models, being applicable to DEM, for the solar particle receivers, modelling direct solar irradiation reflected by mirrors is the essential part of the thermal models. To do so, ray tracing-based approaches are utilized to distribute the solar irradiation to individual particles [60] but the computational burden is generally so high that it is not easily applicable to large scale receivers (>1 million particles). Moreover, due to temperature gradient in the particle film, there is radiation heat exchange by emission. If the thermal radiation from a particle is directed to nearby particles or wall, it is called as “short-range thermal radiation”. However, there is also radiative heat exchange by emission between hot and cold regions of particle film and large surfaces of the receiver due to hollow cylinder-like particle film shape in CentRec. This mechanism is called as “long-range thermal radiation”. Monte Carlo ray tracing (MCRT)

method-based algorithms have been developed to model thermal radiation in particle beds for spherical, monodispersed particles and non-participating fluid phase [60, 102, 103]. The general idea of MCRT-based algorithms is to find the view factor from surface A to surface B in a statistical manner. Rays generated with a random direction and position on surface A are tracked along their path to check if intersection on surface B occurs. Simply, the ratio of number of intersected rays to total number of generated rays gives the view factor from surface A to B for a sufficiently high number of rays such that the ratio is independent of ray number. However, tracking the rays of which number is an order of magnitude higher than the particle number is also computationally expensive.

In order to address these points, a complete thermal model is developed along with CentRec-specific assumptions to reduce the computational burden. The thermal model is developed in MATLAB with its core functions. Thus, there is one-way coupling between LIGGGHTS and MATLAB such that the MATLAB-based thermal model has no effect on LIGGGHTS-based cold particle flow. The x-, y- and z- position of each particle in each thermal coupling time step is stored in a .txt file and used as input in the thermal model. The main advantage of such coupling is that various solar flux distributions can be applied to the same particle packing configuration without running the DEM side repeatedly. During an operation day, the flux distribution on an aperture plane may change with sun's position and it has an effect to particle outlet temperature. Thus, many flux distributions varying in a daytime can be applied to a moving particle film to monitor the time-dependent particle outlet temperature. However, a recent study has shown that for relatively small size ceramic particles, particle DEM contact properties like friction coefficient and rolling resistance change with temperature [104]. The measurements were done for a single particle type and size so temperature dependency of DEM parameters for different material composition, particle size and shape are still an open question. Moreover, the physical explanation of such phenomena is still unrevealed. Thus, one-way coupling is still preferred for the abovementioned advantage in this study but it is possible to embed the developed thermal code to open source DEM codes or integrate it to commercial software via User Defined Functions (UDF).

5.1 Radiation Model

The radiation heat transfer is the main heat transfer mechanism in the CentRec because the particles are mostly heated up by the solar irradiation while they lose energy by thermal radiation, convection and conduction. There are two main radiation modeling efforts for the CentRec. The first is the modeling of solar irradiation. The solar rays crossing the aperture plane are either absorbed by the particle film or reflected to other sections of the particle film or the large surfaces of the receiver like particle distributor plate and ring-shaped collector plate or aperture plane, as seen in Figure 5-2. Depending on particle bulk reflectivity and cavity wall reflectivity, the rays may be reflected several times inside the cavity. If a ray leaves the receiver from the aperture plane, it is considered as "reflection loss". The rays absorbed by the particle film are modelled with a "Radiation penetration model" (Chapter 5.1.1). On the other hand, reflections inside the cavity are modelled with the "Reflection model" (Chapter 5.1.2). The second radiation modeling effort for

the CentRec is the thermal radiation driven by temperature difference. Modelling thermal radiation as two separate mechanisms namely, “short-range” and “long-range” radiation is a useful approach. Each mechanism is modeled separately in Chapters 5.1.3 and 5.1.4. The net thermal radiation into the aperture plane is considered as “emission loss”. The sum of reflection and emission loss gives the total radiation loss.

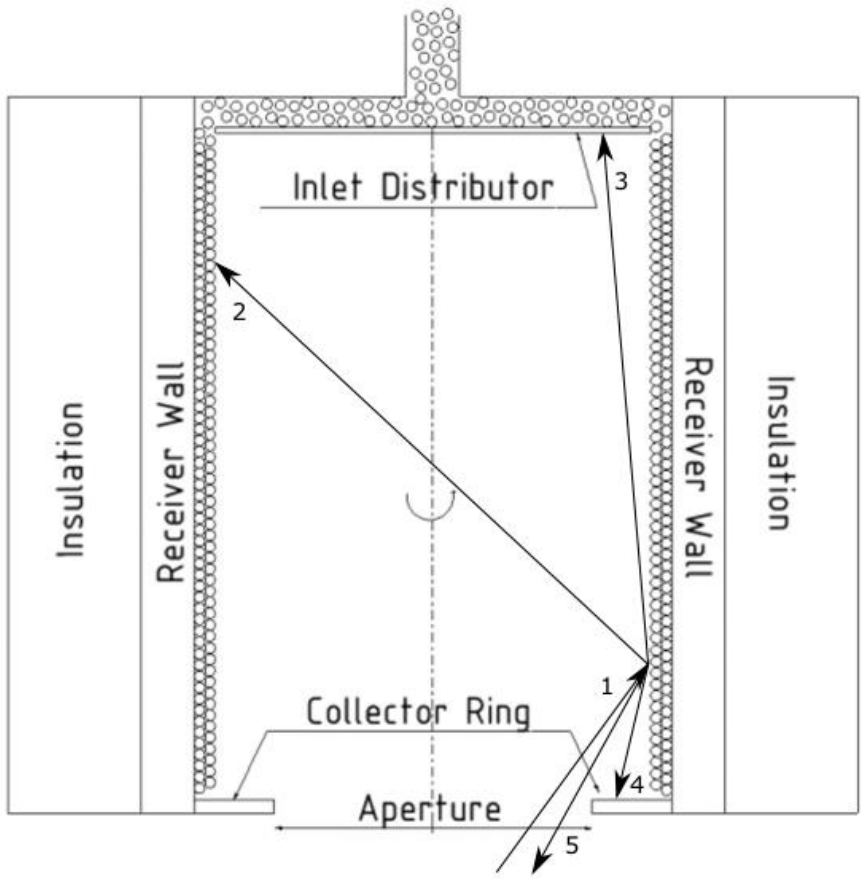

Figure 5-2 Schematic cross-sectional view of the CentRec along with the representative rays: (1) solar irradiation, (2) reflection to other parts of the particle film, (3) reflection to particle distributor, (4) reflection to collector ring, (5) reflection to aperture, i.e. reflection loss.

In this work, reflections and emissions from the particle surface are assumed as gray and diffuse for ceramic particles with a dull and rough surface. Thus, throughout this work, particle absorptivity (α_p) is assumed to be equal to particle emissivity (ϵ_p). Because ceramic particles are opaque, the particle reflectivity is found as ($1 - \alpha_p$) or ($1 - \epsilon_p$). Note that gray and diffuse assumption holds for the individual particle surface, but not for the particle film surface.

5.1.1 Radiation Penetration Model

In the CentRec, the solar irradiation, which can also be referred to as external beam radiation, crosses the aperture plane and strikes the moving particle film. The radiation penetration model is developed to find the reflections from the moving particle film and the beam propagation

inside the film. External beam radiation applied to particle beds has been studied by several researchers numerically [84, 105-107] and experimentally [108-110], mostly for the application of laser sintering of metallic powders. While in most studies, reflections from non-black particles are modelled as specular, Singh and Kaviany [106] found that diffusely reflecting particles result in a lower bed absorptivity than specularly reflecting particles. Gusarov [84] used MCRT to find the radiation penetration into ordered structured beds such as Body Centered Cubic (BCC) ones. In some experimental studies [108, 110], the bulk absorptivity/reflectivity of metallic powder beds are measured while some others [109] measured radiation transmission through a packed bed to correlate radiative thermal conductivity. However, there is no study focusing on absorption/transmission behavior of external beam radiation with various incidence angles in a randomly generated particle bed, and for a wide range of bed porosity and particle absorptivity. Because running MCRT for particle beds composed of more than hundreds of thousands of particles is not practical due to excessive computational burden, an additional DEM-compatible radiation penetration model is addressed in this study. The model considers incidence angle of the beam (β), particle absorptivity (α_p) and solid volume fraction of particle bed (f_s) for a randomly generated bed.

5.1.1.1 Model Development

An open source MCRT code to be used in derivation of the new model was developed and validated to simulate external parallel rays by Johnson et al. [80]. The incidence angle is defined as the angle between the ray direction vector and the surface of the particle bed, as seen in Figure 5-3(a). Because the bed packing structure is direction-independent for lateral directions, there is no need to consider the azimuth angle. In Figure 5-3(b), a trajectory of a single ray is shown for specularly reflecting particles. Note that the nature of reflection (diffuse or specular) can be chosen by the user in the code.

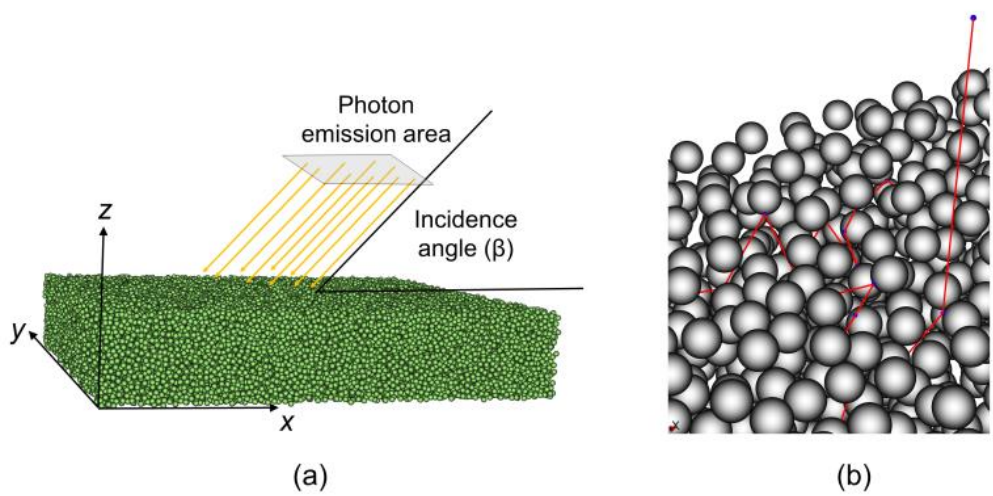

Figure 5-3 Photons striking particle bed in MCRT, showing **(a)** general geometry, and **(b)** a ray reflecting specularly many times before being absorbed.

In this study, the particle bed is characterized by a solid volume fraction of the bed (f_s). To generate the randomly packed particle beds two approaches developed by [80] are followed. For packed beds ($f_s \geq 0.55$), many particles (~100,000) are generated in a DEM domain and allowed to come to rest, in the presence of gravity, against a wall. The bed thickness is set as higher than 10 times of particle diameter so that wall effects are eliminated. By changing DEM particle contact properties such as rolling resistance, one can obtain f_s between 0.55 and 0.64. For dispersed or dilute beds ($f_s < 0.55$), particles with initial velocity are first inserted into the DEM domain of which boundaries are periodic, i.e. if a particle leaves the boundary of the domain, it reappears in the opposite boundary with the same velocity. Then, particles are let to move in the domain without the effect of gravity. Thanks to elastic particle-particle collisions, the total kinetic energy of the system does not change with time. In other words, particles move in the domain indefinitely. After some time when the effect of initial particle configuration is completely invisible, a snapshot of particle position is exported. At the final particle configuration, the local solid fraction is the same everywhere, thus a uniform solid fraction bed can be obtained. By changing the initial particle number or domain volume, one can obtain any f_s smaller than 0.55.

The bed absorptivity (α_{bed}) is a crucial parameter for particle receivers because it directly affects the receiver thermal efficiency. Low α_{bed} leads to more reflection losses. To find α_{bed} for a particle bed, one needs the solid fraction of the bed (f_s), beam incidence angle (β) and particle absorptivity/emissivity (α_p). Johnson et al. [80] found the bed absorptivity for various combinations of these three parameters of which values are listed as:

- f_s: 0.10, 0.20, 0.30, 0.40, 0.50, 0.55, 0.60, and 0.64
- β: 15, 30, 45, 60, 75, 90 degrees
- α_p: 0.20, 0.40, 0.60, 0.80, 1.00

In Figure 5-4(a), it can be noticed that the bed absorptivity is increasing with particle absorptivity for all solid fractions, as expected. Moreover, the solid fraction's importance is higher at lower particle absorptivity. In Figure 5-4(b), the relation between incidence angle and bed absorptivity is shown. The incidence angle has very small effect on bed absorptivity for values higher than 60°. However, in CentRec application, the incidence angle mostly varies between 15° - 60°, thus incidence angle has non-negligible effect on bed absorptivity.

After finding what portion of external beam is absorbed by the bed, the next step is to find the beam propagation length. In MCRT-based simulation, a number of parallel rays are generated. In order to plot the transmission curve in the depth direction of the bed, an absorption location is needed for each ray generated. The first and more realistic approach, called as "absorption location method", is to use the exact absorption location of a propagating ray on the particle surface. However, in many DEM simulations, the particle temperature is assumed as uniform, i.e. no temperature gradient within the particle, thus a single temperature information is tracked for each particle. To make MCRT results more applicable to current DEM simulations, a second approach, called as "particle center method", where particle center is considered as absorption location, can be used. For the cases where rays penetrate through the bed in a specific direction like this study,

there is a little difference between transmission curves generated by these two methods although the slope of the curves are similar, as can be seen in Figure 5-5. However, due to inner particle conductivity and dynamic nature of particles, this difference can be ignored in CentRec application. A more detailed discussion can be found in Chapter 5.2.3. Note that due to bed reflectivity, the transmission at zero depth is some value below 1. In Figure 5-5, the zero depth corresponds the position of center of the topmost particle plus 1 radius; in other words, the tip of the topmost direction. Thus, there is no absorption in the first 1 radius for "particle center method".

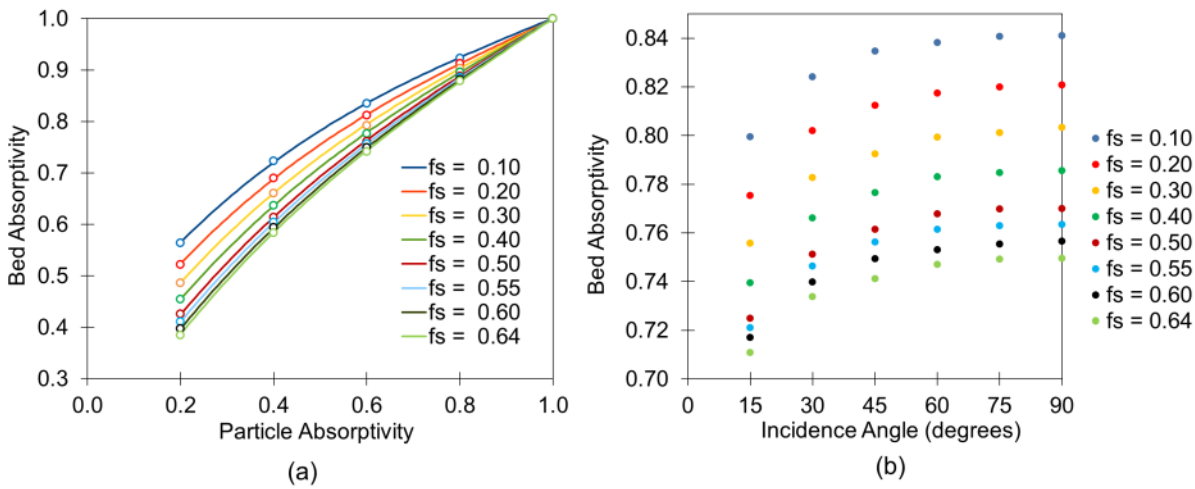

Figure 5-4 (a) Bed absorptivity for various particle absorptivities and solid fractions for β = 45º, where each point is a MCRT simulation result and lines representing best curve fits **(b)** bed absorptivity at various incidence angles and solid fractions, for a particle absorptivity of 0.6 [80].

In Figure 5-6, the effect of particle absorptivity on transmission behavior for many incidence angles are presented. It can be noticed that the transmitted fraction of beams is almost linearly decreasing in depth direction if logarithmic scale is considered. For high α_p values, the effect of incidence angle on transmitted fraction is more prominent.

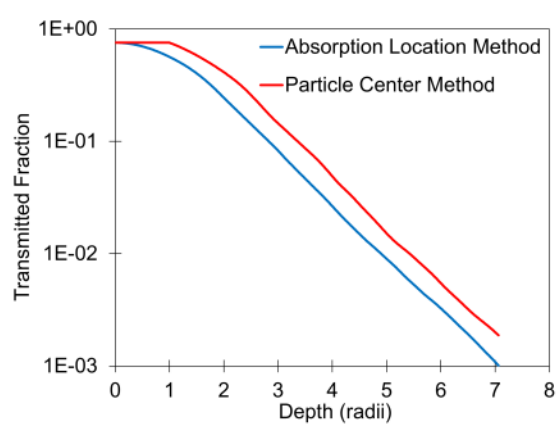

Figure 5-5 Transmitted fraction of incident radiation at various depths, for f_s =0.60, α_p = 0.60, β=90°. Red and blue lines show results by post-processing the MCRT results with two different methods [80].

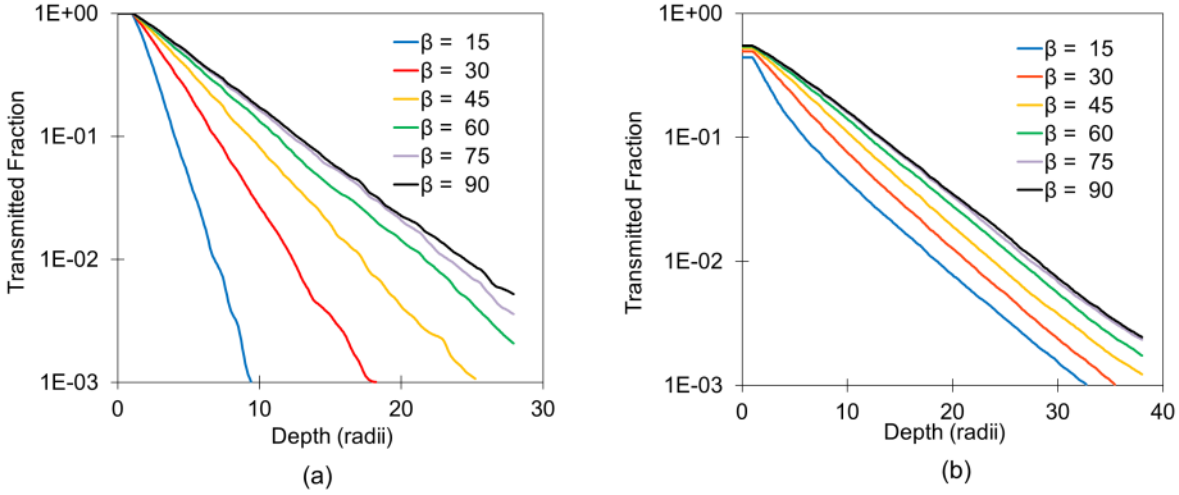

Figure 5-6 Transmitted fraction for f_s =0.20, with **(a)** α_p = 1.00, and **(b)** α_p = 0.20 [80].

By applying MCRT to any uniform solid fraction bed, one can estimate the absorption of each particle in the bed based on their distance to the top of the surface [80]. However, in CentRec, the solid fraction is fluctuating due to layering effects of the wall (blue line in Figure 5-7). This happens when the particle film is thin enough that the local solid fraction does not converge to the bulk solid fraction before the top of the film. However, an effective bulk solid fraction is needed to estimate bulk absorptivity and radiation penetration behavior. Shown in Figure 5-7, this effective bulk solid fraction is found by linearly interpolating between two sequential maxima or minima (black dashed lines), and then the center point is found between that line and the opposing maximum or minimum (red dots). Five of these mean values are found, and the mean is taken to find the effective bulk solid fraction, shown as the red dotted line. This approximation technique gives an estimation of the solid fraction to which the bed would converge if it were thick enough to reach a bulk solid fraction. Using a thin particle film raises the question of whether the transmission curves developed for thick beds are valid, or if the layering effects against the wall change the transmission curve too much to be useful. To investigate this, the transmission curves for beds with thicknesses of 4, 6, 8, and 20 radii are shown in Figure 5-8. Each curve starts with the free surface at 0 so the shape of the curves can be easily compared. The curve for the very deep 20 radii thick bed (black line) represents a thick bed, and there are no near-wall effects visible. The curves for the 8 radii thick bed (red line) and 6 radii thick bed (green line) are nearly on top of the thick-bed line, showing the behavior is essentially the same as the deep bed case. For a bed thickness of 4 radii (blue line), the layering of particles and the oscillations in solid fraction cause some strange changes in curvature. Thus, it can be concluded that for films thicker than 6 radii, the transmission formulas derived for the bulk region can be utilized. This constraint is not a problem for CentRec as the film thickness is always greater than 6 radii.

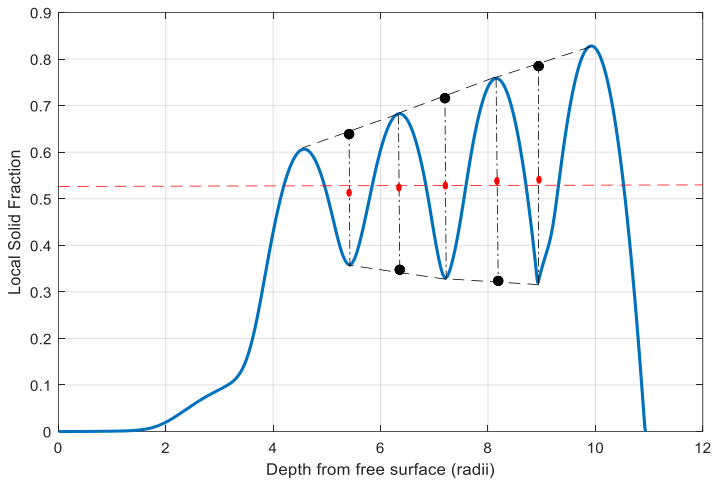

Figure 5-7 Local solid fraction distribution of a particle film taken from CentRec simulation and peak – valley approximation (black and red dots) to find effective bulk solid fraction (red dashed line). Zero depth corresponds the topmost particle plus 1 radius.

As a first step in the algorithm, the α_{bed} is found by using α_p, f_s and β as described above. Though the bed is relatively thin, MCRT modeling showed the portion of incident radiation penetrating entirely through the film to the cylinder wall was less than 0.01% for the CentRec case, so it is assumed that all rays are either absorbed or reflected from the bed surface.

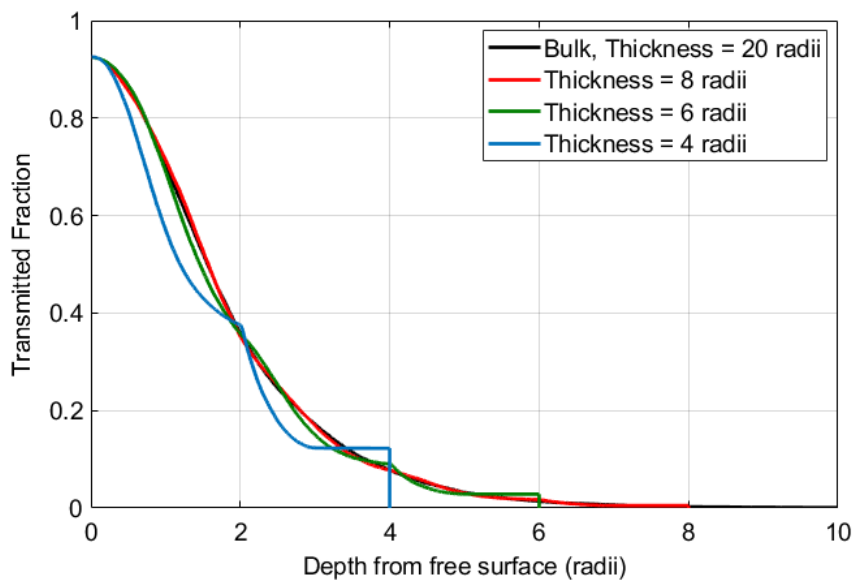

Figure 5-8 Transmission curves for particle films with a thickness of 20 radii, 8 radii, 6 radii and 4 radii, with particle emissivity of 0.86.

To distribute the energy to the particles in a realistic manner, the algorithm relies on two distincts of the transmission curve, as shown in Figure 5-9. The "nonlinear" transmission region is

visible between 0 and 2 radii where the transmission curve (red line) decays in a nonlinear fashion, which is mainly due to the increasing solid fraction in this interval. At depths greater than 2 radii, the "linear" transmission region is seen. The actual transmitted fraction has an exponential decay, but it appears linear when plotted using the natural log on the y-axis.

The transmission curve in the "nonlinear" region is fitted with a 4th order polynomial (Eq. (5-1)), while the curve in the linear region starts at the transmitted fraction at d = 2 radii ($q_{tr}(2)$) and decays with a linear coefficient "b" (Eq. (5-2)). This two-part curve fit is found for each combination of solid fraction and incidence angle, and the coefficients are shown in Table A.1 in the Appendix section, for a particle emissivity of 0.86 to represent sintered bauxite [60]. The coefficients for other particle emissivities can also be derived by using the publicly available code [111].

The particle film is divided into many layers parallel to the wall, each with thickness of t, where t is smaller than the particle radius. Therefore, the radiation absorbed by each layer is the difference between the transmitted fraction at the top (depth of d) and bottom (depth of $d+t$), shown in Eq. (5-3). In these equations, d is the depth coordinate in units of radii. Similar to the transmission curves shown throughout this work (e.g. Figure 5-9), the transmitted fraction at the surface is equal to the bed absorptivity ($q_{tr}(0) = \alpha_{bed}$).

$$q_{tr}(d) = \exp(a_0 + a_1 d^1 + a_2 d^2 + a_3 d^3 + a_4 d^4) \qquad 0 \le d \le 2 \tag{5-1}$$

$$q_{tr}(d) = q_{tr}(2)\exp(-b(d-2)) \qquad d \ge 2 \tag{5-2}$$

$$q_{abs}(d) = q_{tr}(d) - q_{tr}(d+t) \tag{5-3}$$

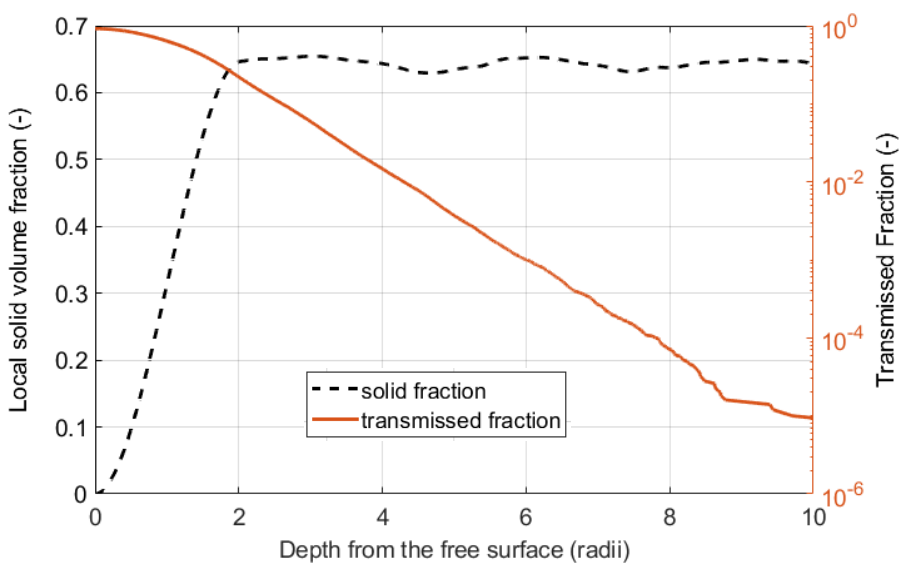

Figure 5-9 Two distinct transmission regions: (0-2 radii) a nonlinear decay; (2-8 radii) a linear decay for 90° of incidence angle, 0.64 of bulk solid fraction and 0.86 of particle emissivity.

In CentRec (and other realistic particle beds) some particles often sit up higher than the rest of the bed, not settling perfectly due to particle-particle friction and the dynamic nature of the CentRec system, as seen in Figure 5-10. Because the rays strike the film from the top surface, handling these "sparse" particles is crucial. Furthermore, in CentRec the thickness of the particle film changes both in time and in the *xy* plane, making the energy distribution algorithm more challenging than in beds with a uniform solid fraction. The algorithm is developed to calculate the energy absorbed by each layer, and then the heat in each layer is distributed to all particles based on their solid fraction inside the layer. To define the surface of the particle film, the depth of 0 is defined as the cap of the highest particle (or equivalently, the center of the particle furthest from the wall plus 1 radius).

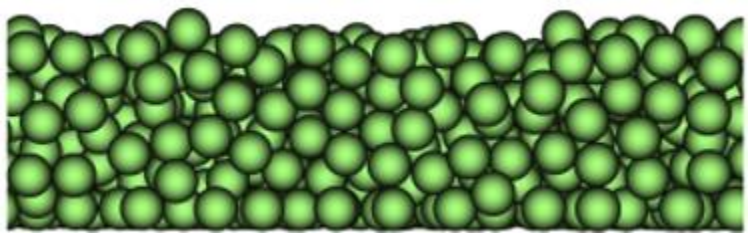

Figure 5-10 2D view of particle film with non-flat free surface due to sparse particles slightly sitting up higher than the rest of the bed.

Based on the transition between the "nonlinear" and "linear" regions being at 2 radii, it is assumed that the layers containing "unshaded" particles - those which are not shaded by others and are directly struck by incident radiation - experience "nonlinear" transmission decay. Deeper layers containing shaded particles experience linear transmission decay. The number of unshaded particles is estimated with Eq. (5-4), where l_x and l_y are the length of the film in the transverse directions, and r and f_{bulk} are the particle radius and bulk solid fraction found as in Figure 5-7. The correction factor c is to account for rays approaching at an angle other than perpendicular to the bed.

$$n_{un,p} = \frac{l_x l_y}{\pi r^2} c f_{bulk} \tag{5-4}$$

As the incidence angle becomes more acute, particles tend to shade each other more, so the number of unshaded particles decreases. To take this effect into account, a correction factor is found by using five benchmark particle configurations taken from CentRec simulations (Cases I-V from

Figure **5-12**) for various incidence angles, and the factor c is expressed in Eq. (5-5), where β is the incidence angle in degrees.

$$c = 0.0081\beta + 0.4112 \quad \beta < 70°$$
$$c = 1 \quad \beta \geq 70° \tag{5-5}$$

The algorithm estimates the energy absorbed by each layer by distributing the "nonlinear" and "linear" portions of the absorption among the applicable layers. It takes into account the sparse particles on the film surface by using the fractions of shaded and unshaded particles contained within each layer, using the methods described below.

First, the number of each type of spherical segment of unshaded particles in each layer is found. By definition, a particle can have fractions in (2*r/t*) number of layers. For example, if the layer thickness is *t*=0.1 radius, a particle is represented by 20 different spherical segments, as can be seen in Figure A-1 (in Appendix section). In this particle, the particle center is found on the boundary between layer 10 and 11. However, in many-particle systems, the layering starts from the tip of the topmost particle, so the centers of other particles may be found within a layer (not at a boundary), which is not convenient for the subsequent steps in the algorithm. To eliminate this problem, the particle center is shifted to the closest layer boundary, and therefore each particle is sliced in exactly the same way, into 2*r/t* sections. This is an acceptable approximation if *t*<<*r*.

To deal with the sparse particles, the same "nonlinear" transmission curves are used as for the bed with a uniform solid fraction (Eq.(5-1)), but it is distributed over the highest $n_{un,p}$ particles. The absorption in layer *k* is $q_{abs,l}$ as shown in Eq. (5-6), which distributes the absorbed heat in each layer (q_{abs}) from the derivation case (uniform solid fractions, Eq. (5-3)) to all layers according to the layer depth of $\frac{(k-k_n)t}{r_p}$, where *t* is the layer thickness. The layer number corresponding to the cap of each unshaded particle is k_n. The value of k_n is only defined for unshaded particles, and for $k < k_n$ the term q_{abs} is equal to zero, meaning that the layer *k* is above the cap of the particle so no radiation is absorbed. Eq. (5-6) is applicable to all layers because q_{abs} is defined for both "nonlinear" and "linear" parts of the film in Eq. (5-3). An example calculation is performed in the Appendix 2.

$$q_{abs,l}(k) = \frac{1}{n_{un,p}} \sum_{n=1}^{n_{un,p}} q_{abs}\left(\frac{(k-k_n)t}{r_p}\right) \tag{5-6}$$

5.1.1.2 Model Validation and Application

In this section, the radiation absorption algorithm is applied to the CentRec receiver by utilizing the particle positions inside the receiver, which have been found previously using DEM

modeling. Furthermore, MCRT simulations are run for the same sets of particle positions, so the accuracy of the algorithm can be shown under various conditions.

A reader may wonder if the algorithm developed is necessary, or if using a less detailed approach would suffice for assigning heat to particles at different depths. In CentRec, the particles on the surface of the particle film have a high velocity compared to the particles at the wall, which are nearly stationary. Thus, the depth at which the photons are absorbed has a large impact on the temperature profile in the particle film, the total heat absorbed by the particles, and the overall thermal efficiency of the solar receiver. Therefore, an accurate model for radiation penetration is critical for the CentRec design.

Before applying the algorithm, the particle domain must be prepared in several ways. Inside the receiver, a thin moving particle film descends along the cylindrically shaped receiver wall. Because the receiver diameter to particle diameter ratio is very high (>100), it is assumed that the receiver wall is flat relative to a single particle, making the tables and equations developed in the previous sections applicable. The algorithm and MCRT simulations are best compared when the domain is flat and rectangular, so the cylindrical particle film is "unrolled", where the distance from the cylinder wall becomes z-component of the particle in a Cartesian coordinate system. This forms a rectangular-shaped particle domain with the overall *x* and *y* dimensions being the cylinder length and circumference. The rectangular domain is further reduced to a square of 50 x 50 particle diameters to reduce the amount of computation necessary.

After these modifications, the absorption algorithm can be applied to the particle bed, and a direct comparison can be made against the results from a full MCRT simulation. Because much of the algorithm difficulty lies in the simulation of the sparse particles, an initial simulation is set up to assess the accuracy of the algorithm under several different configurations of sparse particles along the surface of the particle bed. The particle beds for five different cases are generated by starting with the same particle position snapshot, but all particles above a different level are removed in each case. Case I is the original set of particles with no particles cut off, and cases II, III, IV and V are obtained by removing all particles having their centers located above 0.6, 0.8, 1 and 1.2 radii from the original top level, respectively. In Figure 5-11, this can be seen in the different sizes of the hump in the local solid fraction nearest the free surface, while the solid fraction is unchanged deeper in the bed.

As shown in

Figure **5-12**, the model shows a very close match to the MCRT results, for all five cases and six angles studied, especially up to the first hump in the local solid fraction. The algorithm results deviate slightly from the MCRT results after the first hump, with the transmission overpredicted for low incidence angles (15°) and underpredicted for high incidence angles (90°). From Case I to Case V, the particle density near the top of the film decreases, resulting in a lower local peak in solid fraction distribution and a corresponding increase in penetration depths moving from Case I to Case V. Moreover, the penetration depth is lower for low angles because rays have a large lateral component and a smaller component in the depth direction. As shown in

Figure **5-12**, the current model slightly over-predicts the transmission for all angles in Case I. The reason why sharp changes in deviation occur mostly at the hump location, not between humps, is that the absorption location is considered as the particle center, and the particle centers are most likely present at the hump in the solid fraction. Although there are small deviations between current model and MCRT results for all cases, this error is considered to be in an acceptable range for the CentRec project model, especially given the large savings in computational cost compared to a full MCRT simulation. Moreover, in CentRec, rays with various incidence angles strike the film, so the small errors tend to counterbalance each other.

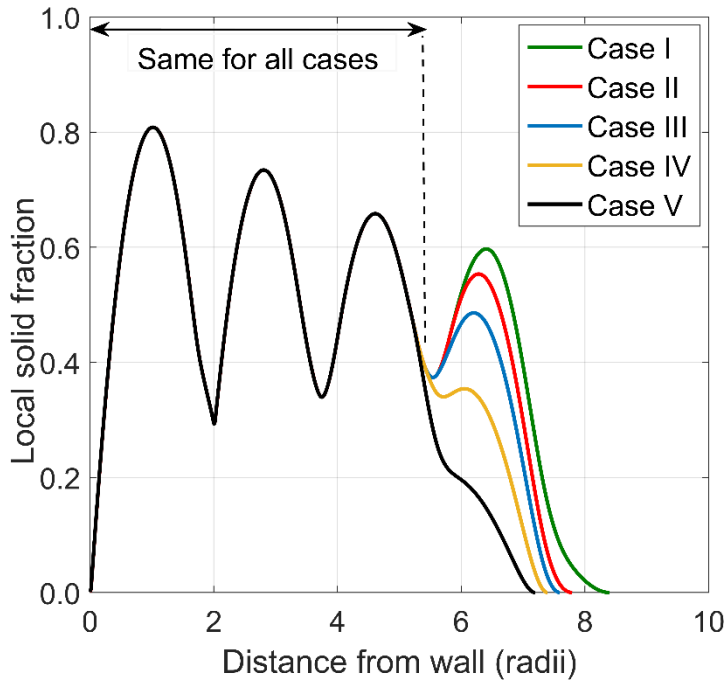

Figure 5-11 Local solid fraction distribution for five different sets of particle positions generated by removing a number of particles from top surface. The film thickness is the z- location of the topmost particle center plus one radius, whereas 0 depth corresponds to wall.

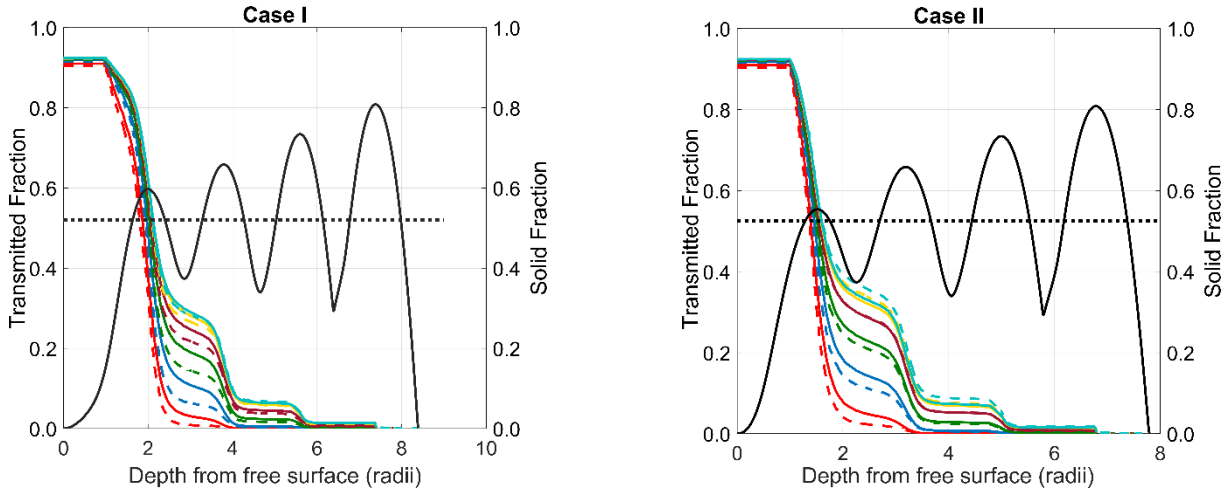

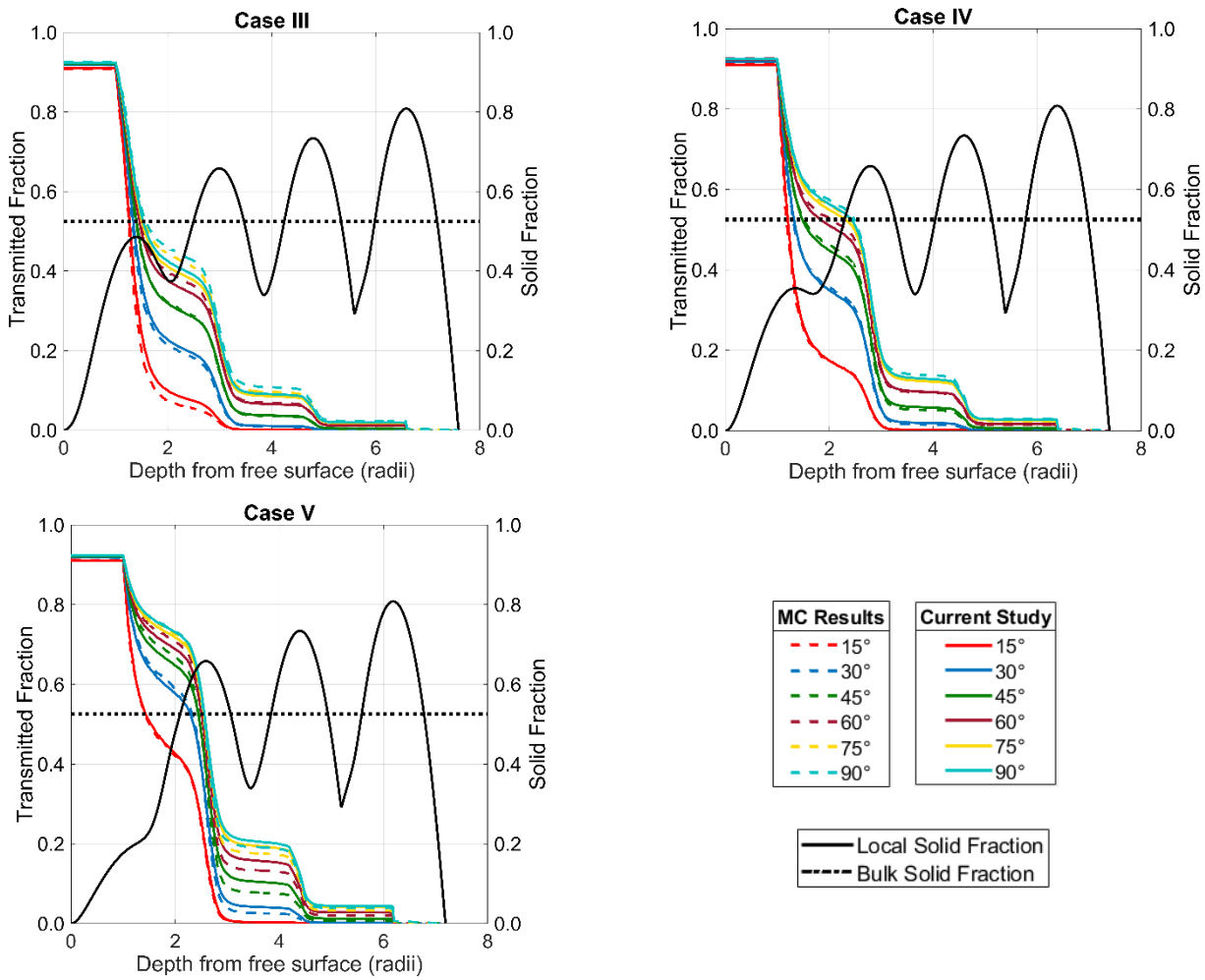

Figure 5-12 Transmitted curve and local solid fraction at depths in particle bed, for six incidence angles. Cases I-V represent the original particle bed and beds where a layer of thickness 0.6, 0.8, 1.0, and 1.2 radii has been removed from top, respectively.

Next, results from the algorithm are compared to the MCRT code in four different realistic particle configurations obtained from four different DEM simulations of CentRec. Different operational parameters, i.e. rotational speed and particle mass flow rate, yield different film thicknesses for each case, as can be deducted from the depth from free surface in Figure 5-13. On the upper-half of the circumference of the cylinder, the particle film surface points downward, so gravity causes the film to become less densely packed than at the bottom of the cylinder. Thus, two particle domains each are taken from the lower region (cases CR1 and CR2) and upper region (cases CR3 and CR4) of the cylinder. As shown in Figure 5-13, the domains from the lower part have a bulk solid fraction of 0.53, while those from the upper part have a solid fraction of 0.48. Unlike the previous test, no particles are removed from the top surface.

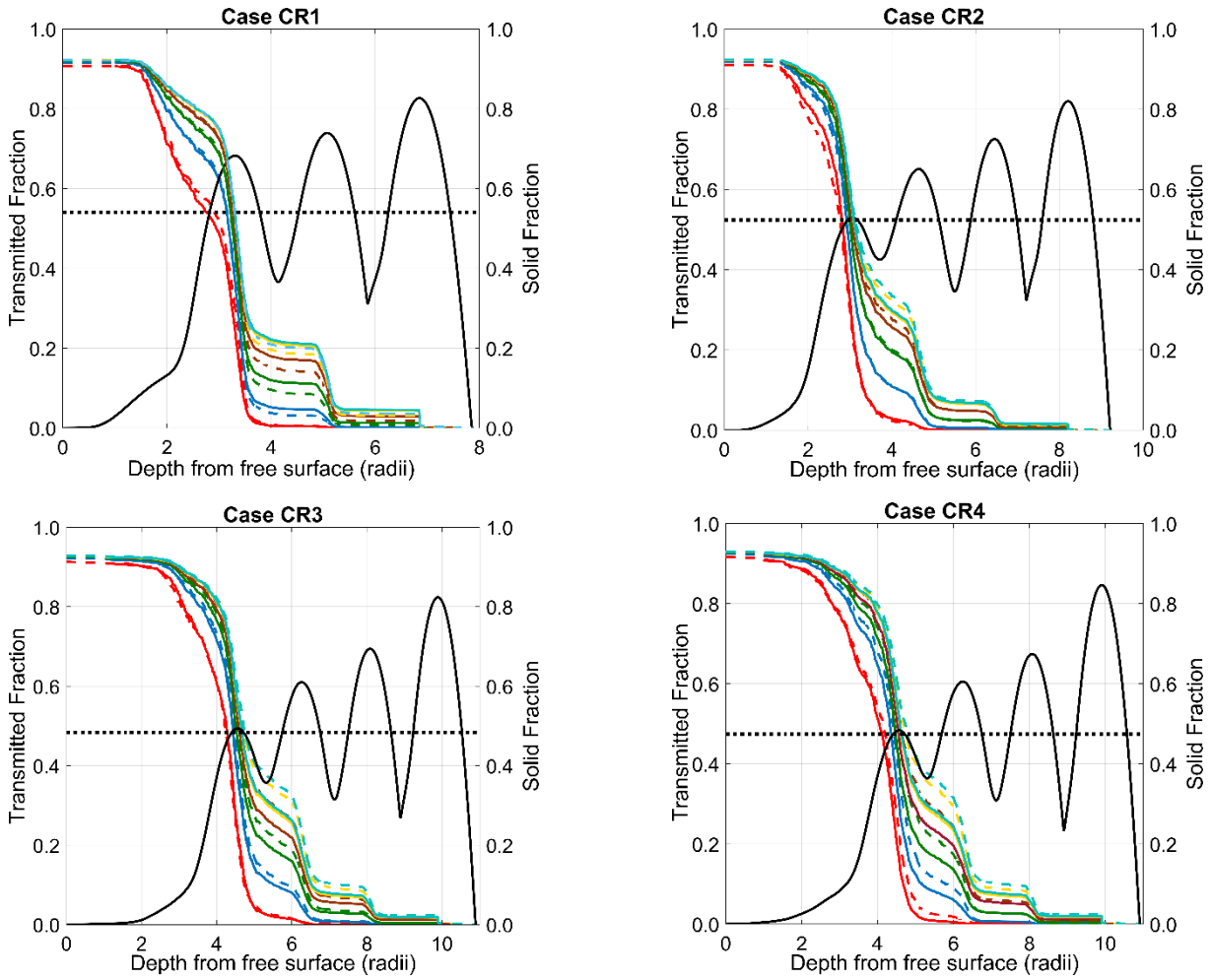

Figure 5-13 Transmission curve and local solid fraction, for six incidence angles. Cases CR1 and CR2 are from the bottom part of the receiver circumference, and CR3 and CR4 are from the top part of the receiver circumference (Legend same as

Figure **5-12**).

The model predicts the MCRT results very well up to the first hump for all cases. Note that a significant portion of the energy is absorbed in this region, especially for low incidence angles, which helps the overall accuracy of the model. For the less-packed cases (CR3 and CR4), some deviation can be seen after the first hump, especially for high incidence angles. In the CentRec, the majority of incident radiation strikes the lower-half (more packed part) of the receiver due to the angle of the receiver in relation to the heliostat field, so this already small error will not lead to significant errors in the CentRec model. Overall, the algorithm produces transmission curves very similar to the MCRT model, even in these challenging cases with a fluctuating solid fraction, and the results are considered accurate enough for the needs of the CentRec heat transfer model.

Finally, a realistic distribution of incidence angles striking CentRec is considered, as rays coming from the heliostat field enter the CentRec aperture at various angles. Previous work has

given the distribution of solar flux at various incidence angles to the particle film for a representative case, as shown in Figure 5-14. For the same four particle beds (CR1-4), the combined transmission curves are found using this weighted distribution of angles, using both the algorithm and MCRT, as shown by the red lines and black lines, respectively, in Figure 5-15. However, computing the combined transmission curve in this way requires running the algorithm for each incidence angle, which still carries some computational burden. Therefore, a single angle is sought to represent the angle distribution, which is taken as the photon density-weighted sinus average.

$$\beta_{avg} = \sin^{-1}\left(\sum_{\beta} \sin(\beta) \frac{photons\ at\ angle\ \beta}{total\ photons}\right) \tag{5-7}$$

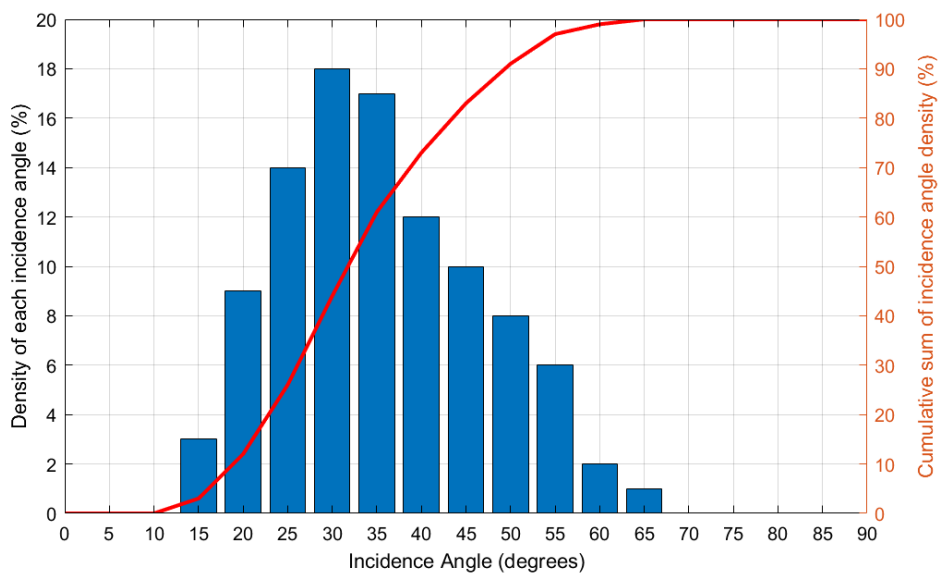

Figure 5-14 Incidence angle distribution on the receiver wall in CentRec.

Therefore, the algorithm only has to be run once, and the resulting transmission curve (blue line) matches the weighted average (red line) very well. Moreover, the algorithm estimates the MCRT results with a very slight error for the representative cases considered. Thus, a sinus-averaged incidence angle for a particle domain can be used to find the absorption of particles with very low computational cost, and it is implemented within the larger DEM heat transfer model of CentRec.

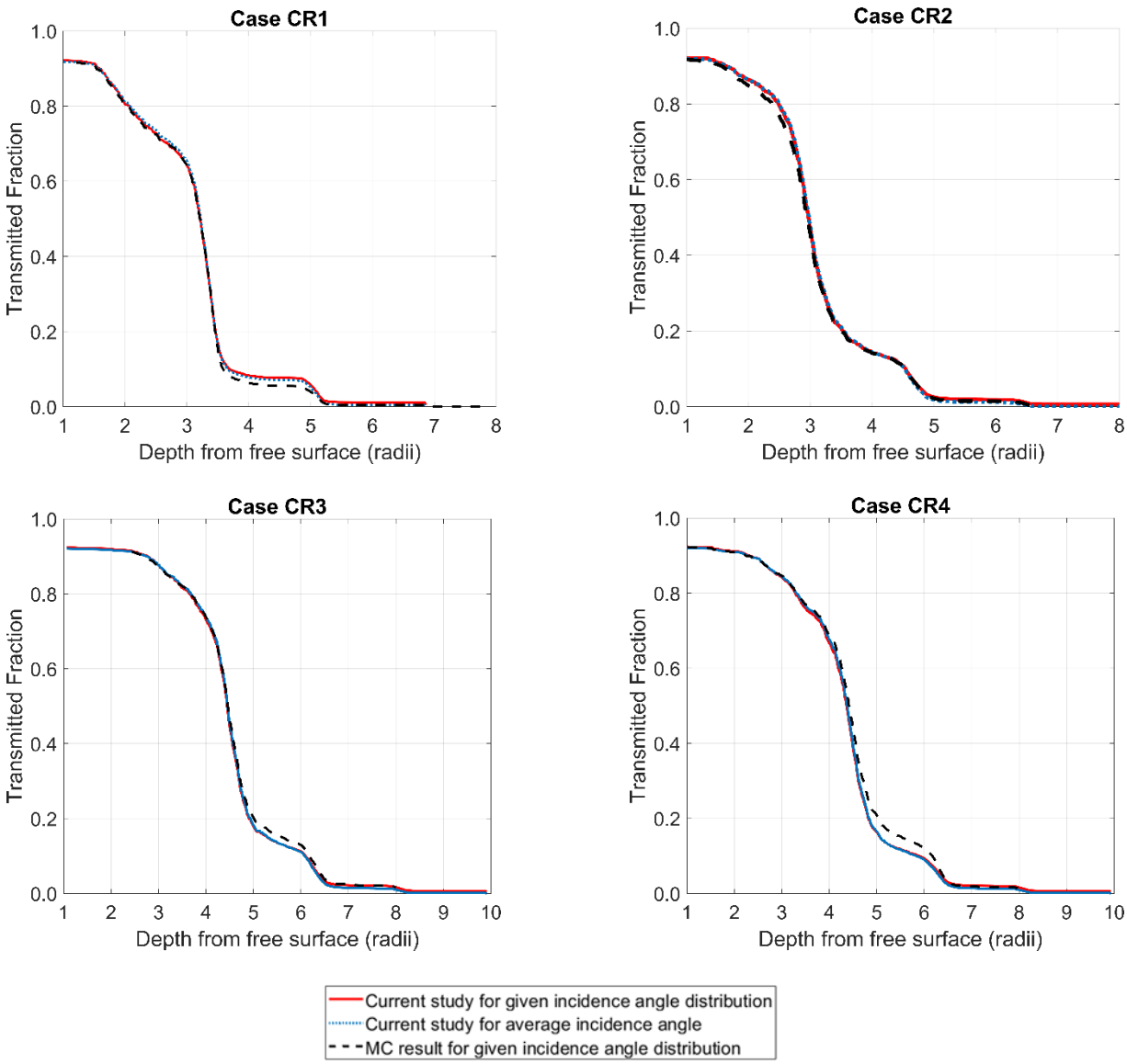

Figure 5-15 Comparison of MC results and algorithm-based results for four different CentRec simulations.

5.1.2 Reflection Model

When non-black particles are used in CentRec, a portion of solar flux striking the particle film is reflected. In Figure 5-4, the relation between particle absorptivity and bed absorptivity is revealed for various incidence angles. Thus, one can estimate the bed absorptivity and eventually bed reflectivity for a given incidence angle and particle absorptivity. Although particle surface is assumed as diffuse for emissions and reflections, it should be checked if the assumption also holds for the particle film surface. In a previous study of the author [112], it is found that if diffuse reflection from the bulk is assumed for CentRec, the reflection loss through the aperture is underestimated by 50% compared to MCRT results. This is mainly because the surface of the film is not flat, it consists of many spheres. Thus, the reflection needs to be modelled as incidence angle dependent. To do so, a reflection model accounting for zenith and azimuth angle dependency of

reflected rays is addressed in this study. The azimuth and zenith angles for a local coordinate system are shown in Figure 5-16. For the model derivation, firstly, a bunch of parallel rays are created with the help of MCRT, and sent to a particle domain like represented in Figure 5-3(a). However, in this time, the vector representation of reflected rays which leaves the domain is found.

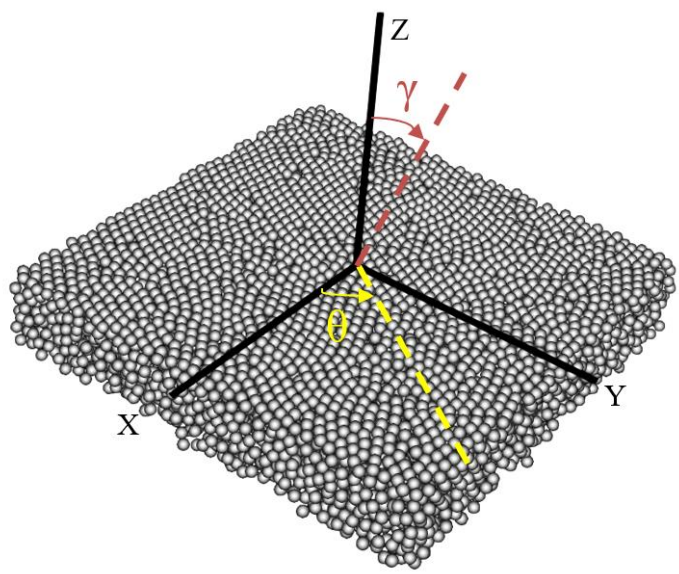

Figure 5-16 The local coordinate system to be used in the reflection model. Azimuth angle (θ) varies between 0 and 2π. Zenith angle (γ) varies between 0 and π/2.

In Figure 5-17, the rays reflected from the particle film surface are plotted along with generated rays for three different zenith angles. Note that although a 2D projection of the domain is plotted, reflected rays travel in a 3D domain. The generated parallel rays have an azimuth angle of 180° so they lie on the xz-plane. From Figure 5-17, it can be noticed that as zenith angle of generated rays increases, the rays are less likely reflected to the opposite side of the film. In other words, due to the spherical surface of particles, rays are more likely bounced off back as zenith angle increases. It should be noted that rays can also leave the domain after several reflections within the particle film.

In Figure 5-18, a more detailed look to the direction-dependent hemispherical distribution of reflected rays is represented for several zenith angles of generated rays. Figure 5-18(a) shows that if generated rays are sent to a particle film with γ_{gen} = 85°, the most rays are reflected with relatively high zenith angles (60° < γ_{ref} < 80°), and the density of reflected rays are higher around azimuth angle (θ_{ref}) of 180°, which equals the azimuth angle of generated rays (θ_{gen}). As γ_{gen} decreases, seen in Figure 5-18 (b) and (c), γ_{ref} also decreases to some extent. Moreover, the distribution of reflected rays becomes more uniform in the azimuth direction. For γ_{gen} = 0°, representing generated rays perpendicular to the particle film, the rays are reflected mostly around

γ_{ref} = 45° due to spherical shape of particles, as seen in Figure 5-18(d). Furthermore, for γ_{gen} = 0°, there is no dependence on azimuth angle for reflected rays.

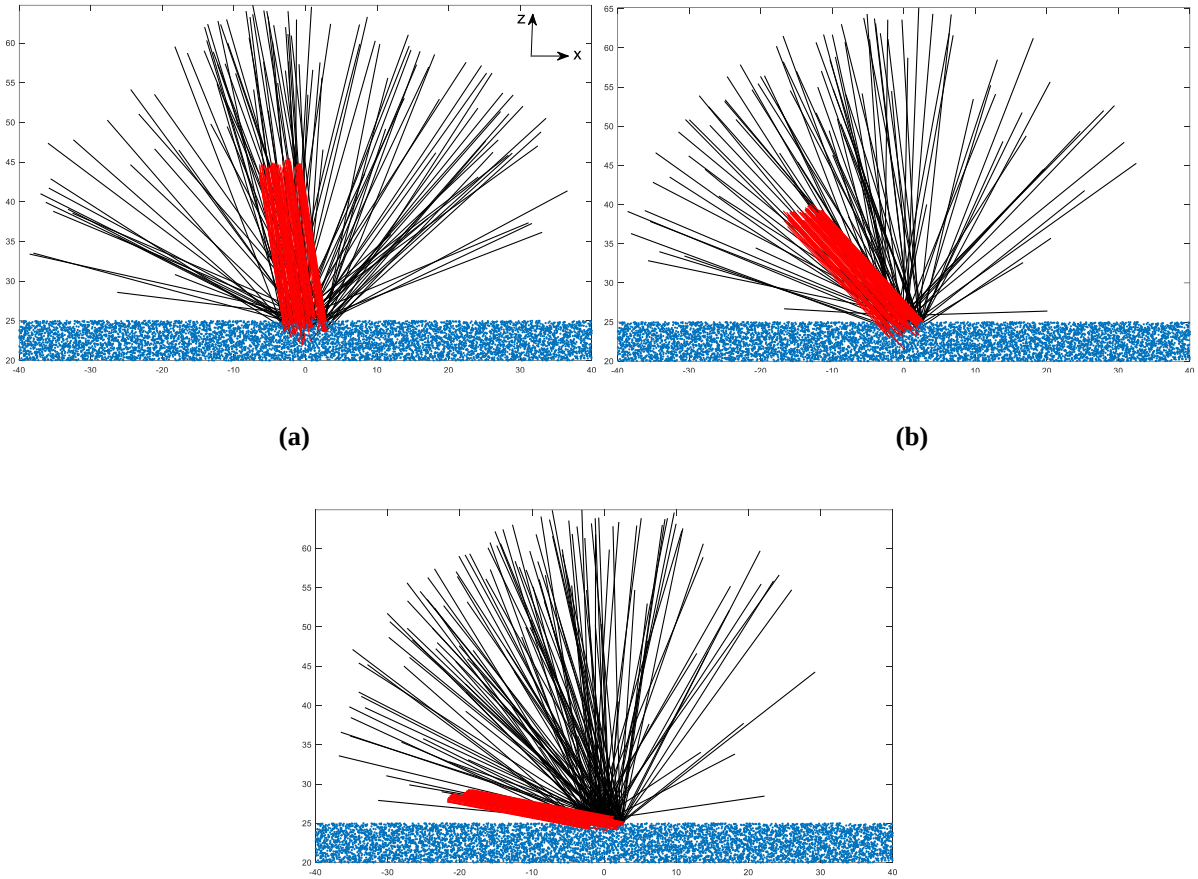

Figure 5-17 Representation of generated parallel rays (red) and reflections from the particle film (black) for **(a)** γ=10° **(b)** γ=45° and **(c)** γ=80°. The blue dots represent particles' center.

To later use in the modelling, direction-dependent hemispherical distribution of reflected rays is found for a range of 0° ≤ γ_{gen} ≤ 89° with 1° intervals. No solution exists for γ_{gen} = 90° because the generated rays are parallel to the surface of the particle film for that case. Moreover, there is no need to consider different θ_{gen} because the particle film is assumed to be isotropic in terms of packing structure in lateral directions. θ_{ref} is directly dependent on θ_{gen}, so derivation for a reference value of θ_{gen} is enough. The resultant reflection matrix "R" has a dimension of 90 x 360 x 90 such that the first dimension is γ_{ref}; the second one is θ_{ref}, and the third one is γ_{gen}. The matrix elements correspond the ray density for couples of θ_{ref} and γ_{ref} and given γ_{gen}.

The main reason of deriving the reflection matrix is to avoid running the costly MCRT algorithm. To do so, it is assumed that the reflected radiation is exchanged between discrete surfaces comprising the particle film surface, not between individual particles. For this purpose, the particle film is discretized in axial and tangential directions into many rectangular-prism shape

discrete volumes, as seen in Figure 5-19. The radiation exchange occurs between inward surfaces of discrete volumes.

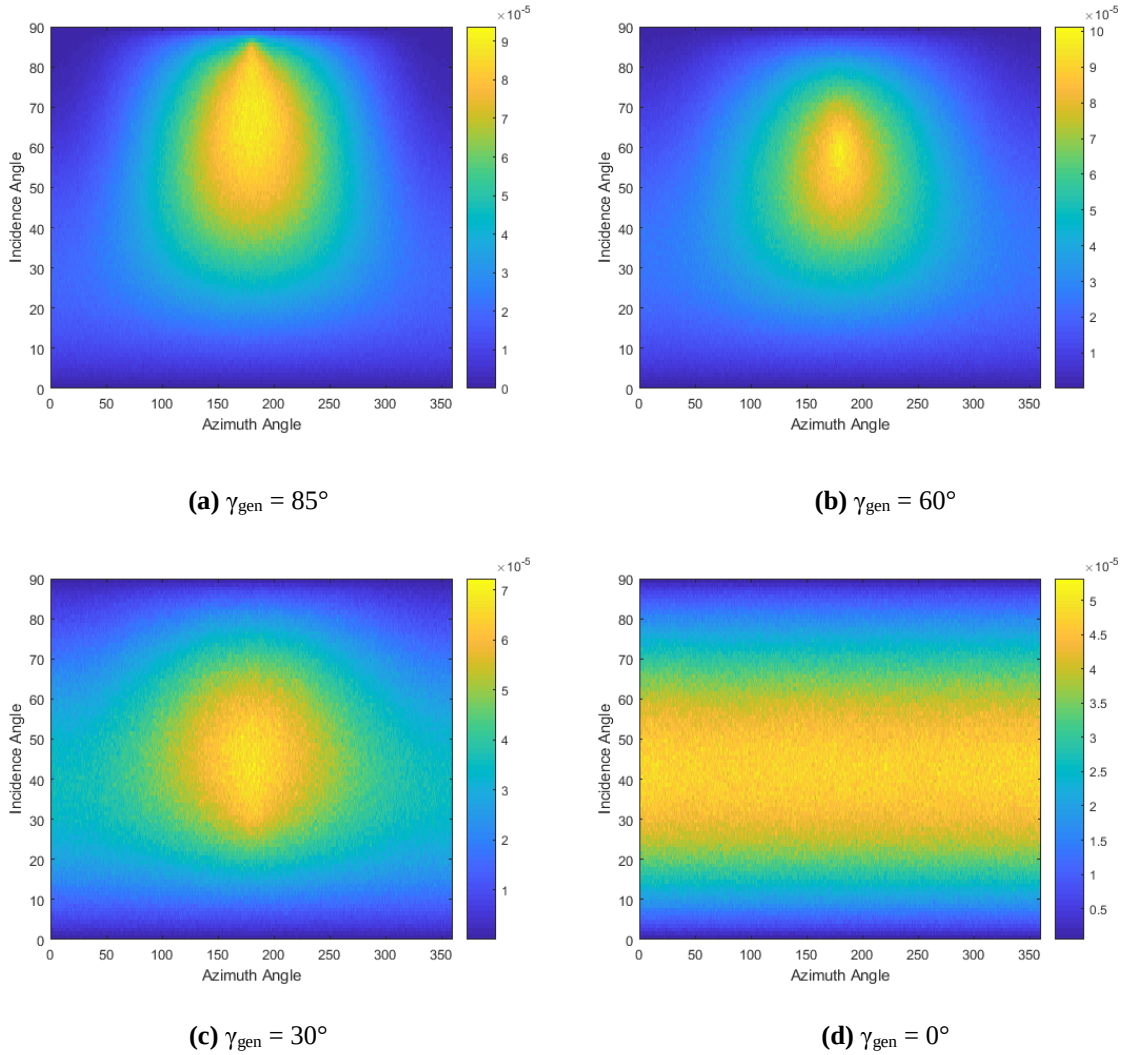

(a) γ_{gen} = 85°

(b) γ_{gen} = 60°

(c) γ_{gen} = 30°

(d) γ_{gen} = 0°

Figure 5-18 The hemispherical density distribution of the reflected rays. The generated parallel rays have an azimuth angle of 180°.

The radiation model accepts user-defined rays as an input, each of them represented by a position on the aperture plane, a direction vector and a thermal energy. All defined rays form a flux distribution on the aperture plane, and their intersections with the particle film surface form the flux distribution on the particle film. To calculate the energy absorbed by a discrete surface for a ray distribution, the average zenith angle of incoming rays ($\gamma_{inc,avg}$), or average incidence angle, is to be estimated. Note that the sum of zenith and incidence angle is 90°. For this purpose, Eq. (5-7) can be reformulated by also accounting for the zenith angle and the case that rays carry various thermal energy.

$$\gamma_{inc,avg} = cos^{-1}\left(\sum_{i=1}^{n} \cos(\gamma_{inc,i}) \frac{energy\ carried\ by\ ray\ "i"\ at\ zenith\ angle\ \gamma_{inc,i}}{total\ energy\ striking\ to\ discrete\ surface}\right) \quad \textbf{(5-8)}$$

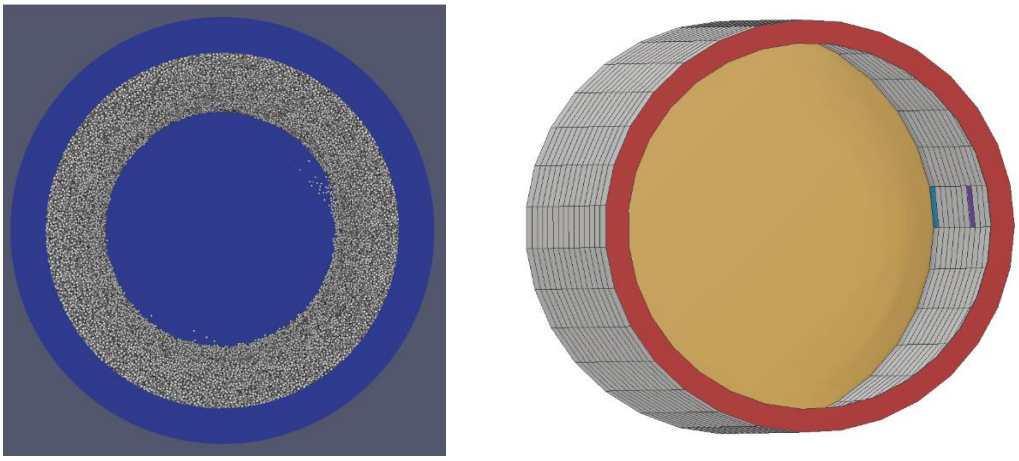

(a) **(b)**

Figure 5-19 (a) Particle film flow in CentRec simulation for a cavity diameter of $100d_p$. **(b)** Meshed particle film surface. The back – yellow surface is the particle distributor and the front – red surface is the collector ring.

The total number of rays striking a discrete surface is denoted by n. Note that azimuth angle of incoming rays has no effect on bed absorptivity. $\gamma_{inc,avg}$ is calculated for each discrete surface, and defined with the respect to local coordinate system of each discrete surface, being located at the center of the discrete surface.

One also needs a bed solid fraction (α_{bed}) to estimate bed absorptivity as discussed in Chapter 5.1.1.1. The solid fraction of each rectangular-prism shaped volume can be calculated with the methodology shown in Figure 5-7. The α_{bed} changes between 0.48 – 0.52 for the particles used in the study but the bed solid fraction for each discrete volume ($\alpha_{discrete\ volume}$) is already calculated for the radiation penetration calculations thus those values are employed to find the bed absorptivity for each discrete volume.

In order to find the direction-dependent hemispherical reflection distribution, azimuth angle (θ_{inc}) and zenith angle (γ_{inc}) of each ray striking a discrete surface are utilized. These angles are also defined with respect to the local coordinate system of the surface on which they strike. At this point, a special function needs to be defined for further calculations.

$$A_{new} = circshift(A, k, x) \quad \textbf{(5-9)}$$

"circshift" is a build-in MATLAB function, which circularly shifts the elements in matrix "A" by "k" positions along the dimension x. By means of this function, the reflection matrix "R_{inc}" can be expressed for any incoming ray with calculated θ_{inc} and γ_{inc}, as follows.

$$R_{inc} = circshift\big(R(:,:,\gamma_{inc}), \theta_{inc} - \theta_{gen}, 2\big) \quad \textbf{(5-10)}$$

In Eq. (5-10), firstly, the general reflection matrix "R" is reduced to $R(:,:,\gamma_{inc})$ for any incoming ray zenith angle (γ_{inc}) and then circularly shifted to any azimuth angle (θ_{inc}) to tailor it for any incoming ray azimuth angle (θ_{inc}). For example, for θ_{inc} = 200°, the matrix $R(:,:,\gamma_{inc})$ should be circularly shifted by 20 because θ_{gen} is 180°, in the derivation case, shown in Figure 5-18. Because γ_{inc} and θ_{inc} should be integer values, the real values can be rounded off to closer integer values. The reflection matrix for any incoming ray "R_{inc}" has dimensions of 90 x 360 such that the first dimension is the reflected zenith angle "γ_{ref}" and the second is the reflected azimuth angle "θ_{ref}". Each element in the matrix corresponds to the density of reflected rays for the corresponding γ_{ref} and θ_{ref}. Thus, the sum of elements of matrix R_{inc} is 1. Then, the reflection matrix "R_{el}" for any discrete surface on which "n" number of rays strike, is calculated as follows.

$$R_{el} = \sum_{i=1}^{n} E_i (1 - \alpha_{discrete\ volume})\, R_{inc}^{i} \quad \textbf{(5-11)}$$

The energy carried by the ith ray is denoted by E_i. By summing up the reflected energy-weighted reflection matrices defined for each ray "R_{inc}^{i}", the reflection matrix "R_{el}" defined for a discrete surface can be found. In this formulation, there are two main assumptions. Firstly, it is assumed that when a ray strikes the film, a portion of its energy ($\alpha_{discrete\ volume}$) is absorbed by the film and the remaining energy ($1 - \alpha_{discrete\ volume}$) is reflected. Secondly, the reflection of a ray is hemispherical, being density-weighted. Thus, the rays are not tracked individually like in MCRT, instead a direction – dependent hemispherical reflection from a discrete surface is found for a given ray distribution.

By finding R_{el}, one can calculate how much portion of the energy is reflected to any azimuth and zenith angle. In the next step, the reflected radiation is to be distributed to the other discrete surfaces forming the particle film, particle distributor, collector ring and aperture, shown in Figure 5-19(b). Note that for the metallic surfaces and aperture it is assumed that each is comprised of a single surface.

Firstly, for a given discrete surface size, aperture size and cavity size, the azimuth angle and the zenith angle intervals for the rays emitted from a surface to each other surfaces are computed by ray tracing. To illustrate this, two representative discrete surfaces are selected: A surface next to the particle distributor (blue surface in Figure 5-19(b)) and mid surface (violet surface in Figure 5-19(b)). In Figure 5-20, the regions enclosed by corresponding zenith angle and azimuth angle intervals from these two surfaces to others are shown. The geometric center of

discrete surfaces is considered for the ray generation point. By creating such angle maps, it is aimed for to determine which angle pair corresponds to which surface. For example, for zenith angle interval of [0,1] and azimuth angle interval of [0,1], rays are emitted from the geometric center of a discrete surface. The surface which the largest portion of emitted rays hit to is saved into a map matrix "M". This procedure is repeated for the complete range of azimuth and zenith angles, and the map matrix M with dimensions of 90 x 360 is obtained such that matrix elements are label of corresponding discrete surfaces. The matrix M is also defined for each discrete surface but not for metallic surfaces or aperture plane because reflections from these surfaces are assumed to be diffuse.

Finally, the reflection from any discrete surface, stored in the reflection matrix "R_{el}", is distributed to other surfaces thanks to the map matrix "M". For example, the amount of energy stored in $R_{el}(1,1)$ is reflected into the surface of which label is saved in $M(1,1)$. The procedure is repeated for all angle couples and all discrete surfaces exposed to solar flux. By summing up energy reflected from other discrete surfaces to a discrete surface, the net energy gain for a discrete surface can be calculated. In the creation of matrices, angle intervals of 1° are found sufficient for the accuracy but smaller intervals can also be employed to further increase the accuracy. Note that map matrix "M" is created once in the beginning of the simulation based on discrete surface size, cavity size and aperture size. Note that the matrices "M", "R_{el}" and "R_{inc}" are defined for every discrete surface excluding the metallic surfaces and aperture. Thus, in the thermal code, another dimension, accounting for the number of discrete surfaces, is added to matrices so all matrices have dimension of 90 x 360 x m, where m is the number of discrete surfaces.

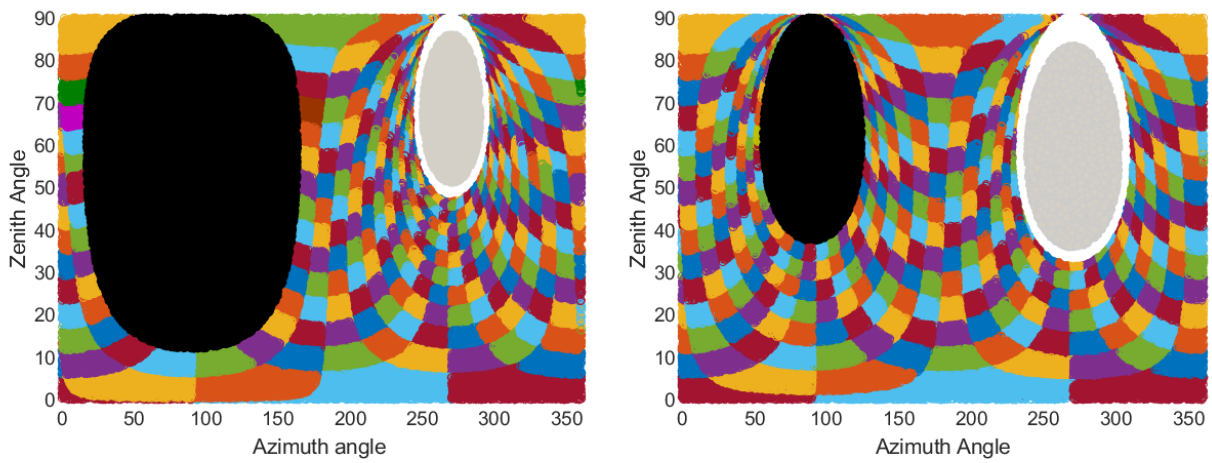

(a) **(b)**

Figure 5-20 Representation of regions enclosed by zenith angle and azimuth angle intervals for rays emitted from **(a)** discrete surface next to particle distributor **(b)** mid surface to all other surfaces. Black region, white region and gray region represents angle intervals from these two surfaces to the particle distributor, the collector ring and the aperture plane, respectively. The colored regions show the intervals to other discrete surfaces.

For the particle type considered in this study (emissivity of 0.86 and bulk solid fraction of 0.5), the bed absorptivity of the particle film is around 92 – 93 % for a representative incidence

angle distribution seen in Figure 5-14. Thus, around 7 – 8 % of the rays are reflected to other parts of the cavity. If the energy is reflected to the aperture back, it is directly considered as reflection loss through aperture. If it is reflected to the particle distributor or the collector ring, it is considered as specular irradiation in the long-range thermal emission model, discussed in Chapter 5.1.3. Because the surface of metallic parts is assumed as diffuse, there is no need to consider this portion of energy in the incidence angle-dependent reflection model. However, a large portion of energy reflected after first strike hits other parts of the particle film. Even if all the reflected energy hits the particle film again, the amount of second reflection from the particle film is always less than 1%, in most cases less than 0.5%, of the incoming energy at the aperture. Thus, to save from the computational burden, calculations for the second reflection, creating negligible error, is not repeated. Therefore, it may be assumed that all the energy reflected after the first strike is completely absorbed at the second strike if the reflection is towards the particle film again. However, there is still the need for the average zenith angle for the second strike to distribute this energy to the particles because the radiation penetration model requires it. However, the rays are not tracked after the first strike. To approximate the ray direction vector from a discrete surface to another, a vector is formed between geometric centers of discrete surfaces. Then, the average zenith angle for a second surface can be calculated by using Eq. (5-8).

The developed model has several pros and cons in terms of computational burden. Firstly, matrices R_{inc} and M depend on cavity dimensions and particle film thickness. Thus, if film thickness changes during operation, they need to be recalculated. However, the current study focuses on steady-state condition in terms of particle flow. Moreover, R_{inc} is developed for a time-independent flux distribution on the particle surface. If flux condition changes, R_{inc} needs to be recalculated. The matrix R depends on bed solid fraction but for the relevant operational range of CentRec application, it is always found as between 0.48 – 0.52 so deriving matrix R once is enough for all conditions. At the beginning of the simulation, these matrices are found once. The main advantage of the developed model is that it is particle-number free so it can still be applied to very large receivers. The flow diagram of all steps is depicted in Figure 5-21.

To validate the developed model, a uniform flux of 3 MW/m^2 is applied to the aperture plane. All rays have an incidence angle of 45° on the aperture plane as shown in Figure 5-22. The cavity dimension and particle size are listed in Table 5-1. For the validation study, the particle mass flow rate and rotation speed are arranged such that a film thickness of 4d_p is obtained. As film thickness increases, the effective cavity diameter decreases. Then a smaller portion of the particle film near the exit is not exposed to solar irradiation directly due to blockage of the collector ring. This fact may be important in the selection of a proper size of the discrete surface because it is assumed that all the irradiation striking a discrete surface is distributed uniformly. Thus, if a large discrete surface size is considered, the flux may be distributed to the particle film near the exit uniformly although that part of the film is not exposed to the solar irradiation in reality.

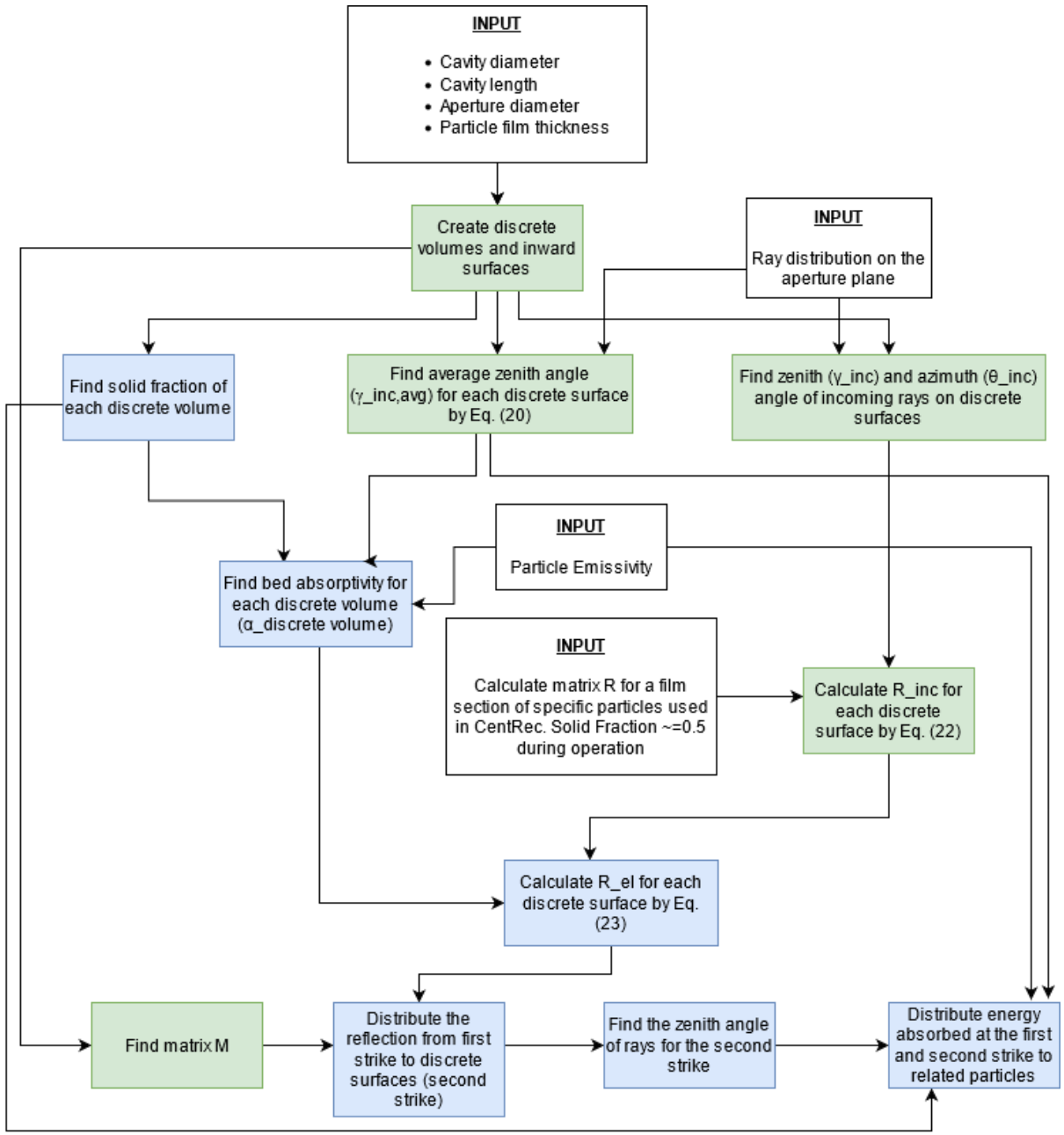

Figure 5-21 The flow diagram of the reflection model. The blue boxes are calculated in each time step while the green boxes are calculated once for a given input parameter set.

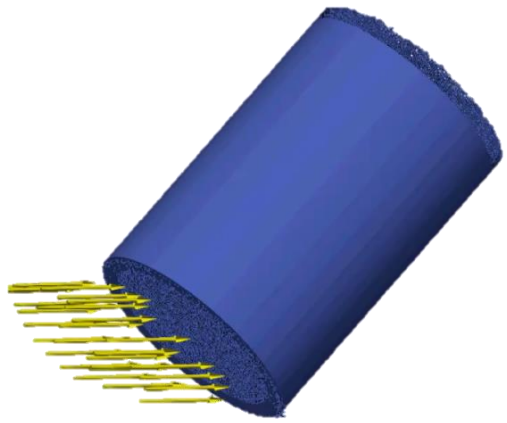

Figure 5-22 Representation of generated rays that have an incidence angle of 45° at the aperture.

Firstly, the effect of the size of the discrete surface should be checked. For this purpose, edge sizes of $L_{cav}/36$, $L_{cav}/18$ and $L_{cav}/9$, which corresponds to ~$4d_p$, $8d_p$ and $16d_p$ are considered, where L_{cav} is the cavity length. In Figure 5-23, the flux distribution on the particle film for several discrete surface sizes is shown. As the size of the discrete surface increases, the boundaries of the high-flux region are more scattered.

Table 5-1 Cavity dimension considered in the validation study of the reflection model.

Cavity diameter	m	0.12
Aperture diameter	m	0.1
Cavity Length	m	0.171
Particle diameter	mm	1.2
Particle Emissivity	-	0.86
Uniform Flux at aperture	MW/m^2	3

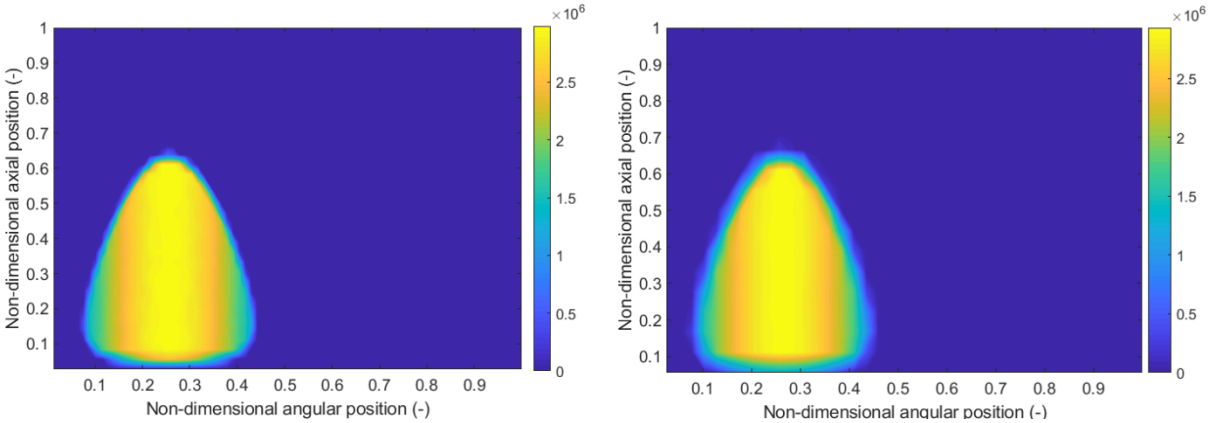

(a) **(b)**

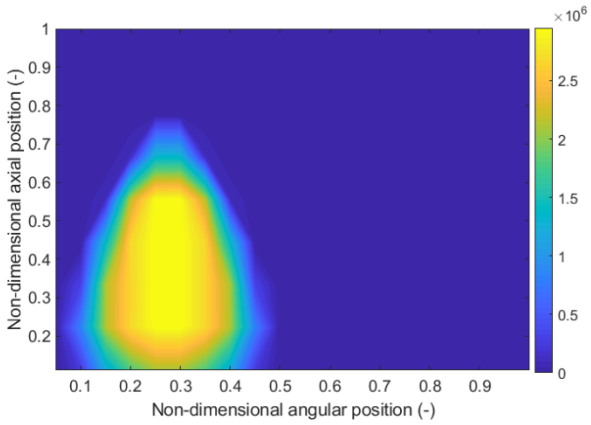

(c)

Figure 5-23 Flux distribution on the particle film before any reflection for a discrete surface size of **(a)** $L_{cav}/36$ **(b)** $L_{cav}/18$ and **(c)** $L_{cav}/9$. The unit of the contour is W/m^2.

The effect of discrete surface sizes on reflection are also plotted in Figure 5-24. The flux density on the peak reflection regions are slightly more concentrated for small discrete surface sizes. Finally, the surface sizes are compared in terms of heat flow to different parts of the receiver, as seen in Table 5-2. Although the heat flow to the collector ring and the particle distributor are similar for all sizes, the heat flow to the aperture starts to deviate for an edge size of $L_{cav}/9$. Thus, a discrete surface size of $L_{cav}/18$ is selected for the rest of the study. It should be noted that for a more dispersed flux distribution, resulting from rays with various incidence angles at the aperture, on the particle film, a smaller edge size may give more accurate results but for uniform flux condition, $L_{cav}/18$ seems to be sufficient. The main advantage of this approach is that the model is particle number-independent, thus it can be applied to larger receivers with no additional cost.

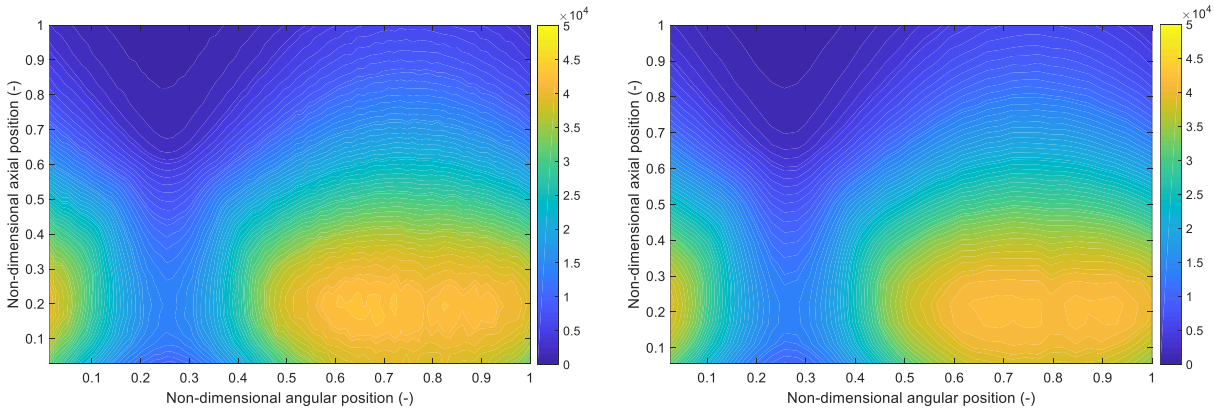

(a) **(b)**

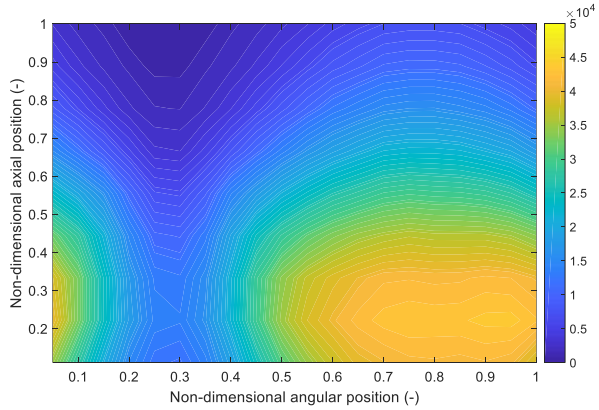

(c)

Figure 5-24 Reflection to other parts of the receiver for a discrete surface size of **(a)** $L_{cav}/36$ **(b)** $L_{cav}/18$ and **(c)** $L_{cav}/9$. The unit of the contour is W/m^2.

In Table 5-2, the model result is also compared with MCRT based results. It seems that MCRT results are predicted very well by the current model by employing an incidence angle-dependent reflection model. The slight difference in reflection loss for the edge size of $L_{cav}/9$ is mainly due to that the flux reaches farther, thus reflection back to the aperture plane is less likely. Moreover, the slight difference in the heat flow to the collector ring is mainly due to a constant film thickness assumption throughout the film in creating a discrete surface. However, as discussed in Chapter 4.1, the film thickness is slightly thinner near the exit thus the collector ring has more surface for reflections in the MCRT model. That's why the heat flow to the collector ring may be underestimated in the current model if the film thickness variation near the exit is high. However, this has negligible effect on receiver thermal efficiency because the error resulting from this is only ~11 W while the particles absorb 22965 W as can be noticed in Table 5-2.

Finally, in Figure 5-23 and Figure 5-24, it can be noticed that the net flux to side regions of the particle film, where the reflected energy is directed to, is around 2% of the peak flux on the particle surface. For lower particle emissivity, this ratio would be higher but no difference in the distribution of reflections along the particle film is expected.

Table 5-2 Distribution of solar irradiation to particles and other parts of the receiver for the current model and MCRT.

		$L_{cav}/36$	$L_{cav}/18$	$L_{cav}/9$	MCRT
Heat Flow to Particles	W	22962	22962	22953	22965
Heat Flow to Aperture	W	539.45	538.19	549.12	526.61
Heat Flow to Collector Ring	W	34.29	35.33	33.57	44.88
Heat Flow to Particle Distributor	W	25.89	26.11	25.92	25.66

5.1.3 Long-range Thermal Radiation Model

A long-range thermal radiation model is addressed to model radiative heat exchange driven by emission because of temperature difference between hot and cold regions of the particle film and large surfaces of the receiver. Unlike the reflection model, a particle emits thermal radiation to all directions outward its surface. Thus, the particle film surface composed of diffusely emitting particles is also assumed to emit diffuse radiation. In long-range thermal radiation calculations, the discrete surfaces created in the reflection model are also employed, so the radiative heat exchange is assumed to happen among discrete surfaces, particle distributor, collector ring and aperture plane. The representative surfaces are depicted in Figure 5-19(b). The emissivity of the film is assumed to be same as the absorptivity of the film. The aperture plane is assumed as black body, i.e., $\varepsilon_{ap} = 1$.

For the model development, an energy balance can be written for each surface.

$$q^{||} = J - G^d - G^s \tag{5-12}$$

In (5-12), the net heat flux to an element, $q^{||}$, is simply the difference between the net radiosity from the element, J, and the sum of diffuse, G^d, and specular, G^s, irradiation to the element. In the reflection model, the reflections from the particle film to the particle distributor and the collector ring is considered in the current model as specular irradiation. Thus, G^s is only applicable to those surfaces and not to the particle film because specular irradiation to the particle film is modelled in the "reflection model". The radiosity from an element can be written as follows.

$$J = E + \rho^d G^d + \rho^s G^s \tag{5-13}$$

In Eq. (5-13), the diffusive and specular reflectivity is denoted as ρ^d and ρ^s, respectively. The emissive power of a surface is represented by E. For a gray and diffuse surface, the radiosity can also be formulated as follows.

$$J = \varepsilon^d E_b + (1 - \varepsilon^d) \cdot G^d + (1 - \varepsilon^s) \cdot G^s \tag{5-14}$$

In Eq. (5-14), E_b is the blackbody emissive power while ε^d and ε^s are diffuse and specular emissivity, respectively. The blackbody emission is simply written as follows.

$$E_b = \sigma T^4 \tag{5-15}$$

Here, σ is the Stefan-Boltzmann constant that equals to 5.67 x 10^{-8} W/(m^2K^4). T denotes the surface temperature. Eq. (5-14) can be rewritten for G^d as follows.

$$G^d = \frac{J - \varepsilon^d E_b - (1 - \varepsilon^s) \cdot G^s}{(1 - \varepsilon^d)} \tag{5-16}$$

If one substitutes Eq. (5-16) into Eq. (5-12), the following equation can be obtained.

$$q^{||} = \frac{\varepsilon^d (E_b - J) + (\varepsilon^d - \varepsilon^s) \cdot G^s}{(1 - \varepsilon^d)} \tag{5-17}$$

The diffuse irradiation to a surface can also be formulated in terms of radiosity of all other surfaces in the radiation enclosure.

$$A_i G_i^d = \sum_{j=1}^{n} F_{ji} A_j J_j \tag{5-18}$$

In Eq. (5-18), A_i and A_j are the surface areas of surface "i" and "j". The view factor from surface "j" to surface "i" is denoted as F_{ji}. According to reciprocity rule, the view factors between surfaces are proportional to area ratio, as described in the following equation.

$$F_{ji} A_j = F_{ij} A_i \tag{5-19}$$

Thus, Eq. (5-18) can be rewritten as follow.

$$G_i^d = \sum_{j=1}^{n} F_{ij} J_j \tag{5-20}$$

One can substitute Eq. (5-20) into Eq. (5-12) for any surface, and obtain the following equation.

$$q_i^{||} = J_i - \sum_{j=1}^{n} F_{ij} J_j - G_i^s \tag{5-21}$$

Finally, the net flux to a surface found in Eq. (5-17) and Eq. (5-21) can be equated to each other, and the following equation can be written for any surface "i".

$$\left(\left(1-\varepsilon_i^d\right)F_{ii} + \varepsilon_i^d\right)J_i - \sum_{\substack{j=1 \\ j\neq i}}^{n}\left(1-\varepsilon_i^d\right)F_{ij}J_j = \varepsilon_i^d E_{b,i} + \left(1-\varepsilon_i^s\right)G_i^s \tag{5-22}$$

For the collector ring and particle distributor specular emissivity and diffuse emissivity is equal to each other. The view factors for each surface pair can be calculated analytically. The analytical correlations for various surface configurations are listed in [113] and not repeated here for brevity. These correlations are utilized in the long-range thermal emission model based on geometric dimensions. Finally, the surface temperature needs to be estimated based on particles located at the top of the film. The number of particles of which the temperature is averaged to find the surface temperature is calculated by using the "unshaded particle" approach described in Eq. (5-4) and (5-5). However, an average incidence angle is required for the estimation. As shown in Eq. (5-7), a sine average of incidence angles is employed to find the averaged value for the range of (0°,90°). The sine-averaged incidence angle is 39.54° for the given range, and this value is used. Then, the surface temperature is assigned as the average of the temperature of the highest $n_{un,p}$ particles.

Eq. (5-22) can be written for all surfaces forming the radiation enclosure and radiosity can be found for each surface by solving "n" equations for "n" unknowns, where n is the total number of surfaces. Note that there is no need to write the equation for the aperture plane because its radiosity is equal to the blackbody emission for ambient temperature according to Eq. (5-13). After finding radiosity for each surface, the net heat flux to/from each surface can be calculated by Eq. (5-17) or (5-21). In order to distribute the energy to/from a surface to particles forming the particle surface, the methodology described in Chapter 5.1.1.1 is utilized. Particle absorptivity and bed solid fraction are already known. The sine-averaged incidence for long-range thermal radiation is also found as 39.54°. If the net flux is negative for a surface, the radiation penetration algorithm runs as if the value is positive, and the heat gain by each particle is considered as heat loss.

The snapshot of the particle positions for the CentRec dimensions listed in Table 5-1 are utilized to validate the developed model. No solar flux is applied to the receiver. Temperature of

all particles in the domain, particle distributor and collector ring are set to 1000 K, and the aperture plane temperature is set to 0 K. Thus, the only active heat transfer mode is the long-range thermal emission. Figure 5-25 shows the emission loss through the aperture found by the MCRT and the current model for various particle emissivities.

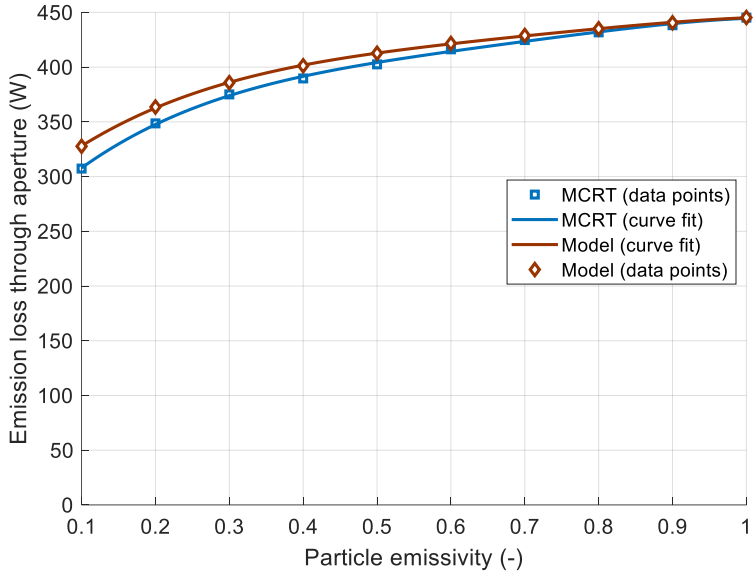

Figure 5-25 Comparison of model and MCRT results for various particle emissivity values in terms of emission loss through the aperture. Wall emissivity equals the particle emissivity for each case.

The deviation is less than 1% for particle emissivity > 0.8, being representative for CSP applications. However, the error increases up to 6% for particle emissivity of 0.1. The one reason of increasing error with decreasing particle emissivity may be the approximation of the constant film thickness in the axial and the tangential directions. The film thickness affects the effective cavity diameter, and it affects the view factor calculations. Note that no error is expected in view factor formulas because they are analytically derived. As surface emissivity decreases, the radiosity from all surfaces and finally the diffuse irradiation to the aperture plane become more dependent on view factors according to Eq. (5-22) and Eq. (5-20), respectively. In most cases, the film gets thinner as it approaches the exit, thus smaller view factors from the discrete surfaces being near to the exit to the aperture plane are expected. Thus, the constant film approximation leads to higher diffuse radiation from those surfaces to the aperture and it eventually causes higher reflection losses for low surface emissivities.

5.1.4 Short – range Thermal Radiation Model

Thermal conductivity due to radiation in monodispersed static beds was studied extensively for several relevant industrial applications, including pebble-bed reactors [114] and methanol reformers [115]. Several correlations are proposed for radiative conductivity by taking the particle size, particle emissivity and temperature into account for packed beds [102, 116]. However, these

models are not directly applicable to moving beds because the view factors between particle pairs are functions of particle-particle distance and shading of other particles, which are continuously changing in moving beds. Thus, particle scale radiation models are needed for thermal DEM simulations. For this purpose, MCRT codes can be directly coupled to DEM solvers such that the radiative heat transfer between all particle pairs and particle wall pairs can be calculated [60, 117]. For static beds, the view factor for each pair may be calculated once but for moving beds, they should be calculated in each coupling time step. Although this approach is very accurate if enough number of rays are emitted, it results in very high computational cost for particle beds composed of hundreds-of-thousands of particles. A particle scale radiation model developed by Cheng and Yu [116] considers Voronoi polyhedrons with various shape and size to discretize the particle domain. Polyhedrons are created in a way that their corners are located at particle centers and each one contains a single particle. This approach neglects the radiative heat transfer between non-neighboring polyhedrons, whose effect increases as the solid fraction decreases. Van Antwerpen et al. [81] developed a Multi Sphere Unit Cell method to account for radiation between both touching and non-touching spheres but the model is only applicable to packed beds. In the CentRec application, particles are not in densely packed state, thus models developed for packed beds are not preferred in this study. Zhou et al. [118] used a "environment temperature" to calculate the radiative heat transfer between a particle and its surrounding. Simply, the temperatures of particles being distant to a particle up to 1.5 particle diameter are averaged to find environment temperature. Although the threshold distance can be increased for dilute beds, the energy may not be conserved locally.

Johnson et al. [119] found radiation distribution factors (RDF) for various particle absorptivity and solid fraction as a function of distance between particle pairs and particle wall pairs. The interstitial fluid is assumed as non-participating medium. Unlike view factors, being solely a geometrical parameter, and considering radiation emitted from surface A and directly absorbed by surface B, RDF also accounts for the radiation emitted from surface A and absorbed indirectly by surface B after one or several reflections from nearby particles. This model is employed in this study for several reasons. Firstly, it can be easily applied to DEM simulations. Secondly, the energy is always conserved locally, i.e. heat gain of a particle always equals to heat loss of another one. Thirdly, it does not require any further discretization of the domain; simply, by knowing the distance between a particle pair and bed porosity, one can easily find the RDF between particles. However, there are two concerns about the applicability of derived RDFs to the CentRec application. Firstly, Johnson et al [119] found RDFs for the bulk region, where bed porosity is direction-independent. However, in CentRec, due to existence of the wall, the local solid fraction is oscillating near the wall. Secondly, the model is originally developed for particle Young's modulus of 10^9 Pa; however, in this study, a lower Young's modulus, $5x10^6$ Pa is used to increase the DEM time step. Using artificially softened particles may affect the distance between touching particles although the particle overlap is around 0.002 times the particle radius for $5x10^6$ Pa in the CentRec simulation. Because the code is publicly available [119], the model is tailored for CentRec application and a new RDF set is found.

For the derivation case, a volume section from the particle film, of which thickness is $8d_p$ and edge length in lateral directions is $40d_p$, is considered. The normal shape of the film is cylindrical (

Figure **5-26**(a)) but it is unrolled to a rectangular domain (

Figure **5-26**(b)) for the ease of computation. Because the cavity diameter ($100d_p$) is much larger than the particle diameter, it can be assumed that the cylindrical receiver wall is flat relative to a single particle, as discussed in Chapter 4.1.

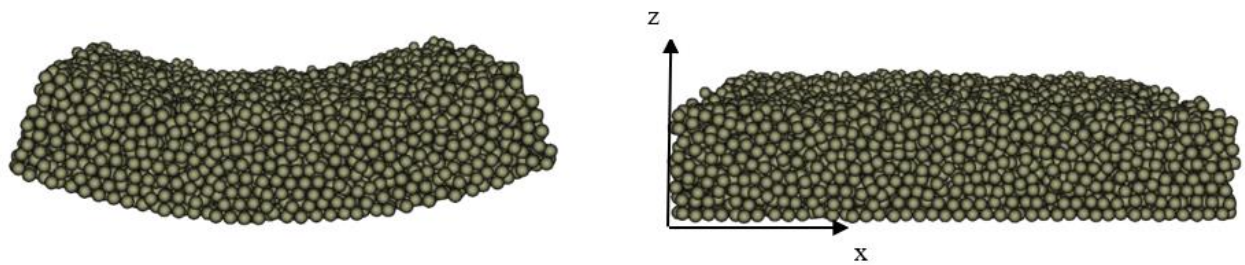

(a) **(b)**

Figure 5-26 (a) Original particle film section **(b)** unrolled particle film section.

To derive the new RDF set, the MCRT code developed by Johnson et al. [119] is used. A number of rays, which have a random direction vector pointing outward from the particle surface and random location on the particle surface are generated. The ray number per particle should be optimized such that found RDF is ray number independent. To optimize the number of rays, a heat transfer model is developed. Temperature of particles of which center lies between z = 0 and z = $1d_p$ is set to 1000 K while the temperature of the ones of which center is above z = $6d_p$ is set to 1010 K. The temperature of the wall at z=0 is also set to 1000 K. Thus, a heat flow from the top surface of the film to particles touching the wall is obtained. The only active heat transfer mode is the short-range radiation which is calculated with the RDFs found by the MCRT code. The particle diameter is 1 mm while particle and wall emissivity are set to 0.86 and 1, respectively. Then, the radiative conductivity (k_{rad}) is calculated as follows.

$$k_{rad} = \frac{q_{ss} t_{film}}{\mathrm{A}(\Delta \mathrm{T})} \tag{5-23}$$

q_{ss}, t_{film}, A are the heat flow at steady state, the heat transfer-enabled film thickness, which is $5d_p$ in this case, and the film cross-sectional area. Particle inner conductivity is assumed as infinite, as discussed in Chapter 5.2.3.

In Figure 5-27, the radiative conductivity for various ray numbers is plotted. It can be concluded that 10^4 rays per particle are sufficient to have ray-independent results. Although the

difference between results for ray number of 10^1 and 10^4 is not significant, it should be noted that obtaining similar radiative conductivity for different ray numbers is not sufficient to determine the optimum ray number.

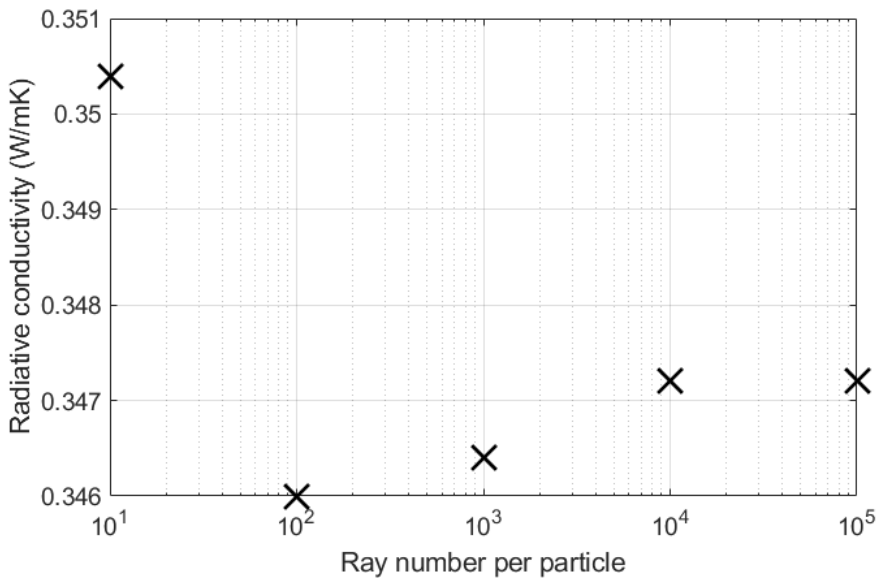

Figure 5-27 The radiative conductivity for various ray numbers at 1000 K.

Figure 5-28 shows that although total heat flow from the hot region to the cold region, or radiative conductivity, is similar for ray numbers of 10^1 and 10^4, there is significant unrealistic temperature variation in lateral directions due to badly predicted RDF between particle pairs. For a large cross-sectional area ($40d_p$ x $40d_p$), this effect is not noticeable if one only compares total heat flow because the effects of underpredicted and overpredicted RDFs counterbalance each other. This leads to inaccurate local heat transfer calculation between particle pairs in MCRT simulations. Thus, 10^4 rays per particle are selected in this study.

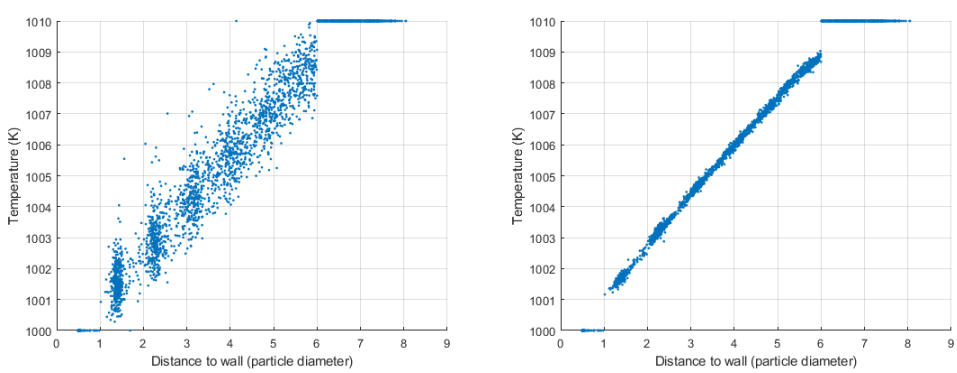

(a) **(b)**

Figure 5-28 Scatter plot of particle temperatures for ray number of **(a)** 10^1 and **(b)** 10^4 per particle.

Figure 5-29 shows the RDF distribution vs particle – particle center distance for the particle film considered in the ray-independency study. As can be noticed, the variance of RDFs increases with the distance. This is mainly because the uncertainty of the effect of shading of neighboring particles increases with increasing particle – particle distance. However, the standard deviation (SD) of scattered data is very low, especially in close particle pairs, where the short-range radiation is more dominant.

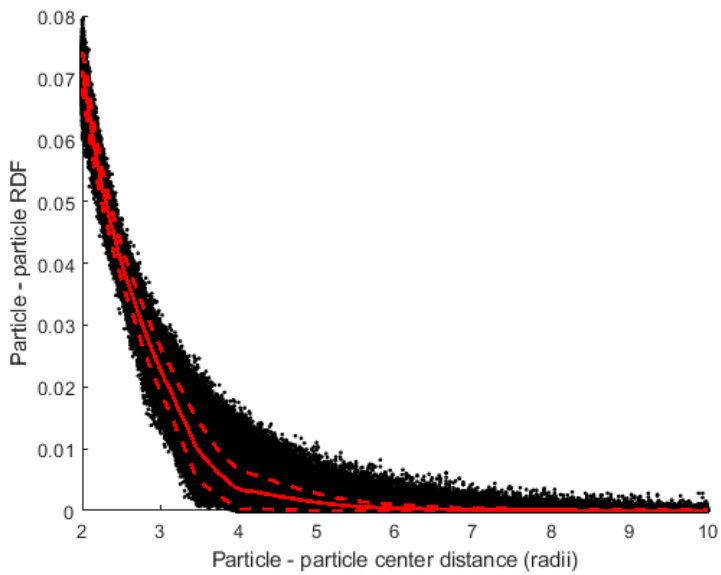

Figure 5-29 Scatter plot of RDF for all particle pairs (black dots) with the best curve (solid red line) and upper and lower limits representing mean + SD and mean – SD, respectively (dashed red lines). Particle emissivity is 0.86 and bulk solid fraction is 0.5.

In Figure 5-30, the oscillating local solid fraction in terms of distance to the wall is presented. Note that the oscillations are damped to the bulk solid fraction value of 0.5 at around 5 d_p. The bulk solid fraction of the particle film for the calibrated particle contact properties is found as 0.48 – 0.52 after checking many rotational speeds and mass flow rates. It decreases slightly in the moving zone and increases by a small amount in the stationary zone. However, this change has negligible effect on the RDF curve thus in this study a representative value, being 0.5, is considered for all short-range radiation calculations to avoid the calculation of local solid fraction in each time step and in each part of the particle film.

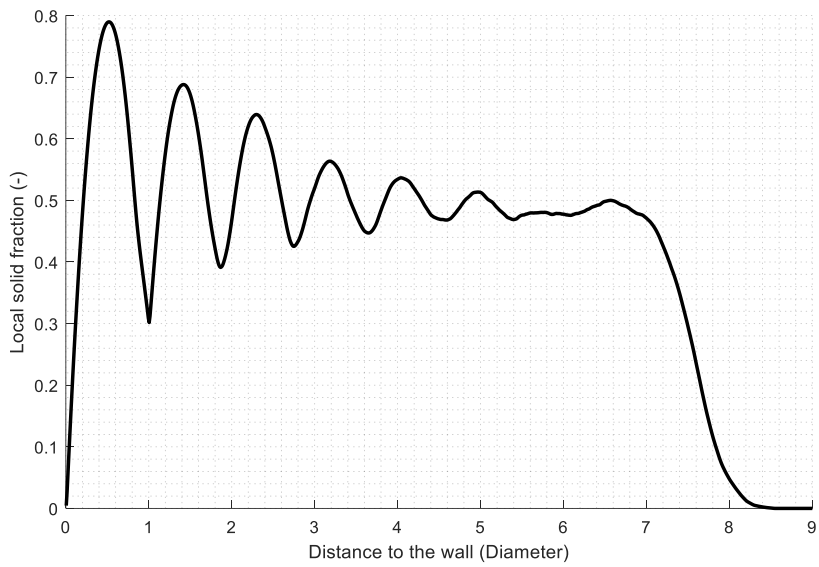

Figure 5-30 Local solid fraction variation in z direction where wall corresponds to z = 0.

As discussed above, due to the non-uniform solid fraction distribution, the RDF curves in the near wall region may not be the same as the ones in the bulk region. In Figure 5-31, the RDF curves for many layers with thickness of $1d_p$ are plotted along with the curve found by Johnson et al. [119] for the bulk region and particles with Young's modulus of 10^9 Pa. The average distance to the wall for a particle pair is found by taking the arithmetic mean of each particle's distance to the wall. The first inference from this figure is that particle layering effect due to the wall has an effect on particle – particle RDF curves up to $z = 3d_p$. After this value, the shape of RDF curves does not change considerably. Secondly, the RDF curves for $z > 3d_p$ are almost the same as the curve found by Johnson et al. [119] for relatively hard particles. Thus, it can be said that using softer particles ($5x10^6$ MPa) has no effect on the RDF curve. The curves for $3d_p < z < 6d_p$ are averaged to find a representative curve for the bulk region. Thus, four RDF curves for particle pairs (3 curves for the first 3 layers and 1 for the bulk) are sufficient to calculate short-range radiation in the particle film.

For the case of a non-black wall, reflections from the wall also play role for particle – particle RDF, especially for the ones near the wall. In Figure 5-32, this effect is investigated for the layers next to the wall and several wall emissivities. Firstly, in Figure 5-32(a), it can be noticed that reflections from the wall is non-negligible as wall emissivity increases for particle pairs touching the wall. However, there is no effect of wall reflections on particles in the 2nd layer next to the wall, as can be seen in Figure 5-32(b).

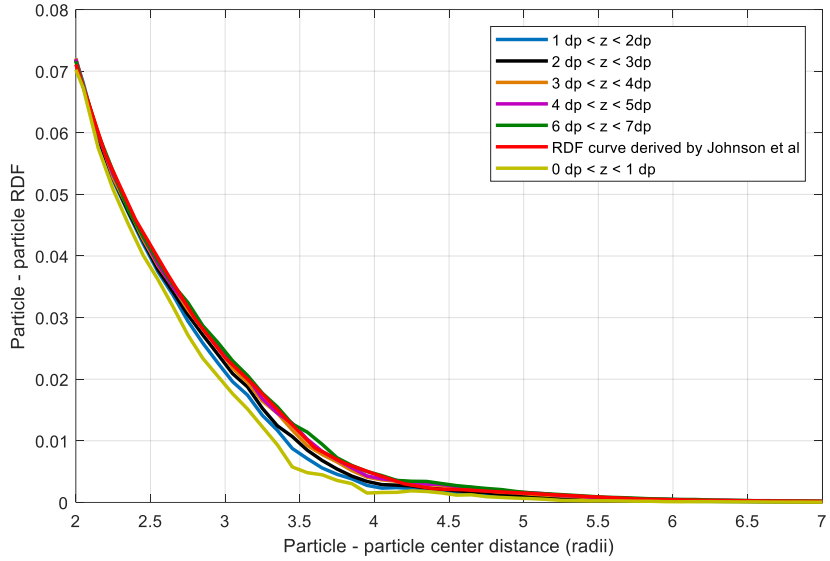

Figure 5-31 RDF curves for various distances to the wall for particle emissivity of 0.86 and wall emissivity of 1.

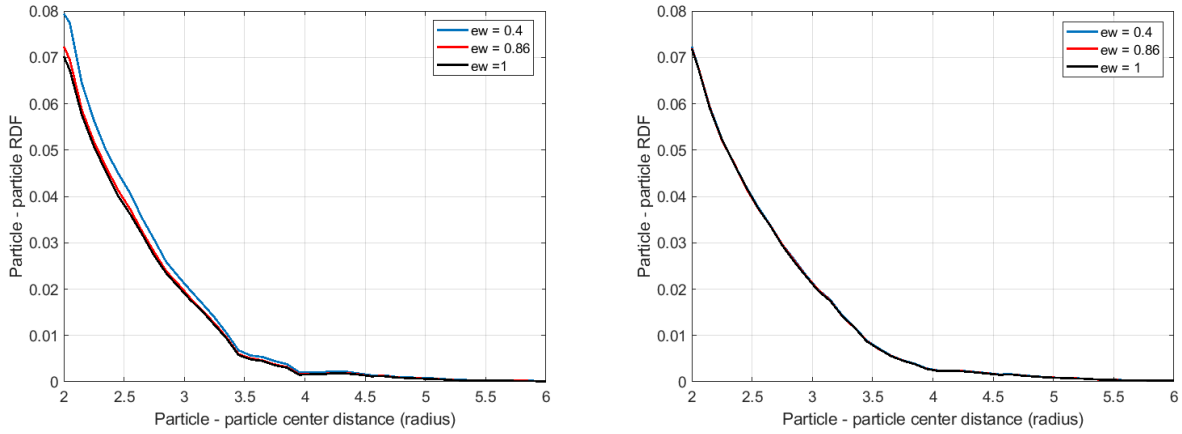

(a) **(b)**

Figure 5-32 The RDF curves for particle pairs for various wall emissivities. Particles center lies on **(a)** $0 < z < 1d_p$ **(b)** $1d_p < z < 2d_p$. Particle emissivity is 0.86.

In Figure 5-33, the RDF curves for particle – wall pairs are plotted against particle center to wall distance. One can notice that particles are aggregating at a distance of 1 radius and 2.8 radii, which corresponds to the first two local peaks in Figure 5-30. As can be expected, the particle – wall radiation is important for particles touching the wall, and proportional to wall emissivity. However, for particles in 2nd layer ($1d_p < z < 2d_p$), the RDF is mostly less than 0.05, which is very low. It is known that wall emissivity has also no effect on particle – particle RDF as can be noticed in Figure 5-32(b). Considering that there is a stationary layer in the CentRec application, as discussed in Chapter 4.2, it can be said that the cylindrical wall emissivity has negligible effect on the short-range radiation in the moving film because only particles at $z > 1d_p$ are moving during

operation. However, increasing particle – wall RDF results in less thermal resistance in radial direction and eventually higher conductive loss in radial direction.

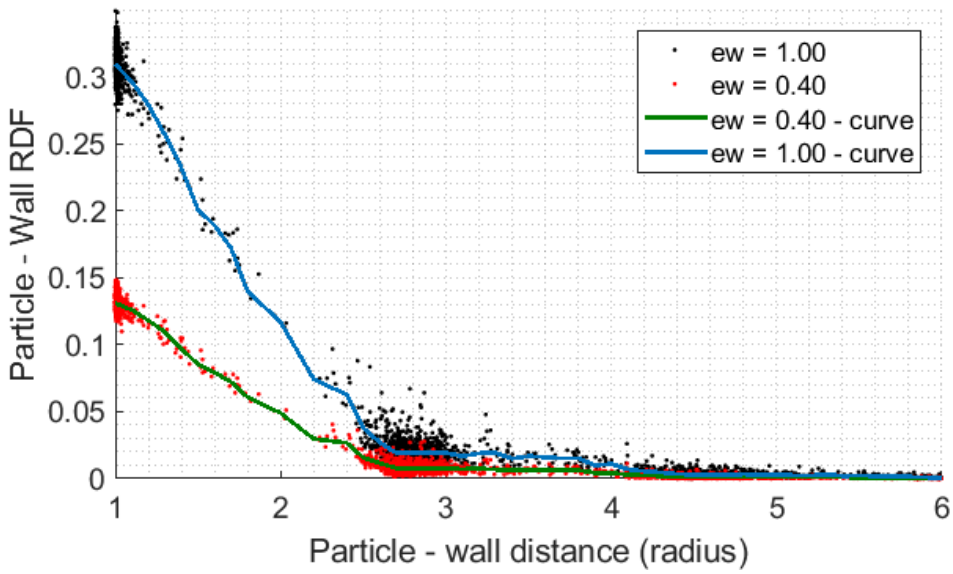

Figure 5-33 The RDF curves for particle – wall pairs for different wall emissivities. Each dot represents a single particle. Particle emissivity is 0.86.

Several attempts were made to find a curve fit to better represent the data but due to low R^2 value, the data for all RDFs is represented as discrete values with interval of distance of 0.1 radii. All these values are embedded into the thermal code.

In order to check the validity of the derived RDFs, a heat transfer model is developed like in the ray-dependence study. A relatively thick particle film (thickness of ~$9d_p$) with lateral direction lengths being $40d_p$ x $40d_p$ is considered. In Figure 5-34(a), the initial temperature distribution of the bed is presented. Here the red particles ($z > 6d_p$) are set to (T + 5) K as a boundary condition and the rest of the film is set to (T – 5) K, where T is the investigated mean film temperature. The temperature of the particles of which center lies at $0 < z < 1d_p$ and the wall is defined as boundary condition so that their temperature is always maintained at (T – 5) K. Thus, there is a heat flow from hot particles ($z > 6d_p$) to cold particles ($z < 1d_p$) and wall, whose temperatures are constant. In Figure 5-34(b), the steady – state temperature distribution is presented. The temperature decrease is quite linear in the z-direction for the relevant range of T because of the low temperature gradient (10 K).

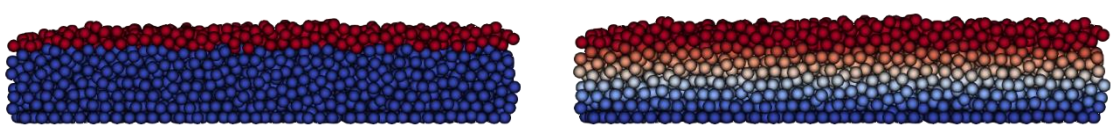

(a) **(b)**

Figure 5-34 (a) Initial temperature distribution **(b)** steady-state temperature distribution. In both cases, the maximum temperature difference is 10 K.

In Figure 5-35, the developed model based on RDF curves is compared with MCRT based simulation results for two particle emissivities and relevant temperature range in the CentRec in terms of radiative conductivity. The model results match very well the MCRT based results, with an error, being < 1% at 1300 K. The model is also compared with various film sections, being thicker and wider than this case thanks to higher rotational speed and mass flow rate, and a similar trend in deviation is observed. Thus, with a key computational advantage, the developed model proves its ability to estimate short-range radiation in particle beds in the near-wall region. However, in this validation study, because the temperature of particles touching to the wall ($0 < z < 1d_p$) are set to a constant value, there is no heat exchange between those particles and the wall. If one also assumes those particle temperatures not constant, i.e. the heat flow from particles at the top to only the wall, the error between radiative conductivities of the model and the MCRT based results is found as ~4% at 1300 K. However, this has negligible effect on effective bulk thermal conductivity of the moving film but only creates slight error on conductive loss in radial direction, being < 1% as discussed in Chapter 6.2.

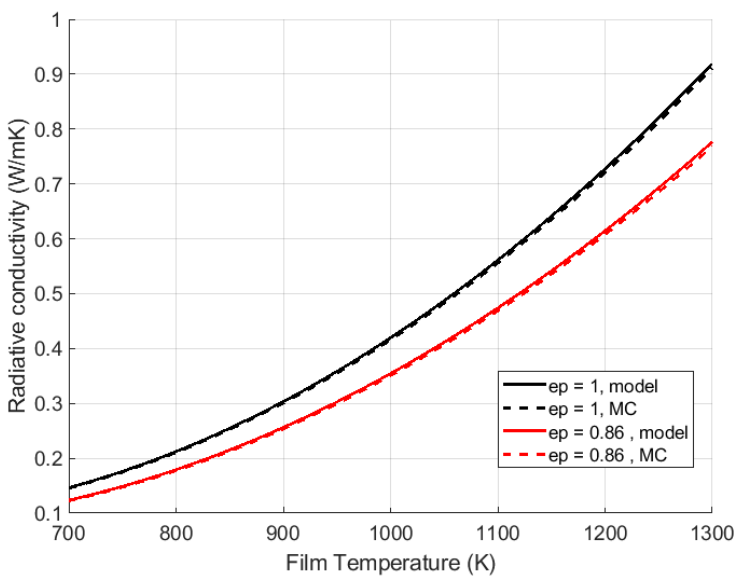

Figure 5-35 The comparison of model results based on derived RDFs with MCRT results. The wall emissivity is assumed the same as the particle emissivity for both cases.

5.2 Particle Scale Conduction Model

In order to model the heat conduction between touching or close particle pairs, efforts were put into the derivation of the particle - particle heat conductance from the bulk thermal conductivity developed for static beds in several studies [60, 120]. However, bulk thermal conductivity models require a porosity value, which is a bulk property and changes significantly at the near wall region. Moreover, the dependence of bed thermal conductivity to the packing structure at near wall region is reported by several researchers [53, 54, 81, 121]. For this purpose, deriving particle scale conductance from bulk thermal conductivity for near-wall region is very complex thus not

preferred in this study. Instead, a particle scale model, being applicable to DEM simulations, is addressed.

Particle scale conduction occurs mainly through two mechanisms for particle pairs. The first one is the heat conduction between touching particles via the contact area (q_{pp}). The second mechanism is the heat conduction via the interstitial fluid filling the gap between particles (q_{pfp}). Because CentRec is an atmospheric receiver, atmospheric air fills the gaps between the particle pairs. Similar models, like particle - wall conduction via contact area (q_{pw}) and via interstitial fluid (q_{pfw}) are required for particle – wall heat transfer interactions. Finally, the inner particle conduction is to be investigated.

5.2.1 Conduction Through Contact Area

For rough particles, the fluid filling the microscopic pores formed in the contact region reduces the heat conduction for the cases that fluid thermal conductivity is much smaller than the particle thermal conductivity [122, 123]. The modelling of rough particles is more important for particle beds under compression because, the size of pores and contact area may change with the magnitude of the applied loads [124, 125]. However, in this study, the microscopic pores on the surface are not modelled because even without considering particle roughness, the contribution of particle conduction via contact area to particle – particle heat transfer is less than 5% [101, 126]. Note that this mechanism becomes dominant in vacuum receivers, where heat is only conducted through the contact area or radiation [60, 127, 128]. Thus, particles are assumed as perfect spheres when they are in contact. Batchelor and O'Brien [129] developed a simple heat conduction model via the contact area, which is as follows.

$$q_{pp} = 2r_c k_s (T_i - T_j) \tag{5-24}$$

The contact radius and solid thermal conductivity are denoted as r_c and k_s, respectively. T_i and T_j are the temperatures of particles being in contact. The center position of two particles is known from DEM simulation. Thus, one can calculate the contact radius by using the distance between two particle centers. A schematic view is depicted in Figure 5-36(b).

$$r_c = \sqrt{r^2 - (r - H)^2} \tag{5-25}$$

Particle radius and half overlap distance is represented as r and H. The model is slightly modified to consider the case that there is a large temperature difference between particles [130].

$$q_{pp} = \frac{4r_c(T_i - T_j)}{\frac{1}{k_{s,i}} + \frac{1}{k_{s,j}}} \tag{5-26}$$

As discussed previously, particle overlap in DEM simulation is higher than in reality due to artificially reduced particle Young's modulus. This leads to an overestimation of contact radius and must be corrected. Zhou et al. [131] developed a correction factor to account for this overestimation by considering real and reduced Young's modulus denoted as E_{DEM} and E_{real}, respectively.

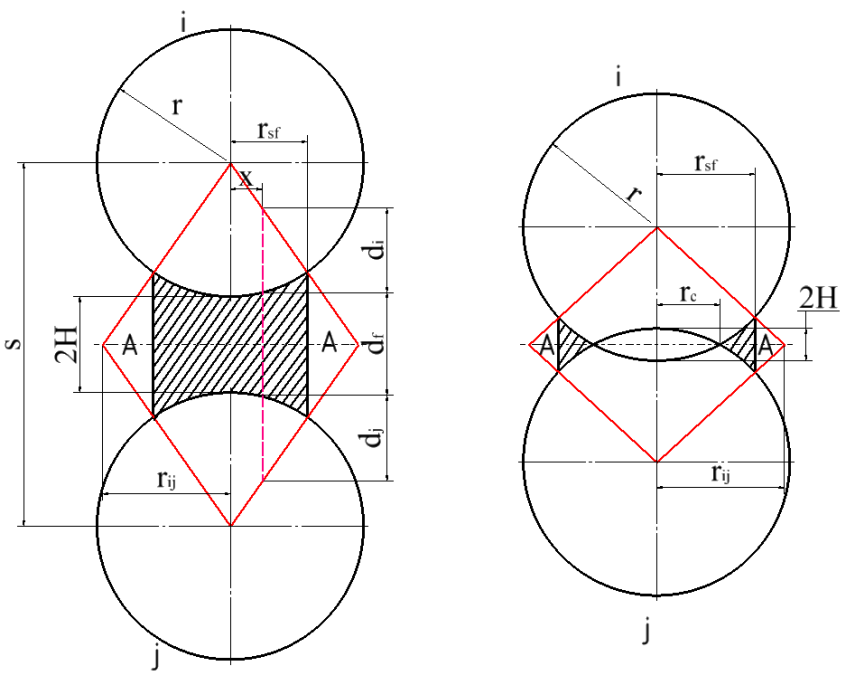

(a) **(b)**

Figure 5-36 Schematic view of **(a)** non-contacting particles **(b)** contacting particles with an overlap.

$$c = \left(\frac{E_{DEM}}{E_{real}}\right)^{0.2} \tag{5-27}$$

Then the resulting formula can be written as follows.

$$q_{pp} = \frac{4cr_c(T_i - T_j)}{\frac{1}{k_{s,i}} + \frac{1}{k_{s,j}}} \tag{5-28}$$

Similarly, particle – wall conduction (Figure 5-37(b)) can be derived as follows.

$$q_{pw} = \frac{4cr_c(T_i - T_w)}{\frac{1}{k_{s,i}}} \tag{5-29}$$

Here, T_w represents the wall surface temperature so the formula accounts for the conduction heat transfer between particle center and wall surface. Because the conduction length is half of the length of particle – particle conduction while the contact areas are same, the conduction doubles for particle – wall interaction.

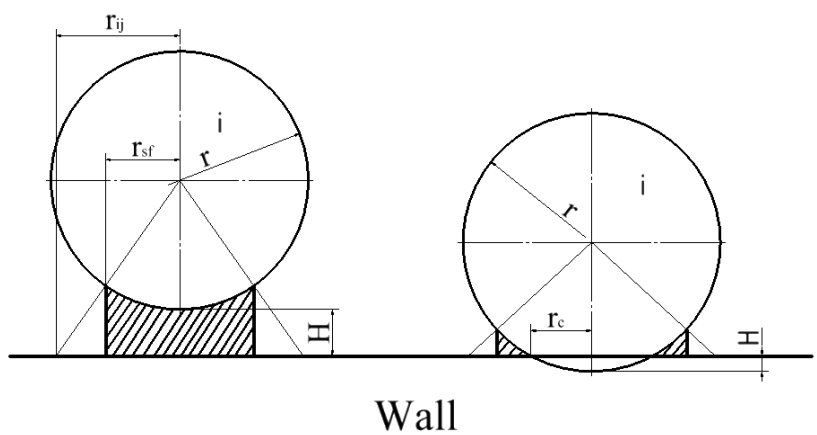

(a) **(b)**

Figure 5-37 Schematic view of **(a)** non-contacting particle - wall **(b)** contacting particle - wall with overlap.

5.2.2 Conduction Through Interstitial Fluid

The second heat transfer mechanism is the heat conduction via the stagnant interstitial fluid. Cheng et al. [130] employed Voronoi polyhedrons to model particle arrangements in a particle bed. In this approach, a double pyramid is created such that centers of two particles are located at the tips of pyramids, and the base plane of the pyramids are constructed by considering the nearby particles. The detail of the polyhedron creation process is not discussed here for brevity and can be found in [130]. Later, the base of the pyramids is approximated as a circle because bases of polygon-like pyramids, having arbitrary edge sizes, are very hard to analytically express. In Figure 5-36, the 2D cross section of the double pyramids for contacting and non-contacting particles are represented. In this model, the heat transfer through the fluid is assumed to be one-dimensional and, in the direction normal to the plane formed by points equidistant to particles' center. Thus, the heat is only conducted inside the shaded area in Figure 5-36, and no heat transfer in the areas labeled as "A". It is also assumed that the surface of the tapered cone is isothermal and equal to the surrounding temperature. The heat flow is represented by many parallel lines. A

representative line (red dashed line in Figure 5-36(a)) start at an arbitrary point (x) between 0 and r_{sf} and comprised of lengths of d_i, d_f and d_j, being the distances within the particle "i", in the fluid and within the particle "j", respectively. Depending on the position of x, the lengths of the line sections changes. d_i and d_j are always equal to each other because monodisperse particles are employed in this study. The geometric quantities shown in Figure 5-36(a) can be found as follows.

$$H = s - 2r \tag{5-30}$$

$$r_{sf} = \frac{r_{ij} r}{\sqrt{(r+H)^2 + r_{ij}^2}} \tag{5-31}$$

$$d_f = 2\left[(r+x) - \sqrt{r^2 - x^2}\right] \tag{5-32}$$

$$d_i = d_j = \sqrt{r^2 - x^2} - \frac{x(r+H)}{r_{ij}} \tag{5-33}$$

$$q_{pfp} = (T_i - T_j) \int_{r_s}^{r_{sf}} \frac{2\pi x \, dx}{\left(\frac{d_i}{k_{s,i}} + \frac{d_f}{k_f} + \frac{d_j}{k_{s,j}}\right)} \tag{5-34}$$

$$r_s = \begin{matrix} 0 \; if \; s \geq 2r \\ r_c \; if \; s < 2r \end{matrix} \tag{5-35}$$

In this formulation, H, r_{ij} and r_{sf} are the distance between tips of spheres, the base radius of the cone and the effective radius for heat transfer, respectively. Note that for contacting particles, H is used as negative value in the formulation as stated in Eq. (5-30) although it is shown as a geometrical parameter in Figure 5-36(b). The fluid and particles' thermal conductivity are represented as k_f, $k_{s,i}$ and $k_{s,j}$, respectively. The lower bound of the integral, r_s, is equal to the contact radius for contacting particles because there is no conduction through the fluid in the contact region. However, to calculate these parameters, one should estimate r_{ij} from the shape of the Voronoi polyhedron, which is given in the original formulation [130] as follows.

$$r_{ij} = \sqrt{\frac{3V_{ij}}{\pi s}} \tag{5-36}$$

The calculation of the volume of the polyhedron, V_{ij}, is not practical in many cases because it requires Voronoi tessellation of the whole domain in every time step. Yang et al. [132] investigated the shape of Voronoi polyhedrons for many porosity values. Zhou et al. [118] developed a simple formula based on results of Yang et al. [132] for the cone base radius as a function of the bed porosity (ϵ).

$$r_{ij} = 0.56r(1-\epsilon)^{-1/3} \quad \textbf{(5-37)}$$

For non-contacting particles, as the distance between particles (s) increases, the conductive heat flux decreases. A cut-off distance is suggested by Zhou et al. [118] such that for the condition of s > 3r, the heat conduction is negligibly small. This condition is also followed in this study.

For contacting particles, like in particle-particle conduction, due to overestimated particle overlap, the distance between particle centers is found less than in reality. This leads to an overestimation of conductive heat flux through the fluid, and must be corrected. The contact radius in simulation ($r_{c,sim}$) can be formulated as a function of the distance between particles in the simulation (s_{sim}) as follows.

$$r_{c,sim} = \sqrt{r^2 - \left(\frac{s_{sim}}{2}\right)^2} \quad \textbf{(5-38)}$$

The true contact radius can be calculated by using the correction factor, c, found in Eq. (5-27).

$$r_{c,true} = cr_{c,sim} \quad \textbf{(5-39)}$$

Then, the true distance to be used in Eqs. (5-30) - (5-35) can be found as follows.

$$s_{true} = 2\sqrt{r^2 - r_{c,true}^2} \quad \textbf{(5-40)}$$

In the thermal code, the conduction through the fluid has to be calculated for all particle pairs of which centers are distant to each other at most 3 particle radii and for every time step. Considering the numerical integration in the calculations, Eq. (5-34), a three-dimensional matrix is formed and embedded into the thermal code for the ease of computation. Each dimension of the matrix corresponds to a variable on which particle - fluid - particle depends. Those variables are s_{sim}, $k_{s,i}$ and $k_{s,j}$. Because the thermal conductivity of air and particles are temperature-dependent, the effect of temperature on conduction should be considered. The fluid temperature is estimated as the arithmetic mean of temperatures of two particles so it is a dependent variable. By employing this 3D matrix, one can calculate q_{pfp} for any particle pair with the distance between them and their temperatures.

Similarly, the conduction via the fluid can be estimated for particle – wall interaction. However, there is only one particle in the system, and the distance taken in the fluid region, d_f, should be halved. The particle-fluid-wall conduction can be written as follows.

$$d_{f_w} = (r + x) - \sqrt{r^2 - x^2} \tag{5-41}$$

$$q_{pfw} = (T_i - T_w) \int_{r_s}^{r_{sf}} \frac{2\pi x \, dx}{\left(\frac{d_i}{k_{s,i}} + \frac{d_{f_w}}{k_f}\right)} \tag{5-42}$$

Other formulas to calculate r_{sf}, r_s and d_i are the same as the ones used for particle – fluid – particle conduction calculation.

5.2.3 Inner Particle Conduction

In most DEM simulations, particles are assumed to have uniform temperature, i.e. the conduction thermal resistance within the particle is much less than the convective, conductive and radiative thermal resistance between particle surface and surrounding [60, 95, 100]. Oschmann et al. [133] developed a 3D resolved model such that temperature distribution in a particle is represented by many points within the particle. To check this effect, a non-dimensional Biot number is employed, especially if the sphere exchange heat by convection with the surrounding.

$$Bi = \frac{h d_p}{k_s} \tag{5-43}$$

Biot number is defined as the ratio of conduction resistance to convection resistance, where h and k_s are the convective heat transfer coefficient and the particle thermal conductivity, respectively. However, it is not directly applicable to the cases where a sphere is heated by radiation. In the CentRec, the most critical heat transfer mechanism is the solar irradiation because particles are exposed to very high fluxes (>1 MW/m^2) in the peak flux region. Thus, only radiation is checked in this study. To further investigate the temperature distribution and heat penetration in the particle, a transient finite difference code is developed. In this code, a sphere is divided into many isothermal concentric spherical segments. The energy balance is checked for each segment while energy exchange between segments is only by conduction except for the outermost segment because the outermost segment gains energy by radiation and loses energy by conduction to the inner segment. In the CentRec, particles are rolling during the motion, thus the assumption that the flux is applied to all particle surface uniformly is valid. For this reason, there is one dimensional heat flow in the particle. The factors affecting the thermal behavior of a particle are the applied

flux ($q^{||}$), particle diameter (d_p), particle thermal conductivity (k_s) and particle thermal diffusivity. For the case that there is no heat sink, thermal steady-state cannot be obtained but the temperature difference between particle center and surface does not change with time after the heat flow reaches the center, which may be called as "quasi thermal steady state". In other words, the applied heat leads to uniform temperature increase in all points after the system reaches the quasi thermal steady state. The quasi thermal steady state condition can be stated as follows.

$$q^{||} \approx \frac{4k_s \Delta T}{d_p} \quad \textbf{(5-44)}$$

The temperature difference between the center and surface is represented as ΔT. Note that in the finite difference code, the sphere cannot be discretized by only spherical segments due to singularity in the center. Thus, as the number of segments increases, the left-hand side approaches the right-hand side in Eq. (6-2). The thermal conductivity of the bauxite particles, being very similar to the particles used in this study in terms of material composition, were measured as ~5.5 W/mK (See Figure 5-38). If we consider the extreme conditions like flux of 2 MW/m^2 and 1 mm particle diameter, the resulting temperature difference is ~ 90 K. In most cases, the flux is much lower than this value, thus uniform temperature assumption is valid. For a representative particle density of 3560 kg/m^3 and specific heat capacity of 1200 J/kgK, the heat flow reaches the center in around 0.01 s for a 1 mm-diameter particle. Heat flux has no effect on heat diffusivity. Thus, heat diffusivity is also not a concern for the CentRec application because of the very small particle diameter.

5.2.4 Model Validation

Bulk thermal conductivity of various types of ceramic particles, being suitable for CSP applications, were measured by several researchers [134-136]. However, there is no measurement made for SG 16/30 particles used in the cold experiments. Chung et al. [134] measured bulk thermal conductivity of bauxite particles, referred to as Carbobead HSP 40/70, with a transient hot wire method. The particle properties such as circularity and bed properties like porosity were also measured. Because material composition of both particles is similar, and measurement details are well reported, this measurement study is considered for the validation of the developed heat conduction model. Grobbel [60] also characterized various sizes of Carbobead HSP particles (16/30 20/40 and 30/60) and SG 16/30 particles in terms of particle size distribution and shape. Note that numbers after the particle name such as "16/30" correspond to the mesh number in the sieve apparatus, and particle size decreases with increasing mesh number. Grobbel [60] found very similar circularity and roundness for all sizes of Carbobead HSP particles and SG 16/30, thus it can be said that particle shape does not change significantly with the particle size for the same particle type. The results show that all particles have very good circularity (~0.95), meaning that they are very close to perfect spheres. However, Chung et al. [134] measured the circularity of Carbobead

HSP much lower (~0.6) but this is mainly due to the definition of the circularity because formulas used for circularity calculation are different. The reason why such discussion is important for the model validation is that the particle scale conduction model is derived for spherical particles. As particle circularity decreases, the applicability of the particle scale model is also questionable. This is because the non-spherical particles may contact each other in many configurations, which results in very uncertain contact radius and fluid conduction path, while the contact of spherical particles is obvious.

Firstly, Chung et al. [134] measured material conductivity of bauxite particles by preparing a very dense pellet composed of bauxite particles. The temperature-dependent thermal conductivity shown in Figure 5-38 is used in this study. The material conductivity above 800 °C is assumed to be the same as the value at 800 °C.

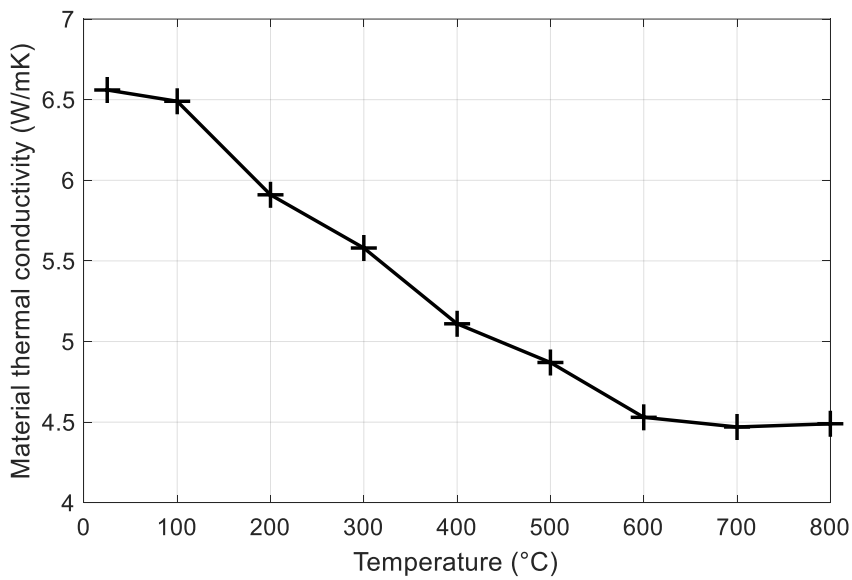

Figure 5-38 Material thermal conductivity of bauxite particles for various temperatures measured by [134].

In the transient hot wire method, a very thin wire being the heat source and temperature sensor, is located at the centerline of a cylinder-shaped measurement device while the particles fill the cylinder cavity. By measuring the transient response of the hot wire to the applied electrical current, the bulk thermal conductivity can be calculated. In the measurement, bed porosity and particle diameter are reported as 0.387 and 0.404 mm. To compare the DEM-based conduction model results with the experiment results, a bed with the same porosity is created with same sized particles. Because the thermal conductivity is independent from the measurement domain or technique, a rectangular prism domain is preferred for the sake of simplicity. Particles are generated randomly in a cubical domain with edge size of 20 d_p by using the technique discussed in Chapter 5.1.1.1. To eliminate the effects resulting from particle overlap, the true particle Young's modulus, being 200 GPa, is considered. MCRT is employed to calculate the radiative heat transfer. Thus, errors which may result from other factors are minimized.

In Figure 5-39, the model results are compared with the experimental results. The model (red solid line) underpredicts the experimental results by around 15% for the temperature range of 10 – 720 °C. There is no significant error difference between results for lowest and highest temperatures in the range. It may indicate that increasing radiation effect with temperature does not cause any change in error percentage thus the radiation models can be said to be accurate. At low temperatures (< 400°C) the conduction models may be the only error sources. However, as can be seen in Figure 5-40, the contribution of conduction to bulk thermal conductivity is negligibly small. Thus, the fluid conduction model seems problematic. In the fluid conduction model (Eq. (5-30) - (5-37)), all parameters are geometric except for cone radius, which is estimated numerically for spherical particles. The author believes that this parameter should be adjusted for non-spherical particles because the tapered cone-shaped fluid conduction region would be different for non-spherical particles. Thus, the Eq. (5-37) is adjusted accordingly to match the experiment results as follows.

$$r_{ij} = 0.75r(1-\epsilon)^{-1/3} \tag{5-45}$$

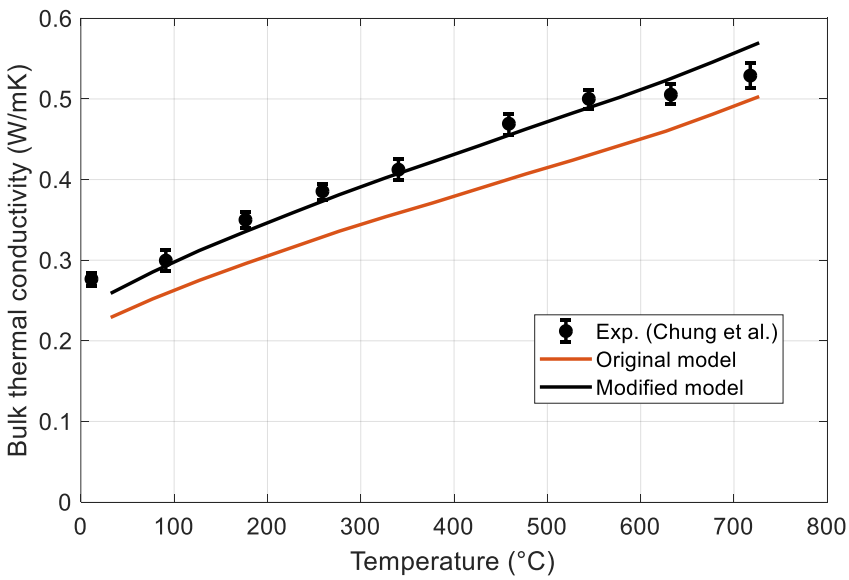

Figure 5-39 Comparison of the developed model with the experiment results.

The validity of the used approach could not be checked for a wide range of particle circularity in this study due to the lack of experimental data but will be addressed as future experimental study. In Figure 5-39, the model results with modified coefficient is also plotted. The results show that the modified parameter can predict the experiment results very well for the relevant temperature range.

In Figure 5-40, the contribution of each mechanism is shown for the experiment case. In preparation of the DEM domain, it is noticed that the conduction via the contact surface changes significantly with the gravity direction. During the post-processing it is observed that if the gravity and heat flow are in the same direction, the conduction via the contact surface is found as two times of the case that they are in the perpendicular direction. This is mainly because that particles have a much looser contact normal to the gravity direction compared to the gravity direction. However, the contribution of this conduction mechanism is found as around 1% at room temperature and even lower for high temperatures. However, it may be important for softer particles with lower Young's modulus. On the other hand, the effects of conduction via fluid and radiation increase with temperature. Note that the increase of radiative conductivity is proportional to T^3 while fluid conductivity is linearly increasing with temperature. Although it seems that fluid conduction is more dominant than radiation even at high temperatures, this trend is not applicable to all particle beds because the contribution of both mechanisms may change with particle size and bed porosity.

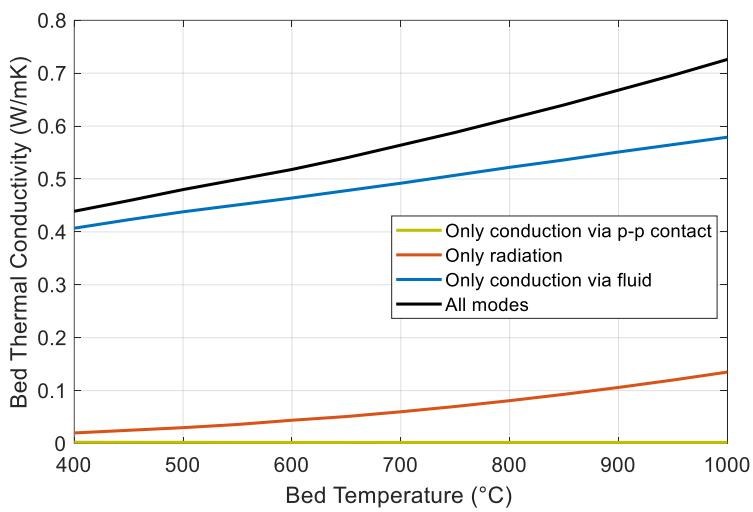

Figure 5-40 Contribution of each heat transfer mode to bed thermal conductivity for d_p = 0.4 mm at f_s = 0.613.

In Figure 5-41, the contributions for the dominant mechanisms are plotted for two particle film sections taken from the CentRec simulations. As discussed in Chapter 1.2.1, the particles are either moving or stationary relative to the rotating receiver, depending on the circumferential position. In the moving zone, the film is a bit thicker and has lower solid fraction while in the stationary zone it is more packed. Compared to smaller particles shown in Figure 5-40, radiation is more important for larger particles as can be noticed in Figure 5-41. Moreover, it has an even larger contribution than conduction. Moreover, as solid fraction decreases, the distances between particles increase, and eventually conduction decreases between particle pairs. In Figure 5-41, it can be noticed that the slight decrease in solid fraction from the stationary zone to the moving zone leads to a slight decrease in thermal conductivity due to conduction while there is no observable effect in radiative contribution for such a small change in solid fraction. Thus, one can assume that

the overall stagnant bulk thermal conductivity for the CentRec does not change with the circumferential position.

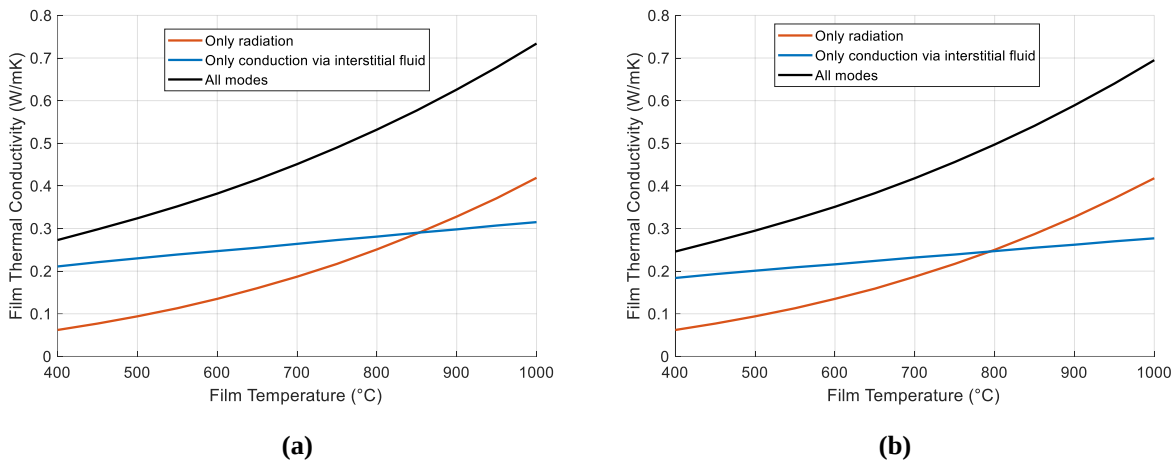

(a) **(b)**

Figure 5-41 Contribution of each heat transfer mode to film thermal conductivity for particle film sections from the CentRec simulation **(a)** stationary zone (f_s = 0.51) **(b)** moving zone (f_s = 0.49). Particle diameter is 1.2 mm.

5.3 Conduction Loss Model

In this study, it is assumed that the receiver loses heat by conduction only through the insulation covering the cylinder wall on the outside as seen in Figure 5-42. In the real application, the heat may also be conducted axially through the particle distributor but this conduction mechanism is neglected for now because of the design complexity. The heat is transferred to the wall from moving and stationary particles by particle - wall conduction and particle - wall radiation in every thermal step, as discussed in Chapter 5.1.4 and 5.2. The solar irradiation does not reach the wall due to the opaque particle film. In order to model the conduction heat transfer inside the wall and the insulation layer, a 3D Finite Difference Code (FDC) is developed in MATLAB. Trapezoid prism-shaped cells are employed in the discretization of the hollow cylinder-like domain, seen in Figure 5-43. In the finite difference code, the temperature information is stored in cell centers. By definition, a cell exchanges heat with 6 neighboring cells which it shares a common surface with. The energy balance formula can be written as in Eq. (5-46). The cell edge size in tangential direction, $\left(\mathrm{r}_i + \frac{\mathrm{dr}}{2}\right)\mathrm{d}\varphi$ or $\left(\mathrm{r}_i - \frac{\mathrm{dr}}{2}\right)\mathrm{d}\varphi$, changes with the radial position of cell center (r_i) due to the shape of the cells. k_w, ρ, C and T represent the wall (or insulation) thermal conductivity, wall density, wall specific heat capacity and wall temperature, respectively. The superscript “t” or “t + dt” corresponds to the current time step and the next time step while subscripts “i”, “j” and “k” correspond to the radial, tangential and axial position of a cell, respectively.

$$\rho_{i,j,k}C_{i,j,k}(r_i drdzd\varphi)\left[T_{i,j,k}^{t+dt} - T_{i,j,k}^{t}\right]$$
$$= \left(\left[\frac{k_w r_i drd\varphi}{dz}\right]\left[T_{i,j,k+1}^{t} + T_{i,j,k-1}^{t} - T_{i,j,k}^{t}\right]\right.$$
$$+ \left[\frac{k_w drdz}{r_i d\varphi}\right]\left[T_{i,j+1,k}^{t} + T_{i,j-1,k}^{t} - 2T_{i,j,k}^{t}\right] \qquad \textbf{(5-46)}$$
$$\left. + \left[\frac{k_w dzd\varphi}{dr}\right]\left[\left(r_i + \frac{dr}{2}\right)T_{i+1,j,k}^{t} + \left(r_i - \frac{dr}{2}\right)T_{i-1,j,k}^{t} - 2r_i T_{i,j,k}^{t}\right]\right) dt$$

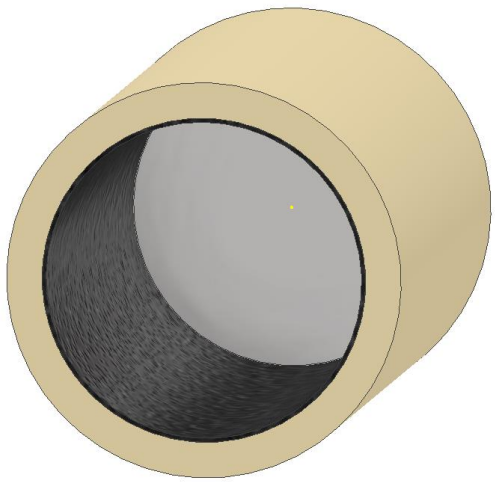

Figure 5-42 Schematic view of CentRec. The yellow outer shell is the insulation layer, and the black inner shell is the receiver wall.

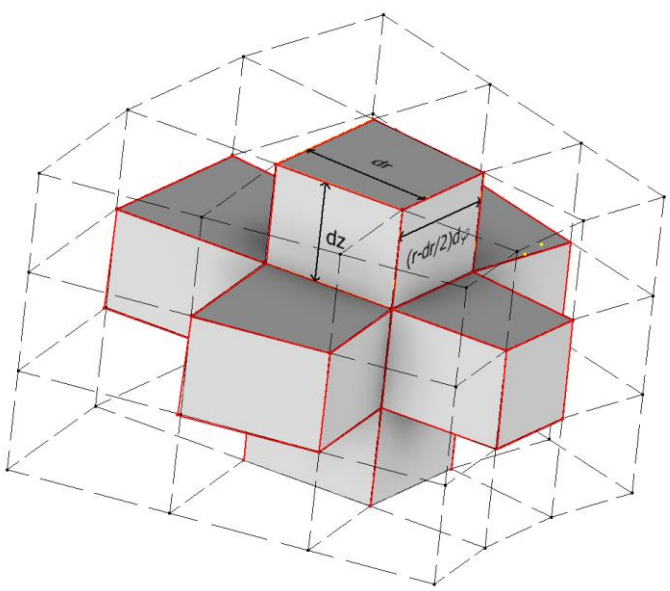

Figure 5-43 Trapezoid prism-shaped cells representing wall and insulation

For cells locating at the lower and upper axial boundaries, there is only heat exchange through five surfaces because the domain is insulated from bottom and top. For the radially innermost cells to which particles contact, there is heat input from particles. For those cells, Eq. (5-46) can be reformulated as follows.

$$\begin{aligned}\rho_{i,j,k}C_{i,j,k}(r_i drdzd\varphi)\left[T_{i,j,k}^{t+dt}-T_{i,j,k}^{t}\right] \\ =\Bigg(\left[\frac{k_w r_i drd\varphi}{dz}\right]\left[T_{i,j,k+1}^{t}+T_{i,j,k-1}^{t}-T_{i,j,k}^{t}\right] \\ +\left[\frac{k_w drdz}{r_i d\varphi}\right]\left[T_{i,j+1,k}^{t}+T_{i,j-1,k}^{t}-2T_{i,j,k}^{t}\right] \\ +\left[\frac{k_w dzd\varphi}{dr}\right]\left[\left(r_i+\frac{dr}{2}\right)\left(T_{i+1,j,k}^{t}-T_{i,j,k}^{t}\right)+q_{pw}^{cond}+q_{pw}^{short-rad}\right]\Bigg)dt\end{aligned} \tag{5-47}$$

Similarly, for radially outermost cells which lose heat to the environment by free convection, the energy balance is written as follows.

$$\begin{aligned}\rho_{i,j,k}C_{i,j,k}(r_i drdzd\varphi)\left[T_{i,j,k}^{t+dt}-T_{i,j,k}^{t}\right] \\ =\Bigg(\left[\frac{k_w r_i drd\varphi}{dz}\right]\left[T_{i,j,k+1}^{t}+T_{i,j,k-1}^{t}-T_{i,j,k}^{t}\right] \\ +\left[\frac{k_w drdz}{r_i d\varphi}\right]\left[T_{i,j+1,k}^{t}+T_{i,j-1,k}^{t}-2T_{i,j,k}^{t}\right] \\ +\left[\frac{k_w dzd\varphi}{dr}\right]\left[\left(r_i-\frac{dr}{2}\right)\left(T_{i-1,j,k}^{t}-T_{i,j,k}^{t}\right)\right] \\ +hdz\left(r_i+\frac{dr}{2}\right)d\varphi\left(T_{air}-T_{i,j,k}^{t}\right)\Bigg)dt\end{aligned} \tag{5-48}$$

In Eq. (5-47) and (5-48), q_{pw}^{cond}, $q_{pw}^{short-rad}$, h and T_{air} correspond to the particle – wall conduction, particle – wall radiation, heat transfer coefficient for natural convection and ambient air temperature, respectively. Stewart [137] derived an analytical correlation to model heat loss from the external surface of an inclined cylinder as a function of Rayleigh Number (Ra), the tilt angle, and the diameter and the length of the cylinder. The heat transfer coefficient for natural convection, h, is found by this model as a function of insulation surface temperature. Note that the receiver is assumed as non-rotating body in this model.

In time discretization of the energy balance equation, an explicit scheme is preferred because it promises less computational burden compared to the implicit scheme. However, for explicit schemes, numerical stability may be a concern. In other words, if the time step size exceeds some threshold value for a given cell size, there may be an unrealistic temperature distribution in the domain. This threshold value is quantified with the Courant number, being a combination of cell size, time step size and thermal diffusivity. It is found that the FDC time step size required for

the combination of the thermal diffusivity of steel (wall material) and mesh size is much higher than for the other heat transfer modes. Thus, much smaller time step size for FDC is used compared to the particle-scale heat transfer calculations. On the other hand, during normal operation, due to a low heat flux to the wall and the high wall thermal inertia, obtaining steady state (SS) temperature distribution within the wall may take an hour or more. To avoid excessive amount of DEM simulations, reaching thermal SS as quickly as possible in the wall is desired. In accordance with this purpose, two approaches can be proposed. The first is to reduce thermal inertia of the wall ($\rho_w C_w$) artificially and the second is to set a temperature distribution for the wall as an initial condition. However, it is not easy to predict the SS wall temperature distribution for the given flux condition and bulk flow, thus the wall thermal inertia is artificially decreased in this study. Note that the thermal conductivity of the wall and insulation does not change because the conductive heat loss is not a function of thermal inertia.

In order to distribute the particle-wall conduction and particle-wall radiation, the following approach is pursued. For each particle transferring heat to the wall by conduction or radiation, a line, being parallel to the aperture plane and passing through both cavity centerline and particle center is formed. The cell of which this line intersects with its surface absorbs the radiation and conduction from that particle. This procedure is repeated for all particle – wall pairs. A schematic view for particle – wall cell pairs is shown in Figure 5-44. Thus, net energy transfer to each innermost cell can be computed and used in the finite difference code via Eq. (5-47).

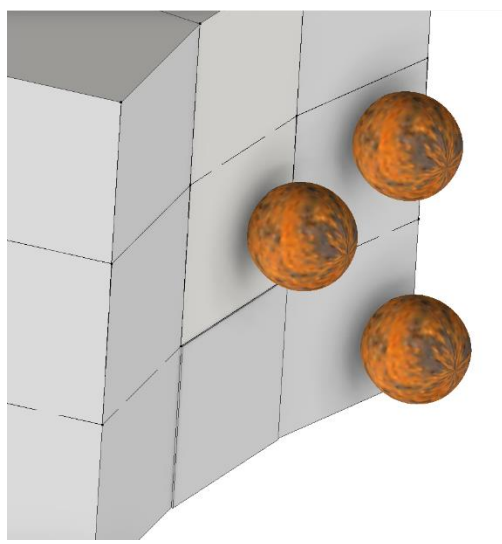

Figure 5-44 Interaction of particles with wall cells.

5.4 Convection from Cylindrical Cavities

In the CentRec application, there is an aperture on the base area of the rotating cylinder. The atmospheric air entering through the aperture circulates inside the cavity and leads to a convective heat loss during operation. The convection loss is one of the main factors affecting the receiver thermal efficiency along with the radiation losses. Although the complex convection

mechanism for a rotating particle receiver is not addressed within the scope of this study, it is implicitly considered by utilizing empirical correlations.

Most studies in the literature focused on experimental models, and various cavity sizes are investigated. In early 1980s, Clausing et al. [138-140] studied convective loss from cubical cavities with isothermal surface for various cavity configuration. An analytical Nusselt number (Nu) expression is also developed for the case of wind but the effect of wind direction was not accounted for. Lee et al. [141] investigated the effect of wind speed (0-12 m/s) and wind yaw angle (0 – 90°) on heat losses from a 15°-tilted cavity whose walls have uniform temperature. Wu et al. [142] also studied convective losses from a fully open, uniformly heated, cylindrical cavity, and measured the resulting temperature distribution inside the cavity for various wind speeds. In most cases, the temperature inside the cavity is not uniform for concentrating solar applications. Several studies focused on this aspect and found that the temperature distribution inside the cavity has non-negligible effect on cavity losses [143, 144]. Wu et al. [145] showed that the impact of aperture position in a partially-open cavity is closely related to tilt angle. Siegrist et al. [146] also considered the tower effect on convection losses because the air flow is disturbed by the tower structure in concentrating solar tower applications. Several CFD-based numerical models are also developed and validated with experimental results for specific conditions [147, 148]. Finally, Wu et al. [149] found that the rotation of the cavity has negligible effect on convective loss for no-wind condition. In all these studies, the effect of one factor or combination of several factors on convective loss are considered. The factors affecting the convective loss are namely cavity tilt angle and wind yaw angle, wind speed, the length and diameter of the cavity, the aperture diameter and temperature distribution inside the cavity. The tower structure and cavity rotation may also affect the convective loss. Finally, there is no study regarding convection loss from a rotating particle receiver according to the best of the author's knowledge. It should be noted that there is no general formula or approach to consider all these effects. Thus, some assumptions are to be made for the CentRec application. Firstly, the cavity rotation is neglected based on the results of Wu et al. [149]. Secondly, the effect of the tower and very complex particle – fluid interactions affecting convection is omitted due to lack of reported data. In CentRec, various temperature distributions may exist, depending on operational conditions and applied solar flux. There is no model accounting for such complex temperature distributions; thus, an average temperature is employed. Because the receiver is located at the top of the tower, the wind at such elevation cannot be neglected. Therefore, a model accounting for wind condition is preferred. The experiment results obtained by Flesch et al. [150] are employed in this study because they cover a broad range of tilt and yaw angles, and the results are scalable to the CentRec application. To adapt the experimental results to the cavity sizes considered in this study, the wind speed, cavity diameter and wall temperature are non-dimensionalized and represented as Reynolds number (Re), Grashof number (Gr) and dimensionless temperature spread (π), respectively.

Clausing [140] stated that there are two distinct zones, called as "stagnant" and "convective", in case there is only natural convection. Figure 5-45 shows these zones for a tilted receiver. The shape of the line separating zones may slightly change with the wind direction but in

this study, it is assumed as shown in Figure 5-45. Thus, the average temperature, $T_{wall\ av}$, is calculated by taking the arithmetic mean of temperatures of all surface meshes lying in the convective zone as described in Chapter 5.1.2. The Grashof number, accounting for natural convection, is defined as follows.

$$Gr = \frac{\beta_{ref}(T_{wall\ av} - T_{\mathrm{air}})gL_{cav}^3}{\nu_{ref}^2} \tag{5-49}$$

In this formula, β_{ref} and ν_{ref} denote the expansion coefficient and the gas kinematic viscosity at $T_{ref} = (T_{wall\ av} - T_{\mathrm{air}})/2$ while the ambient air temperature is denoted by T_∞. L_{cav} is the larger value of the diameter and the length of the cavity. The Reynolds number (Re) is defined as follows.

$$Re = \frac{u_{wind}d_{cav}}{\upsilon_{ref}} \tag{5-50}$$

The cavity diameter and wind velocity are denoted as d_{cav} and u_{wind}, respectively. To consider combined effects of wind and buoyancy, Richardson number is utilized.

$$Ri = \frac{Gr}{Re^2} \tag{5-51}$$

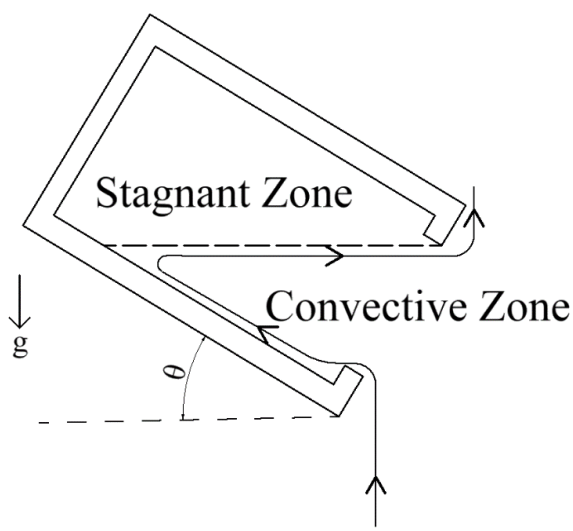

Figure 5-45 Representation of convective and stagnant zones for no-wind condition.

Richardson number is simply the ratio of buoyancy effect to flow shear effect. However, in the context of this study, it can be considered as the ratio of the effect of natural convection to the one of forced convection. In Figure 5-46, the Nusselt number is plotted against inverse Richardson

number for various tilt angles based on experimental results of Flesch et al. [150]. Note that Flesch et al. [150] found side-on wind as the most critical wind direction in terms of convection losses, thus this wind direction is preferred in this study. In Figure 5-46, due to complex interaction of wind and buoyancy effects, there is no obvious trend between 1/Ri and Nu. Thus, for intermediate values of 1/Ri, linear interpolation is employed between the two closest experimental measurements. To obtain the values for a tilt angle of 45°, being representative for this study, a spline interpolation is employed by using all tilt angles considered in the experiment. Then, the convection loss from the complete cavity can be calculated as follows.

$$Q_{conv} = \frac{NuA_{tot}(T_{wall\ av} - T_{\infty})k_{ref}}{d_{cav}} \tag{5-52}$$

In Eq. (5-52), A_{tot} and k_{ref} denote the total area of inner cavity and air thermal conductivity at reference temperature. Then, the found Q_{conv} is distributed to the surface meshes in the convective zone, based on the surface mesh area in the convective zone. To sum up, every thermal DEM time step the procedure below is followed step by step to calculate convective loss.

1. Calculate $T_{wall\ av}$ by considering the surface meshes in the convective zone
2. Calculate Gr, Re and inversed Ri by using Eqs. (5-49) - (5-51)
3. Determine Nu number for any inversed Ri from Figure 5-46. For all intermediate values, use linear interpolation of the closest two points.
4. Calculate Q_{conv} by using Eq. (5-52)
5. Distribute Q_{conv} to the surface meshes.
6. Distribute the convection loss for each mesh to topmost n particles forming the mesh surfaces. The number "n" is found by Eq. (4-5).

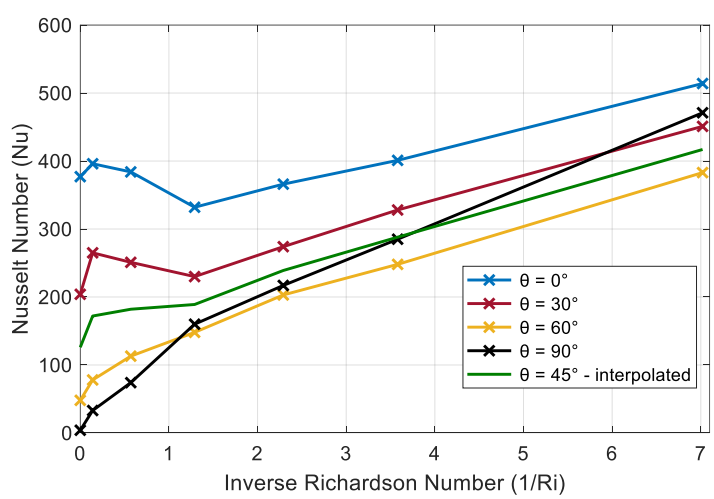

Figure 5-46 Experiment results obtained by Flesch et al. [150] along with interpolated results for tilt angle of 45°. Cross marks (x) correspond to experimental measurement points.

6. THERMAL MODEL APPLICATION TO CENTRIFUGAL SOLAR PARTICLE RECEIVER

The complete numerical thermal developed in Chapter 5 is applied to the CentRec receiver to determine its thermal characteristics under various operational conditions. Although all sub-models have already been tailored for the CentRec, the thermal time step coupling of the DEM model to the developed thermal model needs to be estimated for the relevant range of the operational parameters. In this study, particle positions are exported to *.txt files at each coupling time step in the DEM software. Later, they are used as input in the thermal model. Thus, time step size for coupling is important in terms of the file storage and the computational speed.

There are several input parameters provided by the user for the thermal model. In this study, although only SG 16/30 particles having mean Sauter diameter of 1.2 mm are considered, particle properties like particle emissivity and thermal conductivity are provided by the user. Thus, a sensitivity analysis is conducted for each input parameter to assess their importance on the receiver thermal efficiency or other relevant performance criteria. Finally, the thermal performance of the receiver is found for several receiver sizes and various operational parameters.

6.1 Thermal Coupling Time Step for the CentRec Application

A thermal coupling time step is needed to couple the thermal sub-models to DEM-generated particle positions such that in each time step particle temperatures can be calculated. The main sub-models are long-range and short-range radiation models, reflection model, radiation penetration model and particle-scale conduction model. The convection and conduction loss models are rather supplementary models to calculate the receiver thermal efficiency. The sub-models can be categorized into two groups, namely particle scale and bulk scale sub-models. The particle scale models are short-range radiation and particle scale conduction while the bulk scale models are long-range radiation and reflection models. Although the radiation penetration model also deals with particles individually, its calculation is closely related to the reflection model. Thus, the radiation penetration model is also considered as bulk-scale model. The main difference between particle and bulk scale models is the type of calculations required. In particle scale models, the heat exchange occurs between particles while in bulk scale models, the heat is exchanged between surfaces formed by particles. For example, for the particle scale models, the distances between particle pairs and particle – wall pairs need to be calculated. Similarly, for bulk scale models, temperatures of discrete surfaces need to be estimated. For this reason, coupling the models in each group together is meaningful for the ease of the computation. Thus, two thermal coupling time steps are found for particle scale and bulk scale models. For the convection loss model, the bulk scale thermal coupling time step is utilized because it also considers the surface temperature distribution as input. However, for the conduction loss model, the particle – scale thermal coupling time step is utilized because the heat transfer from the particles to the cylindrical wall by conduction and short-range radiation is found in each particle-scale thermal coupling time step.

Two separate cases are considered in the determination of thermal coupling time steps as shown in Table 6-1. For bulk scale models, the film thickness is not very important because heat exchange occurs between surfaces. Thus, rotational speed and mass flow rate, seen in Case I in Table 6-1, is arranged to obtain a relatively thin particle film (~4 d_p) to reduce the number of particles in the simulation. Later, a uniform heat flux with constant incidence angle is applied to the receiver after cold steady state conditions are achieved. The initial temperature of particles and particle inlet temperature are set to 673.15 K. Only the bulk-scale sub-models are considered for this case, and particle – scale models are deactivated. In the determination of coupling time steps for both cases, a reduced coupling time step in degree corresponding to rotation angle of the receiver is utilized. This reduced coupling time step is simply the ratio of the thermal coupling time step times 360° to the rotation period of receiver.

In the DEM model, particle positions are exported every 0.005 s of simulation time. It corresponds to 4.8° of rotation angle or reduced coupling time step for the rotation speed used in the Case I. In Figure 6-1, steady-state temperature distributions on the particle film surface for various reduced coupling time steps are shown. In the ideal case, where the coupling time step is infinitesimally small, an almost uniform temperature distribution in the tangential direction is expected because particle axial movement in one turn is much smaller than the receiver length. Up to the reduced coupling time step of 76.8°, the temperature gradients in the tangential direction are relatively small. However, for 153.7° and 307.4°, there are unrealistic hot spots near the exit. The location of hot spots periodically changes in tangential direction although the systems reach thermal steady state. It should be stated that the reduced coupling time step should not be an integer divisor of 360°; otherwise, the same parts of the particle film would be exposed to the flux unrealistically in every turn.

Table 6-1 Set of parameters used in the determination of thermal coupling time steps for bulk - scale models (Case I) and particle – scale models (Case II).

	Unit	Case I	Case II
Cavity Diameter	m	0.12	0.12
Cavity Length	m	0.17	0.17
Aperture Diameter	m	0.1	NA
Rotational Speed	rpm	160	167.8
Mass Flow Rate	g/s	35.7	73.4
Average Film Thickness	dp	4	7
Mean Flux at Aperture	MW/m^2	3	NA
Uniform Incidence Angle at Aperture	degree	45	NA
Initial Particle Temperature	K	673.15	700 - 1300
Particle Inlet Temperature	K	673.15	700 - 1300

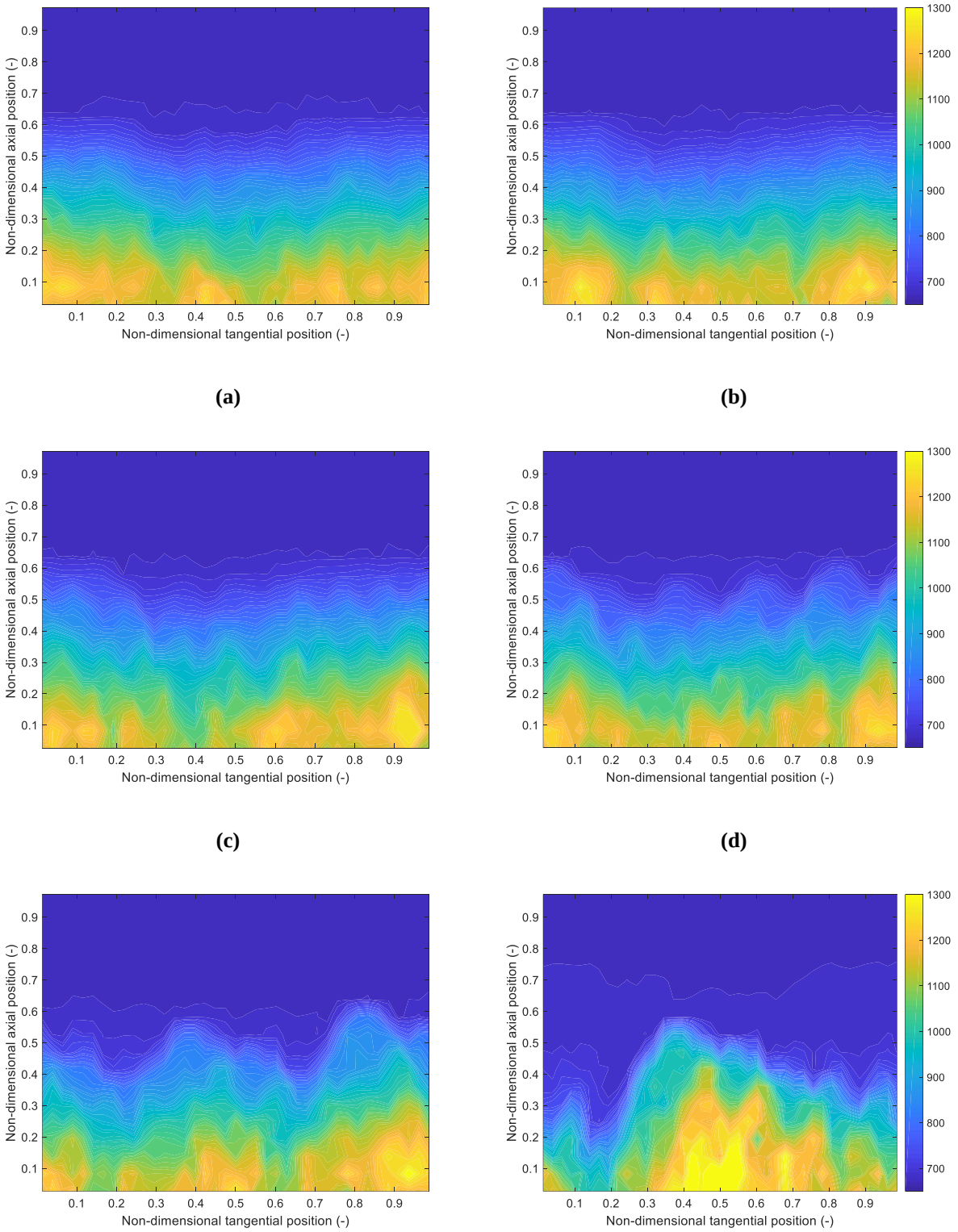

Figure 6-1 Steady-state temperature distribution on particle film surface for Case I given in Table 6-1 and long-range reduced coupling time step of **(a)** 9.6° **(b)** 19.2° **(c)** 38.4° **(d)** 76.8° **(e)** 153.7° **(f)** 307.4°. The color bar is the temperature with unit of Kelvin.

In Figure 6-2(a), the radiation loss through the aperture is compared for several reduced coupling time steps. There is slightly higher emission loss for 307.4° because of the apparent hot spot on the film. Note that the reflection loss is independent of temperature distribution; thus, it is the same for all cases. The particle outlet temperature variation for various reduced coupling time steps is shown in Figure 6-2(b). As the time step increases, the outlet temperature slightly increases. Note that the reason why the outlet temperature is higher for a larger time step although the radiation loss is also higher for that time step is that the convection loss is the lowest for that time step because of lower average surface temperature. The difference between 76.8° and 38.4° is generally very small in terms of the particle outlet temperature. Hence, in the light of qualitative and quantitative results shown in Figure 6-1 and Figure 6-2, the reduced coupling time step of 76.8° is selected for coupling of bulk scale models. Depending on rotation period and DEM file output interval, this time step may change between 75° - 80°.

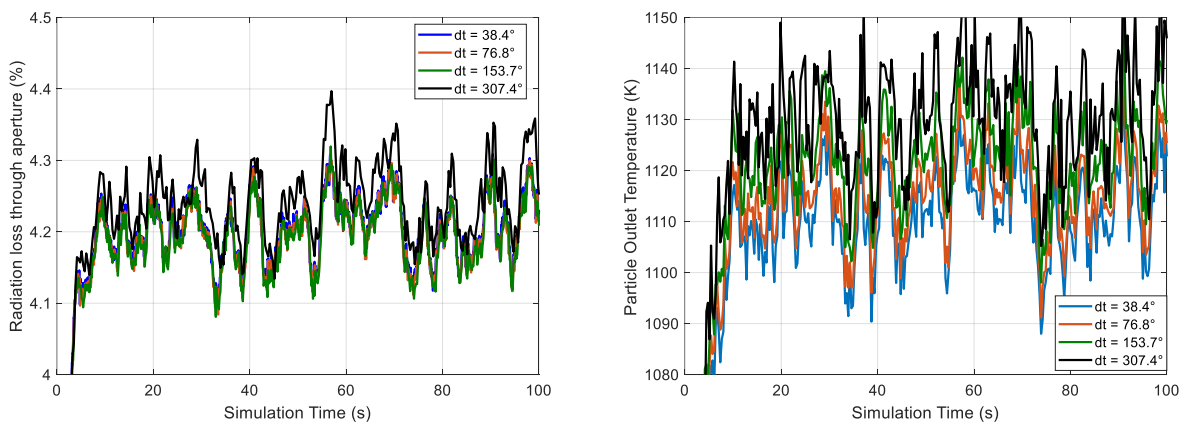

(a) **(b)**

Figure 6-2 Comparison of various bulk - scale reduced coupling time steps in terms of **(a)** radiation loss through aperture and **(b)** particle outlet temperature for the Case I given in Table 6-1.

To determine the coupling time step for particle-scale models, a relatively thick film (~7 d_p) is considered as shown in Case II in Table 6-1. However, in this case, there is no applied flux on the film. Instead, a linear temperature profile is patched as an initial temperature distribution such that particles' temperature increases from 700 K to 1300 K in radial direction from the wall up to the distance of 5 d_p, as shown in Figure 6-3(a). The particle-scale models are more important in inner parts of the film because the first two layers, each having a thickness of d_p, are heated directly by the solar irradiation while inner layers are heated by conduction and short-range radiation. After initial temperature patching, the simulation starts and particles are let to move. The linear temperature profile is also applied as boundary condition for the particles entering the domain. Constant temperature boundary condition is applied for the particles touching the wall so that the heat is lost through the stationary particles next to the wall. Thus, as particles move in axial direction, they mix in radial direction and lose heat from the stationary particles by conduction and short-range radiation. Note that the axially 20% top portion and axially 20% bottom portion of the

film near the inlet and exit is not considered here to avoid the changes in the film thickness in those regions.

In Figure 6-3(a), the radial temperature distribution is plotted for two reduced coupling time step cases and “only mixing” case. Firstly, it must be stated that even the largest time step, being close to the rotation period, gives a very similar temperature distribution at the exit compared to smaller time steps. The smaller time steps are not plotted for the sake of legibility of the figure. Moreover, the heat flow to stationary particles is quite similar for both cases (not plotted here for brevity). The results show that although the conduction and short-range radiation heat transfer may vary locally due to continuously changing particle-particle distances for various reduced coupling time steps, the resulting effective thermal conductivity enhancement in radial direction due to these heat transfer modes is independent of coupling time step up to 1 rotation period. Moreover, the temperature span at the outlet is also compared for two reduced coupling time steps in Figure 6-3(b). The mean outlet temperatures and their standard deviation is also very similar for the considered time steps. Thus, a reduced coupling time step of 307.4° is selected for particle-scale sub-models.

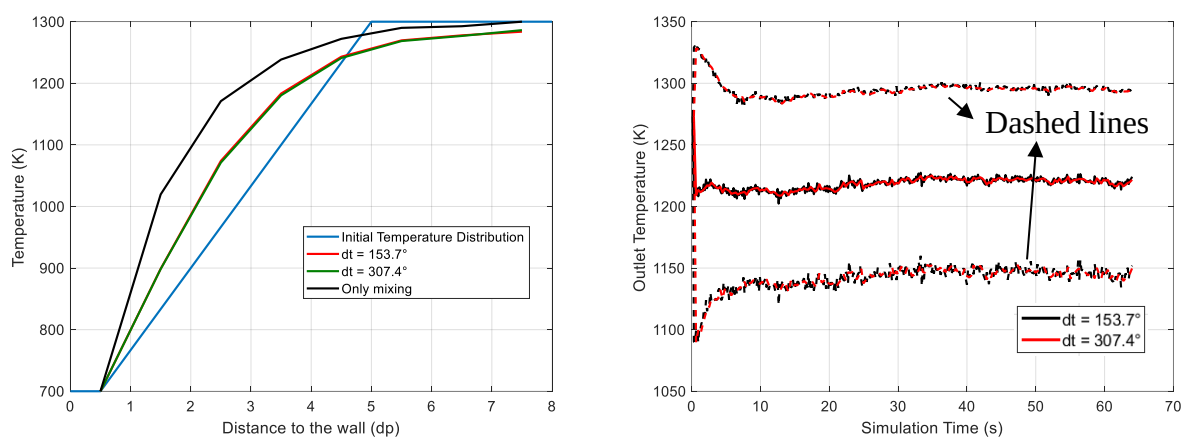

(a) **(b)**

Figure 6-3 (a) Radial temperature distribution at the exit **(b)** outlet temperature at the exit for two different reduced coupling time steps for particle - scale sub-models. Dashed lines are the mean value +/- standard deviation.

In Figure 6-3(a), the temperature distribution at the outlet is also compared for the cases that particle scale heat transfer models are off. Note that there is no heat loss for “only mixing case” because heat is only transported by particle movement for that case. A more detailed discussion about the effect of mixing and particle scale heat transfer models on effective thermal conductivity of moving bulk can be found in Chapter 6.2.1.

Finally, the time step size for the finite difference code, being responsible for the heat transfer within the cylindrical cavity wall and insulation may be discussed. The heat input to wall is at every particle scale coupling time step but this time step is quite large for the numerical stability of the finite difference code. To eliminate this problem, the time step for finite difference

code is reduced to one thousandth of the coupling time step for the particle-scale models. This does not create any sigificant computational burden but numerical stability can be easily achieved by trial and error, and can be monitored during the simulation.

6.2 Model Application

The thermal model developed in Chapter 5 is applied to CentRec for various sizes and various combination of the rotational speed and the particle mass flow rate. As mentioned in Chapter 4.1, the thermal model cannot be applied to the experiment size receiver due to limited computational availability for high-particle-number DEM simulations. Thus, scaled-down receivers are utilized in the application of the thermal model in this study.

Particle thermal properties are to be determined for the thermal model application. Firstly, the specific heat capacity of the particles is modelled as temperature-dependent. Siegel [151] provided the measurement data for bauxite particles and Wu [17] fitted the data to 4th order polynomial as shown in Eq.(6-1), where T and c_p are in °C and J/kgK. For the sake of simplicity, for the temperatures being lower than 25 °C and higher than 1000 °C, the heat capacity is assumed to be equal to lower and upper bound of the defined range, respectively.

$$c_p(T) = -2.583 * 10^{-9}T^4 + 7.059 * 10^{-6}T^3 - 5.795 * 10^{-3}T^2 + 2.439T + 677 \quad \textbf{(6-1)}$$

$$25℃ \leq T \leq 1000℃$$

The material thermal conductivity of the bauxite particles are also modelled as temperature dependent, and the data provided by Chung et al. [134] is utilized as discussed in Chapter 5.2.4. Siegel [151] also measured the solar weighted absorptivity and thermal emissivity of packed beds of several type bauxite particles at 700 °C. The measurements show that the absorptivity and emissivity are in the range of 0.89-0.93 and 0.75-86, respectively. An average value of 0.86 is assumed for both emissivity and absorptivity as suggested by Grobbel [60] because particles are assumed diffuse and gray as discussed in Chapter 5.1. The wall emissivity for all metallic surfaces being oxidized is assumed as 0.4. Unless otherwise specified, the set of these parameters are used in parametric simulations.

In the modelling of the solar flux to the particle film surface, a realistic flux density distribution generated by the ray tracing tool SPRAY for a demonstration power plant in Foggia, Italy is used [152]. As seen in Figure 6-4, the flux distribution has two peak zones near the exit of the receiver. It should be noted that the heliostat configuration optimized for this CSP plant yields that 7.7% of the incident power strikes the back wall, or particle distributor in this study. Thus, 92.3% of the incident power strikes the particle film. Although the flux is also not uniform on the backwall, it is modelled as uniform due to uniform temperature assumption for the backwall as discussed in Chapter 5.1.2. Although the flux density can be integrated to the model, the reflection

and radiation penetration models need incidence angle information as an input. To realistically model the incidence angle, rays are modelled such that they penetrate the receiver cavity at the center of the aperture. Thus, the incidence angle is calculated by drawing a line between the hit point on the film surface and the aperture center. To match the given flux density distribution, the power density of each generated ray can be adjusted. In other words, rays can be generated from a single point (aperture center) in all hemispherical directions and with various power densities to match the given flux density distribution. In Figure 6-4, the mean flux density at the aperture plate is 3 MW/m² for cavity diameter to aperture diameter ratio of 1.42 and cavity length to cavity diameter ratio of 1.42. The mean flux density at the aperture is calculated so that the temperature increase between particle temperatures at the inlet and exit is 600 °C.

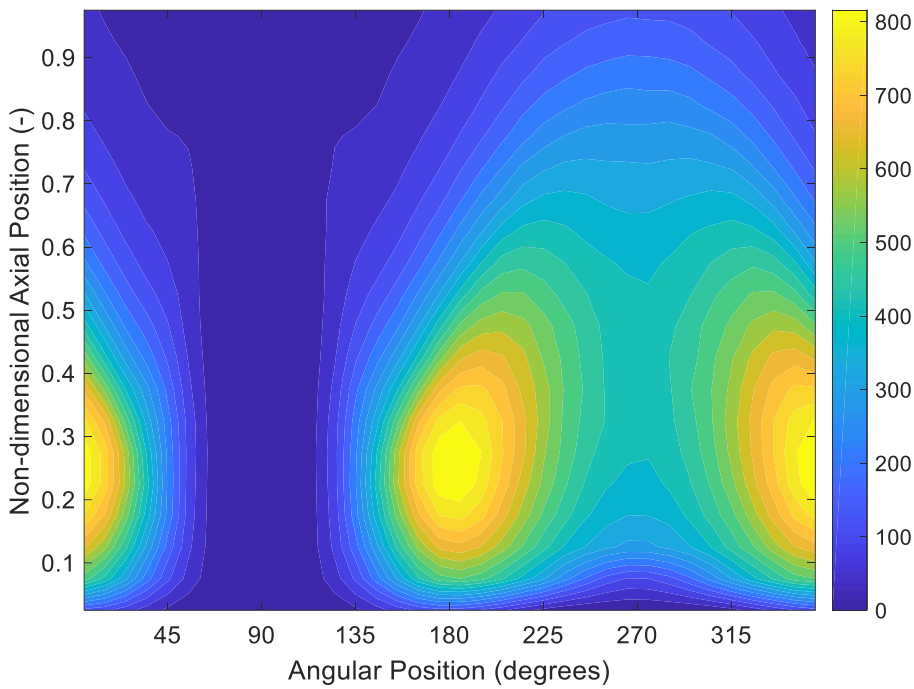

Figure 6-4 A realistic flux distribution on the particle film provided by [152]. The color bar unit is kW/m^2. The mean heat flux on the aperture is 3 MW/m^2.

6.2.1 Effect of Rotational Speed and Particle Mass Flow Rate

The thermal model is applied to the receiver with the cavity diameter of 12 cm to check the effect of the rotational speed and particle mass flow rate on receiver thermal efficiency and thermal losses. In Table 6-2, the set of parameters for the experiment scale and corresponding scaled-down simulation scale is listed. Simulation parameters corresponding to a scaled-down receiver are found by applying the scaling laws described in Chapter 4.1. Because the experiment scale receiver was built up for an indoor cold test campaign, no parameters related to the thermal model were assigned. In the parametric study, the combination of 4 different mass flow rates and 4 different rotational

speeds, in total 16 cases, are considered. The mean flux at the aperture for each mass flow rate is found as follows.

$$q^{||} = \frac{4\dot{m}c_p(T_{outlet} - T_{inlet})}{\eta_{th}{d_{ap}}^2\pi} \tag{6-2}$$

The particle inlet temperature is set to 400°C. The outlet temperature is selected as 900°C, and the thermal efficiency is assumed as 90% in Eq. (6-2) for the calculation of the mean flux at the aperture. However, in parametric cases, the thermal efficiency is not constant and may vary depending on losses. This leads to deviating outlet temperatures in the simulations. It should be noted that the incident power is not a function of the rotational speed.

Table 6-2 The set of parameters considered in the simulation of scaled-down CentRec.

		Simulation Scale	Experiment Scale
Cavity Diameter	m	0.12	0.8
Cavity Length	m	0.17	1.13
Cavity to Aperture Diameter Ratio	m	1.42	(no aperture)
Rotational Speed	rpm	160.1, 162.7, 165.3, 167.8	62, 63, 64, 65
Mass Flow Rate	g/s	13.8, 35.7, 46.8, 73.4	92, 238, 312, 489
Mean Flux at Aperture	MW/m^2	1.62, 4.21, 5.52, 8.65	-
Particle Inlet Temperature	K	673.15	-

In Figure 6-5, the thermal efficiency and thermal losses are plotted for 16 different cases. In all cases, the most dominant loss mechanism is the loss by free convection, as seen in Figure 6-5(b). Especially, for the lowest mass flow rate, the convection loss percentage reaches 30%. The reason of such big loss is that the incident power linearly increases with the mass flow rate while convective loss in unit of Watt increases from the mass flow rate of 13.8 g/s to 73.4 m/s is only 29%. Thus, the ratio of convection loss to incident power increases with decreasing incident power and decreasing mass flow rate.

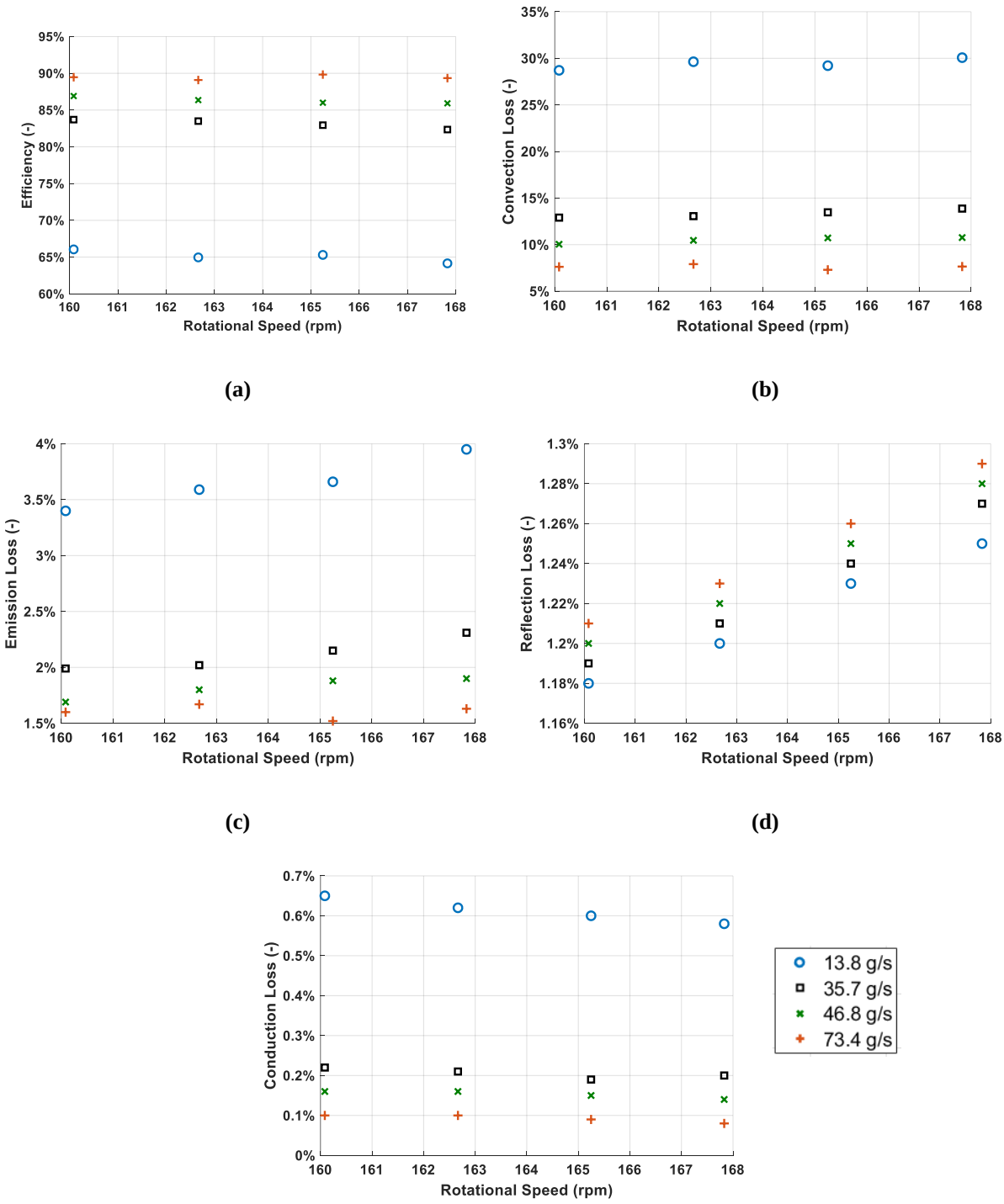

Figure 6-5 Thermal efficiency and loss percentages for cases considered in Table 6-2.

Physically, the particles located radially in deeper location of the particle film do not lose energy by convection. This effect especially results in less convective loss percentage for larger mass flow rates yielding larger film thickness. Thus, as the particle film is getting thicker, less

percentage of the particles is exposed to the convection loss in any time during operation. Note that it is assumed that only particles located at the film surface lose energy by convection as explained in Chapter 5.4. On the other hand, the rotational speed seems to have a smaller effect on the convective loss. Although the residence time of the particles on the film surface slightly increases with the rotational speed, as can be deducted from Figure 4-14, and particles get more exposed to the solar irradiation as rotational speed increases, the change in the film surface temperature is relatively small. In Figure 6-6, temperature maps of 4 cases being the combination of two rotational speeds and two mass flow rates are plotted at steady state. Note that the film thickness is not constant in the axial direction for high rotational speeds and decreases as approaching the exit, as seen in Figure 6-6(a) and (b). If one compares the Figure 6-6(a) and (c) or Figure 6-6(b) and (d), it can be noticed that the temperature distribution on the particle film surface is quite similar so, the rotational speed has a minor effect on the convective loss. Moreover, due to the increased film thickness with increasing rotational speed, the effective diameter for the convection decreases slightly. Although it has an effect on a receiver with 12 cm, this effect is negligible in large receivers. Finally, the effect of the size of the receiver is discussed in Chapter 6.2.2.

Similar to the convection loss, emission loss from particle film surface also only depends on particle surface temperature but in this case, it is proportional to 4th order of this temperature. The emission loss is more sensitive to the rotational speed than the convection loss because increasing rotational speed slightly increases the surface temperature. Conversely, the reflection loss is not a function of the particle surface temperature. The only factor affecting the reflection loss is the particle film thickness because as the film gets thicker, more area of the collector ring is covered by particles. Thus, there is smaller radiation shield area resulting from a collector ring as the film gets thicker. This causes a very small increase in the reflection loss as the rotational speed and the mass flow rate increases. For larger receivers this effect will be negligible, however. Finally, the conduction loss percentage is plotted in Figure 6-5 (e). In the parametric study, the wall and insulation thicknesses are set 2 mm and 50 mm, respectively while the wall has a thermal conductivity of 20 W/mK, and insulation has 0.065 W/mK. As discussed in Chapter 5.3, the thermal inertia of the wall and insulation layer is decreased significantly in the model to reduce the transient time. As the mass flow rate increases, the film gets thicker and the heat conduction inside the moving film in the radial direction is reduced. This causes lower wall temperature and eventually less conduction loss through the outer area of the insulation. In a real application, higher conduction loss is expected because heat can also be conducted through heat bridges (mounting elements) and axial conduction to the particle distributor and other mechanical components.

The thermal efficiency is calculated by dividing net energy gain of the particles to the total incident energy in a time step. In Figure 6-5(a), the thermal efficiency is plotted for all considered cases. The thermal efficiency is higher for the higher mass flow rates if mass flow rate is proportional to flux density in the aperture. In general, increasing incident power increases the efficiency for the considered cases. However, it does not necessarily mean that the efficiency increases with increasing film thickness because although film thickness increases with increasing rotational speed, the efficiency does not change significantly.

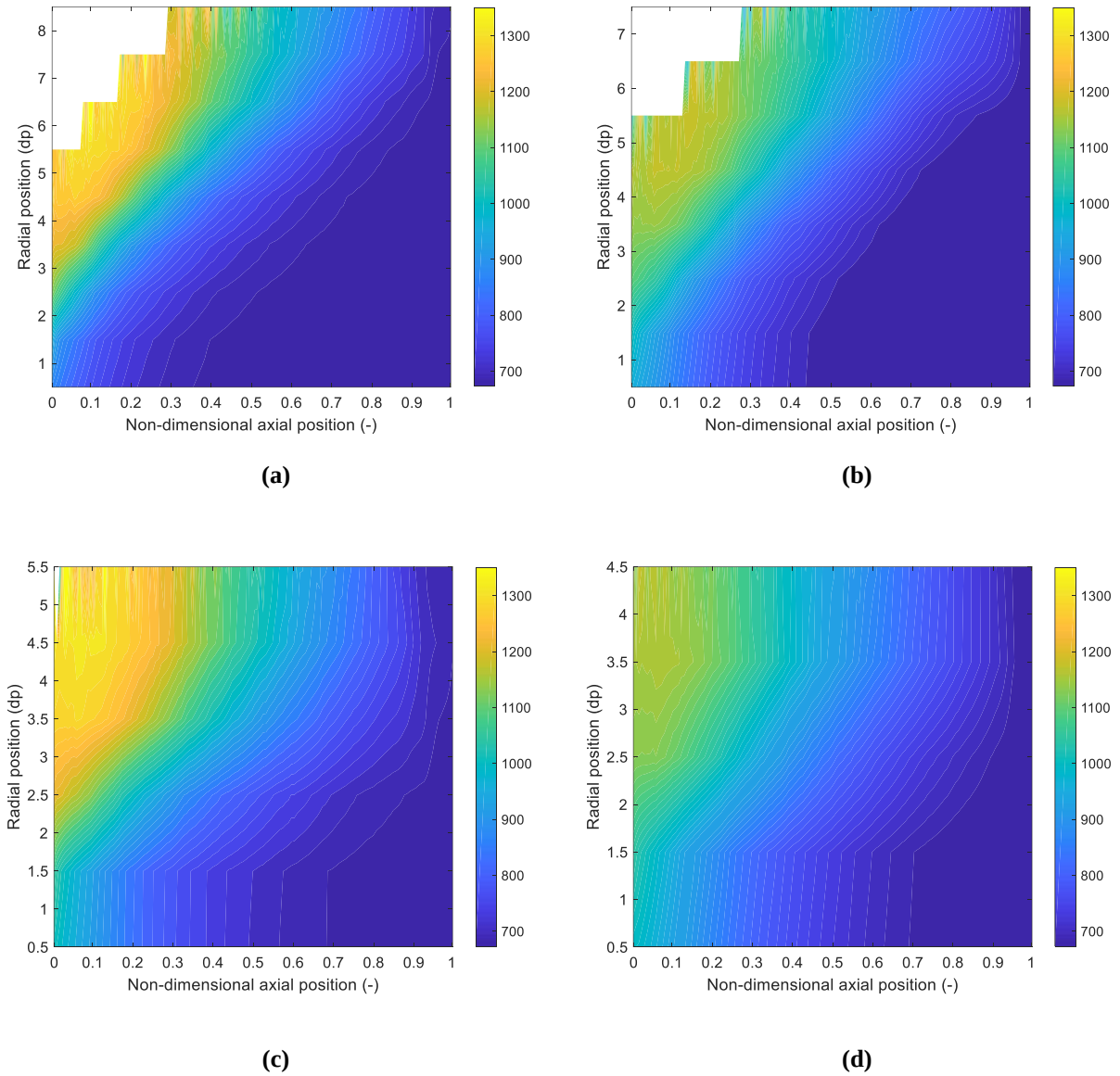

Figure 6-6 Tangentially and temporally averaged steady state temperature profiles **(a)** 167.8 rpm – 73.4 g/s **(b)** 167.8 rpm – 35.7 g/s **(c)** 160.1 rpm - 73.4 g/s **(d)** 160.1 rpm - 35.7 g/s. Non-dimensional axial positions of 0 and 1 corresponds to exit and inlet, respectively. The unit of color bar is Kelvin, and upper and lower limits are 673.15 K and 1350 K, respectively.

In on-sun operation, it is aimed to keep the mean outlet temperature constant for various flux conditions changing during the day. Thus, a more realistic approach is to try to optimize the mass flow rate for various flux conditions: however, this requires a series of iterative simulation, i.e. changing the mass flow rate until the outlet temperature converges to the design point for any given flux. For this reason, this approach is avoided in the scope of this study, and mass flow rates corresponding to cold experiment cases are only considered. For example, in Figure 6-5(a), the thermal efficiency of the lowest mass flow rate being 13.8 g/s is around 65% regardless of rotational speed. This corresponds to ~743°C of particle outlet temperature for 400°C particle inlet

temperature. In order to meet design point being 940°C of particle outlet temperature for a given flux condition, the mass flow rate should be decreased.

In Figure 6-6, steady-state temperature maps of four different cases are plotted. If one compares the Figure 6-6(a) and Figure 6-6(b) or Figure 6-6(c) and Figure 6-6(d), it can be noticed that doubling the mass flow rate slightly increases the film thickness. However, the surface temperature is ~150 K higher for high mass flow rates at the peak flux region in both comparisons. It can also be inferred that as the mass flow rate increases, larger temperature gradients occurs at the exit of the receiver although the average particle temperature is higher because the efficiency is higher for high mass flow rates.

The temperature map of the particle film is mainly affected by three mechanisms. The first one is the particle-scale heat transfer modes like particle-scale conduction and radiation. The second one is the particle mixing in the radial direction. Thanks to these two mechanisms, heat penetrates into the moving film in the radial direction, and the effective thermal conductivity of the moving film enhances. Lastly, thanks to the axial velocity profile in the radial direction, directly irradiated particles have less particle residence time while the particles being closer to the wall have more time to be heated although they are not directly irradiated. This effect also reduces the possibility of high temperature gradients in the radial direction. In order to investigate the effect of mixing on the thermal conductivity of the moving film, a uniform flux is applied to a section of the particle film such that rays are created along the centerline of the receiver, and always hit the particle film perpendicularly. A section of the particle film is taken from the axial middle of the receiver, with a width of half the receiver length. By doing so, the variation in the film thickness near the inlet and exit is eliminated. To simplify the simulation, the emission, reflection and convection loss mechanisms are deactivated, so there is only conduction loss through the wall to let the system reach steady-state. Figure 6-7 shows the temperature distribution in the section of the moving film for a relatively thin and thick particle film. Particle inlet temperature is set to 400°C. The incident power is calculated as 17.1 kW and 35.2 kW for cases (a) and (b) such that around 400°C temperature increase occurs. In the first scenario, both the mixing of particles and particle-scale heat transfer models are considered. However, in the second scenario, the heat transfer models are deactivated so that heat is only conducted in the radial direction by the mass transfer of the particles. Figure 6-7 shows that the mixing plays an important role to reduce the temperature gradients in radial direction. Although there is not a large difference between heat transfer enabled and disabled cases in the first three layers from the free surface in Figure 6-7(a), particle scale heat transfer models become more important in deeper layers of the particle film where mixing is not dominant. Note that the thickness of each layer is one particle diameter. It is interesting that the temperature of the topmost layer is slightly less than the second layer, but it is mainly due to the fact that the mixing in the first two layers is very strong, and both layers absorb the very large portion of irradiated solar rays, so the temperature of both layers is fluctuating in time slightly even in the steady-state. Secondly, one can notice that the first layer next to the wall for the “only mixing” case has a uniform and fixed temperature. This is because this layer consists of stagnant particles, so there is no heat loss through the wall for this case. Figure 6-7(b) also shows

a similar distribution but in this time for a thicker film. Again, up to the third last layer, the case with “heat transfer enabled” yields less temperature gradients in the radial direction. This result implies that the particle scale heat transfer become more important for large scale receivers because much thicker particle films are expected in those cases. Considering that the length of the axial section is just 8.5 cm for cases in Figure 6-7, much larger residence times may provide higher conduction and radiation heat transfer rates in radial direction for large scale receivers.

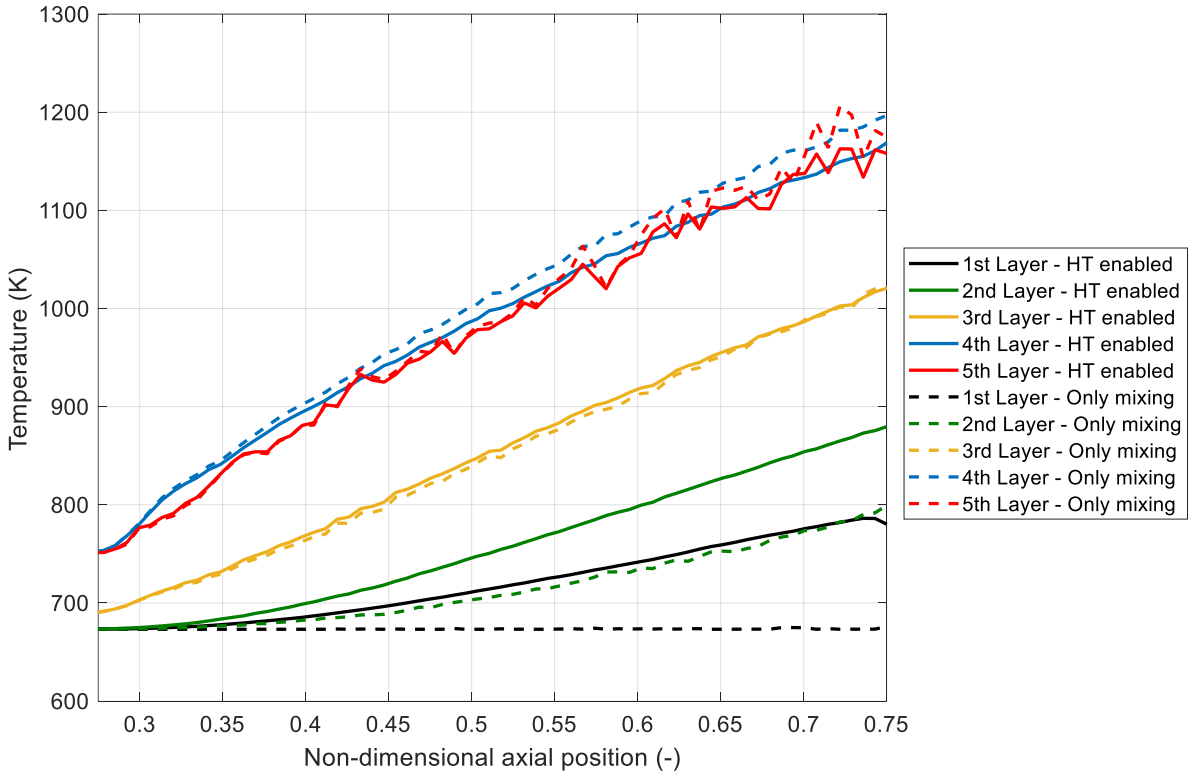

(a)

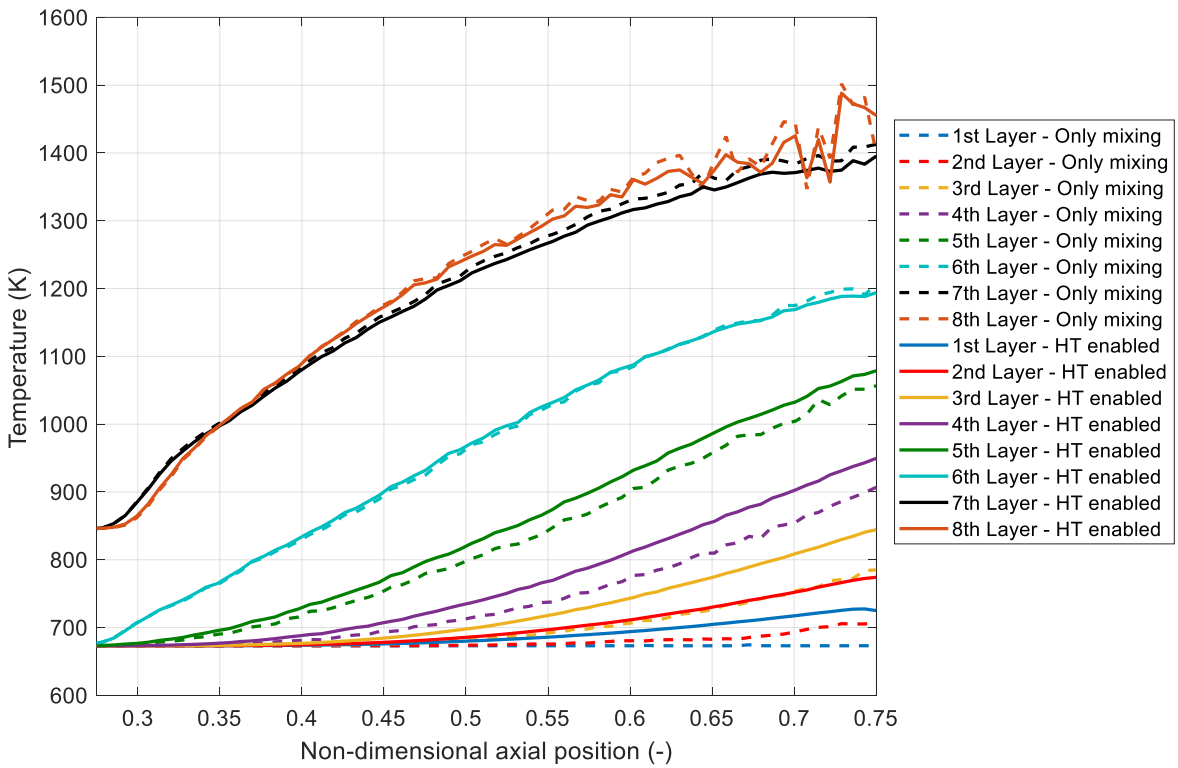

(b)

Figure 6-7 Temperature distribution on the particle film section exposed to the uniform flux for cases that particle scale conduction and radiation heat transfer are enabled and disabled in the simulation. **(a)** 160.1 rpm and 35.7 g/s **(b)** 167.8 rpm and 73.4 g/s.

In Figure 6-8, the particle outlet temperatures are plotted for the same cases considered in Figure 6-7. In both cases, enabling the heat transfer results in a reduction of 100 K of mean standard deviation. For the 8-d_p-thick film case, the standard deviation is around 200 K while for the 5-d_p-thick film case, it is around 100 K. This may be a sign of that as the film gets thicker, larger temperature gradients at the exit may occur. Finally, the mean outlet temperature for heat transfer disabled or "only mixing" case is slightly higher than in the enabled case because for the enabled case there is conduction heat loss through the stationary particle layer. Note that in these cases, the surface losses like convection and radiation loss are not modelled. In reality, due to these surface losses, the film temperature near the free surface is lower than in this ideal case. Thus, the standard deviation in the particle outlet temperature is also lower.

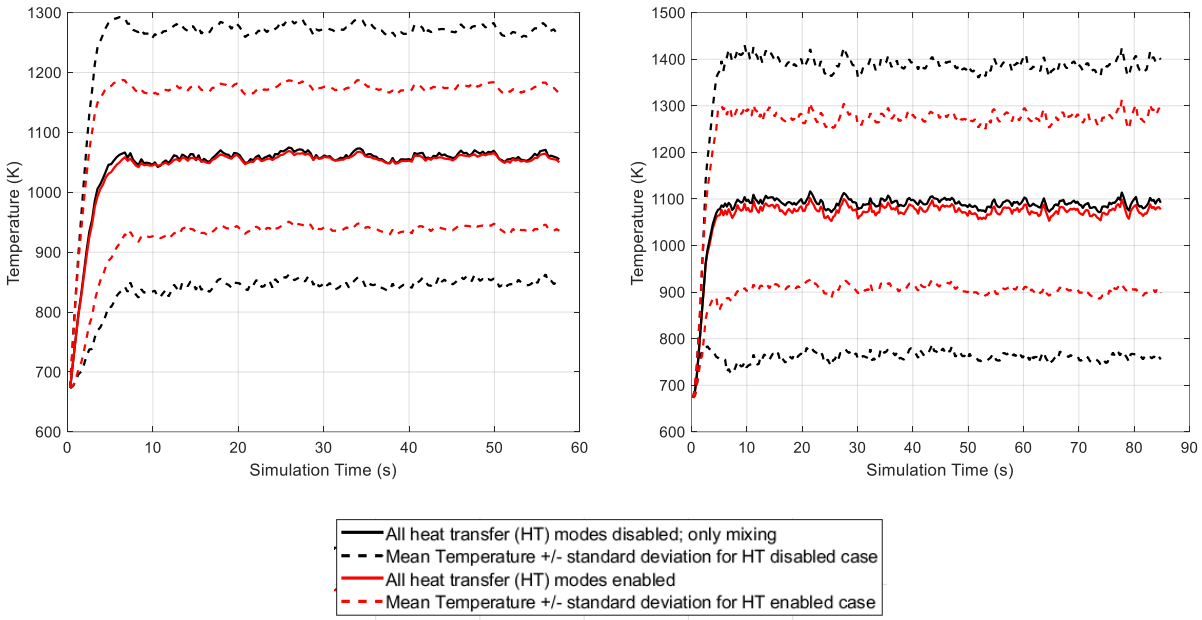

(a) **(b)**

Figure 6-8 Particle outlet temperature variation for the cases in Figure 6-7. Solid lines denote the mean outlet temperature while dashed lines denote +/- mean standard deviation of temperatures of particles at the exit. **(a)** 160.1 rpm and 35.7 g/s **(b)** 167.8 rpm and 73.4 g/s.

6.2.2 Effect of the Receiver Size

The DEM simulation of the demonstration scale receivers with more than ten-million particles for a sufficient time at steady state is currently not computationally feasible. However, one may still simulate a receiver having larger size than the one considered in the parametric study to have a general idea about the effect of the size on the thermal behavior. In Table 6-3, the size-related and operational parameters of three different receiver sizes are tabulated. In this part of the study, the uniform flux density at the aperture plane is kept constant for all receiver sizes because in real application, the flux density is a given input. Then, the mass flow rate is adjusted such that it is proportional to the square of the receiver aperture diameter because of the energy balance, which can also be calculated by Eq. (6-2). This yields increasing film thickness as receiver size increases. Note that the film thickness values shown in Table 6-3 are the summation of the stationary and moving part of the particle film. The number of particles in the simulation for the largest size is around 780,000. The simulation of 1 second of that many particles at steady state takes around 1 hour with Intel Xeon E5-2697v3 processors (14 cores). Finally, the insulation thickness is also adjusted such that the conduction thermal resistance is the same for all sizes.

In Table 6-3, the results about the thermal behavior of the three sizes are also tabulated. In this comparison study, no wind is considered. The convection loss percentage decreases with increasing receiver size if the flux density is the same and mass flow rate is proportional of the square of the aperture diameter for the no wind case. Although the particle film surface temperature slightly increases with increasing receiver size, the convection loss decreases with receiver size.

This is mainly due to that larger receivers have thicker films so that more energy can be absorbed by particles in deeper particle film thanks to particle mixing. However, if the flux density would be inversely proportional with the mass flow rate, the convective loss in percentage would be similar for all cases for the no wind case, as seen in Table 6-4. In Table 6-4, the film thickness is constant for all sizes and operational parameters are adjusted to obtain the same flow characteristics as described in Chapter 4.1.

Table 6-3 Simulation parameters considered for three different receiver sizes where the mass flow is proportional to the incident power.

		Case 1	**Case 2**	**Case 3**
Cavity Diameter	m	0.12	0.17	0.25
Cavity Length	m	0.17	0.24	0.355
Cavity to Aperture Diameter Ratio	m	1.2	1.2	1.2
Rotational Speed	rpm	160.08	134.5	110.91
Mass Flow Rate	g/s	25.2	50.57	109.38
Mean Flux at Aperture	MW/m²	2.5	2.5	2.5
Uniform Incidence Angle at Aperture	degree	45	45	45
Insulation Thickness	cm	5	7.1	10.4
Wind Speed	m/s	0	0	0
Number of Particles	-	~145,000	~315,000	~780,000
Film Thickness	dp	~3.4	~3.9	~4.25
Efficiency	-	80.66%	84.07%	87.00%
Convection Loss	-	14.33%	10.72%	7.62%
Emission Loss	-	2.59%	2.91%	3.19%
Reflection Loss	-	2.18%	2.12%	2.07%
Conduction Loss	-	0.24%	0.18%	0.12%
Particle Mean Outlet Temperature	K	1171	1191	1208

In Table 6-3, for a uniform incidence angle at the aperture, the reflection loss slightly decreases with the size. It is mainly due to the fact that the ratio of the effective cavity diameter to the aperture diameter slightly increases with size, as the film thickness does not scale with cavity diameter. Thus, the shielding of the collector ring increases with size, and more reflection is kept inside the receiver. It is considered that the reflection loss converges to some value as the receiver size increases. However, it should be noted that the incidence angle distribution affects the reflection loss considerably for any receiver size. On the other hand, the emission loss is mainly a function of the particle surface temperature. In Table 6-3, due to slight increase in the particle surface temperature as receiver size increases, the emission loss increases slightly. All in all, as receiver size increases, the convective loss decreases and emission loss increases if uniform flux is applied and the mass flow rate is proportional of the square of the receiver size. The difference in both convective and emission loss between 17-cm-diameter receiver and 25-cm-diameter is less than the ones between 12-cm-diameter receiver and 17-cm-diameter. This may mean that both

losses converge to some value for a certain combination of the flux density and the ratio of the mass flow rate to the square of the aperture diameter as the receiver size increases. This would mean that the receiver thermal efficiency converges to a value being below 1 for the same combination as the receiver size increases.

All in all, it must be stated that the convection loss is calculated based on a semi-empirical approach described in Chapter 5.4. In this approach, Nusselt number is independent of receiver size for no wind condition. However, if Nu changes with the receiver size, this has a non-negligible effect on the convective loss. In other words, an increasing Nu number with receiver diameter would result in a higher convection loss for a larger receiver, and the effect of receiver size on convective loss percentage would be less. The effect of wind on receiver thermal efficiency is not tabulated in this study because there is no consensus about the wind effect on cavity receivers in the literature, as discussed in Chapter 5.4. The wind effect is even more complicated due to existence of the particle film for CentRec. Thus, results are subject to combined effects of many aspects, and the results of semi-empirical model considered in this study might be misleading for the reader.

Table 6-4 Modified simulation parameters for the cases listed in Table 6-3. The mass flow rate and flux at aperture is inversely proportional.

	Unit	Case 4	Case 5	Case 6
Cavity Diameter	m	0.12	0.17	0.25
Cavity Length	m	0.171	0.243	0.35
Cavity to Aperture Diameter Ratio	m	1.2	1.2	1.2
Rotational Speed	rpm	160	134.5	111
Mass Flow Rate	g/s	35.7	50.57	74.4
Mean Flux at Aperture	MW/m^2	3	2.11	1.44
Thermal Efficiency	-	84.27%	83.61%	82.69%
Convection Loss	-	11.37%	11.35%	11.2%
Radiation Loss	-	4.16%	4.83%	5.90%
Particle Outlet Temperature	K	1122	1118	1112

6.3 Sensitivity Analysis

A sensitivity analysis is to be carried out to determine how the input parameters affect the losses and thermal efficiency. The parameters considered in the sensitivity study are namely particle absorptivity, material thermal conductivity and aperture ratio. In Table 6-5, a list of cases used in the sensitivity analysis is presented. For all cases, a uniform flux at the aperture with a constant incidence angle is applied.

Table 6-5 List of cases for various receiver dimensions and operational parameters considered in the sensitivity analysis.

	Unit	Case I	Case II	Case III	Case IV	Case V
Cavity Diameter	m	0.12	0.17	0.17	0.25	0.25
Cavity Length	m	0.171	0.243	0.243	0.350	0.350
Cavity to Aperture Diameter Ratio	m	1.2	1.2	1.42	1.2	1.42
Rotational Speed	rpm	167.8	134.50	134.50	111	111
Mass Flow Rate	g/s	73.4	50.57	50.57	74.4	74.4
Average Film Thickness	dp	7	4	4	4	4
Mean Flux at Aperture	MW/m^2	6.16	2.11	2.96	1.44	2.02
Uniform Incidence Angle at Aperture	Deg.	45	45	45	45	45
Initial Particle Temperature	K	673.15	673.15	673.15	673.15	673.15
Particle Inlet Temperature	K	673.15	673.15	673.15	673.15	673.15

6.3.1 Particle Absorptivity

In this study, particle absorptivity and emissivity are assumed to be the same due to the gray and diffuse particle surface assumption. As absorptivity of a particle increases, the bulk absorptivity of the particle film also increases, eventually this has a positive impact on receiver thermal efficiency. However, as particle absorptivity increases, its emissivity also increases, and there would be more emission loss. In Table 6-6, the thermal efficiency and losses are tabulated for three different particle absorptivities for Case I from Table 6-5. As expected, the reflection loss significantly decreases as particle absorptivity increases. The reflection loss is 2.56% for absorptivity of 0.86 while for the exactly same operational parameters yielding same particle configuration and particle properties, it is 1.29% in Figure 6-5(d). This is mainly due to a different incidence angle on the film. The larger incidence angles cause less reflection losses (See Figure 5-3(a) for the definition of incidence angle). Table 6-6 shows that there is a slight increase in the convection loss with increasing particle absorptivity because the temperatures on the particle film surface also slightly increase. On the other hand, the emission loss increases more prominently because of the combined effect of the increasing particle surface temperature and particle absorptivity. In general, the receiver efficiency and particle outlet temperature increase with the particle absorptivity.

The effect of increasing particle absorptivity on the temperature distribution in the particle film is also investigated. Figure 6-9 shows the temperature distribution in each layer for three different particle absorptivities. It is seen that the temperature of the inner particle layers is almost independent of the particle absorptivity for the considered flux distribution and the receiver size. Only the temperature of the three layers at the top of the film increases with the particle absorptivity because more energy is absorbed. Although the results seem contradictory with the fact that the radiation contributes around 45% to the bulk thermal conductivity at around 1000 K, as seen in Figure 5-41, in fact, increasing the absorptivity from 0.8 to 1 leads to a small increase in particle

to particle RDFs, as seen in Figure 6-10. For large scale receivers with a cavity diameter being larger than a meter, the residence time of particles will also be larger, and the net flux on the particle film is smaller to achieve the same temperature increase between inlet and outlet. For these receivers, the particle absorptivity has a larger effect to reduce the temperature gradients in the radial direction because of higher particle residence time. However, this effect is negligible for a small-scale receiver with the diameter of 12 cm.

Table 6-6 Simulation results for three particle absorptivities in terms of efficiency, losses and particle outlet temperature. Case I in Table 6-5 is considered.

Particle Absorptivity	**0.8**	**0.86**	**1**
Convective loss	6.53%	6.59%	6.76%
Reflection loss	3.72%	2.56%	0%
Emission loss	1.43%	1.49%	1.64%
Thermal efficiency	88.11%	89.16%	91.52%
Outlet Temperature (K)	1145	1150	1161

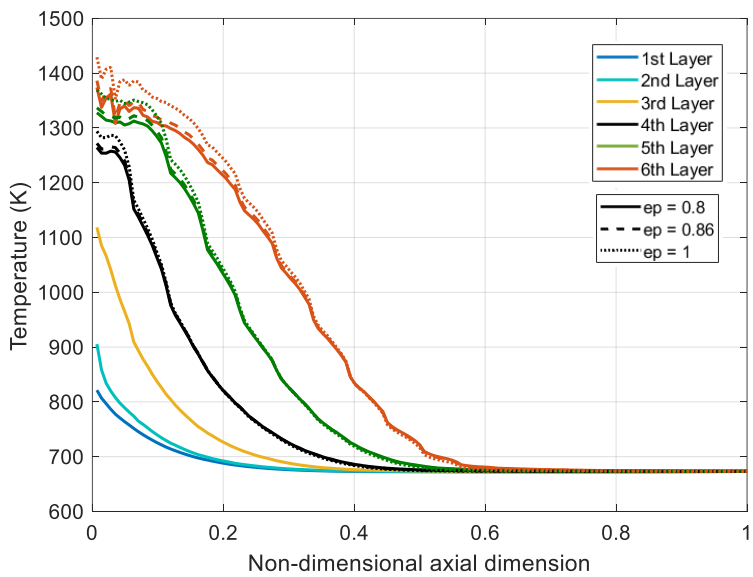

Figure 6-9 Temperature distribution of layers forming the particle film for Case I in Table 6-5 and for three particle emissivity/absorptivity values. The results for the first three layers are plotted only for absorptivity of one for the sake of legibility because lines overlap completely for the current resolution.

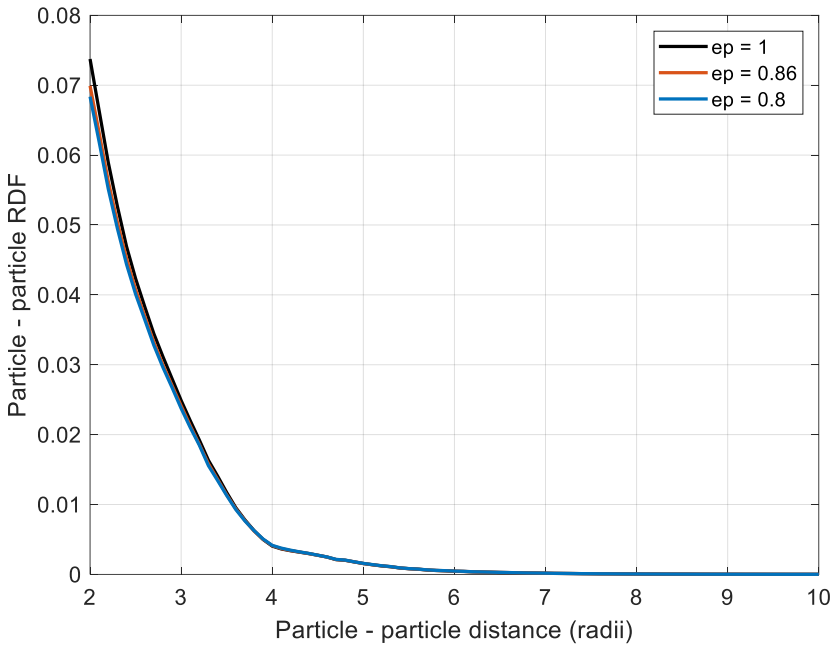

Figure 6-10 Effect of particle absorptivity on particle-particle RDF for average particle – wall distance of $3d_p$.

6.3.2 Material Thermal Conductivity

The material conductivity is an important parameter in static particle beds for the determination of static bulk thermal conductivity because the thermal resistance due to the conduction within the particle needs to be considered. However, in the CentRec application, it is assumed that the particle has a uniform temperature, as discussed in Chapter 5.2.3 because not only particles are small and conductive but also, they are rolling continuously. Material thermal conductivity is an important parameter for an uniform temperature assumption but if this assumption holds, further increasing material thermal conductivity does not improve the thermal efficiency of the receiver. This is mainly due to two reasons. The first is that by assuming uniform temperature, no thermal resistance within the particle is considered, i.e. infinite thermal conductivity for inner particle conduction. Second is that although the material conductivity is a factor affecting the particle-fluid-particle conduction, the thermal resistance due the gap filled by the interstitial fluid is much higher than the one due to the conduction in the particle, as can also be seen in Eq. (5-42). Thus, fluid thermal conductivity is the bottleneck, and further increasing the material thermal conductivity has a marginal effect on particle-fluid-particle conduction. Finally, the material thermal conductivity is strong function in the conduction through particle contact area, but the contact area is very small for spherical particle contacts, and conduction through the contact area is negligible. In Table 6-7, three material thermal conductivities are applied to the case I from Table 6-3. The particle temperatures at the receiver outlet for each particle layer are compared, and a negligibly small difference between cases is found. For this reason, using more conductive

particles is not addressed in the future study even for large scale receivers. However, for particles having smaller conductivities, the uniform temperature assumption has to be checked, as discussed in Chapter 5.2.3

Table 6-7 Effect of material thermal conductivity to the temperature of layers at the receiver outlet for Case I in Table 6-5.

		Material thermal conductivity (W/mK)		
		2	**~5**	**10**
Layer Number	**1**	828	829	830
	2	901	901	902
	3	1127	1127	1127
	4	1340	1340	1339
	5	1436	1436	1435

6.3.3 Aperture Ratio

The aperture ratio being the ratio of the cavity diameter to the aperture diameter is an important parameter to be optimized in CentRec application. The trade-off is that decreasing the aperture diameter reduces the convection and radiation losses while increasing the aperture diameter reduces spillage losses being the solar flux striking the front area of the receiver. The spillage loss is not modeled in this study because it is mainly due to the heliostat configuration. To investigate the effect of the aperture ratio on the receiver thermal efficiency, two different aperture ratios being 1.2 and 1.42 are considered for the 17-cm-diameter receiver. The mean flux at the aperture is adjusted so that the incident power is the same for both cases. Figure 6-11 shows the flux distribution on the particle film. As the aperture diameter decreases, the flux intensity increases.

Table 6-8 shows the effect of aperture ratio on thermal losses and efficiency for receivers with diameter of 17 cm and 25 cm. For both receiver sizes, increasing the aperture ratio slightly increases the efficiency. This is mainly due to the fact that as aperture diameter decreases, there is more shielding for the emission and reflection losses. Although convection loss slightly increases due to the increase in particle surface temperature, in real application, increasing aperture ratio causes less convective zone, as can be noticed in Figure 5-45, and this has a counterbalancing effect on the convection loss. However, the effect of aperture ratio is not considered in the convection loss model in this study.

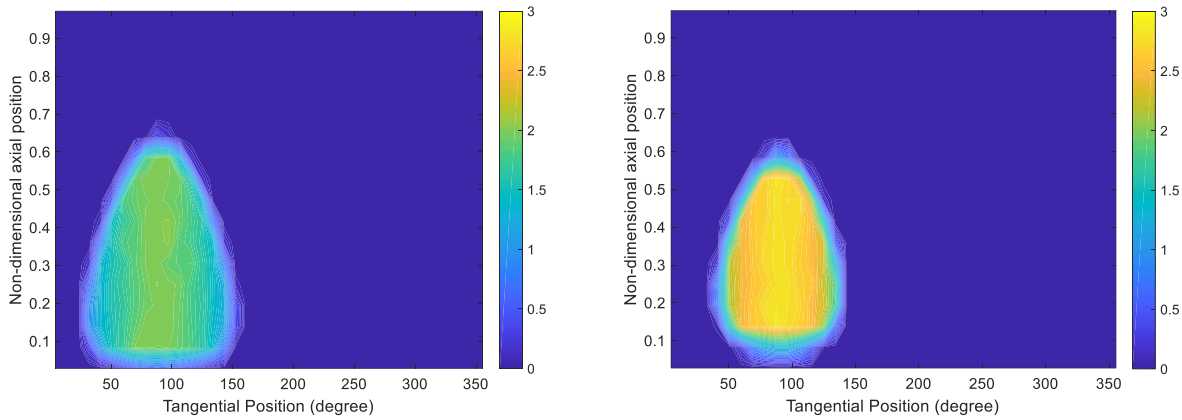

(a) **(b)**

Figure 6-11 Flux distribution on the particle film for cavity diameter of 17 cm. **(a)** Case II and **(b)** Case III in Table 6-5. The unit of the colorbar is MW/m2.

Table 6-8 The effect of aperture diameter to receiver efficiency, losses and particle outlet temperature for receiver diameters of 17 cm and 25 cm.

	Cavity to Aperture Diameter Ratio	Efficiency	Convection Loss	Radiation Loss	Particle Outlet Temperature
Case II	1.2	83.61%	11.35%	4.83%	1118 K
Case III	1.42	84.41%	11.78%	3.60%	1125 K
Case IV	1.2	82.69%	11.20%	5.90%	1112 K
Case V	1.42	83.75%	11.62%	4.43%	1121 K

7. CONCLUSION AND FUTURE WORK

The main objective of this work is to develop a computationally efficient DEM-compatible thermal model which can be applied to CentRec. Thus, a better understanding about the effect of the particle motion on the thermal performance of CentRec is achieved. In order to reach this goal, the PhD study is structured as described in Chapter 1.3. In the following paragraphs, the main conclusions are summarized.

An experimental apparatus including cameras and proper illuminations to measure the flow characteristics of the particle flow in CentRec is designed. Tracer recognition and tracking algorithms have been developed for particle receivers to measure the particles' velocity. The film thickness of the particle film is also measured for various combinations of operational parameters. The post-processing of recorded videos gives valuable information to be used in the validation of the current and further numerical models. On the other hand, a cold DEM model covering the physics of the particle flow has been created by using the open source code LIGGGHTS.

A new approach to scale-down the particle flow in CentRec is developed for the model validation. There are more than 100 million particles in the experiment scale receiver so a scaling approach is a must for simulations. The new approach claims that by applying derived scaling laws, one can obtain the same velocity and film thickness distribution throughout the receiver. This would be very useful for modelling large scale receivers. With this approach, some particle contact properties, namely sliding friction coefficient and rolling resistance, being essential for DEM models are calibrated by using the CentRec experiment results directly. The film thickness found by the DEM model is in good agreement with the experimentally found one but there is up to 20% deviation in surface velocities. This might be an indication of non-uniform velocity profiles in tangential direction.

The main contribution of this study to the literature is certainly the numerical thermal model. Firstly, the costly ray tracing approaches for modeling solar irradiation and thermal radiation are replaced by much more computationally efficient and accurate sub-models. A new radiation penetration model based on local porosity, particle emissivity and incidence angle, is able to predict MCRT-based results very well. This new approach is applicable to all particle films flowing in bulk or near-wall region unless the film thickness is smaller than 3 d_p. Results show that for the particle absorptivity of 0.86, around 7 – 8% of the solar irradiation is reflected from the moving film for a uniform incidence angle of 45°. The first two layers of the particle film (2 d_p of total thickness) absorb around 80% of the solar irradiation for incidence angle of 15°, and 60% for incidence angle of 90°. For a realistic incidence angle distribution, first two-layer absorption is around 75%. Finally, the 3rd layer absorbs 12 – 32% of the solar irradiation depending on the incidence angle. These numbers show that for thicker films, particle mixing and particle scale heat transfer mechanisms play an important role to prevent high temperature gradients in the radial direction.

A new reflection model is also developed from scratch and validated. The results for a representative incidence angle distribution show that a large portion of the reflected rays are absorbed by the particle film at the second strike. The most important conclusion in this model is that the reflection from the particle film is heavily dependent on the incidence angle of the incoming rays. In other words, if the rays strike the film with smaller incidence angles, the possibility of reflection back to aperture is higher because they tend to be reflected back with the incidence angle they strike to the film. This might be an important concern in the further optimization of the heliostat field, i.e. heliostats reflecting the rays with smaller incidence angle causes more reflection loss. On the other hand, a diffuse emission model accounting for the long-range thermal radiation gives accurate results for high particle absorptivity values used for solar applications. Moreover, both reflection and long-range thermal radiation models are particle-number-independent, thus they can easily be implemented to other commercial or open-source tools regardless of particle size.

The models being available in the literature are basically used for the particle scale heat transfer sub-models, but they are tailored for the CentRec application. Firstly, a distance-based radiation model is employed to calculate the short-range radiation between near-by particles. It is found that the results derived for the bulk region are not directly applicable to the near-wall region, thus a new RDF set is derived as a function of particle – particle and particle - wall distance. Similarly, the conduction model is slightly modified to match with the experiment results. The particle scale conduction via fluid and radiation are found to be the most dominant heat transfer mechanisms, especially in the deep particle film where solar irradiation cannot propagate. The conduction via particle-particle contact is found to be negligibly small due to the spherical shape of the particles. Contrary to static packed beds, radiation is found more dominant than conduction via fluid in CentRec because the solid fraction is smaller compared to static packed beds. The conduction within the particles is also investigated, and it is concluded that the uniform temperature assumption is valid for small particles used in CentRec.

The conduction loss through wall and insulation is modelled by 3D FDC and the numerical stability for the code is achieved by adjusting thermal inertia and FDC time step. Thus, quicker convergence to thermal steady-state is achieved. The convection loss is also modelled with semi-empirical correlations based on average particle surface temperature. Although the convection loss model is rather simplistic and does not cover the complex particle – circulating air interface, it gives an insight about the effect of the receiver size on the convection loss.

The developed thermal model is applied to three different CentRec sizes. Firstly, it is found that if the receiver operates at full load, meaning that the incident power is enough to increase particle temperature by 600°C, there are large convection and radiation losses for thin films. However, as the film gets thicker thanks to increasing flow rate, due to effect of mixing and particle-scale heat transfer, the efficiency increases significantly. Increasing rotational speed increases the film thickness but it has marginal effect on the efficiency. All in all, the results are promising about that the flow rate and rotational speed can be adjusted according to changing solar flux during the daytime to optimize the particle outlet temperature.

The particle absorptivity has a strong effect on receiver thermal efficiency but particle thermal conductivity has almost no effect for bauxite particles. However, if a material with lower particle thermal conductivity is employed, the uniform temperature assumption has to be checked.

To sum up, besides the important research findings discussed above, an in-house thermal code has been developed to be used in further CentRec simulations. Although a lot of effort has been put into CentRec technology, there is still a lot of room for improvement to further increase TRL of the technology. One of the main research lines which can be pointed out as future study is to exploit the thesis findings for the thermal modelling of the large-scale receivers. Although a scaling approach for cold particle flow is developed in this study, the thermal model is not easily scalable. Several attempts have been made to also scale-down the thermal model by scaling mean flux on the particle film, but the increasing particle residence time with increasing receiver size have not been successfully scaled by the author because the combined effects of many aspects is not trivial. As a next step, the effective bulk thermal conductivity of the particle film as a function of operational parameters and distance to the wall will be investigated. Thus, a thermal conductivity formula will be applied to more complete FEM-based thermal model as a UDF without running DEM simulations each time.

REFERENCES

[1] IEA, "Net zero by 2050 : A roadmap for the global energy sector," 2021.

[2] NREL. Concentrating Solar Power Projects Operational [Online] Available: https://solarpaces.nrel.gov/

[3] IRENA, "Renewable Capacity Statistics 2022," 2022.

[4] SolarPACES. CSP Projects Around the World [Online] Available: https://www.solarpaces.org/csp-technologies/csp-projects-around-the-world/

[5] IEA-ETSAP and IRENA, "Solar Heat for Industrial Processes - Technology Brief," 2015.

[6] AEE-INTEC. Solar Thermal Plants Database [Online] Available: http://ship-plants.info/solar-thermal-plants

[7] C. K. Ho and J. W. McNamara, "The value of long-duration energy storage: Policy and perception," 2021.

[8] R. Sioshansi and P. Denholm, "The value of concentrating solar power and thermal energy storage," *IEEE Transactions on Sustainable Energy*, vol. 1, no. 3, pp. 173-183, 2010, doi: 10.1109/TSTE.2010.2052078.

[9] IRENA, "Innovation Outlook Thermal Energy Storage," 2020.

[10] P. Denholm, Y.-H. Wan, M. Hummon, and M. Mehos, "The value of CSP with thermal energy storage in the western United States," *Energy Procedia*, vol. 49, pp. 1622-1631, 2013, doi: https://doi.org/10.1016/j.egypro.2014.03.171.

[11] P. K. Falcone, "Technical review of the solid particle receiver program " Sandia National Laboratories, Albuquerque , New Mexico, 1984.

[12] J. M. Hruby and B. R. Steele, "A solid particle central receiver for solar energy," *Chem. Eng. Prog*, vol. 82, no. 2, 1986.

[13] C. K. Ho, "A review of high-temperature particle receivers for concentrating solar power," *Applied Thermal Engineering*, vol. 109, pp. 958-969, 2016, doi: http://dx.doi.org/10.1016/j.applthermaleng.2016.04.1031359-4311/Ó2016

[14] Z. Ma, M. Mehos, G. Glatzmaier, and B. B. Sakadjian, "Development of a concentrating solar power system using fluidizedbed technology for thermal energy conversion and solid particles for thermal energy storage," *Energy Procedia* vol. 69, pp. 1349-1359, 2014, doi: https://doi.org/10.1016/j.egypro.2015.03.136.

[15] B. H. Mills, C. K. Ho, N. R. Schroeder, R. Shaeffer, H. F. Laubscher, and K. J. Albrecht, "Design evaluation of a next-generation high-temperature particle receiver for concentrating solar thermal applications," *Energies* vol. 15, no. 1657, 2022, doi: https://doi.org/10.3390/en15051657.

[16] T. Lee *et al.*, "Numerical simulation of particulate flow in interconnected porous media for central particle-heating receiver applications," *Solar Energy* vol. 113, pp. 14-24, 2015, doi: https://doi.org/10.1016/j.solener.2014.12.017.

[17] W. Wu, "A centrifugal particle receiver for high-temperature solar applications," Ph.D. Thesis, RWTH Aachen University, Aachen, Germany, 2014.

[18] C. Tregambi, M. Troiano, F. Montagnaro, R. Solimene, and P. Salatino, "Fluidized beds for concentrated solar thermal technologies—A review," *Frontiers in Energy Research*, vol. 9, no. 618421, 2021, doi: https://doi.org/10.3389/fenrg.2021.618421.

[19] S. Niederwestberg, F. Schneider, C. Boura, and U. Herrmann, "Introduction to a direct irradiated transparent tube particle receiver," in *SolarPACES*, Virtual, Online, September 28 - October 2 2020, vol. 2445, no. 110007: AIP Conference Proceedings, doi: https://doi.org/10.1063/5.0086735.

[20] K. Jiang, X. Du, Y. Kong, C. Xu, and X. Ju, "A comprehensive review on solid particle receivers of concentrated solar power," *Renewable and Sustainable Energy Reviews* vol. 116, no. 109463, 2019, doi: https://doi.org/10.1016/j.rser.2019.109463.

[21] A. Calderón *et al.*, "High temperature systems using solid particles as TES and HTF material: A review," *Applied Energy* vol. 213, pp. 100-111, 2018, doi: https://doi.org/10.1016/j.apenergy.2017.12.107.

[22] N. P. Siegel, C. K. Ho, S. S. Khalsa, and G. J. Kolb, "Development and evaluation of a prototype solid particle receiver: On-sun testing and model validation," *Journal of Solar Energy Engineering*, vol. 132, no. 021008, pp. 1-8, 2010, doi: https://doi.org/10.1115/1.4001146.

[23] C. K. Ho *et al.*, "Particle mass flow control for high temperature concentrating solar receivers," Sandia National Laboratories, 2018.

[24] R. Shaeffer, B. Mills, L. Yue, and C. K. Ho, "Evaulation of performance factors for a multistage falling particle receiver," in *ASME 2020 14th International Conference on Energy Sustainability ES2020*, Virtual, Online, June 17–18 2020: ASME, doi: https://doi.org/10.1115/ES2020-1692.

[25] J.-S. Kim, W. Gardner, D. Potter, and Y. C. S. Too, "Design of a multi-stage falling particle receiver with truncated-cone geometry," in *SolarPACES*, Daegu, South Korea, October 1 - 4 2019, vol. 2303, no. 030023: AIP Conference Proceedings, doi: https://doi.org/10.1063/5.0029524.

[26] C. K. Ho *et al.*, "On-Sun Performance Evaluation of Alternative High-Temperature Falling Particle Receiver Designs," *Journal of Solar Energy Engineering*, vol. 141, no. 011009, 2019, doi: https://doi.org/10.1115/1.4041100.

[27] C. K. Ho *et al.*, "On-sun testing of an advanced falling particle receiver system," in *SolarPACES 2015*, Cape Town, South Africa, October 13 - 16 2015, vol. 1734, no. 030022 AIP Conference Proceedings, doi: https://doi.org/10.1063/1.4949074.

[28] H. Al-Ansary *et al.*, "On-sun experiments on a particle heating receiver with red sand as the working medium," in *SolarPACES 2017*, Santiago, Chile, September 26 - 29 2017, vol. 2033, no. 040002: AIP Conference Proceedings, doi: https://doi.org/10.1063/1.5067038.

[29] C. K. Ho *et al.*, "Performance evaluation of a high-temperature falling particle receiver," in "ASME 2016 Power & Energy Conference & Exhibition," Sandia National Laboratories, 2016.

[30] H. Al-Ansary *et al.*, "Study of the optimum discrete structure configuration in obstructed flow particle heating receivers," in *SolarPACES*, Daegu, South Korea, September 28 - October 2 2020, vol. 2303, no. 030001: AIP Conference Proceedings, doi: https://doi.org/10.1063/5.0029145.

[31] G. Flamant *et al.*, "Dense suspension of solid particles as a new heat transfer fluid for concentrated solar thermal plants: on-sun proof of concept," *Chemical Engineering Science*, vol. 102, pp. 567-576, 2013, doi: https://doi.org/10.1016/j.ces.2013.08.051.

[32] I. P. López *et al.*, "On-sun first operation of a 150 kWth pilot solar receiver using dense particle suspension as heat transfer fluid," in *SolarPACES* Cape Town, South Africa, October 13 - 16 2015, vol. 1734, no. 030028: AIP Conference Proceedings, doi: https://doi.org/10.1063/1.4949080.

[33] G. Flamant, "Fluidized bed-in-tube solar receiver and the « Next-CSP » solar loop.," in "US Department of Energy's Generation 3 CSP Summit," August 25-26, 2021 2021.

[34] B. Boissiere, R. Ansart, D. Gauthier, G. Flamant, and M. Hemati, "Experimental hydrodynamic study of gas-particle dense suspension upward flow for application as new heat transfer and storage fluid," *The Canadian Journal of Chemical Engineering*, vol. 93, pp. 317-330, 2015, doi: https://doi.org/10.1002/cjce.22087.

[35] K.-H. Funken, B. Pohlmann, E. Luepfert, and R. Dominik, "Application of concentrated solar radiation to high temperature detoxification and recycling processes of hazardous wastes," *Solar Energy*, vol. 65, no. 1, pp. 25-31, 1999, doi: https://doi.org/10.1016/S0038-092X(98)00089-9.

[36] A. Meier, E. Bonaldi, G. M. Cella, W. Lipinski, D. Wuillemin, and R. Palumbo, "Design and experimental investigation of a horizontal rotary reactor for the solar thermal production of lime," *Energy* vol. 29, no. 5-6, pp. 811-821, 2004, doi: https://doi.org/10.1016/S0360-5442(03)00187-7.

[37] A. Meier, E. Bonaldi, G. M. Cella, W. Lipinski, and D. Wuillemin, "Solar chemical reactor technology for industrial production of lime," *Solar Energy* vol. 80, no. 10, pp. 1355-1362, 2006, doi: https://doi.org/10.1016/j.solener.2005.05.017.

[38] L. Amsbeck, "Private Communication," ed, 2020.

[39] J. Mellmann, "The transverse motion of solids in rotating cylinders—forms of motion and transition behavior," *Powder Technology*, vol. 118, no. 3, pp. 251-270, 2001, doi: https://doi.org/10.1016/S0032-5910(00)00402-2.

[40] G. Juarez, P. Chen, and R. M. Lueptow, "Transition to centrifuging granular flow in rotating tumblers: a modified Froude number," *New Journal of Physics*, vol. 13, no. 053055, 2011, doi: doi:10.1088/1367-2630/13/5/053055.

[41] M. Ebert *et al.*, "Upscaling, manufactuirng and test of a centrifugal particle receiver," in *ASME 2016 10th International Conference on Energy Sustainability ES2016*, Charlotte, North Carolina, June 26-30 2016, no. V001T04A007: ASME, doi: https://doi.org/10.1115/ES2016-59252.

[42] L. Amsbeck *et al.*, "First tests of a centrifugal particle receiver with a 1m2 aperture," in *SolarPACES*, Santiago, Chile, September 26 - 29 2017, vol. 2033, no. 040004: AIP Conference Proceedings, doi: https://doi.org/10.1063/1.5067040.

[43] M. Ebert *et al.*, "First on-sun tests of a centrifugal particle receiver system," in *Proceedings of the ASME 2018 Power and Energy Conference PowerEnergy* Lake Buena Vista, Florida, USA, June 24–28 2018, no. V001T11A002: ASME, doi: https://doi.org/10.1115/ES2018-7166.

[44] M. Ebert *et al.*, "Operational experience of a centrifugal particle receiver prototype," in *SolarPACES*, Casablanca, Morocco, October 1-4 2018, vol. 2126, no. 030018: AIP Conference Proceedings, pp. 1-8, doi: https://doi.org/10.1063/1.5117530.

[45] S. Pannala, M. Syamlal, and T. J. O'Brien, *Computational gas-solids flows and reacting systems : Theory, methods and practice*. Hershey - New York, 2011.

[46] S. Hicdurmaz and I. Tari, "Numerical investigation of bubbling fluidized bed to be used as thermal energy storage integrated to high-temperature concentrated solar power," *Multiphase Science and Technology*, vol. 30, no. 2-3, pp. 99 - 120, 2018, doi: 10.1615/MultScienTechn.2018024729.

[47] S. Bilyaz, "Numerical investigation of circulating fluidized bed riser hydrodynamics for concentrating solar thermal receiver applications " M.Sc. Thesis, Middle East Technical University, Ankara/Turkey, 2015.

[48] P. Bartsch and S. Zunft, "Numerical investigation of dense granular flow around horizontal tubes: qualification of CFD model with validated DEM model," *Solar Energy*, vol. 182, pp. 298-303, 2019, doi: https://doi.org/10.1016/j.solener.2019.01.087.

[49] M. Reichart, M. Neises-von-Puttkamer, R. Buck, and R. Pitz-Paal, "Numerical assessment of packing structures for gas-particle trickle flow heat exchanger for application in CSP plants," in *ASME 2021 15th International Conference on Energy Sustainability*, Virtual, Online, June 16-18 2021: ASME, doi: https://doi.org/10.1115/ES2021-62746.

[50] B. Gobereit, "Theoretische und experimentelle Untersuchungen zur Weiterentwicklung von solaren Partikelreceivern," Ph.D. Thesis, Stuttgart University, Stuttgart, Germany, 2015.

[51] D. Kunii and O. Levenspiel, *Fluidization engineering* (Series in Chemical Engineering). Butterworth—Heinemann, 1991.

[52] ANSYS, "ANSYS Theory Guide v12.0," 2009.

[53] A. G. Dixon, A. K. Gurnon, M. Nijemeisland, and E. H. Stitt, "CFD testing of the pointwise use of the Zehner–Schluender formulas for fixed-bed stagnant thermal conductivity," *International Communications in Heat and Mass Transfer*, vol. 42, pp. 1-4, 2013, doi: https://doi.org/10.1016/j.icheatmasstransfer.2012.12.013.

[54] M. D. Beer, P. G. Rousseau, and C. G. D. Toit, "A review of methods to predict the effective thermal conductivity of packed pebble beds, with emphasis on the near-wall region," *Nuclear Engineering and Design*, vol. 331, pp. 248-262, 2018, doi: https://doi.org/10.1016/j.nucengdes.2018.02.029.

[55] H.P.Zhu, Z.Y.Zhou, R.Y.Yang, and A.B.Yu, "Discrete particle simulation of particulate systems : A review of major applications and findings," *Chemical Engineering Science*, vol. 63, no. 23, pp. 5728-5770, 2008, doi: https://doi.org/10.1016/j.ces.2008.08.006.

[56] P. A. Cundall and O. D. L. Strack, "A discrete numerical model for granular assemblies," *Geotechnique* vol. 29, no. 1, pp. 47 - 65, 1979, doi: https://doi.org/10.1680/geot.1979.29.1.47.

[57] J.-F. C. Jun Ai, J. Michael Rotter, Jin Y. Ooi, "Assessment of rolling resistance models in discrete element simulations," 2011.

[58] N. G. Deen, M. V. S. Annaland, M. A. V. d. Hoef, and J. A. M. Kuipers, "Review of discrete particle modeling in fluidzed beds," *Chemical Engineering Science*, vol. 62, no. 1-2, pp. 28-44, 2007, doi: https://doi.org/10.1016/j.ces.2006.08.014.

[59] C. Kloss, C. Goniva, A. Hager, S. Amberger, and S. Pirker, "Models, algorithms and validation for opensource DEM and CFD-DEM," *Progress in Computational Fluid Dynamics* vol. 12, no. 2-3, 2012, doi: 10.1504/PCFD.2012.047457.

[60] J. Grobbel, "Modeling Solar Particle Receivers with the Discrete Element Method," Ph.D. Thesis, RWTH Aachen University, Aachen, Germany, 2019.

[61] Y. Tsuji, T. Tanaka, and T. Ishida, "Lagrangian numerical simulation of plug flow of cohesionless particles in a horizonal pipe," *Powder Technology*, vol. 71, no. 3, pp. 239-250, 1992, doi: https://doi.org/10.1016/0032-5910(92)88030-L.

[62] "LIGGGHTS(R)-PUBLIC Documentation, Version 3.X." https://www.cfdem.com/media/DEM/docu/Manual.html (accessed 2022).

[63] F. Elskamp, H. Kruggel-Emden, M. Hennig, and U. Teipel, "A strategy to determine DEM parameters for spherical and non-spherical particles," *Granular Matter*, vol. 19, no. 46, 2017, doi: https://doi.org/10.1007/s10035-017-0710-0.

[64] "LIGGGHTS Online Documentation." (accessed 2022).

[65] C. K. Ho *et al.*, "Characterization of particle flow in a free-falling solar particle receiver," *J. Solar Energy Engineering*, vol. 139, no. 2, p. 021011, 2017, doi: https://doi.org/10.1115/1.4035258.

[66] N. Jesuthasan, B. R. Baliga, and S. B. Savage, "Use of particle tracking velocimetry for measurements of granular flows: review and application," *KONA Powder and Particle Journal*, vol. 24, pp. 15-26, 2006, doi: https://doi.org/10.14356/kona.2006006.

[67] L. Sarno, Y.-C. Tai, A. Carravetta, R. Martino, M. N. Papa, and C.-Y. Kuo, "Challenges and improvements in applying a particle image velocimetry (PIV) approach to granular flows," *Journal of Physics: Conference Series*, vol. 1249, p. 012011, 2019, doi: https://doi.org/10.1016/j.apt.2018.08.014.

[68] J. A. Quinnell and J. H. Davidson, "Buoyancy driven mass transfer in a liquid desiccant storage tank," *J. Solar Energy Engineering*, vol. 135, no. 4, p. 041009, 2013, doi: https://doi.org/10.1115/1.4024249.

[69] N. Ozalp, M.-H. Chien, and G. Morrison, "Computational fluid dynamics and particle image velocimetry characterization of a solar cyclone reactor," *J. Solar Energy Engineering*, vol. 135, no. 3, p. 031003, 2013, doi: https://doi.org/10.1115/1.4023183.

[70] D. Gollin, W. Brevis, E. Bowman, and P. Shepley, "Performance of PIV and PTV for granular flow measurements," *Granular Matter*, vol. 19, no. 42, pp. 1 - 16, 2017, doi: https://doi.org/10.1007/s10035-017-0730-9.

[71] J. Heikkila and O. Silven, "A four-step camera calibration procedure with implicit image correction," in *IEEE Computer Society Conference on Computer Vision and Pattern Recognition*, San Juan, PR, USA, June 17-19 1997: IEEE, pp. 1106-1112, doi: 10.1109/CVPR.1997.609468.

[72] J. Weng, P. Cohen, and M. Herniou, "Camera calibration with distortion models and accuracy evaluation," *IEEE Transactions on Pattern Analysis and Machine Intelligence*, vol. 14, no. 10, pp. 965 - 980, 1992, doi: https://doi.org/10.1109/34.159901.

[73] L. Liebl, "Development and optimization of an optical system and an image processing code to investigate the particles motion in a solar particle receiver," M.Sc. Thesis, Karlsruhe Institute of Technology, Karlsruhe, Germany, 2020.

[74] N. T. Ouellette, H. Xu, and E. Bodenschatz, "A quantitative study of three-dimensional Lagrangian particle tracking algorithms," *Experiments in Fluids*, vol. 40, pp. 301-313, 2006, doi: https://doi.org/10.1007/s00348-005-0068-7.

[75] A. Franke, "Uebersicht und Auswahl von Technologien zur Messung von Partikelmassenstroemen in solaren Hochtemperaturreceivern," Bachelor Thesis, Stuttgart University, Stuttgart, Germany, 2021.

[76] M. V. Bagepalli, J. D. Yarrington, A. J. Schrader, Z. M. Zhang, D. Ranjan, and P. G. Loutzenhiser, "Measurement of flow properties coupled to experimental and numerical

analyses of dense, granular flows for solar thermal energy storage," *Solar Energy*, vol. 207, pp. 77-90, 2020, doi: https://doi.org/10.1016/j.solener.2020.06.062.

[77] J. Grobbel, S. Brendelberger, M. Henninger, C. Sattler, and R. Pitz-Paal, "Calibration of parameters for DEM simulations of solar particle receivers by bulk experiments and surrogate functions," *Powder Technology*, vol. 364, pp. 831-844, 2020, doi: https://doi.org/10.1016/j.powtec.2019.11.028.

[78] Z. Uykun, "Experimental and numerical investigation of thermo-mechanical properties of particles used for CSP applications " M.Sc. Thesis, Middle East Technical University, Ankara, Turkey, 2021.

[79] H. Barbri, "Pegasus Receiver Tests," in *SolarPACES*, Albuquerque NM, USA, September 27 - 30 2022: AIP Conference Proceedings.

[80] E. F. Johnson, S. Hicdurmaz, R. Buck, and B. Hoffschmidt, "Beam radiation penetration in particle beds for heat transfer modeling of a centrifugal solar particle receiver," *Journal of Quantitative Spectroscopy and Radiative Transfer*, vol. 295, no. 108403, 2022, doi: https://doi.org/10.1016/j.jqsrt.2022.108403.

[81] W. v. Antwerpen, P. G. Rousseau, and C. G. d. Toit, "Multi-sphere unit cell method to calculate the effective thermal conductivity in packed pebble beds of mono-sized spheres," *Nuclear Engineering and Design*, vol. 247, pp. 183-201, 2012, doi: https://doi.org/10.1016/j.nucengdes.2012.03.012.

[82] P. G. Rousseau, C. G. d. Toit, W. v. Antwerpen, and H. J. v. Antwerpen, "Separate effects tests to determine the effective thermal conductivity in the PBMR HTTU test facility," *Nuclear Engineering and Design*, vol. 271, pp. 444-458, 2014, doi: https://doi.org/10.1016/j.nucengdes.2013.12.015.

[83] J. C. Chen, J. R. Grace, and M. R. Golriz, "Heat transfer in fluidized beds: design methods," *Powder Technology*, vol. 150, no. 2, pp. 123-132, 2005, doi: https://doi.org/10.1016/j.powtec.2004.11.035.

[84] A. V. Gusarov, "Radiative transfer, absorption, and reflection by metal powder beds in laser powder bed processing," *Journal of Quantitative Spectroscopy & Radiative Transfer*, vol. 257, no. 107366, 2020, doi: https://doi.org/10.1016/j.jqsrt.2020.107366.

[85] J. Marti, "Gas-particle suspensions as high-temperature heat transfer media for concentrated solar power applications," Ph.D. Thesis, ETH Zurich, Zurich, Switzerland, 2015.

[86] B. Gobereit, L. Amsbeck, R. Buck, R. Pitz-Paal, M. Roeger, and H. Mueller-Steinhagen, "Assessment of a falling solid particle receiver with numerical simulation," *Solar Energy* vol. 115, pp. 505-517, 2015, doi: https://doi.org/10.1016/j.solener.2015.03.013.

[87] T. D. Hadley, Y. Pan, K.-S. Lim, and J. Orellana, "Engineering design of direct contact counter current moving bed heat exchangers," *International Journal of Mineral Processing*, vol. 142, pp. 91-100, 2015, doi: https://doi.org/10.1016/j.minpro.2015.04.018.

[88] S. Warerkar, S. Schmitz, J. Goettsche, B. Hoffschmidt, M. Reißel, and R. Tamme, "Air-sand heat exchanger for high-temperature storage," *Journal of Solar Energy Engineering*, vol. 133, no. 2, p. 021010, 2011, doi: https://doi.org/10.1115/1.4003583.

[89] T. Baumann, S. Zunft, and R. Tamme, "Moving bed heat exchangers for use with heat storage in concentrating solar plants: A multiphase model," *Heat Transfer Engineering*, vol. 35, no. 3, pp. 224-231, 2014, doi: https://doi.org/10.1080/01457632.2013.825154.

[90] W. v. Antwerpen, C. G. d. Toit, and P. G. Rousseau, "A review of correlations to model the packing structure and effective thermal conductivity in packed beds of mono-sized spherical particles," *Nuclear Engineering and Design*, vol. 240, no. 7, pp. 1803–1818, 2010, doi: https://doi.org/10.1016/j.nucengdes.2010.03.009.

[91] P. Zehner and E. U. Schluender, "Waermeleitfaehigkeit von Schuettungen bei maessigen Temperaturen," *Chem. Ing. Tech.*, vol. 42, pp. 933-941, 1970, doi: https://doi.org/10.1002/cite.330421408.

[92] P. Zehner and E. U. Schluender, "Einfluss der Waermestrahlung und des Druckes auf den Waermetransport in nicht durchstroemten Schuettungen," *Chemie Ingenieur Technik*, vol. 44, pp. 1303 - 1308, 1972, doi: https://doi.org/10.1002/cite.330442305.

[93] R. Bauer and E. U. Schluender, "Effective radial thermal conductivity of packings in gas flow. Part II: Thermal conductivity of the packing fraction without gas flow," *Int Chem Eng* vol. 18, pp. 189-204, 1978.

[94] E. F. Johnson, "Conceptual design and heat transfer investigation of a dense granular flow solar receiver " M.Sc. Thesis, Middle East Technical University, Ankara, Turkey, 2017.

[95] S. T. W. Kuruneru, Y. C. S. Too, and J.-S. Kim, "A new numerical method for determining heat transfer and packing distribution in particle heat exchangers for concentrated solar power," *International Journal of Heat and Fluid Flow*, vol. 90, no. 108805, 2021, doi: https://doi.org/10.1016/j.ijheatfluidflow.2021.108805.

[96] H. Wu, N. Gui, X. Yang, J. Tu, and S. Jiang, "Numerical simulation of heat transfer in packed pebble beds: CFD-DEM coupled with particle thermal radiation," *International Journal of Heat and Mass Transfer*, vol. 110, pp. 393-405, 2017, doi: https://doi.org/10.1016/j.ijheatmasstransfer.2017.03.035.

[97] ESSS, "Rocky v4.4 DEM Technical Manual," 2020.

[98] M. Syamlal, W. Rogers, and T. J. O'Brien, "MFIX Documentation Theory Guide," U.S. Department of Energy, 1993.

[99] F. Qi and M. M. Wright, "Particle scale modeling of heat transfer in granular flows in a double screw reactor," *Powder Technology*, vol. 335, pp. 18-34, 2018, doi: https://doi.org/10.1016/j.powtec.2018.04.068.

[100] E. F. Johnson, I. Tarı, and D. Baker, "Modeling heat exchangers with an open source DEM-based code for granular flows," *Solar Energy*, vol. 228, pp. 374-386, 2021, doi: https://doi.org/10.1016/j.solener.2021.09.067.

[101] E. F. Johnson, "Advances in modeling high temperature particle flows in concentrating solar power," Ph.D. Thesis, Middle East Technical University, Ankara, Turkey, 2021. [Online]. Available: https://hdl.handle.net/11511/89717

[102] E. F. Johnson, İ. Tarı, and D. Baker, "A monte carlo method to solve for radiative effective thermal conductivity for particle beds of various solid fractions and emissivities," *Journal of Quantitative Spectroscopy and Radiative Transfer*, vol. 250, no. 107014, 2020, doi: https://doi.org/10.1016/j.jqsrt.2020.107014.

[103] B. K. Liu, J. M. Zhao, and L. H. Liu, "Radiative heat transfer in densely packed spherical particle system by Monte Carlo method," in *16th International Heat Transfer Conference*, Beijing, China, August 10-15 2018, doi: 10.1615/IHTC16.rti.024195.

[104] J. D. Yarrington *et al.*, "Numerical analyses of high temperature dense, granular flows coupled to high temperature flow property measurements for solar thermal energy storage," *Solar Energy*, vol. 213, pp. 350-360, 2021, doi: https://doi.org/10.1016/j.solener.2020.10.085.

[105] O. B. Kovalev, A. V. Gusarov, and V. V. Belyaev, "Morphology of random packing of micro-particles and its effect on the absorption of laser radiation during selective melting of powders," *International Journal of Engineering Science*, vol. 157, no. 103378, 2020, doi: https://doi.org/10.1016/j.ijengsci.2020.103378.

[106] B. P. Singh and M. Kaviany, "Modelling radiative heat transfer in packed beds," *Int. J. Heat Mass Transfer*, vol. 35, no. 6, pp. 1397-1405, 1992, doi: https://doi.org/10.1016/0017-9310(92)90031-M.

[107] C.-A. Wang, L.-X. Ma, J.-Y. Tan, and L.-H. Liu, "Study of radiative transfer in 1D densely packed bed layer containing absorbing–scattering spherical particles," *International Journal of Heat and Mass Transfer*, vol. 102, pp. 669-678, 2016, doi: https://doi.org/10.1016/j.ijheatmasstransfer.2016.06.065.

[108] C. D. Boley, S. C. Mitchell, A. M. Rubenchik, and S. S. Q. Wu, "Metal powder absorptivity: modeling and experiment," *Applied Optics*, vol. 55, no. 23, 2016, doi: http://dx.doi.org/10.1364/AO.55.006496.

[109] J. C. Chen and S. W. Churchill, "Radiant heat transfer in packed beds," *A.I.Ch.E. Journal*, vol. 9, no. 1, pp. 35-41, 1963.

[110] N. K. Tolochko, T. Laoui, Y. V. Khlopkov, S. E. Mozzharov, V. I. Titov, and M. B. Ignatiev, "Absorptance of powder materials suitable for laser sintering," *Rapid Prototyping Journal*, vol. 6, no. 3, pp. 155-161, 2000, doi: https://doi.org/10.1108/13552540010337029.

[111] E. F. Johnson. "https://github.com/ef-johnson/Radiation-Penetration-Depth-in-Particle-Beds." (accessed 02 February 2022, 2022).

[112] S. Hicdurmaz, J. Grobbel, R. Buck, and B. Hoffschmidt, "A numerical radiation model for the centrifugal particle solar receiver," in *SolarPACES 2021*, Virtual, Online, September 27 – October 1 2021, vol. 2815: AIP Conference Proceedings pp. 100005 (1-9), doi: https://doi.org/10.1063/5.0148791.

[113] J. Howell. A catalog of radiation heat transfer configuration factors [Online] Available: http://www.thermalradiation.net/index.html

[114] G. Breitbach and H. Barthels, "The radiant heat transfer in the high temperature reactor core after failure of the afterheat removal systems," *Nuclear Technology*, vol. 49, no. 3, pp. 392 - 399, 1980, doi: http://dx.doi.org/10.13182/NT80-A17687.

[115] J. C. A. C.P. Thurgood, R.F. Mann and B.A. Peppley, "Radiative Heat Transfer in Packed-beds: the Near-wall Region," 2004.

[116] G. J. Cheng and A. B. Yu, "Particle scale evaluation of the effective thermal conductivity from the structure of a packed bed: radiation heat transfer," *Industrial & Engineering Chemistry Research*, vol. 52, pp. 12202–12211, 2013, doi: https://doi.org/10.1021/ie3033137.

[117] Y. S. Yang, J. R. Howell, and D. E. Klein, "Radiative heat transfer through a randomly packed bed of spheres by the monte carlo method," *Journal of Heat Transfer*, vol. 105, no. 2, pp. 325 - 332, 1983, doi: https://doi.org/10.1115/1.3245582.

[118] Z. Y. Zhou, A. B. Yu, and P. Zulli, "Particle scale study of heat transfer in packed and bubbling fluidized beds," *AIChE Journal*, vol. 55, no. 4, pp. 868 - 884, 2009, doi: https://doi.org/10.1002/aic.11823.

[119] E. F. Johnson, I. Tarı, and D. Baker, "Radiative heat transfer in the discrete element method using distance based approximations," *Powder Technology*, vol. 380, pp. 164–182, 2021, doi: https://doi.org/10.1016/j.powtec.2020.11.050.

[120] E. Tsotsas, "Particle-particle heat transfer in thermal DEM: Three competing models and a new equation," *International Journal of Heat and Mass Transfer*, vol. 132, pp. 939-943, 2019, doi: https://doi.org/10.1016/j.ijheatmasstransfer.2018.12.090.

[121] M. D. Beer, C. G. D. Toit, and P. G. Rousseau, "Experimental study of the effective thermal conductivity in the near-wall region of a packed pebble bed," *Nuclear Engineering and Design* vol. 339, pp. 253-268, 2018, doi: https://doi.org/10.1016/j.nucengdes.2018.09.014.

[122] M. Bahrami, M. M. Yovanovich, and J. R. Culham, "Effective thermal conductivity of rough spherical packed beds," *International Journal of Heat and Mass Transfer* vol. 49, no. 19-20, pp. 3691-3701, 2006, doi: https://doi.org/10.1016/j.ijheatmasstransfer.2006.02.021.

[123] I. Mishra, A. M. Lattanzi, C. Q. LaMarche, A. B. Morris, and C. M. Hrenya, "Experimental validation of indirect conduction theory and effect of particle roughness on wall-to-particle heat transfer," *Transport Phenomena and Fluid Mechanics*, vol. 65, 2019, doi: https://doi.org/10.1002/aic.16703.

[124] T. Tsory, N. Ben-Jacob, T. Brosh, and A. Levy, "Thermal DEM–CFD modeling and simulation of heat transfer through packed bed," *Powder Technology*, vol. 244, pp. 52-60, 2013, doi: https://doi.org/10.1016/j.powtec.2013.04.013.

[125] G. Weidenfeld, Y. Weiss, and H. Kalman, "A theoretical model for effective thermal conductivity (ETC) of particulate beds under compression," *Granular Matter*, vol. 6, pp. 121-129, 2004, doi: https://doi.org/10.1007/s10035-004-0170-1.

[126] K. J. Albrecht and C. K. Ho, "Design and operating considerations for a shell-and-plate, moving packed bed, particle-to-sCO2 heat exchanger," *Solar Energy*, vol. 178, pp. 331-340, 2019, doi: https://doi.org/10.1016/j.solener.2018.11.065.

[127] C. K. Chan and C. L. Tien, "Conductance of packed spheres in vacuum," *Heat Transfer*, vol. 95, pp. 302 - 308, 1973, doi: https://doi.org/10.1115/1.3450056.

[128] N. Sakatani, K. Ogawa, Y. Iijima, M. Arakawa, R. Honda, and S. Tanaka, "Thermal conductivity model for powdered materials under vacuum based on experimental studies," *AIP Advances*, vol. 7, no. 015310, 2017, doi: https://doi.org/10.1063/1.4975153.

[129] G. B. Batchelor and R. W. O'Brien, "Thermal or electrical conduction through a granular material," in *Proceedings of the Royal Society of London*, 1977, vol. A355, no. 1682, pp. 313 - 333, doi: https://doi.org/10.1098/rspa.1977.0100.

[130] G. J. Cheng, A. B. Yu, and P. Zulli, "Evaluation of effective thermal conductivity from the structure of a packed bed," *Chemical Engineering Science* vol. 54, pp. 4199 - 4209, 1999, doi: https://doi.org/10.1016/S0009-2509(99)00125-6.

[131] Z. Y. Zhou, A. B. Yu, and P. Zulli, "A new computational method for studying heat transfer in fluid bed reactors," *Powder Technology*, vol. 197, no. 1-2, pp. 102-110, 2010, doi: https://doi.org/10.1016/j.powtec.2009.09.002.

[132] R. Y. Yang, R. P. Zou, and A. B. Yu, "Voronoi tessellation of the packing of fine uniform spheres," *Physical Review E*, vol. 65, pp. 041302 (1-8), 2002, doi: 10.1103/PhysRevE.65.041302

[133] T. Oschmann, M. Schiemann, and H. Kruggel-Emden, "Development and verification of a resolved 3D inner particle heat transfer model for the Discrete Element Method (DEM)," *Powder Technology*, vol. 297, pp. 392-407, 2016, doi: https://doi.org/10.1016/j.powtec.2015.12.008.

[134] K. M. Chung *et al.*, "Measurement and analysis of thermal conductivity of ceramic particle beds for solar thermal energy storage," *Solar Energy Materials and Solar Cells*, vol. 230, no. 11271, 2021, doi: https://doi.org/10.1016/j.solmat.2021.111271.

[135] F. Nie, Z. Cui, F. Bai, and Z. Wang, "Properties of solid particles as heat transfer fluid in a gravity driven moving bed solar receiver," *Solar Energy Materials and Solar Cells*, vol. 200, no. 110007, 2019, doi: https://doi.org/10.1016/j.solmat.2019.110007.

[136] T. Baumann and S. Zunft, "Properties of granular materials as heat transfer and storage medium in CSP application," *Solar Energy Materials and Solar Cells,* vol. 143, pp. 38-47, 2015, doi: https://doi.org/10.1016/j.solmat.2015.06.037.

[137] W. E. Stewart, "Experimental free convection from an inclined cylinder," *Journal of Heat Transfer,* vol. 103, no. 4, pp. 817 - 819, 1981, doi: https://doi.org/10.1115/1.3244549.

[138] A. M. Clausing, "Convective losses from cavity solar receivers - comparisons between analytical predictions and experimental results," *Journal of Solar Energy Engineering,* vol. 105, no. 1, pp. 29 - 33, 1983, doi: https://doi.org/10.1115/1.3266342.

[139] A. M. Clausing, J. M.Waldvogel, and L. D. Lister, "Natural convection from isothermal cubical cavities with a cariety of side-facing apertures," *Journal of Heat Transfer,* vol. 109, no. 2, pp. 407 - 412, 1987, doi: https://doi.org/10.1115/1.3248095.

[140] A. M. Clausing, "An analysis of convective losses from cavity solar central receivers " *Solar Energy,* vol. 27, no. 4, pp. 295-300, 1981, doi: https://doi.org/10.1016/0038-092X(81)90062-1.

[141] K. L. Lee, A. Chinnici, M. Jafarian, M. Arjomandi, B. Dally, and G. Nathan, "Experimental investigation of the effects of wind speed and yaw angle on heat losses from a heated cavity," *Solar Energy,* vol. 165, pp. 178-188, 2018, doi: https://doi.org/10.1016/j.solener.2018.03.023.

[142] S.-Y. Wu, Z.-G. Shen, L. Xiao, and D.-L. Li, "Experimental study on combined convective heat loss of a fully open cylindrical cavity under wind conditions," *International Journal of Heat and Mass Transfer,* vol. 83, pp. 509-521, 2015, doi: https://doi.org/10.1016/j.ijheatmasstransfer.2014.12.029.

[143] K. L. Lee, A. Chinnici, M. Jafarian, M. Arjomandi, B. Dally, and G. Nathan, "The influence of wall temperature distribution on the mixed convective losses from a heated cavity," *Applied Thermal Engineering,* vol. 155, pp. 157-165, 2019, doi: https://doi.org/10.1016/j.applthermaleng.2019.03.052.

[144] E. Abbasi-Shavazia, J. F. Torres, G. Hughes, and J. Pye, "Experimental correlation of natural convection losses from a scale-model solar cavity receiver with non-isothermal surface temperature distribution," *Solar Energy,* vol. 198, pp. 355-375, 2020, doi: https://doi.org/10.1016/j.solener.2020.01.023.

[145] S.-Y. Wu, L. Xiao, and Y.-R. Li, "Effect of aperture position and size on natural convection heat loss of a solar heat-pipe receiver," *Applied Thermal Engineering,* vol. 31, no. 14-15, pp. 2787-2796, 2011, doi: https://doi.org/10.1016/j.applthermaleng.2011.05.004.

[146] S. Siegrist, H. Stadler, and B. Hoffschmidt, "Wind tunnel measurements of forced convective heat loss from multimegawatt cavities of solar central receiver systems," *Solar Energy,* vol. 169, pp. 607-615, 2018, doi: https://doi.org/10.1016/j.solener.2018.04.029.

[147] T. Hu, P. Jia, Y. Wang, and Y. Hao, "Numerical simulation on convective thermal loss of a cavity receiver in a solar tower power plant," *Solar Energy* vol. 150, pp. 202-211, 2017, doi: https://doi.org/10.1016/j.solener.2017.04.008.

[148] R. Flesch, H. Stadler, R. Uhlig, and R. Pitz-Paal, "Numerical analysis of the influence of inclination angle and wind on the heat losses of cavity receivers for solar thermal power towers," *Solar Energy,* vol. 110, pp. 427-437, 2014, doi: https://doi.org/10.1016/j.solener.2014.09.045.

[149] W. Wu, L. Amsbeck, R. Buck, N. Waibel, P. Langner, and R. Pitz-Paal, "On the influence of rotation on thermal convection in a rotating cavity for solar receiver applications," *Applied Thermal Engineering* vol. 70, no. 1, pp. 694-704, 2014, doi: https://doi.org/10.1016/j.applthermaleng.2014.03.059.

[150] R. Flesch, H. Stadler, R. Uhlig, and B. Hoffschmidt, "On the influence of wind on cavity receivers for solar power towers: An experimental analysis," *Applied Thermal Engineering* vol. 87, pp. 721-735, 2015, doi: https://doi.org/10.1016/j.applthermaleng.2015.05.059.

[151] N. P. Siegel, M. D. Gross, and R. Coury, "The development of direct absorption and storage media for falling particle solar central receivers," *Journal of Solar Energy Engineering,* vol. 137, no. 4(041003), 2015, doi: https://doi.org/10.1115/1.4030069.

[152] R. Buck, "Private Communication," ed, 2022.

APPENDICES

Appendix 1

Table A.1 The coefficients in Eq. (5-1) and (5-2) for particle emissivity of 0.86.

Solid Fraction	Incidence Angle	a0	a1	a2	a3	a4	b
0.05	15	-6.17E-02	1.52E-02	-6.81E-02	5.47E-03	1.44E-03	-0.14354
	30	-5.43E-02	-5.28E-04	-3.26E-02	-1.46E-03	2.37E-03	-0.07858
	45	-5.00E-02	-1.03E-03	-3.45E-02	7.74E-03	-2.64E-04	-0.05597
	60	-4.97E-02	3.34E-03	-4.51E-02	1.81E-02	-2.68E-03	-0.04736
	75	-4.91E-02	5.31E-03	-5.20E-02	2.58E-02	-4.78E-03	-0.04169
	90	-4.95E-02	6.83E-03	-5.48E-02	2.81E-02	-5.29E-03	-0.04085
0.1	15	-6.66E-02	1.29E-02	-9.89E-02	-1.07E-02	6.62E-03	-0.30195
	30	-5.62E-02	-1.07E-02	-4.57E-02	-1.42E-02	6.60E-03	-0.16429
	45	-5.30E-02	-6.04E-03	-5.79E-02	6.30E-03	1.76E-03	-0.11736
	60	-5.21E-02	-1.09E-03	-7.42E-02	2.39E-02	-2.33E-03	-0.09737
	75	-5.24E-02	3.82E-03	-8.50E-02	3.44E-02	-4.78E-03	-0.08841
	90	-5.25E-02	5.99E-03	-9.39E-02	4.33E-02	-7.13E-03	-0.08413
0.15	15	-6.74E-02	-1.53E-02	-8.41E-02	-4.42E-02	1.18E-02	-0.47371
	30	-6.09E-02	-7.46E-03	-7.89E-02	-7.07E-03	4.79E-03	-0.25833
	45	-5.70E-02	-1.19E-02	-7.38E-02	7.51E-03	9.95E-04	-0.19213
	60	-5.63E-02	-7.61E-03	-8.65E-02	2.42E-02	-2.62E-03	-0.15324
	75	-5.66E-02	1.63E-03	-1.11E-01	4.51E-02	-7.26E-03	-0.13927
	90	-5.57E-02	-2.37E-03	-1.04E-01	4.25E-02	-6.96E-03	-0.13349
0.2	15	-7.27E-02	-2.58E-02	-5.40E-02	-1.28E-01	3.32E-02	-0.71366
	30	-6.72E-02	8.35E-03	-1.27E-01	-2.91E-03	4.94E-03	-0.38799
	45	-6.28E-02	5.86E-03	-1.30E-01	2.08E-02	2.08E-04	-0.27855
	60	-6.28E-02	1.35E-02	-1.54E-01	4.89E-02	-6.18E-03	-0.22567
	75	-6.37E-02	2.80E-02	-1.91E-01	8.34E-02	-1.45E-02	-0.20382
	90	-6.41E-02	3.44E-02	-2.04E-01	9.36E-02	-1.65E-02	-0.19882
0.25	15	-7.27E-02	-4.47E-02	-1.02E-01	-9.79E-02	2.01E-02	-0.95155
	30	-6.60E-02	-4.18E-02	-7.64E-02	-4.27E-02	1.06E-02	-0.53036
	45	-6.15E-02	-4.53E-02	-7.46E-02	-1.79E-02	5.85E-03	-0.36975
	60	-5.99E-02	-4.50E-02	-8.18E-02	3.85E-03	3.57E-04	-0.30249
	75	-6.02E-02	-3.03E-02	-1.28E-01	4.89E-02	-1.09E-02	-0.27120
	90	-6.16E-02	-2.52E-02	-1.40E-01	6.00E-02	-1.37E-02	-0.26463
0.3	15	-7.84E-02	-1.67E-02	-1.86E-01	-9.59E-02	1.75E-02	-1.20911
	30	-7.20E-02	-6.50E-03	-1.73E-01	-1.13E-02	3.70E-03	-0.6611
	45	-6.76E-02	-1.94E-02	-1.50E-01	4.16E-03	2.05E-03	-0.47738
	60	-6.75E-02	-9.48E-03	-1.87E-01	5.26E-02	-9.15E-03	-0.39221
	75	-6.54E-02	-7.21E-03	-2.13E-01	8.73E-02	-1.85E-02	-0.35767
	90	-6.62E-02	3.20E-03	-2.43E-01	1.14E-01	-2.49E-02	-0.34303
0.35	15	-7.55E-02	-6.02E-02	-1.03E-01	-2.00E-01	3.73E-02	-1.56746
	30	-7.30E-02	-2.96E-02	-1.29E-01	-8.05E-02	2.04E-02	-0.82322
	45	-7.14E-02	-1.96E-02	-1.64E-01	-1.45E-02	7.23E-03	-0.59840
	60	-7.12E-02	-5.64E-03	-2.08E-01	3.91E-02	-4.62E-03	-0.49173
	75	-7.00E-02	1.05E-03	-2.36E-01	7.19E-02	-1.21E-02	-0.44068
	90	-7.03E-02	7.25E-03	-2.59E-01	9.71E-02	-1.90E-02	-0.42869

0.4	**15**	-7.24E-02	-1.07E-01	-2.78E-02	-3.13E-01	5.88E-02	-1.83826
	30	-6.67E-02	-9.20E-02	-2.90E-02	-1.77E-01	3.83E-02	-1.01960
	45	-6.54E-02	-8.02E-02	-6.06E-02	-1.09E-01	2.65E-02	-0.73746
	60	-6.64E-02	-5.21E-02	-1.38E-01	-3.01E-02	1.01E-02	-0.60496
	75	-6.79E-02	-2.89E-02	-2.06E-01	3.37E-02	-4.50E-03	-0.54697
	90	-6.94E-02	-1.38E-02	-2.43E-01	6.65E-02	-1.22E-02	-0.53278
0.45	**15**	-7.23E-02	-1.41E-01	1.84E-02	-4.44E-01	9.44E-02	-2.03312
	30	-7.39E-02	-6.95E-02	-1.12E-01	-1.72E-01	4.09E-02	-1.23030
	45	-7.20E-02	-5.19E-02	-1.64E-01	-7.54E-02	2.24E-02	-0.90409
	60	-7.14E-02	-3.88E-02	-2.20E-01	1.67E-03	4.66E-03	-0.74323
	75	-7.44E-02	-4.90E-03	-3.19E-01	9.12E-02	-1.52E-02	-0.66568
	90	-7.76E-02	2.24E-02	-3.77E-01	1.39E-01	-2.66E-02	-0.64818
0.5	**15**	-7.43E-02	-1.57E-01	2.21E-02	-4.83E-01	9.21E-02	-2.52859
	30	-7.26E-02	-1.05E-01	-5.38E-02	-2.48E-01	5.40E-02	-1.55113
	45	-7.28E-02	-8.44E-02	-1.03E-01	-1.58E-01	4.10E-02	-1.12341
	60	-7.35E-02	-6.31E-02	-1.75E-01	-6.92E-02	2.20E-02	-0.90973
	75	-7.72E-02	-1.83E-02	-2.94E-01	4.50E-02	-5.78E-03	-0.82493
	90	-7.90E-02	3.91E-03	-3.51E-01	9.22E-02	-1.65E-02	-0.80136
0.55	**15**	-6.84E-02	-2.11E-01	1.11E-01	-5.68E-01	1.01E-01	-2.80668
	30	-7.58E-02	-9.52E-02	-1.00E-01	-2.27E-01	4.15E-02	-1.79794
	45	-7.18E-02	-9.94E-02	-9.67E-02	-1.75E-01	3.99E-02	-1.29721
	60	-7.26E-02	-7.90E-02	-1.69E-01	-8.89E-02	2.37E-02	-1.07364
	75	-7.36E-02	-5.73E-02	-2.39E-01	-1.68E-02	7.67E-03	-0.97089
	90	-7.63E-02	-3.48E-02	-2.98E-01	3.55E-02	-4.64E-03	-0.92579
0.6	**15**	-8.34E-02	-9.73E-02	-1.69E-01	-4.17E-01	4.87E-02	-3.14871
	30	-7.54E-02	-1.01E-01	-1.33E-01	-2.29E-01	3.27E-02	-2.11705
	45	-7.79E-02	-6.18E-02	-2.23E-01	-1.01E-01	1.62E-02	-1.56216
	60	-7.83E-02	-3.88E-02	-3.14E-01	1.44E-02	-9.48E-03	-1.30850
	75	-8.33E-02	9.46E-03	-4.36E-01	1.26E-01	-3.48E-02	-1.18477
	90	-8.41E-02	2.36E-02	-4.83E-01	1.72E-01	-4.59E-02	-1.14286
0.65	**15**	-7.98E-02	-1.30E-01	-1.76E-01	-4.08E-01	2.03E-02	-3.53425
	30	-7.58E-02	-1.11E-01	-1.43E-01	-2.35E-01	2.19E-02	-2.53570
	45	-7.48E-02	-9.80E-02	-1.74E-01	-1.53E-01	2.02E-02	-1.88527
	60	-7.41E-02	-9.37E-02	-2.19E-01	-7.87E-02	7.66E-03	-1.53543
	75	-7.65E-02	-5.02E-02	-3.44E-01	4.08E-02	-1.96E-02	-1.37879
	90	-7.95E-02	-2.39E-02	-4.14E-01	1.05E-01	-3.60E-02	-1.34493

Appendix 2

To demonstrate the algorithm for transmission in non-uniform beds, a cross section of a particle film is shown in Figure A-2, and the number of unshaded particles is assumed to be six. The particle bed is sliced by many thin layers of a thickness t (not all shown in Figure A-2) with $t=r_p/100$ used for the CentRec simulations. For the example calculation, the heat distributed to each layer is found with Eq. A.1 – A.6, where k indicates the layer number, and k_1 to k_6 are the layer numbers corresponding to the top of (six) unshaded particles. The heat distributed to each k layer is $q_{abs,l}^{ex}(k)$, which changes based upon which region the layer is in, with respect to the regions defined by the lines k_1 to k_6.

For the first region, between k_1 and k_2, the heat distributed to the layers is found by Eq. (5-6), but it is multiplied by a factor of $1/6$, because only one out of the total 6 unshaded particles occupies this region, resulting in Eq. (A.1). For layers in the region between k_2 and k_3, each layer receives a $1/6$ distribution due to the first particle and a $1/6$ distribution due to the second particle, which are given by the first and second terms in Eq. (A.2) respectively. Likewise, Eq. (A.3) - (A.5) are for layers in between k_3 and k_6, and it has a $1/6$ term for each of the unshaded particles that exist above the k_6 line. After k_6 line, all unshaded particles receive "nonlinear" absorption weighted by a factor of 1/6, as shown in Eq. (A.6) until the topmost particle (#1) has been completely passed. Once the topmost particle (#1) has been completely passed, 1/6 of the particle film section receives "linear" absorption until the second topmost particle (#2) is completed but the absorption formula does not change further because q_{abs} defined in Eq. (5-3) covers both "nonlinear" and "linear" parts. After all unshaded particles are completed, the particle film experiences a pure "linear" transmission decay.

$$q_{abs,l}^{ex}(k) = \frac{q_{abs}((k-k_1)/100)}{6} \qquad k < k_2 \qquad \textbf{(A.1)}$$

$$q_{abs,l}^{ex}(k) = \frac{q_{abs}((k-k_1)/100)}{6} + \frac{q_{abs}((k-k_2)/100)}{6} \qquad k_2 \le k < k_3 \qquad \textbf{(A.2)}$$

$$q_{abs,l}^{ex}(k) = \frac{q_{abs}((k-k_1)/100)}{6} + \frac{q_{abs}((k-k_2)/100)}{6} + \frac{q_{abs}((k-k_3)/100)}{6} \qquad k_3 \le k < k_4 \qquad \textbf{(A.3)}$$

$$q_{abs,l}^{ex}(k) = \frac{q_{abs}((k-k_1)/100)}{6} + \frac{q_{abs}((k-k_2)/100)}{6} + \frac{q_{abs}((k-k_3)/100)}{6} + \frac{q_{abs}((k-k_4)/100)}{6} \qquad k_4 \le k < k_5 \qquad \textbf{(A.4)}$$

$$q_{abs,l}^{ex}(k) = \frac{q_{abs}((k-k_1)/100)}{6} + \frac{q_{abs}((k-k_2)/100)}{6} + \frac{q_{abs}((k-k_3)/100)}{6} + \frac{q_{abs}((k-k_4)/100)}{6} + \frac{q_{abs}((k-k_5)/100)}{6} \qquad k_5 \le k < k_6 \qquad \textbf{(A.5)}$$

$$q_{abs,l}^{ex}(k) = \frac{q_{abs}((k-k_1)/100)}{6} + \frac{q_{abs}((k-k_2)/100)}{6} + \frac{q_{abs}((k-k_3)/100)}{6} + \frac{q_{abs}((k-k_4)/100)}{6} + \frac{q_{abs}((k-k_5)/100)}{6} + \frac{q_{abs}((k-k_6)/100)}{6} \qquad k_6 \le k \qquad \textbf{(A.6)}$$

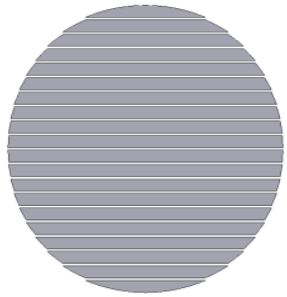

Figure A-1 A particle split by many parallel layers, resulting in spherical segments with different shape and particle volume fraction.

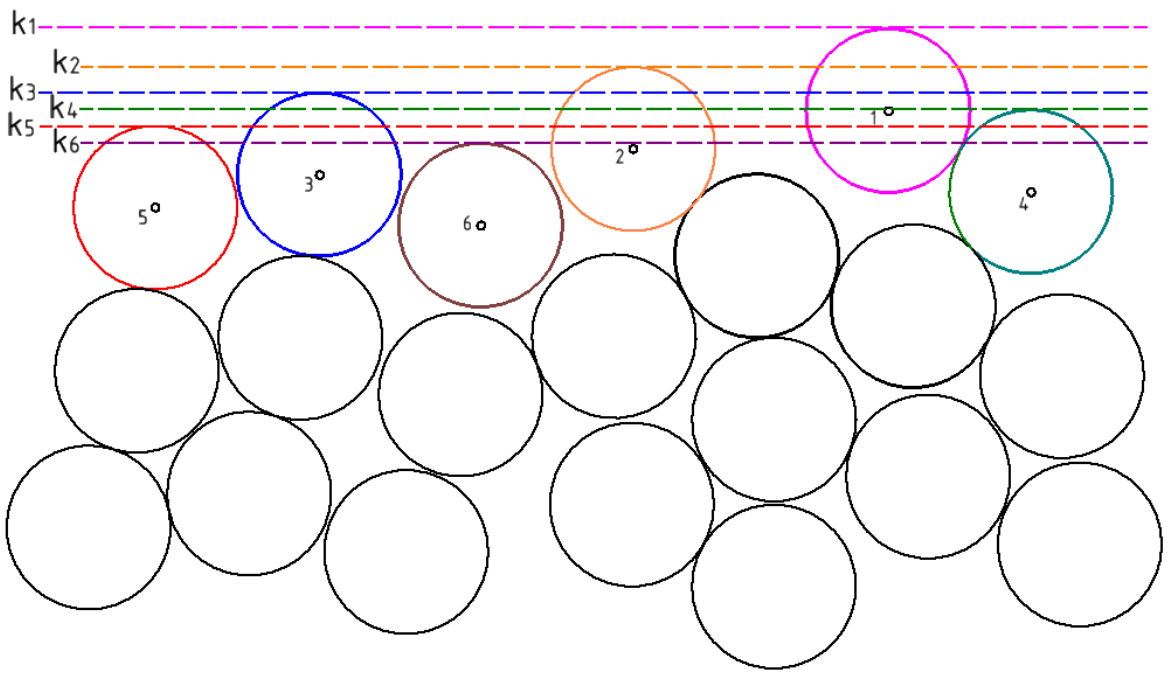

Figure A-2 A 2D schematic view of the particle film section. k_1 to k_6 are the layer numbers corresponding to tips of the total 6 unshaded particles with colored circumference.